ELASTO-VISCOPLASTICITY OF ISOTROPIC POROUS METALS

by

Antonios I. Zavaliangos

Diploma in Mechanical Engineering, National Technical University of Athens, 1986
M.Sc., Civil Engineering and Engineering Mechanics, Columbia University, 1987

Submitted to the Department of
Mechanical Engineering
In Partial Fulfillment of
the Requirements for the Degree of

Doctor of Philosophy in Mechanical Engineering

at the

MASSACHUSETTS INSTITUTE OF TECHNOLOGY

August, 1992

Signature of Author________________________________
Department of Mechanical Engineering
August, 1992

Certified by________________________________
Lallit Anand
Associate Professor of Mechanical Engineering
Thesis Supervisor

Accepted by________________________________
Ain A. Sonin, Chairman
Departmental Committee on Graduate Studies

ACKNOWLEDGEMENTS

It is my priviledge to express my appreciation to Professor Lallit Anand, my thesis advisor, for his continuous guidance all throughout the course of this work that led to this thesis. His meticulosity and high standards of professional excellence were and will be a constant source of inspiration and challenge. I also thank him for his patience and indefatigable efforts in repeatedly reading and fine tuning this dissertation. Special thanks are due to Professor D.M. Parks whose remarkable intuition made every minute of our conversations a rich source of information and ideas. Also I would like to thank Professors Rohan Abeyaratne and Stuart Brown for participating in my thesis committee.

Many thanks go to my office-mates Curt Bronkhorst, Mehrdad Haghi (my mentor in the experimental work), S. Kalidindi, Ellen Arruda, Christine Allan, Fred Haubensak, Wei Tong and Larry Cheng. They have provided a stimulating intellectual environment and a unique friendly atmosphere that helped to keep my spirit high.

Thanks to Gustavo Weber and Allan Lush for helping me to get my research started at M.I.T. Also I would like to thank the friends of Room 1-314. I feel sorry for them because we had fun and air-conditioning in the basement.

It would take several pages to thank personally the numerous friends I made in the Greek student and faculty population of Boston. They helped me to keep my strong greek accent even after 6 years in the States.

Thanks to my brother George for being able to survive the proofreading of two chapters of this thesis (then he gave up) and for babysitting his favorite niece. Also I would like to thank my uncle and aunt Elias and Alexandra Samaras for moral support and friendship.

My heartfelt thanks and love to my wife Athena for her continuous support and affection. Her fighting spirit has been an inspiration for me. Moreover, I am forever indebted to her for giving birth to our daughter Artemis. Artemis, still a baby, has given a new meaning to our lifes and has taught us so much about the preciousness

of life.

Finally this thesis is dedicated to my parents *Γιάννη* and *’Αρτεμη*, simply because everything we have belongs to those who gave us birth and brought us up.

“...ἃ κέκτηται καὶ ἔχει, πάντα εἶναι τῶν γεννησάντων καὶ θρεψαμένων...”
Πλάτωνος Νόμοι

Contents

1 Introduction **15**

1.1 Motivation 15

1.2 Gurson's Model 16

1.3 Goals of this work 19

2 Isotropic Porous Plasticity **22**

2.1 General Framework 23

2.1.1 Elasticity 26

2.1.2 Viscoplasticity 27

2.1.3 Hardening 29

2.1.4 Evolution of Porosity 30

2.1.5 Evolution of temperature θ 30

2.1.6 Elastic and Thermal Properties 31

2.2 Specific Constitutive Functions for the Matrix Material 31

2.2.1 Plastic Potential for the matrix 31

2.2.2 Hardening for the matrix material 33

2.3 Viscoplastic Potentials for Porous Materials 34

2.3.1 Recent Work 34

2.3.2 Selection of the strain rate potential 36

2.3.3 Spherical Cell Models 38

2.4 Hardening of the porous material 45

3 Time Integration Procedures 54

3.1 Euler-Backward Scheme 62

3.2 Forward Gradient Approximation 64

3.3 Jacobian Matrices 65

3.4 One element calculations 71

3.5 Implementation in ABAQUS 72

4 Example Calculations 76

4.1 Tapered Disk Compression 76

4.2 Axisymmetric Notched Bar Experiment: 82

4.3 Plastic Flow Localization In Plane Strain Tension: 88

4.4 Central Bursts During Drawing/Extrusion 94

5 Conclusions 126

A Temperature and Porosity Dependence of Elastic and Thermal Properties 129

B Further examination of the function F(X,m,f) 132

B.1 Periodic Arrays of Voids 133

B.1.1 Geometry and Matrix Model 134

B.1.2 Results 137

B.1.3 Calibration of A_3 139

B.1.4 Calibration of A_2 140

B.1.5 Intermediate Triaxialities 141

B.1.6 Discussion 141

B.2 The Differential Self Consistent Method (DSCM) 142

B.2.1 Integration 145

B.2.2 Solution of the kernel problem 145

C Shape Effects **176**

C.1 Initially spherical voids 177

C.2 Initially non spherical voids 178

D FORTRAN code **185**

E Paper 1 **211**

F Paper 2 **261**

List of Figures

2.1 Cylindrical cell model for periodic array of spherical holes (e.g. Tvergaard 1990).Axial and lateral stresses Σ_A and Σ_L are applied on the unit cell to give desired values of $\Sigma_e = |\Sigma_A - \Sigma_L|$ and $X = (\Sigma_A + 2\Sigma_L)/(3\Sigma_e)$. Note that because of the absolute value in the definition of Σ_e there are two pairs $\{\Sigma_A, \Sigma_L | \Sigma_A < \Sigma_L\}$ and $\{\Sigma_A, \Sigma_L | \Sigma_A > \Sigma_L\}$ which satisfy the desired combination of (Σ_e, X). The open circles in Figs 2.3 and 2.4 correspond to $\Sigma_A > \Sigma_L$ while open squares correspond to $\Sigma_A < \Sigma_L$. The two different stress states correspond to two different values of the third invariant of the stress deviator, $\mathrm{tr}(\mathbf{S}^3) = (2/9)(\Sigma_A - \Sigma_L)^3$. 48

2.2 Dependence of the normalized deviatoric plastic strain rate at zero triaxiality, F_0, on the strain rate sensitivity parameter, m and void volume fraction, f. The numerical results are well fit by the empirical formula, $F_0 = ((1 + 3.34f + 0.25f^2)/(1 - f^2))^{1/(2m)}$ for $0 \leq f \leq 0.10$ and $0.067 \leq m \leq 1$. 49

2.3 Normalized effective and volumetric strain rates versus porosity at X=3. 50

2.4 Yield surfaces corresponding to the rate-independent limit (25,26) of the potential for f=0.01, 0.05 and 0.10. The corresponding surfaces for the Gurson, Tvergaard, and Needleman (GTN) potential are also shown for comparison. 51

2.5 Effect of the third invariant of the stress deviator on the response of a periodic unit cell for two different triaxialities: a) X=0, b) X=3. . . . 52
2.6 Effect of hardening gradient during the expansion of a spherical cell. Comparison between analytical solution and averaging scheme of Section 2.4 53

3.1 Evaluation of the integration algorithm. Uniaxial compression. 74
3.2 Evaluation of the integration algorithm. Hydrostatic compression. . . 75

4.1 Tapered disk compression test for workability evaluation. (a) Schematic. (b) Geometry. (c) Finite element mesh. 99
4.2 Effect of strain rate, temperature and strain rate history on stress-strain behavior of fully dense Fe-2%Si. 100
4.3 Micrograph of gas atomized Fe-2%Si powder and size distribution. . . 101
4.4 Angular voids in Fe-2%Si powder compacts after sintering for 24 hours at 1000°C 102
4.5 Radial and circumferential cracks in a compressed tapered disk (HT1). A close examination of the fractured surface revealed separation along previous particle boundaries. 103
4.6 (a) Near spherical voids in Fe-2%Si powder compacts after sintering for 100 hours at 1100°C. (b) Grain size in HT2 Fe-2%Si. No significant grain growth is observed. 104
4.7 Compression of a tapered disk of porous Fe-2%Si at 800°C at a nominal compressive strain rate 0.008/sec. (a) Initial geometry and porosity (f=4.75%). (b) Load versus stroke curve. (c) Deformed specimen. (d),(e) and (f) Porosity at different radial locations after completion of experiment. 105

4.8 Comparison of the predicted and measured (a) die force versus die stroke, and (b) change in porosity versus normalized radial distance in the tapered disk compression experiment. 106

4.9 Evolution of the porosity in the tapered disk experiment ($f_0 = 4.75\%$). 107

4.10 Evolution of Σ_h/s in the tapered disk experiment ($f_0 = 4.75\%$). . . . 108

4.11 (a) Micrographs of the initial porosity in the notched tension bars. (b) Room temperature compression test on fully dense Fe-2%Si to determine the constitutive parameters for the matrix material. 109

4.12 Notched bar in tension. (a) Geometry. (b) Load versus displacement curve for various porosities. The simulations with f^* are the ones carried out with the void coalescence model of Tvergaard and Needleman [59] (c) Finite element mesh. 110

4.13 Notched bar in tension ($f_0 = 6\%$): (a – c) Porosity at different locations after failure. All three micrographs are at the same magnification. (d) Fracture surface. 111

4.14 Level contours of ϵ^p_m, Σ_h/s, and f for notched specimens with $f_0 = 6\%$ at displacement levels A and B keyed to Fig. 4.12(b). 112

4.15 Porosity distribution after failure along the centerline of the specimen in the axial z-direction in the notched bar with $f_0 = 6\%$. Points A and B are displacement levels keyed to Fig. 4.12(b). 113

4.16 (a) Load versus displacement curve for various porosities based on the GNT model with $q_1 = 1.5$ and $q_2 = 1.0$. The void coalescence model of Tvergaard and Needleman [59] has been used. (b) Sensitivity of the predictions of the GNT model on the parameters q_1 and q_2. 114

4.17 Geometry and the finite element mesh for simulation of a plane strain tension test. The mesh represents only one quarter of the specimen. All views of the specimen in subsequent figures show only region A of the complete mesh. 115

4.18 Effect of strain rate, strain rate history and temperature on the shear stress versus shear strain behavior of dense 1100 aluminum. The solid lines are experimental data from Senseny, Duffy and Hawley (1978). The dashed lines are the representation of this data using our constitutive model for dense materials. 116

4.19 Load versus nominal strain, $e = (v/l_0)t$, curves for fully dense and porous aluminum. 117

4.20 Evolution of the equivalent tensile plastic strain rate in the matrix in the (a) porous and (b) fully dense specimens during the course of the deformation at two points, one at the center of the specimen, point A, and one outside the central region on the axis of symmetry, point B. . 118

4.21 Level contours of $\dot{\epsilon}^p_m$, θ and f at two representative nominal strain levels e_1 and e_2 in the vicinity of the rapid load drop in the plane strain tension calculation for an initially porous material, $f_0 = 0.01$. . 119

4.22 Geometry of axisymmetric, two-step, cold drawing simulation with $r_1/r_0 = r_2/r_1 = 0.915$. This reduction in radii corresponds to a reduction in area of 16.3% in each pass. The nodes on the gripping surface were given a horizontal pulling velocity v, to simulate the drawing operation. 120

4.23 Defect formation in multi-step rod drawing. First step: (a) contours of the equivalent tensile plastic strain rate in the matrix $\dot{\epsilon}^p_m$, (b) pressure contours, and (c) porosity contours. 121

4.24 Defect formation in multi-step rod drawing. Second step: (a) contours of the equivalent tensile plastic strain rate in the matrix $\dot{\epsilon}^p_m$, (b) pressure contours, and (c) porosity contours. 122

4.25 Effect of lack of strain hardening, $h_0 = 0$, on drawing: (a) contours of the equivalent tensile plastic strain rate in the matrix $\dot{\epsilon}^p_m$, (b) pressure contours, and (c) porosity contours. Compare with Fig. 4.23. 123

4.26 Effect of strain rate sensitivity on defect formation during multi-step (a) rod drawing and (b) rod extrusion. 124

4.27 Effect of temperature increase due to plastic dissipation: (a) contours of the equivalent tensile plastic strain rate in the matrix $\dot{\epsilon}^p_m$, (b) pressure contours, (c) porosity contours, and (d) temperature contours. Compare with Fig. 4.23. 125

A.1 3-D periodic unit cell. 154

A.2 Predictions of the axisymmetric unit cell calculations for $f = 1\%$, for various values of m. 155

A.3 Predictions of the axisymmetric unit cell calculations for $f = 10\%$, for various values of m. 156

A.4 Comparison of axisymmetric and 3-D unit cell results at $f = 10\%$. . . 157

A.5 $F(X = 0)$ versus $1/m$, for different values of porosity. 158

A.6 (a) Prediction of the dilatation rate of the periodic cell normalized by the corresponding predictions of the spherical cell under the same pressure. (b) Same with (a) but plotted in terms of pressures needed to cause the same dilatation rate. 159

A.7 By fitting the results of the periodic array of voids at $X = 0$ and $X = \infty$ different interpolations of F can be obtained, by varying A_1. Interpolations with $A_1 = 1$ and $A_1 = 0$ are compared with the results of the periodic array of voids for $f = 0.01$ and $m = 0.33$. 160

A.8 Interpolations with $A_1 = 1$ and $A_1 = 0$ compared with the results of the periodic array of voids for $f = 0.01$ and $m = 0.1$. 161

A.9 Interpolations with $A_1 = 1$ and $A_1 = 0$ compared with the results of the periodic array of voids for $f = 0.1$ and $m = 0.33$. 162

A.10 Interpolations with $A_1 = 1$ and $A_1 = 0$ compared with the results of the periodic array of voids for $f = 0.1$ and $m = 0.1$. 163

A.11 The Differential Self Consistent Scheme. 164

A.12 The perturbation field method. 165

A.13 Finite element mesh for the solution of the kernel problem. 166

A.14 Effect of the selection of the functional form of F on the results of the DSCM. 167

A.15 Error associated with the selection of $F(X, f, m)$. 168

A.16 Variation of A_i's with porosity for $m = 0.1, 0.2, 0.33$ 169

A.17 Predictions of the DSCM, for $f = 0.01$ 170

A.18 Predictions of the DSCM, for $f = 0.10$ 171

A.19 Comparison of the predictions of the periodic array of voids against those of the DSCM, for $f = 0.01$, and $m = 0.33$ 172

A.20 Comparison of the predictions of the periodic array of voids against those of the DSCM, for $f = 0.01$, and $m = 0.1$ 173

A.21 Comparison of the predictions of the periodic array of voids against those of the DSCM, for $f = 0.10$, and $m = 0.33$ 174

A.22 Comparison of the predictions of the periodic array of voids against those of the DSCM, for $f = 0.10$, and $m = 0.1$ 175

A.24 Effect of the void evolution during the deformation of a porous material, subjected to tensile triaxiality loading. 180

A.25 Effect of the void evolution during the deformation of a porous material, subjected to compressive triaxiality loading. 181

A.26 Evolution of the shape of voids with different initial shapes. (finite element analysis of periodic axisymmetric unit cell). 182

A.27 Porosity evolution during compression of axisymmetric unit cells with initial voids of different geometries. 183

A.28 Stress response of periodic axisymmetric unit cells with initial voids of different geometries, in simple compression. 184

Chapter 1

Introduction

1.1 Motivation

Recent efforts in modeling the plasticity of isotropic, intact materials have been very successful (e.g., Brown, Kim and Anand [79], Lush, Weber and Anand [86], Weber and Anand [89]). The resulting constitutive models and corresponding numerical procedures have been employed for the prediction of (i) loads, (ii) deformed shapes, and (iii) stress and strain fields. However, this information is usually insufficient to predict the "success" of a forming operation. The success of forming operations can be limited by "failures" such as shear localization, ductile fracture, or other undesirable conditions such as lack of die fill, unwanted properties of the final products etc. (Johnson and Mamalis [29]). The most important "property" of the final product is its structural integrity. Therefore, in order to carry out any processing operation successfully and to avoid failures during service, it is important to be able to predict and minimize any kind of internal or surface damage. To predict the formation of damage in forming we need to know the properties of the material, the local state of stress, and the effect of damage on the properties of the material. In other words there is need for a plasticity theory that takes into account structural damage. Here we shall limit our attention to damage in the form of porosity that may lead to ductile fracture.

Considerable attention has been paid to the study of void nucleation, growth and coalescence as a micro-mechanism of ductile fracture (e.g., Tipper [2], Puttick [3], [4], Rogers [5], Bluhm [7]), to the development of micro-mechanical models of void growth (e.g., McClintock [12]; Rice [13]), and to the formulation of macroscopic constitutive models for microporous ductile solids (e.g., Kuhn and Downey [17], Green [20], Shima and Oyane [32], Gurson [34], Guennouni and Francois [70]), under isothermal conditions at low homologous temperatures where the matrix behavior may be adequately modeled as rate-independent. In the following section we review Gurson's model, which has recently become popular.

1.2 Gurson's Model

Gurson's constitutive model is the most widely used model available for the rate-independent, isothermal, idealization of plastic flow at low homologous temperatures. By applying limit analysis on spherical and cylindrical shells of a rigid-perfectly plastic material, an upper bound of the yield locus was obtained:

$$\left(\frac{\Sigma_e}{s_0}\right)^2 + 2f\cosh\left(\frac{3\Sigma_h}{2s_0}\right) - 1 - f^2 = 0, \tag{1.1}$$

where Σ_e and Σ_h are the equivalent and the mean part of the macroscopic stress, respectively, s_0 is the yield stress of the matrix, and f is the volume fraction of voids. This model was modified slightly by Tvergaard [43, 49] to push it towards agreement with certain aspects of his two-dimensional finite element calculations of shear localization in a square array of cylindrical holes. The modified version of equation (1.1) proposed by Tvergaard is given by:

$$\left(\frac{\Sigma_e}{s_0}\right)^2 + 2q_1\cosh\left(\frac{3q_2\Sigma_h}{2s_0}\right) - (1 + q_3f^2) = 0, \tag{1.2}$$

with $q_1 = 1.5$, $q_2 = 1.0$ and $q_3 = q_1^2$. For a recent comparison of predictions from Gurson-Tvergaard type constitutive equations and corresponding three-dimensional computations of void growth of initially spherical voids in periodic cubic arrays, see the work of Hom and McMeeking [81, 87] and Worswick and Pick [90].

The rate-independent idealization of Gurson's model was relaxed by Pan, Saje and Needleman [53], who took the response of the matrix material to be power-law viscoplastic, and proposed a flow potential for the macroscopic plastic stretching based on Gurson's yield function, as modified by Tvergaard (GNT model). The plastic potential, a function of the stress and the porosity, defines the direction and the magnitude of the plastic stretching $\mathbf{D}^p$ via the normality flow rule:

$$\mathbf{D}^p = \dot{\gamma}\frac{\partial \Phi}{\partial \mathbf{T}} \; . \tag{1.3}$$

In this case, equation (1.2) is used as the plastic potential with the yield stress s_0 substituted by an equivalent tensile stress in the matrix σ_m:

$$\Phi = \left(\frac{\Sigma_e}{\sigma_m}\right)^2 + 2q_1 \cosh\left(\frac{3q_2\Sigma_h}{2\sigma_m}\right) - (1 + q_3 f^2) \; . \tag{1.4}$$

Equation (1.4) not only provides the form of the flow potential but is also an implicit equation for the equivalent stress in the matrix σ_m by setting

$$\Phi(\Sigma_e, \Sigma_h, \sigma_m, f) = 0 \; . \tag{1.5}$$

The strain rate sensitivity is introduced by defining an equivalent tensile plastic strain rate in the matrix:

$$\dot{\epsilon}_m^p = \dot{\epsilon}_0 \left(\frac{\sigma_m}{s_0}\right)^{\frac{1}{m}} \; , \tag{1.6}$$

where m is the material stain rate sensitivity. Note that *the potential (1.4) does not explicitly depend on the strain rate sensitivity of the material.* Equation (1.6) is used to determine the parameter $\dot{\gamma}$ appearing in the flow rule (1.3) from the dissipated power expression

$$\mathbf{T} \cdot \mathbf{D}^p = (1 - f)\, \sigma_m \, \dot{\epsilon}^p_m \ , \tag{1.7}$$

which gives

$$\dot{\gamma} = \left[\frac{(1 - f)\, \sigma_m}{\mathbf{T} \cdot \dfrac{\partial \Phi}{\partial \mathbf{T}}} \right] \dot{\epsilon}^p_m \ . \tag{1.8}$$

The inadequate treatment of the rate sensitivity effects sets the limits of applicability of this model to near rate independent regimes. Although modifications of the model can be suggested making the parameters q_1 and q_2 dependent on the rate sensitivity, they are not enough to remedy the unacceptable predictions of the model at the linear viscous limit. When $m = 1$, Gurson's model predicts triaxiality dependent shear and bulk moduli for a porous material.

For purposes of numerical implementation in finite element programs, Needleman and co-workers (e.g., [58], [66]) have developed a semi-implicit "forward gradient" type tangent modulus time-integration procedure for the rate-dependent case. Using their constitutive models and computational procedures, Needleman, Tvergaard and co-workers have developed a computational capability for dealing with the mechanics of void growth as a basic failure mechanism. They have performed numerical analyses of various "standard test specimens" (e.g., Tvergaard and Needleman [59], [73]) , Becker, Needleman, Richmond, and Tvergaard [74]) to illustrate the ability of the constitutive models of porous ductile solids to simulate tensile ductile fracture in structural materials; for a recent review see Tvergaard [88].

In a recent paper Zavaliangos and Anand [106] reported on a complete framework of Gurson type models for large deformations of isotropic, thermo-elastic-viscoplastic, porous materials, and a new semi-implicit, incrementally objective time-integration procedure for these constitutive equations. Temperature dependence and coupling of thermal and mechanical effects were introduced in that work. Their time-integration algorithm offers substantial improvement over the widely used scheme of Pierce, Shih and Needleman ([58]). It is incrementally objective, it takes better account of possible changes in the direction of plastic flow, it has variable time stepping to control the stability and accuracy of the procedure, and it takes full account of thermo-mechanical coupling. Using that work Zavaliangos, Anand and Turkovich ([97]) explored the possibility of using these models in the prediction of defect formation during deformation processing. For completeness, the text of these two paper appears in Appendices E and F.

1.3 Goals of this work

Broadly defined goals of this work have been:

- The development of realistic constitutive equations, for inherently rate dependent porous materials, intended for material rate-sensitivities in the entire range spanning from nearly rate-insensitive behavior at low homologous temperatures to highly rate-dependent behavior at high homologous temperatures.
- The development of stable, accurate and efficient computational time integration procedures for this class of constitutive equations and their implementations in finite element programs.
- The verification of the models and numerical procedures.

The impact of this work is twofold:

- During deformation processing the material related defects are expected to be associated with the nucleation, growth and coalescence of pores. Although in most bulk forming operations the workpiece is deformed by a mainly compressive stress field, primary or secondary tension does occur, causing void growth and occasionally fracture. It is important to note that the computational capability presented here allows one to explore the formation of defects during both cold-working, when the material rate sensitivity is low, as well as hot-working, when the material is highly rate sensitive. Results from this work, along with similar other studies that have recently appeared in the literature represent the beginning of a truly predictive simulation capability for the formation of defects during bulk deformation processing.

- Powder metallurgy (P/M) products are inherently porous, ranging from parts with controlled density to fully dense P/M wrought metals. Components capable of combining the alloying flexibility and the near-net design features of P/M are very marketable. Hot-pressing and high precision forging of P/M preforms without flash are the main processes used in die-forging of powder metal materials. Since the material is forged from an initial ≈ 80-90 % density to near full density in a completely filled cavity, it is essential to control the densification of the workpiece, because overloading and possible fracture of the dies can easily occur [62]. Moreover the properties of high tech materials, such as high temperature superconductors, metal matrix composites [92], soft magnetic materials [96] etc., which are produced via the P/M route, depend strongly on residual porosity. The results of this work can be used to model the late stages of the densification of porous compacts.

In this work we report on:

- A complete framework for rate dependent thermo-elasto-viscoplasticity.
- The modification and generalization of the model of Haghi and Anand [100].
- The use of the periodic arrays of voids and the differential self consistent method to estimate the viscoplastic potential of porous materials.

- A new fully implicit, fully thermomechanically coupled time integration procedure for a general class of porous plasticity models.
- An implementation of the constitutive equations and time-integration procedure in a finite element program (ABAQUS).
- Example calculations and experiments which demonstrate the versatility of the proposed constitutive model and the robustness of the time-integration procedure.

Chapter 2

Isotropic Porous Plasticity

Notation

A	preexponential factor
c	specific heat
$\mathbf{D}$	stretching rate
$\mathbf{E}$	strain measure
$\dot{E}_e$	equivalent tensile strain rate
$\dot{E}_h$	hydrostatic strain rate
$\dot{E}$	equivalent tensile strain rate in the fully dense material
$\mathbf{F}$	deformation gradient
f	volume fraction of voids
$\mathcal{K}$	compliance tensor
$\mathcal{L}$	elasticity tensor
$\mathbf{L}$	spatial velocity gradient
$\mathbf{N}$	direction of the deviatoric stress
$m = 1/N$	strain rate sensitivity
Q	activation energy
R	universal gas constant
$\mathbf{R}$	rotation
$\mathbf{S}$	deviatoric stress

Σ_h	hydrostatic stress (pressure)
Σ_e	equivalent tensile stress
Σ_h	hydrostatic stress (pressure)
s	isotropic deformation resistance
$\mathbf{T}$	Cauchy stress
$\bar{\mathbf{T}}$	work equivalent stress to **E**
$\mathbf{U}$	stretching
$\mathbf{W}$	spin
X	stress field triaxiality
α	thermal expansion coefficient
$\dot{\epsilon}^p_m$	equivalent tensile plastic strain rate in the matrix
θ	temperature
μ	shear modulus
κ	bulk modulus
λ	thermal conductivity
ρ	density
Φ	plastic potential
σ_m	equivalent stress in the matrix
ω	fraction of plastic work converted to heat

2.1 General Framework

We confine our attention to moderately porous materials with volume fractions of voids less than approximately 15%. We assume that the population of voids:

- exhibits near spherical shapes,
- is randomly distributed in the material,
- exhibits narrow size distribution, with mean size much smaller that the macroscopic dimensions of the porous body,

- has an average spacing larger than other microstructural lengths.

Such a voided material may be reasonably considered to be *isotropic* in its overall macroscopic response.

At any time, the variables governing the response of the material are taken to be:

a) the deformation gradient $\mathbf{F}$, which is defined as the macroscopic average of the local deformation gradient

$$\mathbf{F} \equiv \frac{1}{V} \int_V \mathbf{F}(\mathbf{x}) dV = \frac{1}{V} \int_S \xi \otimes \mathbf{n} \, dA \tag{2.1}$$

where ξ is the current position of a material point on the surface $\mathbf{n}dA$ of a representative macro-element with volume much larger that the volume of a void. The macroscopic deformation gradient can be derived from measurements on the surface of the macro-element. Since it is an average quantity, it may correspond to many different motions of the material.

b) the absolute temperature of the matrix θ. The temperature θ is an average of the temperature distribution in the matrix. The temperature gradients are assumed to be small (i.e., they do not correspond to significant temperature differences over lengths comparable to the spacing of voids). This assumption may imply a restriction on the deformation rate. At ultra high strain rates the heat generation due to plasticity may give rise to temperature gradients in the material around the voids that can not be smoothed out by the heat conduction.

c) a list of variables describing the response of the material. In the case of isotropic porous materials this list consists of (i) the plastic deformation gradient $\mathbf{F}^p$, with $\det\mathbf{F}^p > 0$, and (ii) the scalars (s, f) that describe the most representative aspects of the underlying microstructure.

- The variable s has the physical dimensions of stress and represents an "average" isotropic resistance to plastic flow offered by the *matrix material.* The presence of voids causes strong variations of the local isotropic resistance of the matrix. The exact description of the macroscopic behavior of the porous material requires a detailed knowledge of the spacial distribution of the local isotropic resistance of the matrix. However this is not feasible. When the gradients of the local isotropic deformation resistance are mild, s represents an "averaged" measure of the deformation resistance offered by the matrix.

- The variable f provides a first order description of the porosity and corresponds to the volume fraction of voids, which can be experimentally measured:

  $$f = \frac{V_v}{V_v + V_m}$$

  where V_v is the volume of voids and V_m is the volume of the matrix. By using a single scalar parameter, the effects of void shape and porosity distribution statistics can not be taken into account. Although under certain conditions these effects can be significant, they require higher order representations (e.g. tensorial measures of porosity, two-point correlation functions [44], or the orientation distribution function [42]) and will not be considered here.

The rate-dependent constitutive model that we shall consider consists of an equation for the stress, and coupled equations for the variables ($\mathbf{F}^p$, s, f). The evolution equation for the temperature is provided by the equation for balance of energy. In this work, the "direction" of plastic flow is taken to be normal to a plastic potential surface. No yield condition and switching rules are employed. Plastic flow is assumed to occur for all non-zero values of stress, although at low stresses the rate of flow may be immeasurably small. This rate-dependent model belongs to the so-called class of "unified constitutive equations" in which "plasticity" and "creep" are unified, in that they are described by the same set of flow and evolutionary equations.

2.1.1 Elasticity

When elastic strains remain small, the hypoelastic form of the constitutive equation for stress is a good approximation for metals. However, it has long been recognized that, in the absence of plastic flow, hypoelastic equations for stress lead to dissipation. For this reason, and also since even metals can undergo large elastic dilational changes under certain conditions, we will use a total hyperelastic equation for the stress. From the numerical integration point of view, the hyperelastic formulation is inherently objective and therefore superior to the hypoelastic one[1]. The only disadvantage of the hyperelastic formulation is that the value of $\mathbf{F}^p$ must be carried along during the computation.

The elastic response of the material is given by:

$$\bar{\mathbf{T}} = \mathcal{L}[\mathbf{E}^e - \mathbf{E}^\theta] \tag{2.2}$$

where $\mathcal{L}$ is the elasticity tensor. For isotropic material $\mathcal{L} \equiv 2\mu\mathcal{I} + \{\kappa - (2/3)\mu\}\mathbf{1} \otimes \mathbf{1}$, with $\mu = \hat{\mu}(\theta, f)$, $\kappa = \hat{\kappa}(\theta, f)$, $\mathbf{1}$, and $\mathcal{I}$, the shear modulus, the bulk modulus, the second order identity, and the fourth order identity, respectively. $\bar{\mathbf{T}}$ and $\mathbf{E}^e$ is an elastic work conjugate pair of stress and strain measures. It has been shown (Anand [37, 64], that the selection of the logarithmic strain measure can incorporate moderate strain nonlinearities and makes the hyperelastic stress-strain relation an excellent generalization of the classical Hooke's law. From the multiplicative decomposition of the deformation gradient

$$\mathbf{F} = \mathbf{F}^e\mathbf{F}^p \tag{2.3}$$

---

[1] The formulation of time-integration schemes which ensure objectivity during computations has been bothersome. A detailed examination of this issue and suggested solutions were presented recently by Weber, Lush, Zavaliangos and Anand [84].

the elastic part can be obtained by

$$\mathbf{F}^e = \mathbf{F}\mathbf{F}^{p-1} \ , \tag{2.4}$$

and admits the polar decomposition:

$$\mathbf{F}^e = \mathbf{R}^e\mathbf{U}^e \ . \tag{2.5}$$

Then the logarithmic strain is defined by:

$$\mathbf{E}^e = \ln\mathbf{U}^e \ , \tag{2.6}$$

where $\mathbf{U}^e$ is the elastic right stretch tensor.

The elastic work conjugate stress measure to the logarithmic strain is given by:

$$\bar{\mathbf{T}} = \mathbf{R}^{eT}(\det\mathbf{U}^e)\mathbf{T}\mathbf{R}^e \ , \tag{2.7}$$

where $\mathbf{T}$ is the applied Cauchy stress.

In equation (2.2), $\mathbf{E}^\theta$ is the contribution of thermal expansion. In an isotropic porous material thermal expansion is independent of porosity (see for example the self-consistent argument of Budiansky[1970]), therefore:

$$\mathbf{E}^\theta(\theta, f) = \mathbf{E}^\theta(\theta) = A(\theta)\mathbf{1} = \alpha(\theta_0,\ \theta)(\theta - \theta_0)\mathbf{1} \tag{2.8}$$

where $\alpha(\theta_0,\ \theta) = \bar{\alpha}|_{\theta_0}^{\theta}$ is the mean thermal expansion coefficient between θ_0 and θ.

2.1.2 Viscoplasticity

The evolution equation for the plastic part of the deformation gradient ("flow rule") is given by

$$\begin{aligned}\dot{\mathbf{F}}^p &= \mathbf{L}^p\mathbf{F}^p, \qquad \mathbf{L}^p = \mathbf{W}^p + \mathbf{D}^p\,, &(2.9)\\ \mathbf{W}^p &= \mathbf{0}\,, &(2.10)\\ \mathbf{D}^p &= \frac{\partial\Phi}{\partial\bar{\mathbf{T}}}\,, &(2.11)\end{aligned}$$

where

$$\Phi = \hat{\Phi}\left(\bar{\mathbf{T}}, s, f, \theta\right) \tag{2.12}$$

is a viscoplastic potential function. For an isotropic material, the function Φ is isotropic , therefore it depends on the stress $\bar{\mathbf{T}}$ only through its invariants. Neglecting the effect of the third invariant:

$$\Phi = \hat{\Phi}(\Sigma_e, \Sigma_h, s, f, \theta, m) \tag{2.13}$$

where $\Sigma_h = (1/3)\ \mathrm{tr}\ \bar{\mathbf{T}}$ is the pressure, and with $\bar{\mathbf{S}} = \bar{\mathbf{T}} - \Sigma_h\mathbf{1}$, defining the deviator of $\bar{\mathbf{T}}$, $\Sigma_e = \sqrt{(3/2)\,\bar{\mathbf{S}}\cdot\bar{\mathbf{S}}}$, is the effective stress. With Φ given by equation (2.13) the plastic stretching tensor $\mathbf{D}^p$ is given by:

$$\mathbf{D}^p = \sqrt{\frac{3}{2}}\dot{E}_e^p\bar{\mathbf{N}} + \frac{1}{3}\dot{E}_h^p\mathbf{1} \tag{2.14}$$

where

$$\bar{\mathbf{N}} = \sqrt{\frac{3}{2}}\frac{\bar{\mathbf{S}}}{\Sigma_e} \tag{2.15}$$

$$\dot{E}_e^p \equiv \sqrt{\frac{2}{3}\mathbf{D}^{p\prime}\cdot\mathbf{D}^{p\prime}} = \frac{\partial\Phi}{\partial\Sigma_e} \tag{2.16}$$

$$\dot{E}_h^p \equiv \mathrm{tr}\mathbf{D}^p = \frac{\partial\Phi}{\partial\Sigma_h} \tag{2.17}$$

2.1.3 Hardening

To formulate the evolution equation for the matrix deformation resistance of a porous material, we first define an ***equivalent stress in the matrix.*** This variable characterizes the severity of the stress state, "felt" by the matrix due to the amplification of the macroscopic stress field by the presense of porosity. It can be defined via the equality of the macroscopic and microscopic dissipated power:

$$\bar{\mathbf{T}} \cdot \mathbf{D}^p = \frac{1-f}{V_{matrix}} \int_{V_{matrix}} \sigma \dot{\epsilon}^p dV \tag{2.18}$$

where σ and $\dot{\epsilon}^p$ are the equivalent tensile stress and equivalent plastic strain rate at each point in the matrix.

Let σ_m be the equivalent stress in the matrix and $\dot{\epsilon}^p_m$ the equivalent plastic strain rate in the matrix. These variable give an "overall measure" of the stress and strain rate state of the matrix. Their product is equal to the average dissipated power in the matrix per unit volume:

$$\sigma_m \dot{\epsilon}^p_m = \frac{1}{V_{matrix}} \int_{V_{matrix}} \sigma \dot{\epsilon}^p dV \tag{2.19}$$

These variables are assumed to be related by:

$$\dot{\epsilon}^p_m = \frac{\partial \phi_{matrix}}{\partial \sigma_m} = \hat{\dot{\epsilon}}^p_m(\sigma_m, \theta, s) \tag{2.20}$$

where ϕ_{matrix} is the plastic potential for the matrix. Combining equations (2.11, 2.18, 2.20, 2.19) we arrive at the following equation:

$$(1-f)\sigma_m \frac{\partial \phi_{matrix}}{\partial \sigma_m} = \mathbf{T} \cdot \frac{\partial \Phi}{\partial \mathbf{T}} \tag{2.21}$$

which is an implicit equation for σ_m. With σ_m so defined and $\dot{\epsilon}^p_m$ defined in equation (2.20) the evolution of the deformation resistance of the matrix material is taken to be governed by:

$$\dot{s} = h(\sigma_m, \theta, s)\dot{\epsilon}^p_m - \dot{r}(\theta, s) \tag{2.22}$$

The function h governs the rate of strain hardening and dynamic recovery. The function $\dot{r}$ governs the rate of static recovery. The initial value of s is temperature dependent and is denoted by $s_0(\theta)$.

2.1.4 Evolution of Porosity

From plastic incompressibility of the matrix and the balance of mass, we obtain:

$$\det \mathbf{F}^p = \frac{1 - f_0}{1 - f} \tag{2.23}$$

The time differentiation of this equation provides the evolution equation for f is

$$\dot{f} = (1 - f)\ \mathrm{tr}\,\mathbf{D}^p. \tag{2.24}$$

In order to model void nucleation effects, additional terms can be introduced in the right hand side of this equation (e.g., [59]). However this possibility is not pursued here.

2.1.5 Evolution of temperature θ

From the equation of energy balance and Fourier's law of heat conduction we obtain:

$$\dot{\theta} \doteq (\rho c)^{-1}\ \{\mathrm{div}\,(\lambda\, \mathrm{grad}\theta) + \omega\, \mathbf{T} \cdot \mathbf{D}^p\}\,, \tag{2.25}$$

where $c = \hat{c}(\theta, f)$ is the specific heat, and $\lambda = \hat{\lambda}(\theta, f)$ is the thermal conductivity. Also ω is a scalar in the range $0.85 \leq \omega \leq 1$ representing the fraction of plastic work converted to heat. The rest of the plastic work increases the configuration energy associated with the generation and multiplication of dislocations. For convenience this variable is taken to be a constant.

2.1.6 Elastic and Thermal Properties

From the constitutive framework for the rate and temperature dependent deformation behavior for isotropic porous metals outlined above, it is clear that to complete the thermo-elastic part of the constitutive model we need to provide specific forms of the functions $\mu = \hat{\mu}(\theta, f)$, $\kappa = \hat{\kappa}(\theta, f)$, and $\alpha = \hat{\alpha}(\theta, f)$ for the shear modulus, the bulk modulus, and the coefficient of thermal expansion, respectively. Also, for the thermal part of the problem we need to specify the functions $\rho = \hat{\rho}(\theta, f)$, $c = \hat{c}(\theta, f)$, and $\lambda = \hat{\lambda}(\theta, f)$ for the mass density, specific heat and the thermal conductivity. The results of theoretical estimates for the dependence of $\mu, \kappa, \alpha, \rho, c,$ and λ on f and the corresponding properties of the matrix material, based on "self-consistent" calculations for a macroscopically isotropic composite of a random dispersion of roughly spherical holes in a matrix material and are given in appendix A.

2.2 Specific Constitutive Functions for the Matrix Material

2.2.1 Plastic Potential for the matrix

In this section we adopt specific forms for the constitutive functions of the viscoplastic potential and the evolution of the deformation resistance s. In the limit of a fully dense solid, the potential function Φ has the classical power-law form:

$$\phi_{matrix} \left(\equiv \lim_{f \to 0} \hat{\Phi} \right) = \frac{\dot{\epsilon}_o \, s}{1/m + 1} \left(\frac{\Sigma_e}{s} \right)^{1/m+1} , \tag{2.26}$$

with

$$\dot{\epsilon}_o = \hat{\dot{\epsilon}}_o(\vartheta), \quad m = \hat{m}(\theta) , \tag{2.27}$$

where $\dot{\epsilon}_o$ and m are temperature dependent reference strain rate and strain rate sensitivity parameters, respectively. These properties should be preserved in the representation of macroscopic response of the porous material by the function Φ. The plastic stretching for the fully dense material characterized by this potential is:

$$\mathbf{D}^p = \frac{\partial \phi_{matrix}}{\partial \bar{\mathbf{T}}} = \sqrt{\frac{3}{2}} \dot{E}^p \bar{\mathbf{N}} , \tag{2.28}$$

where $\bar{\mathbf{N}}$ is given by equation (2.15) and

$$\dot{E}^p = \dot{\epsilon}_o \left\{ \frac{\Sigma_e}{s} \right\}^{1/m} \tag{2.29}$$

is the effective plastic strain rate.

For absolute temperatures $\theta \geq 0.6\theta_m$, where θ_m is the melting (solidus) temperature of the material, it is common to represent the effect of the temperature θ on the reference strain rate $\dot{\epsilon}_0$ by the Arrhenius expression

$$\dot{\epsilon}_0(\theta) = A \exp\left(-\frac{Q}{R\theta}\right), \quad \text{for} \quad \theta \geq 0.6\theta_m, \tag{2.30}$$

where the *constant* parameters A and Q are a pre-exponential factor and an activation energy, respectively, and R is the universal gas constant.

When the temperature sensitivity of $\dot{\epsilon}_0$ is expressed in such an Arrhenius like expression, it has been found that although it is reasonable to consider the activation energy Q to be approximately constant at high homologous temperatures, at temperatures $\theta \leq 0.6\theta_m$, Q becomes temperature sensitive[2]. Miller has suggested the following functional form for the temperature sensitivity of $\dot{\epsilon}_0$ in pure metals for

---

[2] Another, perhaps more physical, possibility is to model the activation energy to be *stress dependent* at low temperatures (e.g. Cocks, Ashby and Argon [16]). We do not follow such a possibility here, but adopt instead the simple phenomenological representation suggested by Miller [30].

$\theta < 0.6\theta_m$:

$$\dot{\epsilon}_0(\theta) = A\exp\left\{\left[-\frac{Q}{0.6\theta_m R}\right]\left[\ln\left(\frac{0.6\theta_m}{\theta}\right)+1\right]\right\}, \quad \text{for} \quad \theta \leq 0.6\theta_m, \tag{2.31}$$

with the same value for Q as in equation (2.30) above.

2.2.2 Hardening for the matrix material

Based on the work of Anand [45] and Brown, Kim and Anand [79] we model the evolution for the deformation resistance of the matrix material s by:

$$\dot{s} = h\,\dot{\epsilon}^p, \tag{2.32}$$

with

$$h = h_0\ |1-(s/s^*)|^q\ \mathrm{sign}\,(1-(s/s^*)), \quad s^* = \tilde{s}\left[\frac{\dot{\epsilon}^p}{\dot{\epsilon}_o}\right]^n, \tag{2.33}$$

where $h_o, q, \tilde{s}$ and n are hardening parameters.

For the materials and the strain rate and temperature ranges examined by Brown *et al.* [79], the static recovery function $\dot{r}$ in equation (2.22) was shown not to be of significance. This constitutive model for dense materials has been shown to be capable of accurately predicting (a) strain rate sensitivity, (b) temperature sensitivity, (c) strain rate and temperature history effects, and (d) strain hardening together with the restoration process of dynamic recovery in the hot-working regime. As we shall see in Chapter 4, the phenomenological constitutive framework for the matrix material described above is also useful in the low homologous temperature regime, provided $\dot{\epsilon}_o$ is represented by equation (2.31), and the parameters m and n are taken to be temperature dependent.

2.3 Viscoplastic Potentials for Porous Materials

2.3.1 Recent Work

The efforts to incorporate the rate sensitivity effect have their origin in the work of Budiansky, Hutchinson & Slutsky [46] who have carried out a micro-mechanical study on the growth of a spherical void in an infinite, isotropic, incompressible, non-hardening, power-law, viscoplastic material under general axisymmetric remote stress states. Duva & Hutchinson [56], based on this work, have proposed a flow potential for the macroscopic plastic stretching of a matrix containing a dilute concentration of spherical voids.

$$\Phi = F\phi_{matrix}, \tag{2.34}$$

where ϕ_{matrix} is the power law strain rate potential of the matrix and F a function linear in the porosity f that represents the amplification of the flow due to the presense of voids. The major limitation of this proposal is that it is useful only for dilute solutions. Dilute solutions are useful only if interactions can be neglected. Void-to-void interactions are strong even for small concentrations ($f < 0.01$) rendering the range of applicability of dilute solutions unpractically small.

PonteCastañeda and Willis [77] proposed a new variational structure that yields a prescription for the effective potentials of non-linear composites in terms of the corresponding potentials for linear composites with the same microstructural distribution. As recently shown by Lee and Mear [102] the quality of these results deteriorates quickly as the matrix nonlinearity and especially the stress triaxiality increase, even for dilute solutions. Cocks [80] working in a similar way with Gurson [34] (e.g. by selecting admissible velocity fields in a sphere) presented bounds of the strain rate potential for rate-dependent porous materials. These bounds are one-sided and therefore of unknown quality. Moreover, differentiation necessary to obtain the stress-strain behavior may introduce additional error. Although the direct usefulness of the variational methods is questionable, they extended the convenient formalism of equation (2.34) for non-dilute porosities by using a strain rate potential Φ with the representation,

$$\Phi(\Sigma_e, \Sigma_h, f, m) = F(X, f, m)\phi_{matrix}(\Sigma_e) \ , \tag{2.35}$$

where $X = \Sigma_h / Sigma_e$ is the stress triaxiality and F is an elliptical interpolation of the predicted behavior at $X = 0$ and $X = \infty$ of the form

$$F = (AX^2 + B)^{(1/m+1)/2} \ . \tag{2.36}$$

Using similar forms several investigators Duva and Crow [99], Haghi and Anand [100][3], Sofronis and McMeeking [105], and Michel and Suquet [103] recently proposed models that approximate the behavior of the material under pure hydrostatic pressure by a hollow sphere subjected to external pressure. We shall refer to these kind of models as *spherical cell models.* The origin of this idea is traced back to the model proposed by Torre [1] for the prediction of the densification of powders. The advantage of this approach is that practically every detail of the behavior of the matrix material can be accounted for (e.g. strain hardening, Hewitt *et al.* [22], temperature distribution, Carroll *et al.* [67], creep, boundary and lattice diffusion, Ashby and coworkers [25], [50], [61], strain rate sensitivity and hardening, Haghi and Anand [93]).

The contribution of these four new models is the extention of the spherical cell results to triaxialities other than infinity. The behavior at zero triaxiality is approximated differently by the various spherical cell models, while the behavior in intermediate triaxialities is given by an elliptic interpolation (similar to equation (2.36)). Although these models point to the correct direction their accuracy has not been examined extensively.

---

[3] Haghi and Anand's form is slightly different.

2.3.2 Selection of the strain rate potential

The properties of convexity and homogeneity of the power-law matrix potential must be preserved in the transition from the matrix to the macroscopic potential (Hutchinson [28]). A form of $\Phi = \hat{\Phi}\ (\Sigma_e, \Sigma_h, s, f, \theta)$ that satisfies this requirement is given below:

$$\Phi = \phi_{matrix}\, F\ , \qquad \text{with} \qquad F = \hat{F}\ (X, f, m)\ , \tag{2.37}$$

where

$$X = \Sigma_h / \Sigma_e \tag{2.38}$$

is the stress triaxiality, and the function F accounts for the presence of voids. With the representation (2.37) for the macroscopic plastic potential Φ, the plastic stretching is given by:

$$\mathbf{D}^p = \dot{\epsilon}_0 \left[\frac{3}{2} \left(F - \frac{XF'}{1/m + 1} \right) \frac{\mathbf{S}}{\Sigma_e} + \frac{F'}{3(1/m+1)} \mathbf{1} \right] \left(\frac{\Sigma_e}{s} \right)^{1/m} \tag{2.39}$$

Guidance for the proper selection of the function F can be obtained from asymptotics and convexity requirements. Namely, the function F must satisfy the following requirements:

- At the fully dense limit:

$$\lim_{f \to 0} F(X, f, m) = 1 \tag{2.40}$$

- Under pure hydrostatic pressure, the condition $\mathrm{tr}\,\mathbf{D}^p \neq 0$ from equation (2.39) requires:

$$\lim_{X \to \infty} F(X, f, m) \propto X^{1/m+1} \tag{2.41}$$

  to ensure the proper limit of Φ, as X approaches infinity.

- As $f \to 0$, F must reduce to a form compatible with the dilute solution of Duva and Hutchinson ([56]).

- At the linear limit ($m = 1$) there are several known approximate solutions which must be compatible with F.

The convexity condition is satisfied if the following equation holds (Rodin and Parks [68]):

$$FF'' - \frac{1}{m+1}F'^2 > 0 \tag{2.42}$$

or

$$Y = \frac{\dot{E}_h^p}{\dot{E}_e^p} = \frac{mF'}{(m+1)F - mXF'} \quad \text{is monotonic in } X \tag{2.43}$$

There is no doubt that experimentally motivated equations for F are highly desirable. The list of variables that play a crucial role is rather long, and the number of required experiments is prohibitively high.

The theoretical derivation of constitutive equations for porous materials belongs to a larger class of problems, namely the prediction of effective properties of composites materials.

In this study we have examined in detail the accuracy of the spherical cell type of models by using calculations on periodic arrays of voids. Moreover, a refined approach to determine the plastic potential has been explored by using the differential self consistent scheme. We found that the main differences between the various models appear to occur at triaxialitites higher than ≈ 2. An effort undertaken in our group to perform high triaxiality experiments was not successful. Unfortunately, experiments that produce large plastic strains under high confining pressures, and preferably high temperature are very difficult to design and perform (for some more thoughts on this issue see Haghi's thesis [94]). Since we have no clean experimental data to verify the quality of the various models in the triaxiality range $X > 2$, we relegate the presentation and discussion of the results from the periodic arrays of voids and the differential self consistent method to Appendices B.1 and B.2.

In the following sections we concentrate on major modifications necessary for the spherical cell models.

2.3.3 Spherical Cell Models

Following the suggestions of PonteCastañeda and Willis [77] and Cocks [80] several investigators Haghi and Anand [100], Duva and Crow [99], Sofronis and McMeeking [105], Michel and Suquet [103] proposed models that attempt to account for the rate dependent behavior of porous power law solids, by using a strain rate potential of the form (2.37), where the function F is given by:

$$F = A_1 + (A_2 X^2 + A_3)^{((1/m+1)/2)}, \quad A_i = \hat{A}_i(f, m) \tag{2.44}$$

As mentioned before their common characteristic is the approximation of the behavior of the porous material under pure hydrostatic pressure with a hollow sphere loaded by external pressure. Under pure hydrostatic loading the flow potential (equations (2.37)(2.44)) gives

$$\operatorname{tr} \mathbf{D}^p = \chi \dot{\epsilon}_o \, A_2^{\frac{(1/m)+1}{2}} \left\{ \frac{|\Sigma_h|}{s} \right\}^{\frac{1}{m}}, \tag{2.45}$$

where $\chi = \operatorname{sign}(\Sigma_h)$. The function A_2 in all the models is chosen in such a way that it reproduces the analytical solution for the dilatational strain rate of a thick-walled spherical shell made from an isotropic, incompressible, power-law viscoplastic material, subjected to hydrostatic loading:

$$\operatorname{tr} \mathbf{D}^p \quad = \dot{E}_h^p = \quad \chi \left(\frac{\dot{\epsilon}_o}{s^{\frac{1}{m}}} \right) \frac{3}{2} \left[\frac{f}{(1 - f^m)^{\frac{1}{m}}} \right] \left\{ \frac{3}{2} m \, |\Sigma_h| \right\}^{1/m}. \tag{2.46}$$

In the limit of a non-hardening material ($s = s_0$), the equation above is due to Wilkinson and Ashby ([25]) For strain-hardening materials, s is a weighted average of the local deformation resistance and the solution is due to Haghi and Anand [93]. Comparing equations (2.45) and (2.46) we obtain:

$$A_2^s = (9/4)\left((1/m)\left(f^{-m}-1\right)\right)^{-\frac{2}{1+m}} \tag{2.47}$$

where the superscript s refers to the spherical cell.

The other A_i's are given in the following table:

A_1	A_3	by	Comments
0	$\frac{1+2f/3}{(1-f)^{2/(1+m)}}$	Duva and Crow [99]	A_3 from lower bound (PonteCastañeda [95])
0	$\left(\frac{1+f}{1-f}\right)^{\frac{2}{1+m}}$	Sofronis and McMeeking [105]	A_3 from FEM at X=0 on unit spherical cell
1	$g(f/m)^{\frac{2}{1/m+1}}$	Haghi and Anand [100]	$g = const$, from FEM on unit axisymmetric cell

In the proposals of Duva and Crow [99] and Michel and Suquet [103], A_3 has the same form as in the lower bound estimates for F derived by PonteCastañeda [95]. Michel and Suquet [103] state that their rational, for adopting this lower bound estimate for A_3 is that there is no exact solution for the problem of a hollow sphere under a purely deviatoric macroscopic stress state.

The estimate for A_3 in the proposal by Sofronis and McMeeking [105] is a fit to numerical finite-element results of a sphere under purely deviatoric macroscopic stress state. They state that their estimate exceeds the lower bound developed by PonteCastañeda and Willis [77] for small values of f, and approximates well the results of Duva and Hutchinson [56]. However, note that for non-hardening, ($s = s_0$), incompressible linear viscous, ($m = 1$), materials in the dilute limit, ($f \to 0$), any proposed potential should agree with the known potential (Duva and Hutchinson [56])

$$\Phi_{\text{linear viscous}} = \frac{\dot{\epsilon}_0}{2\,s_0}\,\Sigma_e^2\left\{1 + f\left(\frac{9}{4}X^2 + \frac{5}{3}\right)\right\}.$$

The potential proposed by Sofronis and McMeeking [105] does not satisfy this limit.

With $A_1 = 1$, A_2 given in the table above, and $A_3 = (f/m)^{\frac{2}{1+1/m}} \times g(f,m)$, Haghi and Anand [100] estimated the function $g(f,m)$ by fitting their numerical finite-element results for incipient ($s = s_0, f = f_0$) macroscopic effective strain rates

$$\dot{E}^p_e = \partial\Phi/\partial\Sigma_e \ ,$$

and volumetric strain rates

$$\dot{E}^p_h = \partial\Phi/\partial\Sigma_h \ ,$$

from axisymmetric unit cell calculations representing various porosities f in the range $0 \leq f \leq 0.1$, subjected to various triaxialities in the range $0 \leq X \leq 5$, but for a fixed rate sensitivity $m = 0.16$, which is a representative value for an Fe-2%Si material at 1000°C. For this high value of m they estimated that

$$g(f, m = 0.16) \approx 1.3,$$

independent of f. In the rate-independent limit $m = 0$, they estimated that g was approximately linear in f:

$$g_0(f) \equiv g(f, m = 0) \approx 1 + 3.5\, f.$$

Haghi and Anand [100] also showed (their Fig. 12) that at low porosities the choice of $A_1 = 1$ was crucial in matching their unit-cell finite element results for volumetric strain rates. For more details of that issue, see Appendix B.1.

In what follows we adopt the specific forms for A_i of Haghi and Anand [100]

$$\begin{aligned} A_1 &= 1 \ , \\ A_2 &= \frac{9}{4}\left[\frac{1}{m}\left\{f^{-m} - 1\right\}\right]^{-\frac{2}{1+m}} \ , \\ A_3 &= \left(\frac{f}{m}\right)^{\frac{2}{1+1/m}} \times \ g(f, m), \end{aligned} \tag{2.48}$$

and improve on their estimate for the function g.

We have determined this function by performing axi-symmetric unit cell calculations[4] of the type schematically depicted in Fig. 2.1, for $X = 0$. The results from the finite element unit cell calculations for the incipient $\dot{E}^p_e$ at $X = 0$, normalized by the effective plastic strain rate for a fully dense material,

$$\dot{E}^p = \partial\,\phi_{matrix}/\partial\Sigma_e = \dot{\epsilon}_0\,\left(\Sigma_e/s\right)^{1/m}$$

caused by the same macroscopic stress Σ_e, are plotted in Fig. 2.2 for various values of initial porosities, f, and inverse of the rate sensitivity parameter, m. From equations (2.37) and (2.44)

$$\frac{\dot{E}^p_e\,(X=0)}{\dot{E}^p} = F(X=0) \equiv F_0\,, \qquad \text{with} \qquad F_0 = \hat{F}_0\,(f,m)\,.$$

Our numerical results for F_0 are well fit by the empirical relation

$$F_0 = \left(\frac{1 + 3.34\,f + 0.25\,f^2}{1-f^2}\right)^{\frac{1}{2m}},$$

for f and m in the ranges $0 \leq f \leq 0.1$ and $0.0667 \leq m \leq 1.0$. The quality of the fit is shown in Fig. 2.2. Note that the quadratic dependence of F_0 on f in this expression is necessary to match the results of our numerical experiments. Also, the specific form for the denominator in this empirical expression is chosen so that the material loses all load carrying capacity as $f \to 1$.

To summarize, using equations (2.44) and (2.48), our improved estimate for the function g of Haghi and Anand [100] is:

$$g(f,m) = \left[\frac{m}{f}\,(F_0 - 1)\right]^{\frac{2}{1+1/m}} \quad \text{with} \quad F_0 = \left(\frac{1 + 3.34\,f + 0.25\,f^2}{1-f^2}\right)^{\frac{1}{2m}}, \qquad (2.49)$$

---

[4] These calculations are similar to those carried out by Haghi and Anand [100], who only reported results for a fixed value of $m = 0.16$. Details on an extensive set of the calculations can be found in Appendix B.1.

for f in the range $0 \leq f \leq 0.1$, and m in the range $0.0667 \leq m \leq 1.0$. Although our unit-cell calculations have only been performed for rate sensitivities as low as 0.0667, we will also use this form for g for lower values of $m \to 0$.

As a test of the viscoplastic potential (2.37), (2.44), (2.48), (2.49), using values for g from (2.49) corresponding to a fixed value of $m = 0.1541$ (which represents the rate sensitivity of an Fe-2% Si material at 800°C, Chapter 4.) in Fig. 2.3 we show the incipient, macroscopic effective strain rate $\dot{E}^p_e = \partial\Phi/\partial\Sigma_e$ and volumetric strain rate $\dot{E}^p_h = \partial\Phi/\partial\Sigma_h$ predicted by the viscoplastic potential for $X = 3$. In this figure, the predictions from the viscoplastic potential are compared against results from corresponding finite element unit cell calculations.

It should be noted that in comparing strain rates, we are looking at a very sensitive measure of the predictive power of the model. The predictions from the constitutive model are in reasonable agreement with the numerical experiments. We have conducted similar calculations for different values of triaxialities X and different values of rate sensitivities m, and the quality of the match between the predictions from the constitutive model and the numerical experiments is discussed in Appendix B.1

The rate independent limit of this model is given by the yield locus

$$\lim_{m\to 0} F^{\frac{1}{1+1/m}}\left(\frac{\Sigma_e}{s}\right) = 1\ . \tag{2.50}$$

As shown by Haghi and Anand [100], in the limit of rate-independent behavior, $m \to 0$, the viscoplastic potential (equations (2.37), (2.44) and (2.48)) corresponds to the yield surface

$$\left[\left\{\frac{3}{2}\frac{1}{\ln(f)}\right\}^2\left(\frac{\Sigma_h}{s}\right)^2 + g_0(f)\left(\frac{\Sigma_e}{s}\right)^2\right]^{1/2} = 1, \tag{2.51}$$

and their numerical unit-cell experiments for *a rate-independent material* with f in the range $0 \leq f \leq 0.1$ and $\Sigma_h = 0$, gave[5]

$$g_0(f) = \frac{1 + 3.34\,f + 0.25\,f^2}{1 - f^2}. \tag{2.52}$$

Note that this simple "elliptical" form (2.51) for the yield surface, reduces to the Mises form

$$\Sigma_e = s$$

for $f = 0$, and for pure hydrostatic stresses reduces to the classical result for a sphere under external hydrostatic tension

$$\Sigma_h = -\frac{2}{3}\,s\,\ln(f). \tag{2.53}$$

Fig. 2.4, which is similar to Fig. 11 in the the paper of HAGHI and ANAND (1992), shows the yield surfaces corresponding to (2.51) with g_0 given by (2.52), for various values of f, and compared with representative points on the yield surface obtained from numerical unit cell calculations for a rate-independent material. Also shown for comparison in this figure is the yield surface

$$\left[2\,q_1\,f\,\cosh\left(q_2\,\frac{3}{2}\,\frac{\Sigma_h}{s}\right) + \frac{\Sigma_e^2}{s^2} - (q_1\,f)^2\right] = 1, \tag{2.54}$$

corresponding to the GTN model with $q_1 = 1.5$ and $q_2 = 1.0$. Our simple yield surface represented by equations (2.51) and (2.52) is in substantial agreement with the points on the yield surface from the numerical experiments. The GTN model, with the widely used values of $q_1 = 1.5$ and $q_2 = 1.0$, does not capture the shape of the rate-independent yield loci as well. However, the performance of the GTN model can be improved by choosing a value $q_2 = 0.88$ ([100]).

---

[5] In the rate-independent limit Haghi and Anand [100] actually suggested the function $g_0(f) = 1 + 3.5\,f$. The difference between their suggestion, and equation (2.52), which corresponds to the limit of (2.49) as $m \rightarrow 0$, is inconsequential.

As noted earlier, it is important to recognize that material rate-sensitivity was introduced into Gurson's constitutive model by Pan *et al.* [53] only for slightly rate-sensitive behavior at low homologous temperatures. On the other hand, the constitutive model considered here is for ***inherently rate dependent materials at low or high temperatures, and is intended for material rate-sensitivities*** m ***in the entire range*** $0 \leq m \leq 1$.

While in models for the plasticity of soils, the importance of the third stress invariant has been consistently emphasized, in the corresponding formulations of porous plasticity for metals it has been a common assumption to ignore its effect. To the best of our knowledge there has been no effort to justify this assumption.

In our axisymmetric calculations axial and lateral stresses Σ_A and Σ_L are applied on the unit cell to give desired values of $\Sigma_e = |\Sigma_A - \Sigma_L|$ and $X = (\Sigma_A + 2\Sigma_L)/(3\Sigma_e)$. Note that because of the absolute value in the definition of Σ_e there are two pairs $\{\Sigma_A, \Sigma_L | \Sigma_A < \Sigma_L\}$ and $\{\Sigma_A, \Sigma_L | \Sigma_A > \Sigma_L\}$ which satisfy the desired combination of (Σ_e, X). The open circles in Figs 2.3 and 2.4 correspond to $\Sigma_A > \Sigma_L$ while open squares correspond to $\Sigma_A < \Sigma_L$. The two different stress states correspond to two different values if the third invariant of the stress deviator,

$$\mathrm{tr}(\mathbf{S}^3) = (2/9)(\Sigma_A - \Sigma_L)^3 \, . \tag{2.55}$$

Using the three dimensional unit cells employed in the Appendix B.1, we explored the dependence of the plastic potential on the third invariant of the stress deviator. In Fig. 2.5 we present the results of these calculations for two different triaxialities ($X = 0$ and $X = 3$) and strain rate sensitivities ($m = 0.1$ and $m = 0.2$). All results correspond to a porosity level of $f = 0.10$.

When the matrix material is described by the power law plastic potential (2.26) there is no effect of the third invariant if $f = 0$. Also existing solutions for the linear viscous solid (both numerical and analytical) show that there is no effect of the third invariant when $m = 1$. From our calculations we conclude that, the effect of the third invariant increases with decreasing m and increasing f, and is maximum at medium triaxialities (X$\approx$ 3).

The magnitude of the effect of the third invariant when $m = 0$ can also be seen in Fig. 2.4 where the circles and squares correspond to the maximum and minimum of the third invariant respectively. From our calculations we can conclude that in a first order approach, the effect of the third invariant is not very significant at the higher strain rate sensitivities. We expect this effect to be more important when the voids are ellipsoidal.

2.4 Hardening of the porous material

With the plastic potential given by equation (2.44), the equivalent plastic strain rate in the matrix has the same functional form as in the fully dense material (2.29) but with the macroscopic stress replaced by the equivalent stress in the matrix:

$$\dot{\epsilon}^p_m = \dot{\epsilon} \left(\frac{\sigma_m}{s} \right)^{1/m} \tag{2.56}$$

With Φ given by (2.37) and $\dot{\epsilon}^p_m$ by (2.56), equation (2.21) provides the following explicit expression for the equivalent tensile stress in the matrix:

$$\sigma_m = k\Sigma_e \quad \text{with} \quad k = \left(\frac{F}{1-f} \right)^{1/(1/m+1)} \tag{2.57}$$

The factor k may be interpreted as a dimensionless concentration factor for the equivalent stress in the matrix caused by the presence of voids. The corresponding definition of the same variable in a Gurson type model (1.4, 1.5) is ad hoc, ambiguous and does not include the effect of the strain rate sensitivity. At the contrary, the functional form of equation (2.57) reflects properly all the necessary dependencies of σ_m on the relevant material properties, the macroscopic stress field and the porosity.

Using the value of σ_m obtain this way, the value of $\dot{\epsilon}^p_m$ can be calculated by equation (2.56) and the same hardening laws used for the matrix material can be used to evolve the effective hardness of the matrix in the porous material.

With σ_m given in (2.57), and $\dot{\epsilon}^p_m$ defined in equation (2.56), the evolution equation for the deformation resistance s of the matrix material is taken to have the same form as that described in Section 2.2.2. In other words:

$$\dot{s} = h \, \dot{\epsilon}^p_m, \tag{2.58}$$

with

$$h = h_o \, |1 - (s/s^*)|^q \, \mathrm{sign}\,(1 - (s/s^*)), \quad s^* = \tilde{s} \left(\frac{\dot{\epsilon}^p_m}{\dot{\epsilon}_o} \right)^n, \tag{2.59}$$

where $h_o, q, \tilde{s}$ and n are hardening parameters that may depend on temperature.

Although the structure of our approach is attractive and clean, it is not sure whether the equation relating σ_m and $\dot{\epsilon}^p_m$ should be given by (2.56). In fact, if these two quantities represent some kind of averages of the corresponding local quantities, it is certain that when $m \neq 1$ and the stress or strain rate field gradient in the matrix is strong, then the rate of hardening differs from point to point and equation (2.56) is inaccurate [6]. Haghi and Anand [93] examined the case of a spherical cell subjected to external pressure, and proposed to represent s with an *appropriately weighted average* of the local deformation resistance. This method requires exaxct knowledge of the distribution of the local deformation resistance at every material point. However this is not easy for triaxialities different than $X = \infty$, for which there is no analytical solution.

The effect of the strain rate gradient depends on the hardening law and the triaxiality. The worst combination appears to be that of high triaxiality together with strong linear hardening. To demonstrate this effect we examined the expansion of

---

[6] In an analogous example, if a variable x has a distribution with mean $\bar{x}$ and $y = ax^b$ then the mean of y is in general section different than $a\bar{x}^b$ unless $b = 1$.

a hollow sphere made of incompressible power law material under external pressure using finite elements. A sphere with an internal radius chosen to correspond to an initial volume fraction $f_0 = 0.01$ was selected. The strain rate sensitivity was taken to be $m = 0.1674$. Linear hardening behavior was simulated by taking $q = 0$ in equation (2.33) i.e. $\dot{s} = h_0 \dot{\epsilon}^p_m$ with $h_0 = s_0$. A displacement boundary condition was imposed compatible with a macroscopic main strain rate $\dot{E}_h = 3\dot{\epsilon}_0$. If the averaging scheme presented in this section were accurate, the strain rate response of the sphere could have been predicted by using any of the spherical cell models.

In Fig. 2.6 we plot the pressure history obtained by the finite element calculation and by the spherical cell model. The difference in the two responses is due to the intense strain rate gradient. Note that the local strain rate in the matrix is proportional to $1/r^3$, where r is the radius. The large deformation near the internal surface of the spherical cell is responsible for the stong hardening around the void, causing a high macroscopic pressure response. On the other hand, the hardening rule based on equations (2.57) predicts a macroscopic deformation resistance that corresponds to an average value of the local deformation resistance and results in a lower macroscopic pressure.

As mentioned before, this case represents an extreme behavior. At lower triaxialities and with saturation hardening laws, the method presented in this section gives acceptable results.

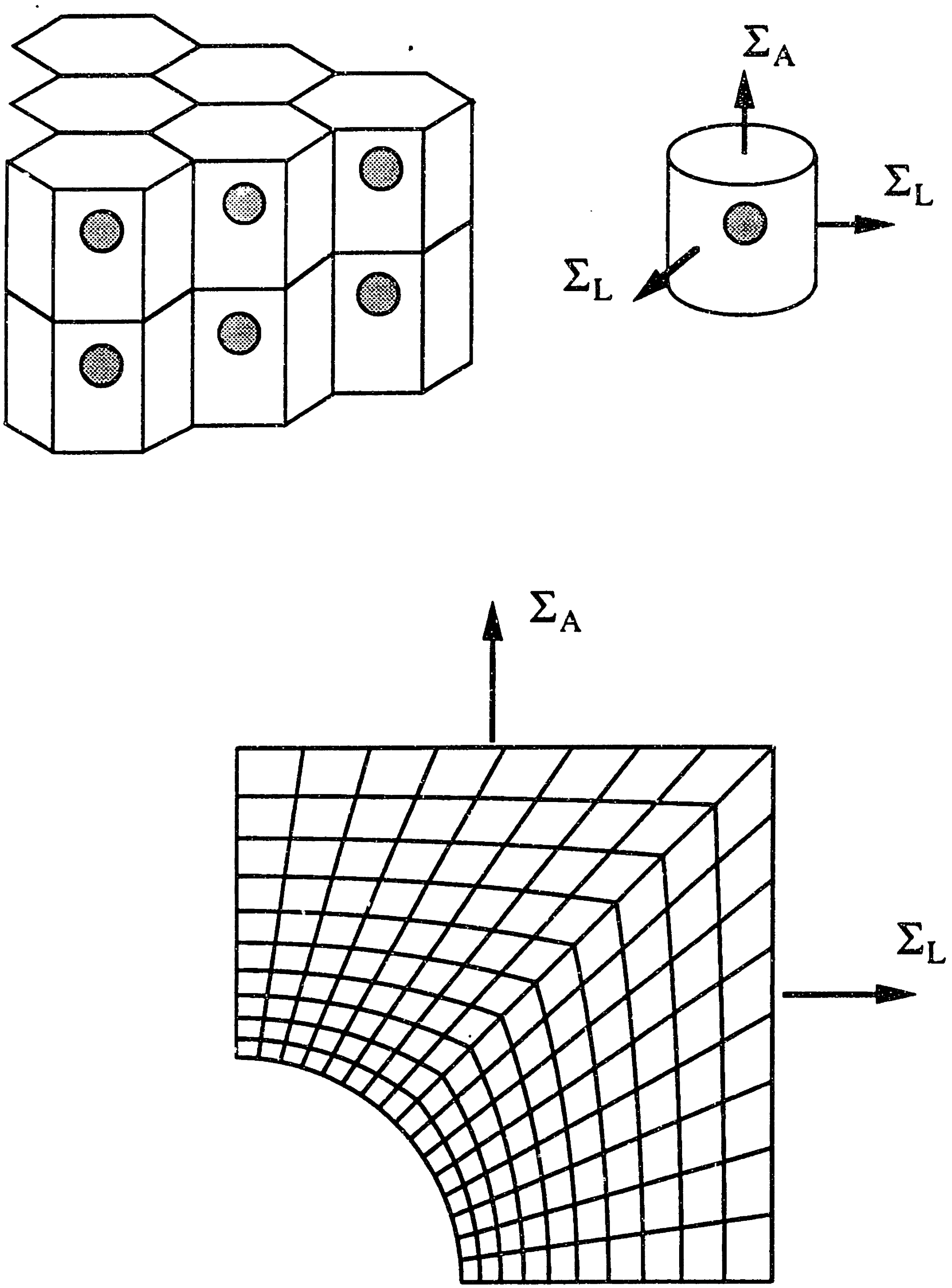

Figure 2.1: Cylindrical cell model for periodic array of spherical holes (e.g. Tvergaard 1990). Axial and lateral stresses Σ_A and Σ_L are applied on the unit cell to give desired values of $\Sigma_e = |\Sigma_A - \Sigma_L|$ and $X = (\Sigma_A + 2\Sigma_L)/(3\Sigma_e)$. Note that because of the absolute value in the definition of Σ_e there are two pairs $\{\Sigma_A, \Sigma_L | \Sigma_A < \Sigma_L\}$ and $\{\Sigma_A, \Sigma_L | \Sigma_A > \Sigma_L\}$ which satisfy the desired combination of (Σ_e, X). The open circles in Figs 2.3 and 2.4 correspond to $\Sigma_A > \Sigma_L$ while open squares correspond to $\Sigma_A < \Sigma_L$. The two different stress states correspond to two different values of the third invariant of the stress deviator, $\mathrm{tr}(\mathbf{S}^3) = (2/9)(\Sigma_A - \Sigma_L)^3$.

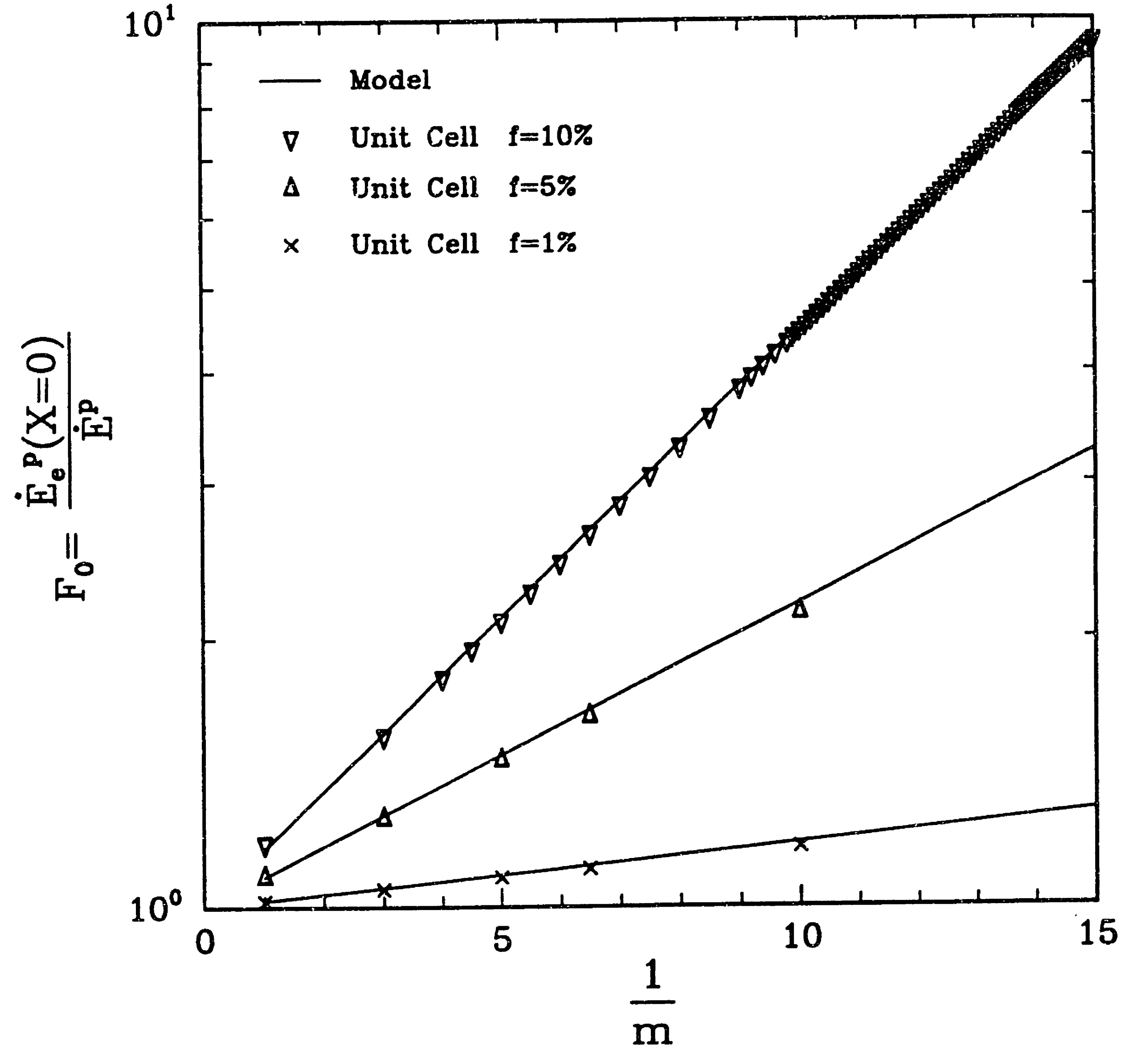

Figure 2.2: Dependence of the normalized deviatoric plastic strain rate at zero triaxiality, F_0, on the strain rate sensitivity parameter, m and void volume fraction, f. The numerical results are well fit by the empirical formula, $F_0 = ((1 + 3.34f + 0.25f^2)/(1 - f^2))^{1/(2m)}$ for $0 \leq f \leq 0.10$ and $0.067 \leq m \leq 1$.

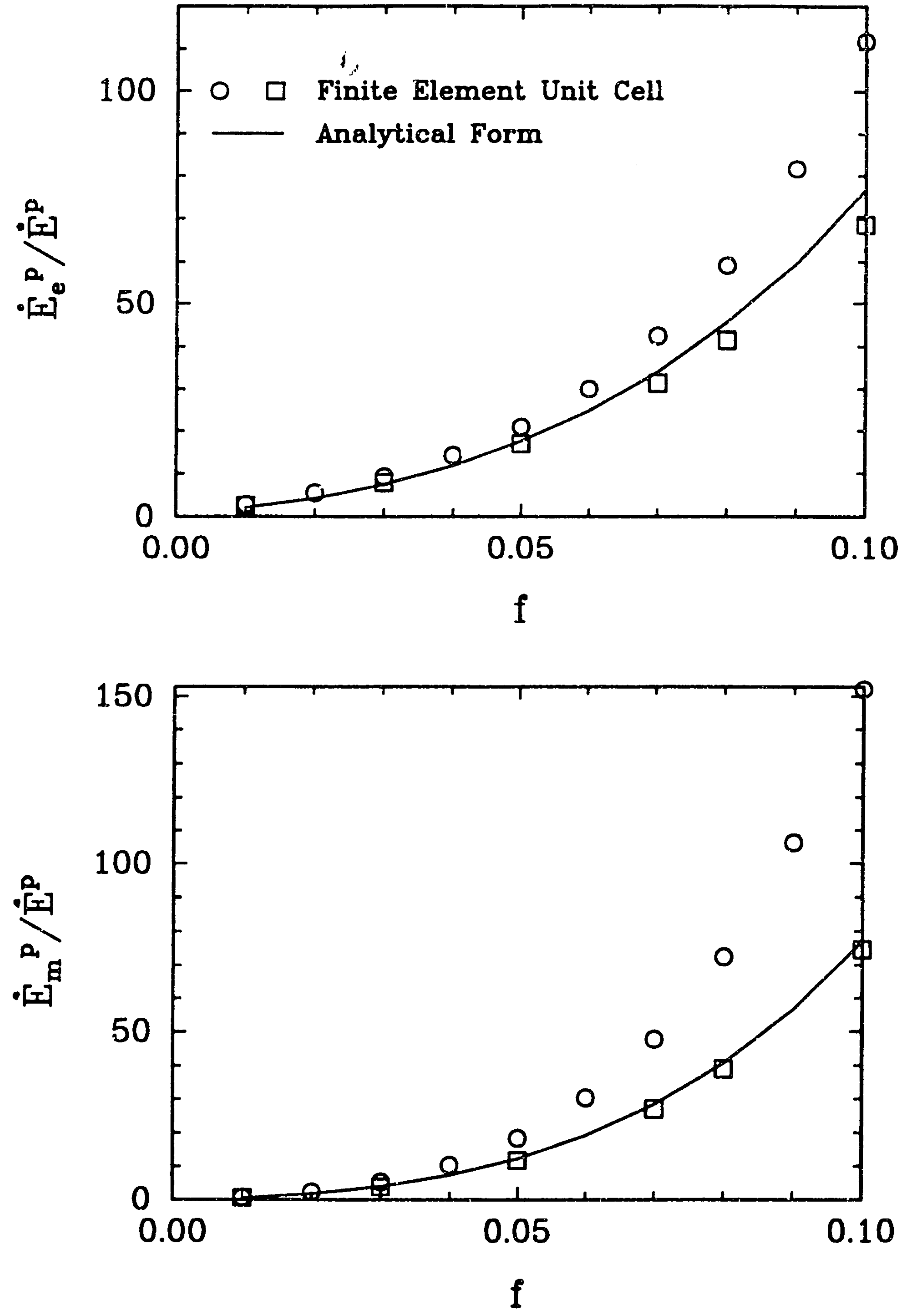

Figure 2.3: Normalized effective and volumetric strain rates versus porosity at X=3.

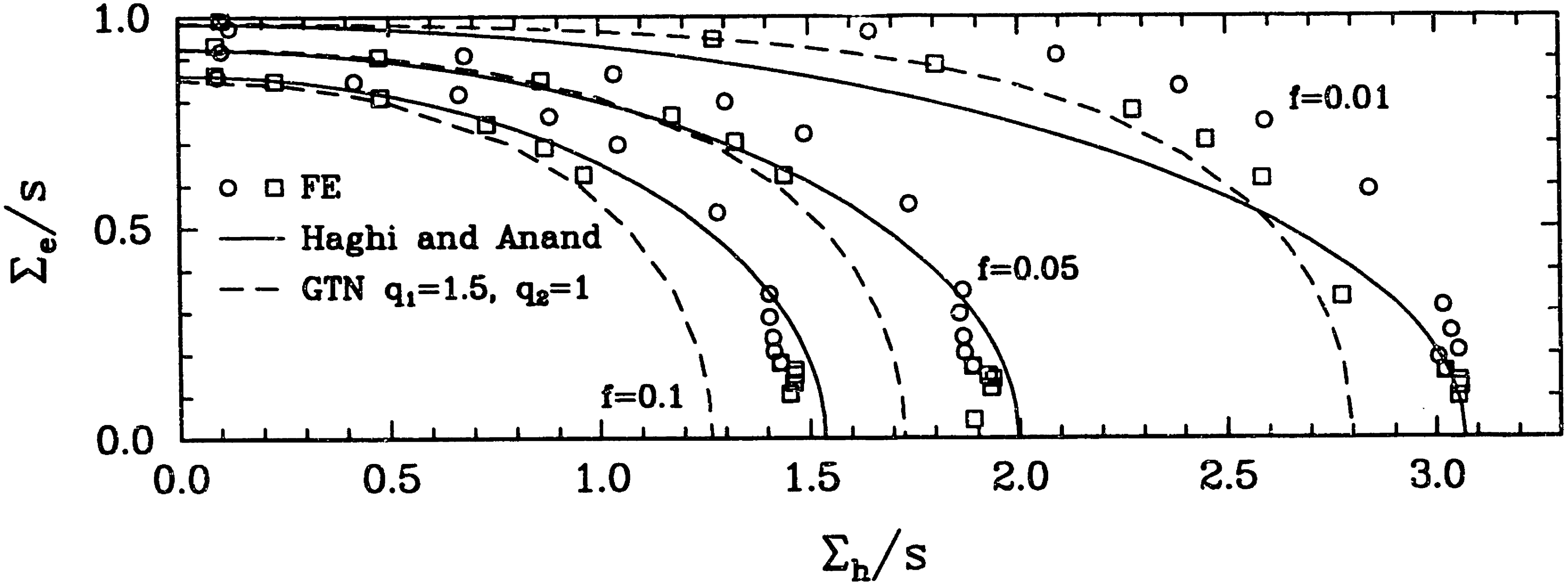

Figure 2.4: Yield surfaces corresponding to the rate-independent limit (25,26) of the potential for f=0.01, 0.05 and 0.10. The corresponding surfaces for the Gurson, Tvergaard, and Needleman (GTN) potential are also shown for comparison.

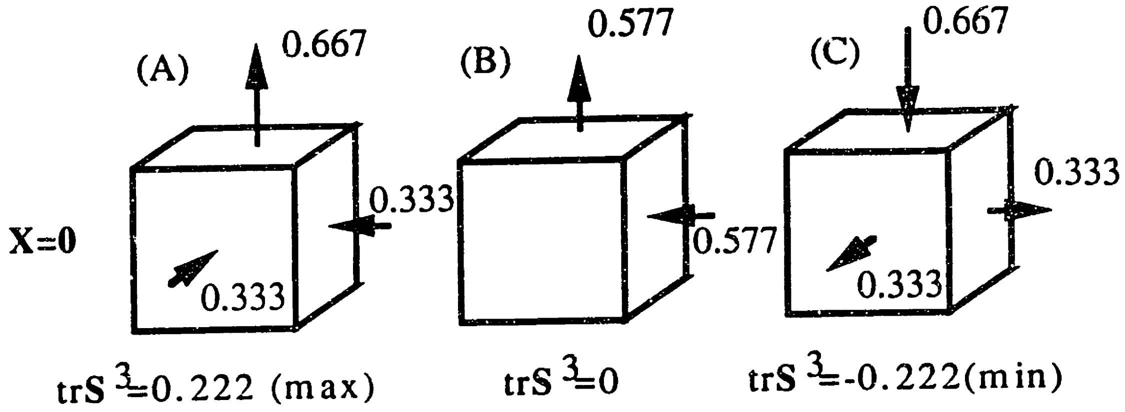

m	$\dot{E}_e^{(A)}/\dot{E}_e^{(C)}$	$\dot{E}_e^{(B)}/\dot{E}_e^{(c)}$	$\dot{E}_h^{(A)}/\dot{E}_h^{(C)}$	$\dot{E}_h^{(B)}/\dot{E}_h^{(C)}$
0.2	1.0	1.04	-	-
0.1	1.0	1.11	-	-

(a)

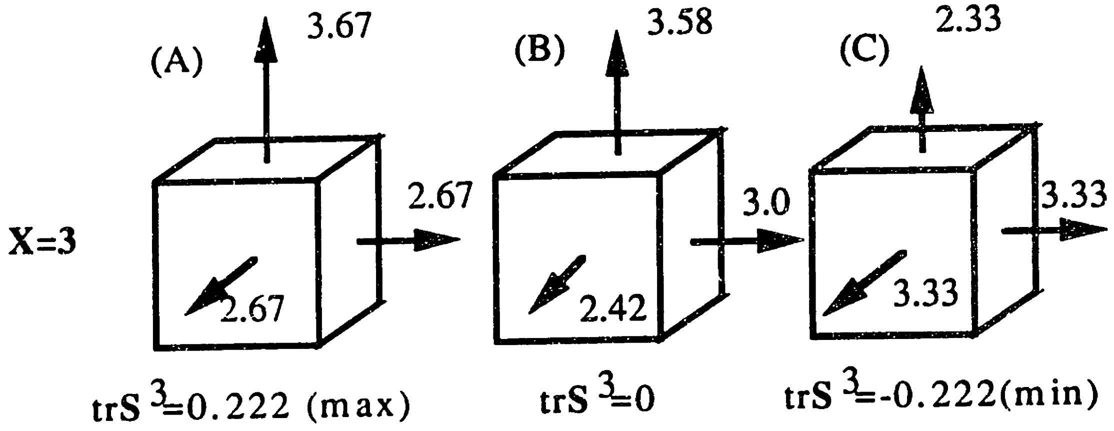

m	$\dot{E}_e^{(A)}/\dot{E}_e^{(C)}$	$\dot{E}_e^{(B)}/\dot{E}_e^{(C)}$	$\dot{E}_h^{(A)}/\dot{E}_h^{(C)}$	$\dot{E}_h^{(B)}/\dot{E}_h^{(C)}$
0.2	1.13	1.06	1.08	1.04
0.1	1.43	1.19	1.36	1.17

(b)

Figure 2.5: Effect of the third invariant of the stress deviator on the response of a periodic unit cell for two different triaxialities: a) X=0, b) X=3.

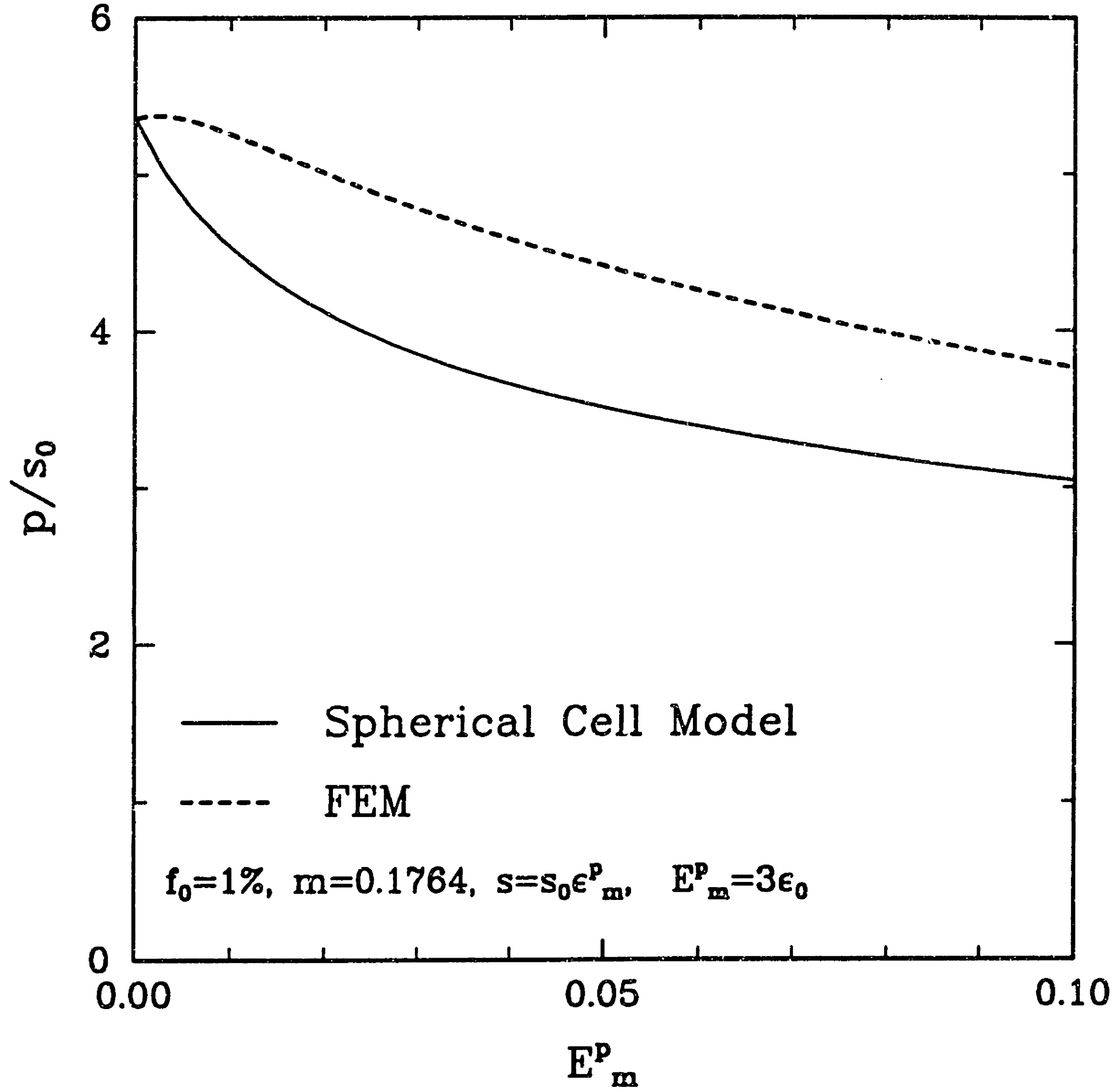

Figure 2.6: Effect of hardening gradient during the expansion of a spherical cell. Comparison between analytical solution and averaging scheme of Section 2.4

Chapter 3

Time Integration Procedures

Typical "implicit" finite element procedures for coupled thermo-mechanical problems which use nonlinear constitutive models, generate estimates of increments in nodal displacements and temperatures which are used to calculate the integration point values of the stress $\mathbf{T}$, temperature θ, and other field variables at the end of a time increment. If these stresses and temperatures do not satisfy the weak forms of the equations for equilibrium and balance of energy, then the estimates of the incremental displacement and temperatures are revised, and new end-of-increment stresses and temperatures are calculated. Iteration continues until the weak forms of the equilibrium equation and the equation for energy balance are satisfied to within acceptable tolerances.

Accordingly, we assume (i) that we are given a point $(\mathbf{p}, \theta_0)$ in the reference configuration $\mathcal{B}_0$, a corresponding point $(\mathbf{x}, \theta)$ in the current configuration $\mathcal{B}_t$ at time t and the list of variables

$$\{\mathbf{F}^p(\mathbf{x},t), s(\mathbf{x},t), f(\mathbf{x},t)\}, \tag{3.1}$$

and (ii) that we are also given the same material point $(\mathbf{z}, \theta)$ in the final configuration $\mathcal{B}_\tau$ at time τ. With these given, we take the computational problems to be:

1. A stable, accurate and efficient computation of the list $\{\mathbf{T}(\mathbf{z},\tau), s(\mathbf{z},\tau), f(\mathbf{z},\tau)\}$.
2. The computation of derivatives, consistent with the time integration procedure, to be used in a Newton type iterative method for revising the estimated nodal displacements and temperatures.

These are the main problems at hand, with item 1 above being the *central problem*, because derivative matrices are used only in the search for displacement and temperature fields, but in the end have no effect on the accuracy of the solution. It is important to note that the use of inaccurate jacobians may significantly deteriorate the convergence characteristics of the global iteration algorithm in "implicit" finite element procedures. "Explicit" finite element procedures, which are used in large scale inelastic analysis (e.g. dynamic problems, sheet metal forming etc.), do not require derivative matrices, and item 1 above is the only function required of a "constitutive equation subroutine".

Thus, the problem at hand is, given an estimate of the deformation gradient $\mathbf{F}(\tau)$ and the temperature increment field $\Delta\theta = \theta(\tau) - \theta(t)$ between two neighboring configurations $\mathcal{B}_t$ and $\mathcal{B}_\tau$ of a body, to integrate the constitutive equations across a time-step[1], $\Delta t = \tau - t$, to obtain $\{\mathbf{T}(\mathbf{z},\tau), s(\mathbf{z},\tau), f(\mathbf{z},\tau)\}$.

The time-integration procedure discussed below is an extension of that developed by WEBER & ANAND (1990) for isothermal deformations of fully dense materials. *Here we generalize their procedure to incorporate the effects of porosity and temperature* [2]. We formulate the time-integration procedure for the general form of the constitutive equations presented in sections 2.1.1 — 2.1.5. The specific forms discussed in the previous chapter are used for the illustrative calculations discussed later.

---

[1] Since plasticity is path-dependent, we must restrict the time increment Δt, the relative deformation gradient $\mathbf{F}_t(\tau) \equiv \mathbf{F}(\tau)\mathbf{F}(t)^{-1}$ and the temperature increment $\Delta\theta$ to be (in some sense) "small".

[2] A fully implicit Euler backward algorithm for the isothermal, rate-independent Gurson model has been recently formulated by Aravas [69]

The evolution of the plastic deformation gradient (2.9) can be integrated by means of the operator:

$$\mathbf{F}^p(\tau) = \exp(\Delta t \bar{\mathbf{D}}^p(\tau))\mathbf{F}^p(t) \tag{3.2}$$

while s and f are integrated via an Euler backward operator:

$$s(\tau) = s(t) + \Delta t\, \hat{\dot{s}}(\sigma_e(\tau), \theta(\tau), s(\tau)), \tag{3.3}$$

$$f(\tau) = f(t) + \Delta t\ (1 - f(\tau))\ \mathrm{tr}\ \mathbf{D}^p(\tau)\,. \tag{3.4}$$

Using (2.3) and (3.2) the elastic deformation gradient is given by

$$\mathbf{F}^e(\tau) = \mathbf{F}^e_* \exp(-\Delta t \bar{\mathbf{D}}^p(\tau))\ , \tag{3.5}$$

where:

$$\mathbf{F}^e_* = \mathbf{F}(\tau)\mathbf{F}^p(t)^{-1} \tag{3.6}$$

is a "trial value" of the elastic deformation gradient and corresponds to the elastic part of the deformation gradient if the time step (t, τ) were entirely elastic.

The tensors $\mathbf{F}^e(\tau)$ and $\mathbf{F}^e_*$ admit the polar decomposition:

$$\mathbf{F}^e(\tau) = \mathbf{R}^e(\tau)\mathbf{U}^e(\tau); \quad \mathbf{F}^e_* = \mathbf{R}^e_*\mathbf{U}^e_*\ . \tag{3.7}$$

Using the uniqueness of the polar decomposition and the isotropic character of the stress-strain relation, it can be proved that $\mathbf{U}^e(\tau)\exp(\Delta t \bar{\mathbf{D}}^p(\tau))$ is symmetric and:

$$\mathbf{R}^e(\tau) = \mathbf{R}^e_* \tag{3.8}$$

$$\mathbf{U}^e(\tau)\exp(\Delta t \bar{\mathbf{D}}^p(\tau)) = \mathbf{U}^e_* \tag{3.9}$$

The later implies that $\mathbf{U}^e(\tau)$ and $\mathbf{U}^e_*$ have the same principal directions. Thus, taking the logarithm of both sides and rearranging, we get:

$$\mathbf{E}^e(\tau) = \mathbf{E}^e_* - \Delta t\bar{\mathbf{D}}^p(\tau) \tag{3.10}$$

where:

$$\mathbf{E}^e_* = ln\mathbf{U}^e_* \tag{3.11}$$

is a " trial strain".

Substituting equation (3.10) in (2.2) we obtain the stress update:

$$\bar{\mathbf{T}}(\tau) = \bar{\mathbf{T}}^*(\tau) - \mathcal{L}[\Delta t\bar{\mathbf{D}}^p(\tau) + \mathbf{E}^\theta(\tau)] \tag{3.12}$$

where:

$$\bar{\mathbf{T}}^*(\tau) = \mathcal{L}[\mathbf{E}^e_*] \tag{3.13}$$

is a "trial stress".

Using eqns (3.12,3.13,3.3,3.4) we obtain:

$$\begin{aligned}
\bar{\mathbf{S}}(\tau) &= \bar{\mathbf{S}}^*(\tau) - 2\mu(\tau)\,\Delta t\,\frac{\partial\Phi}{\partial\Sigma_e}(\tau)\,\mathbf{N}(\tau), && (3.14)\\
\Sigma_h(\tau) &= \Sigma^*_h(\tau) - \kappa(\tau)\,\Delta t\,\frac{\partial\Phi}{\partial\Sigma_h}(\tau) + 3\,\kappa(\tau)\,A(\theta(\tau)), && (3.15)\\
s(\tau) &= s(t) + \Delta t\,g\,(\sigma_m(\tau), s(\tau), \theta(\tau))\,, && (3.16)\\
f(\tau) &= f(t) - (1 - f(\tau))\;\Delta t\,\frac{\partial\Phi}{\partial\Sigma_e}(\tau) && (3.17)
\end{aligned}$$

where

$$\begin{aligned}
\bar{\mathbf{S}}^*(\tau) &= 2\mu(\tau)\,\mathbf{E}^{e\prime}_*, && (3.18)\\
\Sigma_e{}^*(\tau) &= \sqrt{\frac{3}{2}\bar{\mathbf{S}}^*\cdot\bar{\mathbf{S}}^*} && (3.19)\\
\Sigma_h{}^*(\tau) &= -\kappa(\tau)\,\mathrm{tr}\,\mathbf{E}^e_*, && (3.20)
\end{aligned}$$

are *trial* values for the stress deviator, the equivalent stress and the pressure at the end of the increment. For simplicity, since the dependence on f of the thermo-elastic constants is not expected to be strong, in the equations above the values of μ and κ, are taken to be functions of the porosity f at the beginning of the time-step.

In a displacement based finite element method, the trial strain $\mathbf{E}^e_*$ is calculated from the kinematics and therefore the stress $\mathbf{T}^*(\tau)$ can be calculated in terms of quantities known at the beginning of the increment. Further, equation (3.14) shows that the tensorial direction of $\bar{\mathbf{S}}(\tau)$ is the same with that of $\bar{\mathbf{S}}^*(\tau)$:

$$\bar{\mathbf{N}}(\tau) = \frac{\bar{\mathbf{S}}(\tau)}{\Sigma_e(\tau)} = \frac{\mathbf{S}(\bar{\tau})^*}{\Sigma_e{}^*(\tau)} \,. \tag{3.21}$$

Thus, the set of equations (3.14-3.17) can be reduced to the following set of *scalar* equations: the equivalent stress

$$\Sigma_e = \Sigma_e{}^* - 3\,\mu\,\Delta t\,\frac{\partial\Phi}{\partial\Sigma_e} \tag{3.22}$$

$$\Sigma_h = \Sigma_h{}^* + 3\kappa\,A(\theta) - \kappa\,\Delta t\,\frac{\partial\Phi}{\partial\Sigma_e} \tag{3.23}$$

$$s = s(t) + g\,(\sigma_m, s, \theta)\;\Delta t \tag{3.24}$$

$$f = f(t) - (1-f)\;\Delta t\,\frac{\partial\Phi}{\partial\Sigma_e} \tag{3.25}$$

In the previous set of equations and now on, (τ) is dropped for notation convenience, and all variables are taken at the end of the step unless explicitly noted otherwise.

Let

$$\mathbf{X} = \left\{ \begin{array}{c} \Sigma_e \\ \Sigma_h \\ s \\ f \end{array} \right\}, \tag{3.26}$$

and

$$\mathbf{G}(\mathbf{X}) = \left\{ \begin{array}{c} G_1(\cdots) \\ G_2(\cdots) \\ G_3(\cdots) \\ G_4(\cdots) \end{array} \right\} = \left\{ \begin{array}{l} \Sigma_e{}^* - 3\,\mu\Delta t \,\dfrac{\partial\Phi}{\partial\Sigma_e} \\ \Sigma_h{}^* + 3\kappa\, A(\theta) - \kappa\Delta t\, \dfrac{\partial\Phi}{\partial\Sigma_h} \\ s(t) + g\,(\sigma_m, s, \theta)\,\Delta t \\ f(t) - (1-f)\;\Delta t\, \dfrac{\partial\Phi}{\partial\Sigma_e} \end{array} \right\}, \tag{3.27}$$

then the implicit system of scalar equations to be solved for $\mathbf{X}(\tau)$ can be written as

$$\mathbf{X} = \mathbf{G}\,(\mathbf{X};\theta)\,. \tag{3.28}$$

In the next two sections we elaborate on the solution of the system (3.28).

Once $\{\Sigma_e(\tau), \Sigma_h(\tau), s(\tau), f(\tau)\}$ have been computed, from (3.21) we obtain

$$\bar{\mathbf{T}}(\tau) = \eta(\tau)\,\bar{\mathbf{S}}^*(\tau) + \frac{1}{3}\,\Sigma_h(\tau)\,\mathbf{1}, \qquad \eta(\tau) = \frac{\Sigma_e(\tau)}{\Sigma_e{}^*(\tau)}\,. \tag{3.29}$$

Next, from (3.2) and (3.9) we note that to calculate $\mathbf{F}^p(\tau)$ we need to calculate

$$\exp\{\Delta t\,\mathbf{D}^p(\tau)\} = (\mathbf{U}^e(\tau))^{-1}\;\mathbf{U}^e_*\,. \tag{3.30}$$

Let

$$\mathbf{U}^e_* = \sum_{i=1}^{3} \lambda_*{}^{(i)}\,\mathbf{l}_*{}^{(i)} \otimes \mathbf{l}_*{}^{(i)} \tag{3.31}$$

denote the spectral decomposition of $\mathbf{U}^e_*$. Then, since the principal directions of $\mathbf{U}^e_*$, $\mathbf{U}^e(\tau)$, $\mathbf{E}^e(\tau)$ and $\exp\{\Delta t\,\mathbf{D}^p(\tau)\}$ are all coincident, the principal values of $\mathbf{U}^e(\tau)$ are

$$\lambda^{e\,(i)} = \exp\left(e^{(i)}\right), \tag{3.32}$$

where

$$e^{(i)} = \mathbf{l}_*{}^{(i)} \cdot \mathbf{E}^e(\tau)\,\mathbf{l}_*{}^{(i)} \tag{3.33}$$

and

$$\mathbf{U}^e_* = \sum_{i=1}^{3} \lambda_*{}^{(i)}\,\mathbf{l}_*{}^{(i)} \otimes \mathbf{l}_*{}^{(i)} \tag{3.34}$$

denote the spectral decomposition of $\mathbf{U}^e_*$, and $e^{(i)}$ are the principal values of $\mathbf{E}^e(\tau)$, which is given by (see, equation (2.2))

$$\mathbf{E}^e(\tau) = \frac{1}{2\,\mu(\tau)}\,\bar{\mathbf{S}}(\tau) + \left\{\frac{\Sigma_h(\tau)}{3\,\kappa(\tau)} + \alpha(\tau)\ \{\theta(\tau) - \theta_0\}\right\}\mathbf{1}\ . \tag{3.35}$$

Thus

$$\exp\{\Delta t\,\mathbf{D}^p(\tau)\} = (\mathbf{U}^e(\tau))^{-1}\ \mathbf{U}^e_* = \sum_{i=1}^{3}\frac{\lambda_*^{(i)}}{\lambda^{e\,(i)}}\,\mathbf{l}_*^{(i)} \otimes \mathbf{l}_*^{(i)},$$

and

$$\mathbf{F}^p(\tau) = \left\{\sum_{i=1}^{3}\frac{\lambda_*^{(i)}}{\lambda^{e\,(i)}}\,\mathbf{l}_*^{(i)} \otimes \mathbf{l}_*^{(i)}\right\}\mathbf{F}^p(t)\,. \tag{3.36}$$

Finally, using (2.2) and (3.8), the Cauchy stress $\mathbf{T}(\tau)$ at the end of the increment is given by

$$\mathbf{T}(\tau) = \left\{\lambda^{e\,(1)}\,\lambda^{e\,(2)}\,\lambda^{e\,(3)}\right\}^{-1}\,\mathbf{R}^e_*\,\bar{\mathbf{T}}(\tau)\,\mathbf{R}^{eT}_*. \tag{3.37}$$

Summary of the time-integration algorithm:

Step 1. Calculate the trial elastic deformation gradient

$$\mathbf{F}^e_* = \mathbf{F}(\tau)\,(\mathbf{F}^p(t))^{-1}\,.$$

Step 2. Calculate the kinematical quantities

$$\begin{aligned}
\mathbf{U}^e_* &= \sum_{i=1}^{3}\lambda_*^{(i)}\,\mathbf{l}_*^{(i)} \otimes \mathbf{l}_*^{(i)}\,,\\
\mathbf{R}^e_* &= \mathbf{F}^e_*\,(\mathbf{U}^e_*)^{-1}\,,\\
\mathbf{E}^e_* &= \sum_{i=1}^{3}\ln\left(\lambda_*^{(i)}\right)\mathbf{l}_*^{(i)} \otimes \mathbf{l}_*^{(i)}\,.
\end{aligned}$$

Step 3. Calculate the trial stress and associated quantities

$$\begin{aligned}\bar{\mathbf{T}}^{*}(\tau) &= \boldsymbol{\mathcal{L}}[\mathbf{E}^{e}_{*}]\,,\\ \Sigma_h{}^{*}(\tau) &= \frac{1}{3}\,\mathrm{tr}\,\bar{\mathbf{T}}^{*}(\tau)\,,\\ \bar{\mathbf{S}}^{*}(\tau) &= \bar{\mathbf{T}}^{*}(\tau) - \Sigma_h{}^{*}(\tau)\,\mathbf{1}\,,\\ \Sigma_e{}^{*}(\tau) &= \sqrt{(3/2)\,\bar{\mathbf{S}}^{*}(\tau)\cdot\bar{\mathbf{S}}^{*}(\tau)}\,.\end{aligned}$$

Step 4. Calculate $\Sigma_e(\tau)$, $\Sigma_h(\tau)$, $s(\tau)$, and $f(\tau)$ by solving

$$\begin{aligned}\Sigma_e(\tau) &= \Sigma_e{}^{*}(\tau) - 3\,\mu(\tau)\,\Delta t\left(\frac{\partial\Phi}{\partial\Sigma_e}\right)(\tau),\\ \Sigma_h(\tau) &= \Sigma_h{}^{*}(\tau) - 3\,\kappa(\tau)\,\alpha(\tau)\,\left\{\theta(\tau)-\theta_0\right\} - \kappa(\tau)\,\Delta t\left(\frac{\partial\Phi}{\partial\Sigma_h}\right)(\tau)\,,\\ s(\tau) &= s(t) + \Delta t\,\hat{\dot{s}}(\sigma_e(\tau),\theta(\tau),s(\tau)),\\ f(\tau) &= f(t) + \Delta t\,(1-f(\tau))\left(\frac{\partial\Phi}{\partial\Sigma_h}\right)(\tau)\,,\end{aligned}$$

where $\sigma_e(\tau)$ is implicitly defined by the equation

$$\frac{\partial\Phi}{\partial\Sigma_e}(\tau)\,\Sigma_e(\tau) + \frac{\partial\Phi}{\partial\Sigma_h}(\tau)\,\Sigma_h(\tau) - (1-f(\tau))\;\sigma_e(\tau)\,\hat{\dot{\epsilon}}^{p}(\sigma_e(\tau),\theta(\tau),s(\tau)) = 0\,.$$

Step 5. Update the stress $\bar{\mathbf{T}}$:

$$\bar{\mathbf{T}}(\tau) = \eta(\tau)\,\bar{\mathbf{S}}^{*}(\tau) + \Sigma_h(\tau)\,\mathbf{1}, \qquad \eta(\tau) = \frac{\Sigma_e(\tau)}{\Sigma_e{}^{*}(\tau)}\,.$$

Step 6. Update $\bar{\mathbf{F}}^{p}$:

$$\begin{aligned}\mathbf{E}^{e}(\tau) &= \frac{1}{2\,\mu(\tau)}\,\bar{\mathbf{S}}(\tau) + \left\{\frac{\Sigma_h(\tau)}{3\,\kappa(\tau)} + \alpha(\tau)\,\left\{\theta(\tau)-\theta_0\right\}\right\}\,\mathbf{1}\,,\\ e^{(i)} &= \mathbf{l}_{*}{}^{(i)}\cdot\mathbf{E}^{e}(\tau)\,\mathbf{l}_{*}{}^{(i)}\,,\\ \lambda^{e\,(i)} &= \exp\left(e^{(i)}\right)\,,\end{aligned}$$

$$\mathbf{F}^p(\tau) = \left\{\sum_{i=1}^{3} \frac{\lambda_*^{(i)}}{\lambda^{e(i)}} \mathbf{l}_*^{(i)} \otimes \mathbf{l}_*^{(i)}\right\} \mathbf{F}^p(t).$$

Step 7. Transform $\bar{\mathbf{T}}$ to $\mathbf{T}$:

$$\mathbf{T}(\tau) = \left\{\lambda^{e(1)}\lambda^{e(2)}\lambda^{e(3)}\right\}^{-1} \mathbf{R}^e_* \bar{\mathbf{T}}(\tau) \mathbf{R}^{eT}_*.$$

3.1 Euler-Backward Scheme

In the context of an implicit finite element program, it is usually desirable to be able to solve (3.28) across large time steps. In the case of fully dense material, where the system (3.28) reduces to two equations, Lush et al. [86] were able to employ a Newton-Raphson procedure, effectively utilizing strict existing bounds on the solution. For porous materials the number of the equations is larger, and their complexity is such that no generic bounds can be found. Therefore a pure Newton-Raphson scheme will often diverge. An alternative is a constrained (β-type) Newton-Raphson procedure, in which only a fraction β of the correction is used in every iteration:

$$\mathbf{X}_{i+1} = \mathbf{X}_i + \beta\Delta\mathbf{X}, \quad \Delta\mathbf{X} = -\mathcal{A}^{*-1}[\mathrm{G} - \mathrm{X}], \quad \beta \le 1\ . \tag{3.38}$$

Its jacobian is given by:

$$\mathcal{A}^* = (\mathcal{I} - \frac{\partial \mathrm{G}}{\partial \mathbf{X}})\,|_{\mathbf{X}=\mathbf{X}_i,\theta=\theta}\ , \tag{3.39}$$

where $\mathbf{X}_i$ is the estimate of the solution in the i-th iteration. Although proper selection of β can ensure convergence, the required number of iterations maybe large.

The difficulty in the solution of the system (3.28) is due to terms of the form:

$$\left(\frac{\Sigma_e}{s}\right)^{1/m}, \quad \left(\frac{\Sigma_h}{s}\right)^{1/m}, \tag{3.40}$$

that are present in the derivatives of the potential Φ. In these terms a small variation of Σ_e or Σ_h is magnified by the power exponent ($1/m \geq 1$). Therefore the computed corrections by a pure Newton-Raphson scheme may be excessively large if the current estimate is not close enough to the solution point. A heuristic scheme, that was found to work very well, is to impose a specific constraint on the correction $\Delta\mathbf{X}$, so that the new estimate does not produce "excessive" change in the terms (3.40), between iterations. Let:

$$\dot{\Delta} = \frac{\partial\Phi}{\partial\Sigma_e} + \left|\frac{\partial\Phi}{\partial\Sigma_h}\right| \tag{3.41}$$

The two terms correspond to the deviatoric and mean parts of $\mathbf{D}^p$ respectively. The following restriction is enforced:

$$\left|\dot{\Delta}(\mathbf{X}_{i+1}) - \dot{\Delta}(\mathbf{X}_i)\right| \quad \Delta t \leq \delta \tag{3.42}$$

If the new estimate is such that the above inequality is violated, the correction vector $\Delta\mathbf{X}$ is scaled down by multiplying it by a number RKUT (RKUT < 1) which is estimated as follows:

If $\dot{\Delta}(\mathbf{X}_{i+1}) - \dot{\Delta}(\mathbf{X}_i) > 0$ then the condition (3.42) can be written as:

$$\dot{\Delta}(\mathbf{X}_{i+1}) \leq \dot{\Delta}(\mathbf{X}_i) + \frac{\delta}{\Delta t}$$

and RKUT is defined as:

$$\mathrm{RKUT} = \left(\frac{\dot{\Delta}(\mathbf{X}_{i+1})}{\delta/\Delta t + \dot{\Delta}(\mathbf{X}_i)}\right)^m$$

If $\dot{\Delta}(\mathbf{X}_{i+1}) - \dot{\Delta}(\mathbf{X}_i) < 0$ then the condition (3.42) can be written as:

$$\dot{\Delta}(\mathbf{X}_{i+1}) \geq \dot{\Delta}(\mathbf{X}_i) - \frac{\delta}{\Delta t}$$

and RKUT is defined as:

$$\mathrm{RKUT} = \left(\frac{\dot{\Delta}(\mathbf{X}_i) - \delta/\Delta t}{\dot{\Delta}(\mathbf{X}_{i+1})} \right)^m$$

The number in the parenthesis is raised to the strain rate sensitivity m, since the cutback of the correction is applied mainly on stress type quantities. The new estimate is given by:

$$\mathbf{X}_{i+1} = \mathbf{X}_i + \mathrm{RKUT}\ \Delta\mathbf{X}$$

A value $\delta = 0.1$ was found to be satisfactory for the range of problems we dealt with. RKUT is activated when large time steps are taken or when the strain rate sensitivity is low. The algorithm has been tested successfully even to very low strain rate sensitivities ($m = 0.001$). At those values of m it was found necessary to revise the correction several times until the condition (3.42) is met.

3.2 Forward Gradient Approximation

Occasionally, the time step is restricted to very small values, e.g. a) in explicit finite element programs, b) in implicit finite elements when there are difficulties of convergence due to contact and friction. In those cases there is no need for the Euler-backward scheme. It is preferable to obtain the solution of the system in a non-iterative manner. A semi-implicit forward gradient type of approximation is described in [106]. That procedure is equivalent to one step (unconstrained) Newton-Raphson correction. In contrast to the unconditionally stable Euler-Backward, it is not guaranteed to be stable but it usually is. Restrictions on the time step are necessary in order to ensure stability and accuracy (see [106] for details).

3.3 Jacobian Matrices

In this section we summarize the derivatives, consistent with the time integration procedure, to be used in a Newton type iterative method for revising the estimates of nodal displacements and temperatures in implicit finite-element procedures for coupled thermo-mechanical problems. In those cases the solution of the non-linear set of equations (which come from the finite element descritization of the weak variational statement of the incremental mixed problem) requires a linearization around the last estimate of the displacement $\bar{\mathbf{u}}$ and temperature θ solution. The differential change $d\mathbf{u}$ (which corresponds to a change in the deformation gradient) results in a differential change in the kinematics and the calculated final stress. As shown in Weber and Anand ([89]), a complete and consistent linearization for the isothermal problem, requires the calculation of $\partial\bar{\mathbf{T}}/\partial\mathbf{E}^e_*$, $d\mathbf{E}^e_*$ and $(d\mathbf{R}^e_*)\mathbf{R}^e_*$. In the fully coupled problem additional derivatives for the rate of heat generation by plastic work are needed. Although these quantities can be at least well approximated, it was not possible to implement them consistently (for reasons intrinsic to ABAQUS). We list below approximations to these jacobians that we have used in our calculations. Jacobian matrices play a very important role in the rate of convergence of the solution to the global problem, but in the end they have no effect on the accuracy of the solution. For the series of problems presented in chapter 4, the convergence characteristics of the solutions were excellent.

The Cauchy stress at the end of the increment can be written as:

$$\mathbf{T}(\tau) = 2\,\mu(\tau)\,\mathbf{E}' + \kappa(\tau)\;(\mathrm{tr}\,\mathbf{E})\;\mathbf{1} + \{\Sigma_e(\tau) - \Sigma_e^*(\tau)\}\;\mathbf{N}(\tau) + \{\Sigma_h(\tau) - \Sigma_h^*(\tau)\}\;\mathbf{1}\,, \tag{3.43}$$

where

$$\mathbf{E} \equiv \mathbf{R}^e\;\mathbf{E}^e_*\,\mathbf{R}^{eT}, \quad \text{and} \quad \mathbf{N}(\tau) \equiv \frac{\mathbf{S}(\tau)}{\Sigma_e(\tau)}\,. \tag{3.44}$$

Also, since the viscoplastic potential Φ is homogeneous of degree $\left(\frac{1}{m}+1\right)$ in the stress, $\bar{\mathbf{T}} \cdot \mathbf{D}^p = \bar{\mathbf{T}} \cdot \dfrac{\partial \Phi}{\partial \bar{\mathbf{T}}} = \left(\frac{1}{m}+1\right)\Phi$, and the plastic power dissipation in the matrix at the end of the time-step may be written as

$$r^{pl}(\tau) = \omega\left(\frac{1}{m}+1\right)\Phi(\tau)\,. \tag{3.45}$$

The necessary derivatives to be computed, pertain to the variations of $\mathbf{T}(\tau)$ and $r^{pl}(\tau)$ with respect to variations in $\mathbf{E}$ and $\theta(\tau)$. We denote these derivatives by

$$\mathcal{C} = \frac{\partial \mathbf{T}}{\partial \mathbf{E}}, \tag{3.46}$$

$$\mathbf{C} = \frac{\partial \mathbf{T}}{\partial \theta}, \tag{3.47}$$

$$\mathbf{H} = \frac{\partial r^{pl}}{\partial \mathbf{E}}, \tag{3.48}$$

$$H = \frac{\partial r^{pl}}{\partial \theta}. \tag{3.49}$$

In what follows, we assume for simplicity that the dependence of the thermo-elastic moduli on (θ, f) is weak, so that variation of these moduli may be neglected in the calculation of the derivatives.

The Derivative $\mathcal{C}$:

From (3.43)

$$\mathcal{C} = 2\,\mu(\tau)\left\{\mathcal{I} - \frac{1}{3}(\mathbf{1}\otimes\mathbf{1})\right\} + \kappa(\tau)\,\mathbf{1}\otimes\mathbf{1} + \{\Sigma_e(\tau) - \Sigma_e^*(\tau)\}\,\frac{\partial}{\partial \mathbf{E}}\mathbf{N}(\tau) \tag{3.50}$$

$$+\mathbf{N}(\tau)\otimes\frac{\partial}{\partial\mathbf{E}}\left\{\Sigma_e(\tau)-\Sigma_e^*(\tau)\right\}+\mathbf{1}\otimes\frac{\partial}{\partial\mathbf{E}}\left\{\Sigma_h(\tau)-\Sigma_h^*(\tau)\right\}.$$

Straightforward calculations give

$$\frac{\partial}{\partial\mathbf{E}}\mathbf{N}(\tau)=\frac{1}{\Sigma_e^*(\tau)}\left[2\,\mu(\tau)\left\{\mathcal{I}-\left(\frac{1}{3}\right)\mathbf{1}\otimes\mathbf{1}\right\}-3\,\mu(\tau)\,\mathbf{N}(\tau)\otimes\mathbf{N}(\tau)\right]. \tag{3.51}$$

Next, noting that $\mathbf{E}$ enters the equations through $\Sigma_e^*(\tau)$ and $\Sigma_h^*(\tau)$, we have

$$\frac{\partial}{\partial\mathbf{E}}\equiv\frac{\partial}{\partial\Sigma_e^*(\tau)}\left\{\frac{\partial\Sigma_e^*(\tau)}{\partial\mathbf{E}}\right\}+\frac{\partial}{\partial\Sigma_h^*(\tau)}\left\{\frac{\partial\Sigma_h^*(\tau)}{\partial\mathbf{E}}\right\}, \tag{3.52}$$

with

$$\begin{aligned}\frac{\partial\Sigma_e^*(\tau)}{\partial\mathbf{E}} &= 3\,\mu(\tau)\,\mathbf{N}(\tau), && (3.53)\\ \frac{\partial\Sigma_h^*(\tau)}{\partial\mathbf{E}} &= \kappa(\tau)\,\mathbf{1}. && (3.54)\end{aligned}$$

Thus,

$$\begin{aligned}\frac{\partial}{\partial\mathbf{E}}\left\{\Sigma_e(\tau)-\Sigma_e^*(\tau)\right\} &= 3\mu(\tau)\left\{\frac{\partial\Sigma_e(\tau)}{\partial\Sigma_e^*(\tau)}-1\right\}\mathbf{N}(\tau)+\kappa(\tau)\left\{\frac{\partial\Sigma_e(\tau)}{\partial\Sigma_h^*(\tau)}\right\} && (3.55)\\ \frac{\partial}{\partial\mathbf{E}}\left\{\Sigma_h(\tau)-\Sigma_h^*(\tau)\right\} &= 3\mu(\tau)\left\{\frac{\partial\Sigma_h(\tau)}{\partial\Sigma_e^*(\tau)}\right\}\mathbf{N}(\tau)+\kappa(\tau)\left\{\frac{\partial\Sigma_h(\tau)}{\partial\Sigma_h^*(\tau)}-1\right\} && (3.56)\end{aligned}$$

Substituting (3.51), (3.55) and (3.56) in (3.51) and rearranging we have

$$\mathcal{C}=c_1\,\mathcal{I}+c_2\,\mathbf{1}\otimes\mathbf{1}+c_3\,\mathbf{S}(\tau)\otimes\mathbf{S}(\tau)+c_4\,\mathbf{1}\otimes\mathbf{S}(\tau)+c_5\,\mathbf{S}(\tau)\otimes\mathbf{1}, \tag{3.57}$$

with

$$\begin{aligned}c_1 &= 2\,\tilde{\mu}(\tau), && (3.58)\\ c_2 &= \tilde{\kappa}(\tau)-(2/3)\,\tilde{\mu}(\tau), &&\\ c_3 &= -3\,\mu(\tau)\left(\eta(\tau)-\frac{\partial\Sigma_e(\tau)}{\partial\Sigma_e^*(\tau)}\right)/\Sigma_e^2(\tau), &&\end{aligned}$$

$$
\begin{aligned}
c_4 &= 3\,\mu(\tau)\left(\frac{\partial\Sigma_h(\tau)}{\partial\Sigma_e^*(\tau)}\right)/\Sigma_e(\tau), \\
c_5 &= \kappa(\tau)\left(\frac{\partial\Sigma_e(\tau)}{\partial\Sigma_h^*(\tau)}\right)/\Sigma_e(\tau),
\end{aligned}
$$

where

$$
\begin{aligned}
\eta(\tau) &= \Sigma_e(\tau)/\Sigma_e^*(\tau), \\
\tilde{\mu}(\tau) &= \eta(\tau)\,\mu(\tau), \\
\tilde{\kappa}(\tau) &= \left(\frac{\partial\Sigma_h(\tau)}{\partial\Sigma_h^*(\tau)}\right)\kappa(\tau).
\end{aligned}
\tag{3.59}
$$

The derivatives $\frac{\partial\Sigma_e(\tau)}{\partial\Sigma_e^*(\tau)}$, $\frac{\partial\Sigma_e(\tau)}{\partial\Sigma_h^*(\tau)}$, $\frac{\partial\Sigma_h(\tau)}{\partial\Sigma_e^*(\tau)}$, and $\frac{\partial\Sigma_h(\tau)}{\partial\Sigma_h^*(\tau)}$ are determined as follows.

Using the definitions

$$
\mathbf{X} \equiv \left\{ \begin{array}{c} \Sigma_e(\tau) \\ \Sigma_h(\tau) \\ s(\tau) \\ f(\tau) \end{array} \right\}, \tag{3.60}
$$

and

$$
\mathbf{Y} \equiv \left\{ \begin{array}{c} \Sigma_e^*(\tau) \\ \Sigma_h^*(\tau) \end{array} \right\}, \tag{3.61}
$$

the system of equations (3.28) may be written as

$$
\mathbf{X} = \mathbf{G}(\mathbf{X};\mathbf{Y}), \tag{3.62}
$$

where

$$\mathbf{G} \equiv \left\{ \begin{array}{l} \Sigma_e^*(\tau) - 3\,\mu(\tau)\,\Delta t\, \left(\frac{\partial\Phi}{\partial\Sigma_e}\right)(\tau), \\ \Sigma_h^*(\tau) - 3\,\kappa(\tau)\,\alpha(\tau)\, \{\theta(\tau) - \theta_0\} - \kappa(\tau)\,\Delta t\, \left(\frac{\partial\Phi}{\partial\Sigma_h}\right)(\tau)\,, \\ s(t) + \Delta t\, \hat{\dot{s}}(\sigma_e(\tau), \theta(\tau), s(\tau)), \\ f(t) + \Delta t\, (1 - f(\tau))\, \left(\frac{\partial\Phi}{\partial\Sigma_h}\right)(\tau) \end{array} \right\}. \tag{3.63}$$

Differentiating (3.62) with respect to $\mathbf{Y}$ (at the solution point) we obtain

$$\frac{\partial\mathbf{X}}{\partial\mathbf{Y}} = \frac{\partial\mathbf{G}(\mathbf{X};\mathbf{Y})}{\partial\mathbf{Y}} + \frac{\partial\mathbf{G}(\mathbf{X};\mathbf{Y})}{\partial\mathbf{X}}\,\frac{\partial\mathbf{X}}{\partial\mathbf{Y}},$$

from which

$$\frac{\partial\mathbf{X}}{\partial\mathbf{Y}} = \mathcal{A}^* \left(\frac{\partial\mathbf{G}(\mathbf{X};\mathbf{Y})}{\partial\mathbf{Y}}\right), \tag{3.64}$$

where

$$\mathcal{A}^* = \left\{\mathcal{I} - \frac{\partial\mathbf{G}(\mathbf{X};\mathbf{Y})}{\partial\mathbf{X}}\right\}^{-1}. \tag{3.65}$$

Finally, using (3.63) we obtain

$$\frac{\partial\Sigma_e(\tau)}{\partial\Sigma_e^*(\tau)} = \mathcal{A}_{11}^*, \quad \frac{\partial\Sigma_e(\tau)}{\partial\Sigma_h^*(\tau)} = \mathcal{A}_{12}^*, \quad \frac{\partial\Sigma_h(\tau)}{\partial\Sigma_e^*(\tau)} = \mathcal{A}_{21}^*, \quad \frac{\partial\Sigma_h(\tau)}{\partial\Sigma_h^*(\tau)} = \mathcal{A}_{22}^*. \tag{3.66}$$

The Derivative C:

From (3.43)

$$\mathbf{C} = \left\{\frac{\partial\Sigma_e(\tau)}{\partial\theta(\tau)}\right\} \mathrm{N}(\tau) + \left\{\frac{\partial\Sigma_h(\tau)}{\partial\theta(\tau)}\right\} \mathbf{1}. \tag{3.67}$$

Explicitly recognizing the dependence of the system of equations (3.62) on θ, we write

$$\mathbf{X} = \mathbf{G}(\mathbf{X};\theta), \tag{3.68}$$

from which

$$\frac{\partial \mathbf{X}}{\partial \theta} = \frac{\partial \mathbf{G}(\mathbf{X};\theta)}{\partial \theta} + \frac{\partial \mathbf{G}(\mathbf{X};\theta)}{\partial \mathbf{X}} \frac{\partial \mathbf{X}}{\partial \theta},$$

and hence

$$\frac{\partial \mathbf{X}}{\partial \theta} = \mathcal{A}^{*} \left(\frac{\partial \mathbf{G}(\mathbf{X};\theta)}{\partial \theta} \right). \tag{3.69}$$

The first two elements of the vector $\frac{\partial \mathbf{X}}{\partial \theta}$ are the derivatives $\frac{\partial \Sigma_e(\tau)}{\partial \theta(\tau)}$, $\frac{\partial \Sigma_h(\tau)}{\partial \theta(\tau)}$ needed for calculating **C** in equation (3.67) above.

The Derivative H:

From (3.45)

$$\mathbf{H} \equiv \frac{\partial r^{pl}}{\partial \mathbf{E}} = \omega \left(\frac{1}{m} + 1 \right) \frac{\partial \Phi(\tau)}{\partial \mathbf{E}}. \tag{3.70}$$

Recalling the dependence of Φ on **X**, of **X** on **Y**, and **Y** on **E**, and using the chain rule we obtain

$$\frac{\partial \Phi}{\partial \mathbf{E}} = \left[\frac{\partial \Phi}{\partial \mathbf{X}} \left\{ \frac{\partial \mathbf{X}}{\partial \mathbf{Y}} \right\} \right] \frac{\partial \mathbf{Y}}{\partial \mathbf{E}}.$$

Using (3.64) we obtain

$$\frac{\partial \Phi}{\partial \mathbf{E}} = \left[\frac{\partial \Phi}{\partial \mathbf{X}} \left\{ \mathcal{A}^{*} \left(\frac{\partial \mathbf{G}(\mathbf{X};\mathbf{Y})}{\partial \mathbf{Y}} \right) \right\} \right] \frac{\partial \mathbf{Y}}{\partial \mathbf{E}}, \tag{3.71}$$

and upon substitution of (3.71) in (3.70) we obtain the required derivative **H**.

The Derivative H:

From (3.45)

$$H \equiv \frac{\partial r^{pl}}{\partial \theta} = \omega \left(\frac{1}{m} + 1 \right) \left\{ \frac{\partial \Phi(\tau)}{\partial \theta} + \frac{\partial \Phi(\tau)}{\delta \mathbf{X}} \frac{\partial \mathbf{X}}{\partial \theta} \right\}, \tag{3.72}$$

with $\frac{\partial \mathbf{X}}{\partial \theta}$ given by (3.69).

3.4 One element calculations

The performance of the Euler Backward time-integration procedure for the chosen constitutive equations was evaluated in a series of one element calculations. The efficiency of the schemes and the effect of the magnitude of the strain step on the accuracy of the solution was determined.

For the following simulations we used the model presented in Chapter 2 with matrix properties, those of 2%Si-Fe (see Table 1, Chapter 4). Fig. 3.1 presents the uniaxial stress-strain and densification curves obtained for a constant strain rate (1/sec) compression simulation of a porous material with initial porosity $f_0 = 0.045$, with equivalent plastic strain increments of 2% and 10%. For reference an accurate forward gradient solution (10000 increment) is included in the figure. The number of Newton-Raphson iterations never exceeded 7 for both cases. After the knee, 5.3 and 5.6 is the average number of iterations for the two cases. It should be noted that in more complicated problems a 10% increment is rather impractical since the number of global equilibrium iterations is high. A 2 – 5% limit on the macroscopic equivalent plastic strain step is a reasonable choice.

Fig. 3.2 presents the densification of a porous material of initial porosity $f_0 = 0.012$ in a isostatic compaction with constant trace of macroscopic strain rate (3×10^{-5}/sec) with different strain steps. With increasing strain step the accuracy of the integration of equations (3.24,3.25) is decreasing. An 3% limit on the trace of the plastic strain rate seams reasonable. The number of iterations of the system of equations (3.14-3.17) never exceeded 8. Combining the two limits, a criterion for an automatic time stepping algorithm can be constructed. By defining a measure of the severity of the rate of the deformation:

$$\dot{\Delta} = \left(\frac{\partial \Phi}{\Sigma_e} + \left| \frac{\partial \Phi}{\Sigma_h} \right| \right) \tag{3.73}$$

an automatic time-stepping algorithm similar to Lush *et al.* [86] can be implemented using the ratio:

$$R = \frac{\dot{\Delta}(\tau)^{max}\Delta t}{\Delta} \tag{3.74}$$

where $\dot{\Delta}(\tau)^{max}$ is the maximum value of $\dot{\Delta}$ at all integration points at the end of the increment. A value of 0.03 was selected for Δ.

3.5 Implementation in ABAQUS

The constitutive equations and time-integration procedures described in this chapter have been implemented in the implicit finite element code ABAQUS (Version 4.9) [1990], by writing a "user material" subroutine, UMAT. The generality of the other features of ABAQUS, combined with the provision for adding a separate "user material" subroutine, makes it an extremely useful tool for the implementation of new constitutive equations.

The subroutine UMAT is called once for each integration point in the model for every global iteration. In order to use our time-integration algorithm, we have to obtain the deformation gradient $\mathbf{F}(\tau)$ at the end of an increment [3]. With these inputs, the output expected from UMAT consists of the values of the stress and the internal state variables at the end of the increment, $(\mathbf{T}(\tau), s(\tau), f(\tau))$, the plastic power dissipation $r^{pl}(\tau) = \beta\mathbf{T}(\tau)\cdot\mathbf{D}^p(\tau)$, plus the consistent derivative matrices $\mathcal{C}$, $\mathbf{C}$, $\mathbf{H}$, and H (see the APPENDIX), to be used in the Newton scheme for global balance of equilibrium and energy. Note that the stress and the internal variables at the beginning of the increment are used to guide the solution of the system (3.22-3.25).

---

[3] This information is not currently routinely supplied as input to UMAT. Instead, ABAQUS supplies a strain increment calculated by using the HUGHES & WINGET [1980] algorithm. Appropriate subroutines that need to be called to obtain $\mathbf{F}(\tau)$ were kindly supplied to us by Dr. H. D. Hibbitt of HKS, Inc. We use this information about the deformation gradient to construct the total kinematic quantities for our time-integration procedure.

ABAQUS calculations presented here were performed by using either the static or the coupled temperature-displacement analysis procedures. Variable time-stepping to control the stability and accuracy of the constitutive time-integrations, was implemented by suitably modifying this analysis procedure.

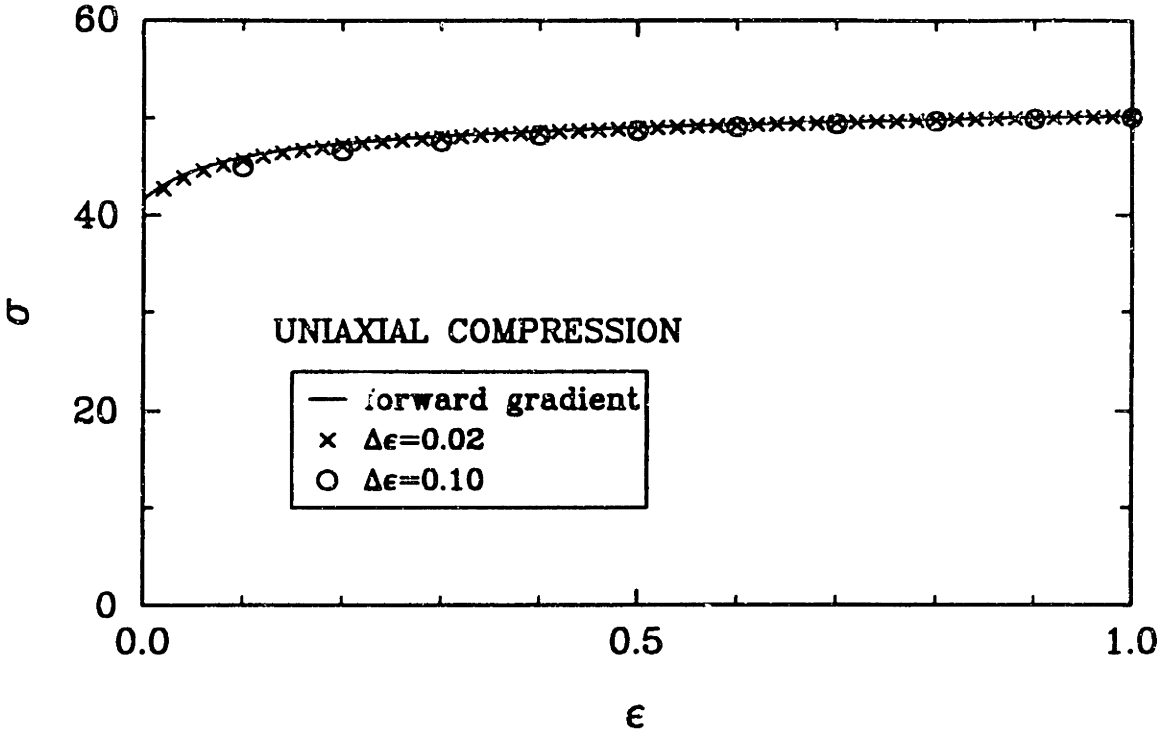

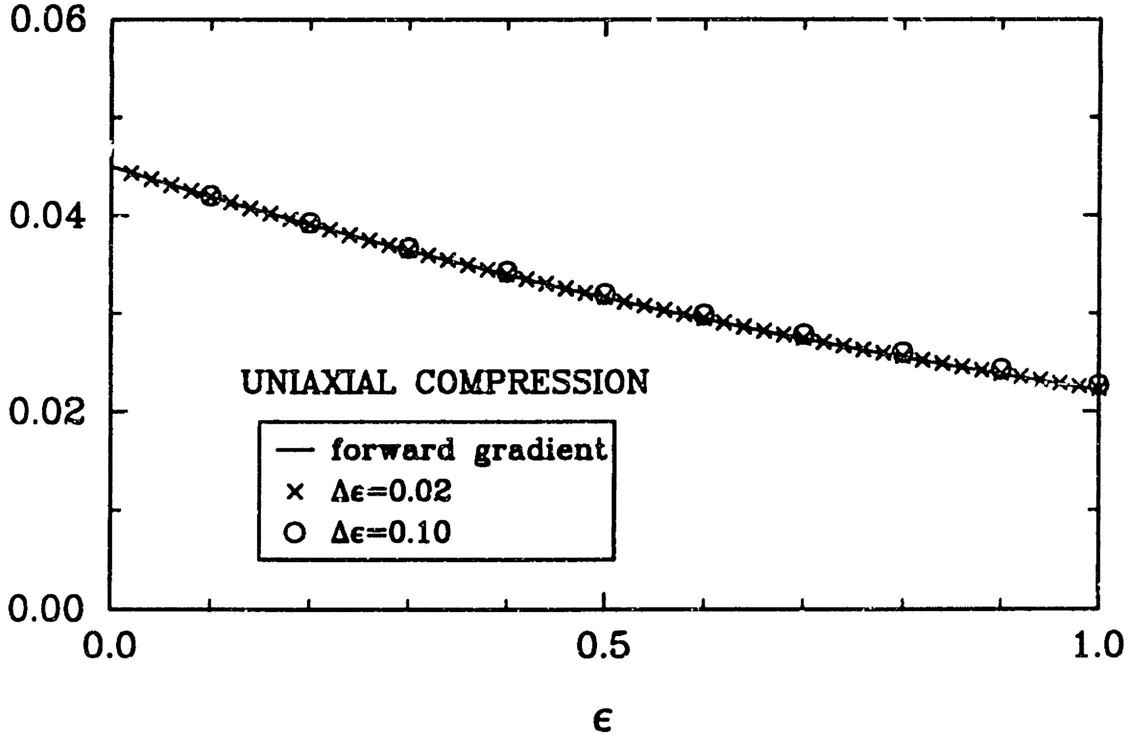

Figure 3.1: Evaluation of the integration algorithm. Uniaxial compression.

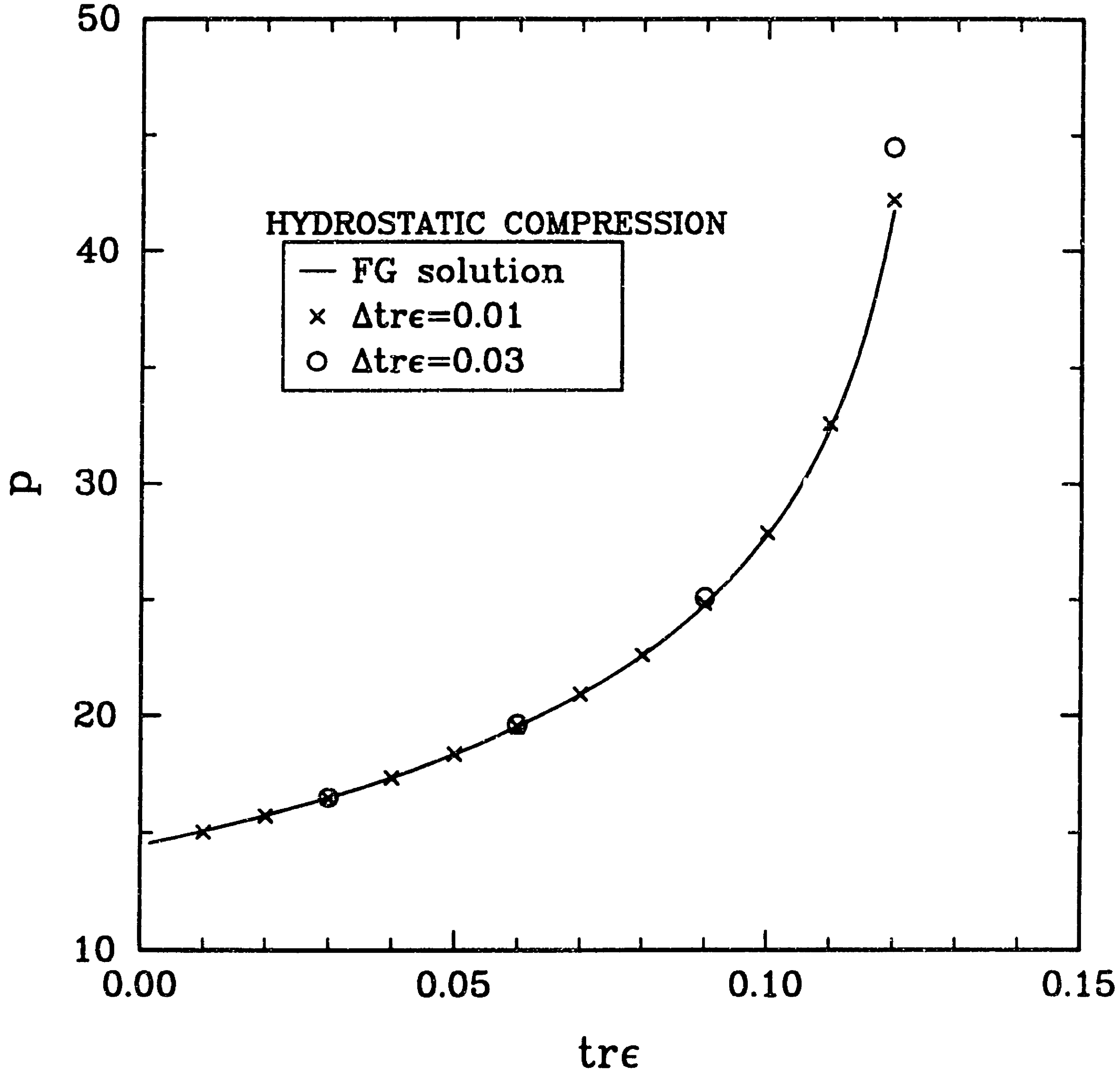

Figure 3.2: Evaluation of the integration algorithm. Hydrostatic compression.

Chapter 4

Example Calculations

In this section we present four example calculations which demonstrate the versatility of the proposed constitutive model and the robustness of the time-integration procedure. The examples explored below are: (a) isothermal hot compression of a tapered disk made from an initially porous material, to illustrate the effect of secondary tensile stresses on hot workability of such metals; (b) isothermal cold tension of notched axisymmetric bars made from initially porous materials, to illustrate the effect of multiaxial stress states on cold workability; (c) fully-coupled, high rate plane strain tension test, to illustrate the physical effects of flow softening due the combined effects of void growth and deformation heating on shear band formation; and (d) formation of internal damage during multi-step drawing of a rod at low homologous temperatures under isothermal conditions.

4.1 Tapered Disk Compression

The compression of an axisymmetric tapered disk between flat unlubricated dies under "sticking friction" conditions has been proposed as a useful hot-workability test by Malas *et al* [52]. A schematic of such an experiment is shown in Fig. 4.1. As the material is compressed along the vertical direction in the center of the specimen, an outward radial flow is induced, and since the material at the perimeter of the specimen is unconstrained and initially not subject to compressive displacements there, a tensile hoop stress and a negative pressure develops in this region and this can cause void nucleation and growth, which occasionally leads to fracture.

This is a useful hot workability test, because it combines the advantages of simple geometry and ability to impose tensile deformations at high temperatures without the restrictions of necking. An estimate of the elongation at fracture can be easily obtained in the case of fractured specimens. However a possible failure (in the form of surface cracks) cannot be detected during the test, since it is not reflected in the load versus stoke curve. It can be used as a pass/fail test, i.e. whether the material can sustain a certain level of tensile elongation without loosing its structural integrity.

An isothermal hot-compression tapered disk experiment on an initially porous, $f_o = 0.0475$, Fe-2%Si material at 800°C has been conducted and also simulated numerically. Fe-2% Si was chosen as a model material for this experiment because unlike other iron based materials it does not exhibit a phase transformation from bcc to fcc crystal structure upon heating to high temperatures, and also because it does not exhibit any dynamic recrystallization. A phase transformation and/or dynamic recrystallization would have masked the primary effects of viscoplastic void growth at high temperature under study.

Characterization of the matrix [Haghi 1991]

The material parameters $\{A, Q, m, h_0, q, \tilde{s}, n\}$ for the fully dense matrix material have been obtained by Haghi [94]. He has performed hot compression experiments[1] on a fully dense Fe-2% Si alloy, to determine these material parameters. The experiments needed to determine the material parameters are monotonic constant true strain rate experiments at various strain rates, as well as strain rate jump experiments. Fig.

---

[1] He followed the experimental procedures similar to those of Brown, Kim, and Anand [79], who have previously performed similar experiments on wrought, fully dense Fe-2% Si.

4.2a, b, and c from Haghi's thesis show representative examples of such experiments on the fully dense Fe-2%Si in the strain rate range 10^{-3} — $1.0\,\mathrm{s}^{-1}$ and temperature range 1073 — 1273°K. With $\theta_m = 1773$°K for Fe-2%Si, this temperature range corresponds to temperatures $\theta \geq 0.6\theta_m$. Accordingly, we use the form (2.30) for the temperature dependence of $\dot{\epsilon}_o$, and take the parameters $\{A, Q, m, h_o, q, \tilde{s}, n\}$ as constants, independent of temperature. The material parameters determined by Haghi from his experiments are listed in Table 2. The values for the initial deformation resistances s_o at different temperatures are listed in Table 3. Fig. 4.2a,b, and c also present the simulations of the isothermal, constant true strain rate and a strain rate jump experiments, together with the original experimental data. Comparison of the simulations against the data shows that the constitutive model reasonably well duplicates the physical data upon which the model is based and from which the material parameters of the model have been determined. The correlation between the model and the experimental data is very good.

Table 2

Material Parameters

for dense Fe-2%Si

A	10^{12}	s^{-1}
Q	324.51	kJ/mol
m	0.1541	
h_0	1325	MPa
q	1.6	
$\tilde{s}$	31.98	MPa
n	0.01474	

Table 3

Values of s_o

θ ,° K	s_o, MPa
1073	30.50
1173	29.33
1273	28.72
1373	27.95

Among the various experiments that Haghi has performed to test the predictive capability of this model are experiments in which the strain rate is increased, decreased and then increased again. Fig. 4.2d shows the results from such an experiment. This figure also shows that the constitutive model for the matrix material *predicts* the outcome of such an experiment very well, duplicating both the instantaneous, constant structure strain rate dependence, and the subsequent strain hardening.

As noted earlier, this constitutive model for the matrix material accounts for the physical phenomena of strain rate and temperature sensitivity, strain rate history effects, strain hardening and the restoration process of dynamic recovery. As compared to other currently used constitutive models which take the equivalent plastic strain rate to be a simple power-law (or a hyperbolic sine function) of the equivalent stress, together with a temperature dependence of an Arrhenius form, and which do not account for any internal structural evolution, the constitutive model considered here represents a major improvement.

Experiment

Specimens of controlled porosity were produced by powder metallurgy. Solid stock of Fe-2%Si was inert gas atomized to produce near spherical powder (see Fig. 4.3(a)). The product of the atomization was sieved below -325 mesh ($44 \mu m$) to obtain a fairly narrow size distribution (see Fig. 4.3(b)). The powder was subsequently vacuumenclosed in cans. Before welding, the cans were heated to 200°C for 30 minutes for degassing. The cans were hot-isostatically pressed under different pressure and temperature schedules to produce compacts of different porosities. Following HIPing the compacts were initially sintered at 960°C for 24 hours in argon to improve the bonding of the particles (heat treatment HT1). After this heat treatment the pores were still angular due to the initial spherical shape and the narrow size distribution of the powder (see Fig. 4.4).

Tapered disk compression tests on this material demonstrated its low ductility (what a way to show the usefulness of the test!). Several radial cracks developed around the specimen. The angular shape of the voids acted as a stress concentration and led to quick failure along previous particle boundaries (Fig. 4.5(a)). Examination of the surface of the compressed disk revealed numerous concentric cracks on the face of the disk (Fig. 4.4(b). Due to the high friction, once the material comes into contact with the die, it stops moving, while adjacent parts of the material are still moving in the radial direction causing strong local tension leading to a stick-fracture sequence.

In order to obtain a stronger material the specimen were subjected to a second long sintering schedule (heat treatment HT2: 100 hours at 1100°C in vacuum), which resulted in rounding of pores and substantial increase of the strength of the porous compact. No significant grain growth occurred during that heat treatment as can be verified from Fig. 4.6. Using this material isothermal tapered disk experiments were performed on Fe-2% Si at high temperatures in vacuum. In that way there is no need for an oxidation barrier coating. The loading train consisted of low thermal conductivity 94% alumina rods and short TZM flat end caps. With this configuration the head conduction through the loading rods was kept to a minimum, leading to a negligible temperature gradient along the specimen. The usual heating up time was approximately 2 hours for each experiment. Then the temperature was held constant for 30 minutes before each test in order to reach a steady state in the heating zone.

The lower platen was moved with a constant speed of 0.8 mm/sec.

Fig. 4.7(b) shows the resulting load deflection curve, and Fig. 4.7(c) shows the deformed shape of the specimen at the end of the experiment. After the test, the deformed specimens were sliced, photographed and image-analyzed to measure the distribution of residual porosity. Fig. 4.7(d), (e) and (f) show micrographs from representative radial locations after the experiment. These figures clearly show the gradients in porosity at the end of the experiment. Near the surface of the specimen the void volume fraction has grown, while at the center void closure is observed.

Simulation

Using the symmetry of the geometry only one quarter of the specimen is modeled. The undeformed finite element mesh consisting of 276, 4-noded ABAQUS type CAX4 axisymmetric elements is shown in Fig. 4.1(c). Using the values for the material parameters for the viscoplastic part of the constitutive functions selected by Haghi, and the values $E = 135\text{MPa}$ and $\nu = 0.35$ for the elastic constants for the dense Fe-2%Si at 800°C (Brown, Kim and Anand, [79]), the isothermal, hot-compression tapered disk test on an initially porous material, $f_o = 0.0475$, has been simulated using the finite element program ABAQUS together with our UMAT.

Fig. 4.8(a) shows a comparison of the die force versus die stroke curves from the experiment and the corresponding simulation. The jumps in the die force occur in the calculated result whenever new nodes come into contact with the die. Fig. 4.8(b) shows the corresponding comparison for the variation of (f/f_0), the void volume fraction normalized by the initial volume fraction, as a function of (x/r), where x is the radial distance measured from the center of the deformed specimen along the mid-plane, and r is the mid-plane radius of the deformed specimen. The quantitative agreement between the simulations and the experimental measurements is very good.

Fig. 4.9 contains sequential contour plots from the numerical simulation which show the *process of evolution of porosity* in this experiment. Fig. 4.10 shows the corresponding contour plots for the variation of (Σ_h/s) during the experiment. Due to the sticking friction conditions between the die and the porous workpiece, the material under the die is highly constrained and initially forms a "dead metal zone" there. Subsequently, the material first densifies along a classical "cross" pattern, with the densification concentrated in the center of the specimen. The densification front then propagates along the axial direction, and finally along the radial direction, at which point it induces tensile stresses on the surface that cause the voids to grow. The major qualitative features of the tapered disk compression test are captured by the simulation.

4.2 Axisymmetric Notched Bar Experiment:

A classic cold workability test is an axisymmetric notched bar specimen tested in tension (e.g., Hancock and Mackenzie, [26], Brown, Hancock, Thomson and Parks, [38] Hancock and Brown, [51], Needleman and Tvergaard, [57]). Recently, Becker, Needleman, Richmond and Tvergaard, [74], have used such experiments to carry out a detailed study of void growth and ductile failure under non-uniform multiaxial stress states in notched tensile specimens machined from porous iron compacts. They used the GTN constitutive model (with $q_1 = 1.25$, $q_2 = 0.95$ in equation (1.2)) to carry out numerical simulations of these experiments and found quite good agreement between experiments and computations for several combinations of notch shape and initial void volume fractions. Here, we briefly report on our own similar study on isothermal, room temperature, tension experiments on notched specimens made from porous Fe-2%Si, the same material as the one used in our hot workability experiments. In our simulations we shall use the constitutive model and computational procedures presented in the previous sections.

Porous Fe-2%Si was manufactured with initial porosities of 0.004, 0.06, and 0.13.

Micrographs of the porous material are shown in Fig. 4.11(a). Note that the pores are fairly random and nearly spherical. The material parameters for the matrix material were determined by conducting compression tests on fully dense Fe-2%Si material. Two experiments were conducted: (*i*) a strain rate jump experiment from $10^{-1}\,\mathrm{s}^{-1}$ to room $10^{-4}\,\mathrm{s}^{-1}$ to determine the strain rate sensitivity parameter m, and (*ii*) a monotonic experiment at a strain rate of $10^{-2}\,\mathrm{s}^{-1}$ to determine the hardening parameters $\{h_o, q, \tilde{s}, s_o\}$. The values of the various material parameters determined from these experiments are given in Table 4.

Table 4. Material Parameters
Dense Fe-2%Si
(Room Temperature)

$\dot{\epsilon}_0$	0.01	s^{-1}
h_0	7754.	MPa
q	1.92	
$\tilde{s}$	925.	MPa
s_0	335.	MPa
m	0.007	
n	0.	

Note the low value $m = 0.007$ for the strain rate sensitivity parameter; the material response at room temperature is almost rate-insensitive. For present purposes, the value of the parameter n which governs the rate sensitivity of the rate of strain hardening has been approximated as zero. Also, we use the values $E = 200\,\mathrm{MPa}$ and $\nu = 0.3$ for the Young's modulus and Poisson's ratio for the dense Fe-2%Si. The quality of the match between the experimental data and the stress strain curve in simple compression resulting from the use of these material parameters is shown in Fig. 4.11(b).

The geometry of the notched tension bar is shown in Fig. 4.12(a). The notch acuity, measured as the ratio of the initial radius $R_0 = 3\,\mathrm{mm}$ of the minimum cross-section, to the initial notch root radius $r_0 = 1.5\,\mathrm{mm}$, is $R_0/r_0 = 2$. Isothermal room temperature tension tests on axisymmetric notched bars were conducted in which the ends of the specimens were pulled apart at a relative velocity of $10^{-3}\,\mathrm{mm\,s^{-1}}$. Fig. 4.12(b) shows the resulting load-displacement curves for specimens made from each of the three porosities $f_0 = 0.004, 0.06,$ and 0.13.

Fig. 4.13(a), (b) and (c) show micrographs from representative locations in the longitudinal cross-section of the specimen after failure in the experiment on the specimen with initial porosity $f_0 = 0.06$. Fig. 4.13(d) shows a scanning electron micrograph of the fracture surface. Ductile failure occurs primarily by hole growth and coalescence. The micrographs show that in the vicinity of the root of the notch, slightly away from the fracture surface, some voids have elongated and coalesced, Fig. 4.13(c) At the center of the specimen where the triaxiality is higher but the strains achieved are smaller, the voids grow in a more spherical manner, but the amount of void growth is slightly smaller, Fig. 4.13(b). Also, as expected, in the shoulder region there is essentially no change in the amount of the porosity from its initial value, Fig. 4.13(a).

The axisymmetric notched bar tension tests have been simulated using the finite element mesh shown in Fig. 4.12(c). Because of the symmetry of the specimen, only one quarter of the geometry is modeled. The mesh consists of 408 ABAQUS CAX8R-type, axisymmetric, eight-noded, quadratic elements with reduced integration. The material parameters used were those listed in Table 4. Fig. 4.12(b) shows a comparison of the load-displacement curve from the experiments and the simulation for the three initial porosities $f_0 = 0.004$, 0.06, and 0.13. The constitutive model and computational procedures nicely capture the shapes of the load versus displacement curves, and the decrease in the load carrying capacity of the specimens due to increase in porosity. The load-displacement response of the specimen with $f_0 = 0.13$ is slightly overestimated. We attribute this overestimation to the fact that for such large initial porosities, the pores are partially interconnected, Fig. 4.11(a), and as mentioned earlier, our constitutive model is expected to be useful only for situations with isolated and initially approximately spherical pores.

Fig. 4.14 shows the level contours of the the ratio (Σ_h/s), the equivalent tensile plastic strain in the matrix, ϵ^p_m, and the porosity f predicted by the simulation for specimens with $f_0 = 0.06$ at the time when the specimen actually fails during the physical experiment, point A in Fig. 4.12(b). This figure shows that for this relatively low triaxiality specimen, while the maximum triaxiality (~ 1) occurs at the center of the specimen, the equivalent tensile plastic strain is largest at the notch root, and that these two factors lead to maximum porosity growth and ductile fracture initiation at some distance ahead of the notch root. This contrasts with the predictions of Needleman and Tvergaard, [57], who have reported that in all their simulations of axisymmetric notched bar specimens fracture initiates at the center of the specimen.

The void volume fraction along the center line of the specimen in the axial z-direction, measured after the experiment on the specimen with initial porosity $f_0 = 0.06$, is shown in Fig. 4.15. This figure also shows the corresponding prediction from the finite element calculation. There is good agreement between the prediction and the measurement, except for the point next to the fracture surface, where the measured porosity is higher than the predicted one.

As expected, since our constitutive model has no built-in coalescence and failure criterion, we are unable to predict the ductility of the specimens. It has long been known that failure in ductile materials is associated with the coalescence of voids. Tvergaard and Needleman, [59] have proposed an approximate way of incorporating the effect of coalescence into the Gurson model for porous plasticity. They have suggested the replacement of the void volume fraction f in the yield function/plastic potential in Gurson's model by

$$f^* = \hat{f}^*(f) = \left\{ \begin{array}{ll} f & \text{if } f \leq f_c \\ f_c + ((f_u^* - f_c)/(f_f - f_c))\,(f - f_c) & \text{otherwise} \end{array} \right\}. \tag{4.1}$$

In this modification the effects of void coalescence start when the void volume fraction f reaches a critical value f_c, and final fracture occurs at a volume fraction f_f, at which point f^* has a value $f^*(f_f) = f_u^* = 1/q_1$, where q_1, in the range 1.25 to 2, is a parameter in the GTN yield function, equation (28). Tvergaard [88] has reviewed the unit-cell model studies of Koplik and Needleman [76] and Becker *et al.* [74] conducted to arrive at estimates of f_c and f_f. These micro-mechanical studies have shown that the parameter f_c is strongly dependent on the initial porosity f_0 (see Fig. 10 of Tvergaard [80]). For example, Becker *et al.* [74] found f_c to be 0.04, 0.07, and 0.12 for initial void volume fractions f_o of 0.004, 0.026 and 0.06, respectively. These authors obtained good agreement of ductility predictions with their experimental measurement when they used these initial porosity dependent values of f_c, together with $f_f = 0.25$, and $f_u^* = 1/q_1 = 0.8$.

We have implemented this coalescence and failure criterion in our deformation model for porous materials by replacing the void volume fraction f by the modified porosity f^* defined in (4.1), together with $f_u^* = 1$. Using this modification, we have repeated the notched bar tension simulations with $f_f = 0.25$, and values f_c equal to 0.04, 0.12, 0.20 for the initial porosities f_0 equal to 0.004, 0.06, 0.13, respectively. These values of f_c were obtained by interpolating and extrapolating the results of the f_0 dependence of f_c summarized by Tvergaard [88] (his Fig. 10).

The predicted load-displacement curves for all three porosities are shown as dashed lines in Fig. 4.12(c). In these calculations, once the porosity reaches the critical value f_c in some material neighborhood, the deformation in that material neighborhood very quickly accelerates, and the macroscopic load drops rapidly, indicating impending ductile fracture. The use of the coalescence and fracture initiation criterion of Tvergaard and Needleman does bring the predictions for the rapid load drop towards some agreement with that observed in the experiments, however the numerical simulations still overestimate these events for all three initial porosities.

The level contours of the the ratio (Σ_h/s), the equivalent tensile plastic strain in the matrix, ϵ_m^p, and the porosity f predicted by the simulation for specimens with $f_0 = 0.06$ at the time just before the value of the porosity in the simulation reaches the failure initiation porosity $f_f = 0.25$, point B in Fig. 4.12, are shown in Fig. 4.14. The corresponding predictions of f along the center line of the specimen in the axial direction are shown in Fig. 4.15. As expected, the actual measurements of f are bracketed by the simulations using no coalescence criterion, and the one using the rapid coalescence criterion of Tvergaard and Needleman.

It is possible to adjust the values of $\{f_c, f_f, f_u^*\}$ to bring the predictions in better agreement with experimental measurements, but we do not pursue such an exercise here. Much remains to be done to develop better quantitative models of void growth, coalescence, ductile fracture initiation, and transition to failure which account for anisotropies due to void shapes, sizes, distributions, and other statistical effects.

Finally we attempted a comparison of the prediction of our model with those of the GNT model. This model has recently gain popularity in applications with near rate insensitive materials. Consistently correct qualitative predictions and encouraging comparisons with experiments have been reported mainly by Needleman and coworkers (e.g., [53, 57, 59, 66, 74]).

We simulated the notched bar tension experiments using the GNT model (1.2) with $q_1 = 1.5$ and $q_2 = 1$. In Fig. 4.16(a) the predicted load displacement curves are compared against the the experimental ones. The agreement is good in terms of the predicted load levels, slightly better that the one predicted by our model. The predictions of ductility (again based on the coalescence model of Needleman and

Tvergaard [57] (equation 4.1)), show similar trends with those of our model.

It should be noted, however, that the predictions of Gurson's model depend strongly on the selected values of the parameters q_1 and q_2. Various suggestions of the values of q_1 and q_2 have appeared in the literature:

- In the original Gurson model [34] both q_1 and q_2 were taken to be equal to 1.
- Based on shear band localization in a periodic array of voids Tvergaaard [43] suggested $q_1 = 1.5$ and $q2 = 1$.
- Becker *et al.* [74] used the values $q_1 = 1.25$ and $q_2 = 0.95$ in their analysis of axisymmetric notched bars in- tension.
- Haghi and Anand [100] suggested that $q_2 = 0.88$ brings the Gurson model to a better aggreement with the spherical cell result at $X = \infty$.

In other words there has been no consistent way of deriving these two parameters. The effect of varying these parameters is shown in Fig. 4.16(b). Both parameters seem to have a very strong effect on the ductility predictions.

4.3 Plastic Flow Localization In Plane Strain Tension:

Localization in the sense of deformation patterns involving one or more intense "shear bands" frequently occurs in a wide variety of solids, and it is well known that the plane strain mode of deformation is particularly prone to the formation of shear bands (e.g., Rice [35]; Anand and Spitzig, [39]. For a recent review of analyses of plastic flow localization in metals see Needleman and Tvergaard [104] where a majority of the references to the previous literature on this important subject may also be found.

Here we investigate the combined effects of softening induced by material damage/porosity *and* softening induced by heating due to plastic dissipation on the *onset and development* of shear bands in a plane strain tension test. We (Zavaliangos and Anand [106]) have recently reported on an analysis similar to the one presented here, but with a different constitutive model and a different time integration procedure. The constitutive model and computational procedures considered here are, in our opinion, much improved over those used in our previous paper.

The geometry and the initial mesh chosen to model one quarter of the specimen are shown in Fig. 4.17. The mesh consists of 442 8-noded ABAQUS type CPE8RT elements with 1471 nodes. The CPE8RT is a quadratic plane strain element with reduced integration and linear interpolation of the temperature. The mesh has been refined in the region of anticipated shear band formation.

The specimen is assumed to be initially at room temperature, 298°K, and the top boundary of the specimen is pulled at a constant speed, v of 25 $\mathrm{m\,s^{-1}}$, which for the geometry of the specimen considered here gives a nominal strain rate (v/l_0) of $500\,\mathrm{s}^{-1}$ in the central gage section. The boundaries of the specimen are taken to be insulated and therefore there is no heat conduction away from the surface of the specimen to the environment. In the numerical analysis the effects of inertia are neglected and using the coupled temperature-displacement procedure of the finite element code ABAQUS, the fully-coupled thermomechanical problem is solved. Because the geometry of the specimen the deformation is slightly inhomogeneous right from the beginning of the test, there is no need for any perturbation of the initial data to trigger the diffuse necking and the shear band localization phenomena.

In what follows we report on the results of our fully-coupled simulations for specimens made from a porous aluminum with an initial void volume fraction of $f_o = 1\%$, as well as a dense aluminum.

The material parameters for the aluminum matrix used in this example have been determined by fitting our constitutive model to the shear stress τ versus shear strain γ data reported by Senseny, Duffy and Hawley [36] for 1100-O aluminum. Their data is reproduced as the solid lines in Fig. 4.18. Their experimental data covers the strain rate range $0.0002 \leq \dot{\gamma} \leq 300\,\mathrm{s}^{-1}$ at few selected temperatures. Here we concentrate on their data for 298°K and 523°K. In this range of temperatures we use the expression (2.31) for the temperature dependence of $\dot{\epsilon}_o$. The values for the material parameters for the dense 1100 aluminum alloy determined by fitting the data of Senseny *et al.* [36] to our constitutive model are listed in Table 5. The representation of this experimental data by our simple rate and temperature dependent constitutive model is shown in Fig. 4.18 by the dashed lines. The quality of the curve-fit is very good.

Table 5. Material Parameters

Dense Al-1100

A	10^{14}	s^{-1}
Q	77.15	kJ/mol
h_0	5250	MPa
q	2.0	
$\tilde{s}$	133.4	MPa
$s_0(298^o\ \mathrm{K})$	30.5	MPa
$s_0(523^o\ \mathrm{K})$	16.3	MPa
$m(298^o\ \mathrm{K})$	0.007	
$m(523^o\ \mathrm{K})$	0.011	
$n(298^o\ \mathrm{K})$	0.024	
$n(523^o\ \mathrm{K})$	0.052	

Note that unlike the situation at high temperatures, Table 2, where the constant structure strain rate sensitivity parameter m is larger in value than the parameter n which models the effect of strain rate on the rate of strain hardening, at low temperatures the value of m is smaller than that of n. For lack of experimental data, in our calculations we will use a linear interpolation for the values of the parameters m and n between 298°K and 523°K.

For the thermo-elastic properties of the matrix material we use:

$\mu_{m,0} = 26\,\text{GPa}$, $\kappa_{m,0} = 68\,\text{GPa}$, $\chi_1 = 0.5$, $\chi_2 = 0.333$,
$\alpha_m = 22.6 \times 10^{-6}/^\circ\text{K}$, $\rho_m = 2,770\,\text{kg/m}^3$, $c_m = 875\,\text{J/(kg}^\circ\text{K)}$, $\lambda_m = 160\,(\text{W/m}^\circ\text{K})$,
$\omega = 0.9$, $\theta_m = 933^\circ\text{K}$.

Currently, ABAQUS does not have any provisions to include the effects of variation of the thermal expansion coefficient α, the specific heat c, and the thermal conductivity λ with the values of solution dependent variables. For the example problem under study the temperature increase is expected to be of the order of 100°K above room temperature. The variation in the values of α_m, c_m and λ_m for this temperature rise is known to be small, and we neglect this variation in our calculations. However, it is important to consider the variation of ρ and c with with porosity. For the near adiabatic conditions of our numerical experiment we incorporate this dependence by using (A.3) and (A.5) to modify (16) as:

$$\dot{\theta} \approx (\rho_m c_m)^{-1} \left\{ \text{div}\ (\lambda_m\, \text{grad}\theta) + \left(\frac{\omega}{(1-f)^2} \right) \bar{\mathbf{T}} \cdot \mathbf{D}^p \right\}.$$

Fig. 4.19 shows the load versus nominal strain, $e \equiv (v/l_0)\,t$, curves for both the fully dense and initially porous materials. As expected, the flow curve for the porous material is lower than that for the fully dense material. Also, while the fully coupled calculation for the dense material shows a gradual load drop at large nominal strains, the corresponding calculation for the porous material shows a sharp drop in the load.

Fig. 4.20(a) shows the evolution of the equivalent tensile plastic strain rate in the matrix, $\dot{\epsilon}^p_m$, during the course of the deformation at two points, one at the center of the specimen, point A, and one outside the central region on the axis of symmetry of the specimen, point B, for the porous material. Fig. 4.20(b) shows the corresponding plot for the dense material. In these figures the point of separation of the curves for points A and B indicates the instability point associated with the formation of a *diffuse neck* in the specimen, and the rapid increase in the strain rate for point A in Fig. 4.20(a) is associated with the shear band localization in the porous specimen. In the fully dense specimen, Fig. 4.20(b), the strain rate at the center of the neck increases, but at a slower rate.

In order to differentiate between the effect of softening due to thermal effects and that due to void growth, the load versus strain curve for the porous material under isothermal conditions is also shown in Fig. 4.19. As expected, the sharp drop off in the load occurs at a later stage in this experiment. The acceleration of localization due to thermal effects over that due to microvoid growth alone is also clearly brought out in Fig. 4.20(a).

Under the particular conditions of our numerical experiment, the calculation for the fully dense material shows that thermal softening alone is not strong enough to develop a sharp shear band. In the case of the initially porous specimen, thermal softening and growth of microvoids are two competing and interacting softening mechanisms. In this simulation softening due to microvoid growth is the major reason for the shear band development and it is *assisted* by the softening due to thermal effects.

The level contours of $\dot{\epsilon}^p_m$, θ and f at two representative nominal strain, e, levels e_1 and e_2 (keyed to the load versus nominal strain plot) in the vicinity of the load drop in the fully-coupled calculation for the porous material are shown in Fig. 4.21. This figure clearly shows the rapid localization of deformation into a shear band in the vicinity of the macroscopic load drop, Fig. 4.21. The increase in the temperature, Fig. 4.21(b), and the porosity, Fig. 4.21(c), in the band is also clearly brought out in these contour plots. Due to the pressure dependence and dilatancy of plastic flow of the constitutive model the inclination of the shear band is different from 45° and it is estimated to be $\approx 38°$ with respect to the horizontal, Fig. 4.21(a). As can be seen in Fig. 4.21(c), the porosity outside the shear band increases from 1% to only 3%, while that inside the band reaches values ranging up to 14% at the center of the specimen. Since our constitutive model does not contain an explicit failure criterion, we terminated our calculations slightly beyond the nominal strain e_2. In these calculations we did not use the void coalescence model, equation (4.1), of Tvergaard and Needleman [59]. Upon repeating the coupled calculations for the porous material using the modified porosity function f^*, equation (4.1), together with $f_c = 0.055$ for $f_0 = 0.01$ we find that the rapid drop begins to occur at a nominal strain between e_1 and e_2, and thereafter the load drop is much steeper (dashed lines in the load strain curve of Fig. 4.21). Other aspects of the results from our simulations are essentially the same.

Beyond the strain e_2 the shear band quickly collapses to the minimum width resolvable by the finite element mesh. The shear band tends to collapse to a zero thickness surface because in our first-order constitutive model for the mechanical part of the problem, there is no characteristic length. Also, the characteristic length associated with heat conduction [2] is much too small to be resolved by the mesh employed.

To summarize, we have performed a thermo-mechanically coupled finite element simulation of a high-rate plane strain tension test on a microporous solid. Elasticity, thermal expansion and large geometry changes are accounted for, but inertial effects have been neglected. We have used the numerical simulation of the plane strain tension test to study the competing effects of porosity softening and thermal softening, and also to follow the initiation and growth of band-like regions of localization through slow early growth to severe localization.

---

[2] This length is defined by $\sqrt{\lambda/(\rho c \dot{\epsilon}_b)}$, where $\dot{\epsilon}_b$ is a representative strain rate within the band.

As is clear from the calculations presented above, for realistic values of the thermal conductivity of metals, in conventional finite elements the mesh size sets the lower limit to the spatial resolution of shear bands. Much remains to be done concerning spatial discretization methods and adaptive meshing techniques employed in finite element procedures to adequately capture post localization behavior and the transition from localization to failure. To this end, the development of specialized elements for shear band calculations and the development of various adaptive mesh refinement techniques is an active area of current research. For a recent discussion of these and other research issues concerning shear bands and transition to ductile failure, see the recent report (Anand *et al.*, [85]) of a US-NSF workshop on localized plastic instabilities and failure criteria.

4.4 Central Bursts During Drawing/Extrusion

The development of internal damage in the form of central bursts is frequently encountered during cold drawing/extrusion of wires and rods. This internal damage may lead to breaks during the deformation process itself, or to premature fracture when the product is put in tension during service. Central bursts usually occur for large die angles and small area reductions, after severe cold working of the rod or wire, usually during the final steps of a multi-step drawing process (e.g., Pepe, [31]; Roesch and Sanz, [54]).

The factors leading to such internal damage are qualitatively understood. After large strains in a multi-step drawing operation, most materials have lost their strain hardening capacity, microvoids have nucleated at second phase particles and inclusions, and large die angles and small reductions in a drawing pass give rise to large hydrostatic tension on the wire axis in the die zone, and this leads to the formation of central bursts.

Early analytical studies of the plane strain version of the problem, based on limit analysis and slip line theory, are due to Coffin and Rogers [9], Avitzur [11] and Rogers [18]. Also Zimerman and Avitzur [15] and Avitzur [23] have presented "fail-safe" diagrams for single pass drawing. These diagrams are plotted in the plane of cross-sectional reduction in a pass versus the semi-cone angle of the die. A curved line in this plane separates regions which are either safe against central bursting, or unsafe. Roesch and Sanz [54] report that the effect of geometrical parameters is qualitatively well accounted for in these diagrams, but the risk of central burst formation in industrial practice is overestimated by such diagrams. Their experiments on wire drawing with geometries in the "unsafe" regions of such curves do not always produce central bursts. Also, central bursts seldom appear in the first step of a multi-step wire drawing process. Therefore the development of central burst cannot be explained simply on the basis of tool geometry alone.

Although the analyses of Avitzur and co-workers of single pass operations have lead to a substantial qualitative understanding of drawing, damage accumulation is a *process*, and in a multistep operation the cumulative effect of successive draws has to be taken into account. The only predictive approach appears to be detailed stress and strain path analyses of multi-step operations using constitutive models which incorporate the effect of internal damage evolution, together with valid fracture criteria.

Aravas [65] has carried out a quasi-static, isothermal, frictionless study of the growth of voids during a two-step axisymmetric extrusion of a rate independent material in which the Gurson model is used to account for the effects of microvoids. Mathur and Dawson [71] simulated the damage accumulation during a multi-step plane strain strip drawing using a damage model by Cocks and Ashby [47] together with the state-variable model of Hart [27] for the matrix material. Here we carry out a study similar to the one by Aravas, but use our rate-dependent constitutive model.

We have carried out numerical simulations of an axisymmetric, coupled, frictionless, two-step rod drawing operation with dies of average semicone angle 15° and area reductions of 16.3% in each pass. Heat conduction to the dies was ignored. The material being drawn is taken to be the same aluminum alloy with the same material parameters considered in the previous example of shear band formation. To numerically trigger the development of defects produced during the process, the material was assumed to have an initial porosity of $f_o = 0.01$.

The geometry of the two-step drawing operation, and the deformed finite element mesh is shown in Fig. 4.22. Because of the symmetry of the process, only one half of the problem is modeled. The mesh consists of 287 4-noded ABAQUS type CAX4 axisymmetric elements. In each pass the rod is gripped at the stepped-down end and pulled through the drawing dies at a rate of 1. mm/sec.

Fig. 4.23(a) and Fig. 4.24(a) show the contours of the equivalent plastic strain rate in the matrix during the first and second steps. These figures indicate, as expected, that the material is deforming plastically primarily in the reduction region of the dies. Fig. 4.23(b) and Fig. 4.24(b) show contours of the mean normal stress Σ_h normalized by the deformation resistance s. These contours show that a substantial hydrostatic tension can develop along the axis of the billet, and it is this hydrostatic tension that promotes void growth. Fig. 4.23(c) and Fig. 4.24(c) show the level contours of the void volume fraction f. After the material leaves the reduction region in the first step, the porosity along the axis has increased from $f = 0.01$ to $f = 0.02$. After the second step the maximum porosity in the specimen reaches $f = 0.038$. At some point after a number of such passes the voids will start to coalesce and fracture will eventually occur. To model this final fracture process a ductile fracture criterion is necessary, but that is still an outstanding issue which is not the object of the present paper.

Note that Fig. 4.23(b) and Fig. 4.24(b) also show that the material on the surface of the rod is under a residual hydrostatic tension after the exit from the die. This residual surface hydrostatic tension should have some connection with the formation of surface cracks which occasionally appear during drawing.

As is well known, if the strain hardening capacity of a material is exhausted, then the material is more prone to central bursting. We have confirmed this by carrying out a single draw calculation in which we set the strain hardening to zero, $h_0 = 0$, but kept all other material parameters at their previous values. Hydrostatic tension along the wire axis increases as strain hardening capacity decreases, Fig. 4.25, and the porosity along the centerline resulting from such a calculation is $f = 0.028$, which is higher than the one obtained previously, $f = 0.02$, when we used the full set of material properties for a hardening material. Thus, as expected, strain hardening of the matrix delays the opening of the internal pores, which agrees with existing experimental observations (Roesch and Sanz [54]).

In order to demonstrate the effects of the strain rate sensitivity on the formation of central bursts during drawing, we have repeated our calculations and conducted a parametric study by varying the strain rate sensitivity exponents m in the range 0.005 — 0.1. The material was assumed not to strain harden, $h_0 = 0$, in these calculations. The results of such parametric calculations are plotted in Fig. 4.26(a). The porosity along the centerline of the rod after each of the two steps, normalized by the initial porosity, is plotted against the strain rate sensitivity parameter m. A dramatic effect of the strain rate sensitivity on the development of central bursts is observed. The worst case, that is maximum void growth, corresponds to the rate independent limit — values of m close to zero. At higher values of m the growth of voids is much lower. Similar results were obtain for a rod extrusion with the same die geometry Fig. 4.26(b).

Our computational procedures are at present unable to account for the important effects of the heat generation due to friction between the die and the workpiece. Nevertheless, to qualitatively investigate the effect of heat generation due to plastic dissipation in the workpiece, we carried out a thermo-mechanically coupled calculation (with insulated boundaries) of a single draw operation, with a draw speed [3] of 10 m/sec. Although a maximum temperature increase of approximately $25°K$ is observed for the region in the vicinity of the surface of the rod, Fig. 4.27(d), a comparison of Fig. 4.27(b) and (c) against Fig. 4.24(b) and (c) shows that the contours of the hydrostatic tension and the porosity are essentially identical. The effects of temperature in this simulation are not significant. In realistic situations, friction may be a more important source of heat generation than plastic deformation.

These results show that the computational procedures of the type described in this work can be used to qualitatively check whether a particular process might lead to central burst formation for a particular material. In addition, different die designs may be analyzed to plot "processing maps" to delineate safe and unsafe combinations of area reductions and die semi-cone angles for a particular material with a known initial state in single draw operations. For multi-draw operations the evolution of the material properties, the internal state and the accumulation of damage must be carefully followed in order to conclude (with the use of a realistic fracture criterion) on the possibility of central burst formation in the process. Our state variable rate and temperature dependent constitutive model and computational procedures form the basis for such a potential design capability. The focus of this paper has been constitutive models and computational procedures for the workpiece. Much work needs to be done to formulate suitable mathematical models and numerical capabilities for the tool-workpiece interface to obtain a truly predictive design capability.

---

[3] Recall that our previous isothermal calculation was carried out for a draw speed of 1.0 mm/sec.

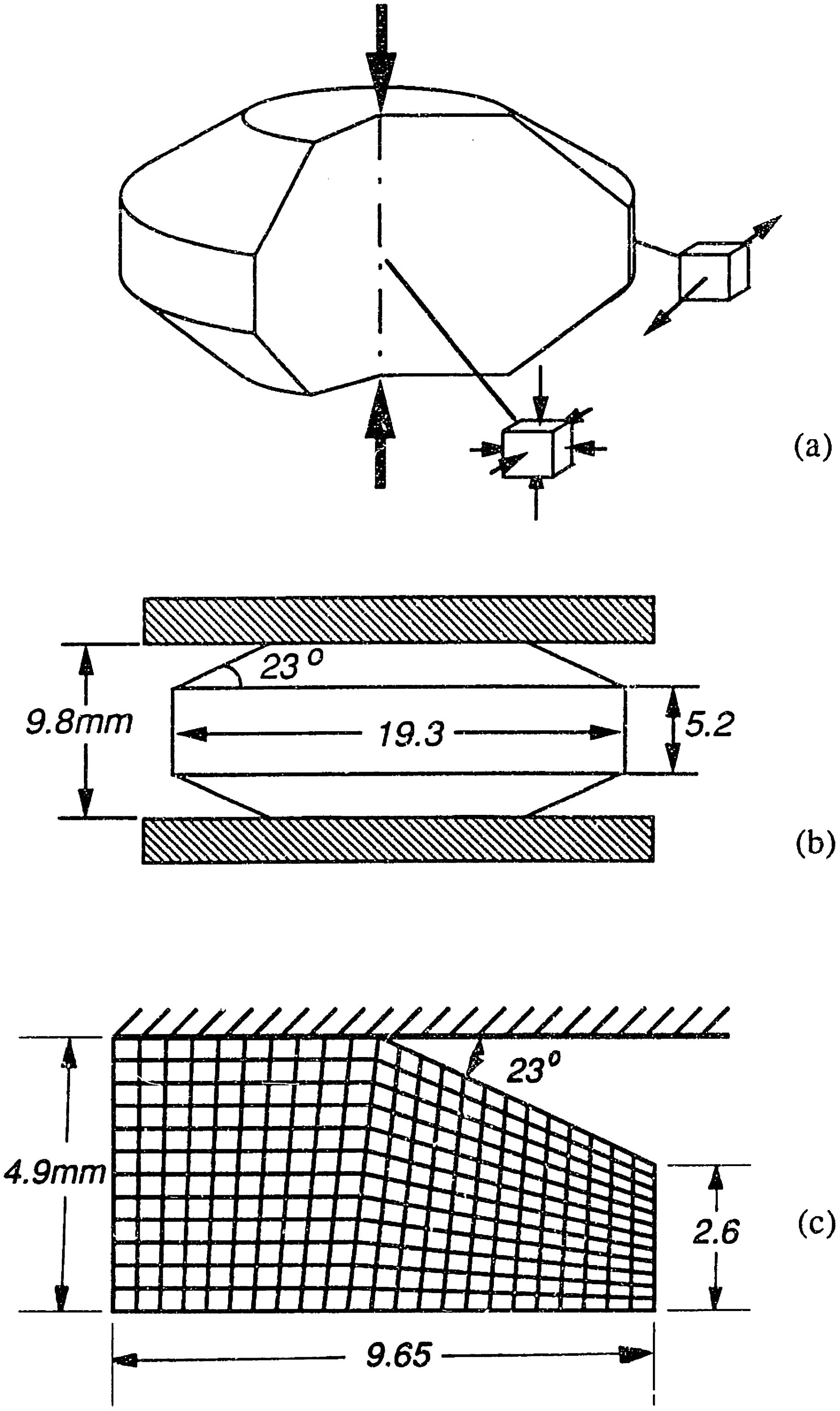

Figure 4.1: Tapered disk compression test for workability evaluation. (a) Schematic. (b) Geometry. (c) Finite element mesh.

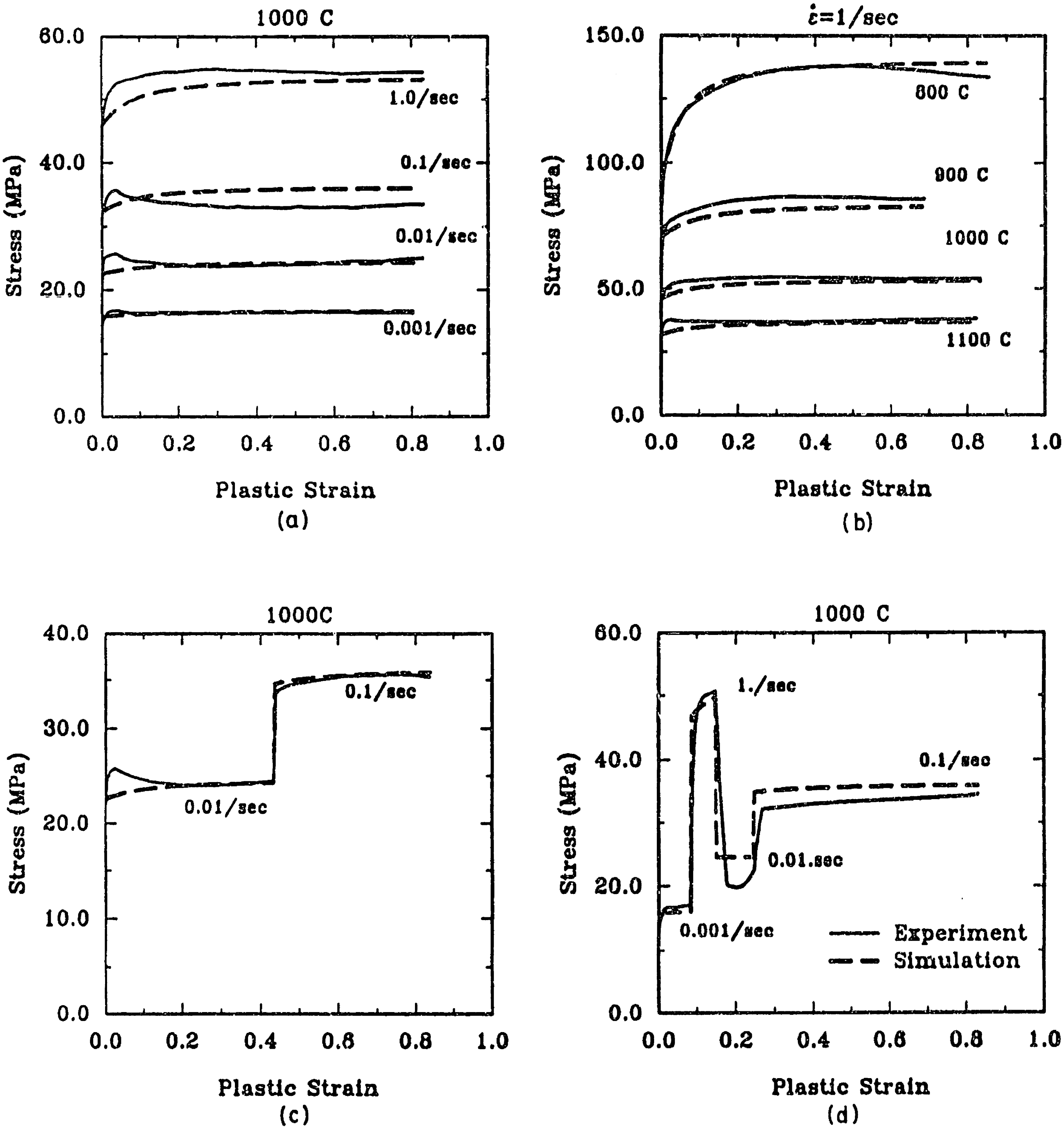

Figure 4.2: Effect of strain rate, temperature and strain rate history on stress-strain behavior of fully dense Fe-2%Si.

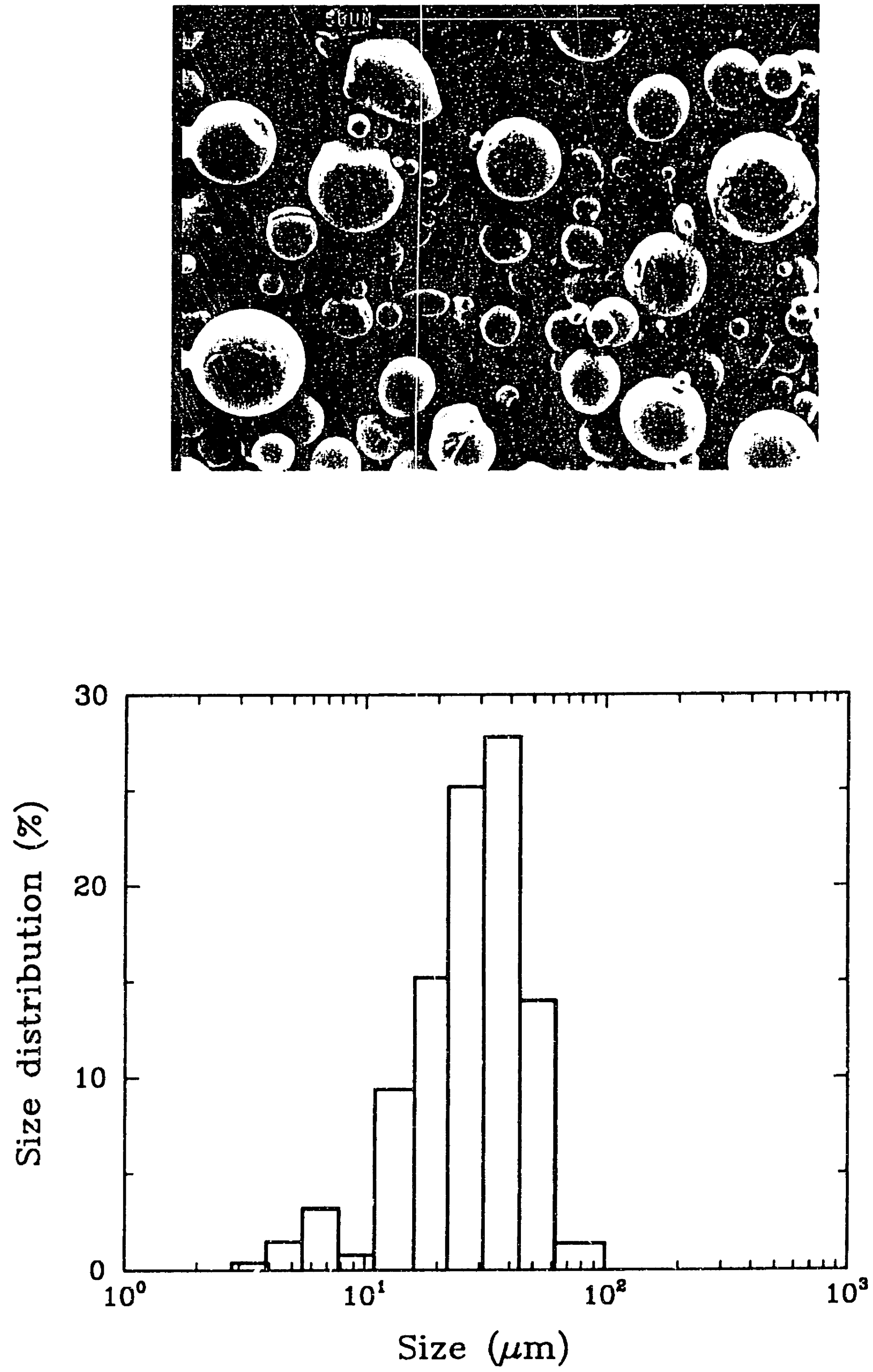

Figure 4.3: Micrograph of gas atomized Fe-2%Si powder and size distribution.

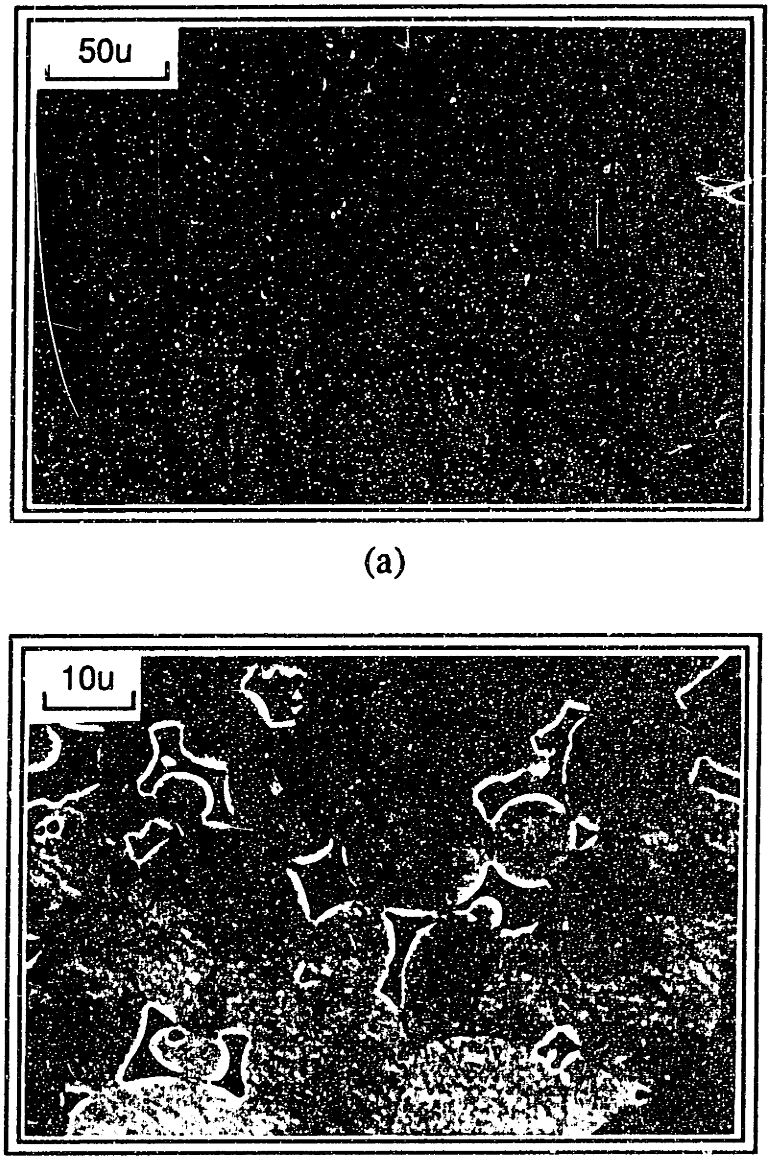

(a)

(b)

Figure 4.4: Angular voids in Fe-2%Si powder compacts after sintering for 24 hours at 1000°C.

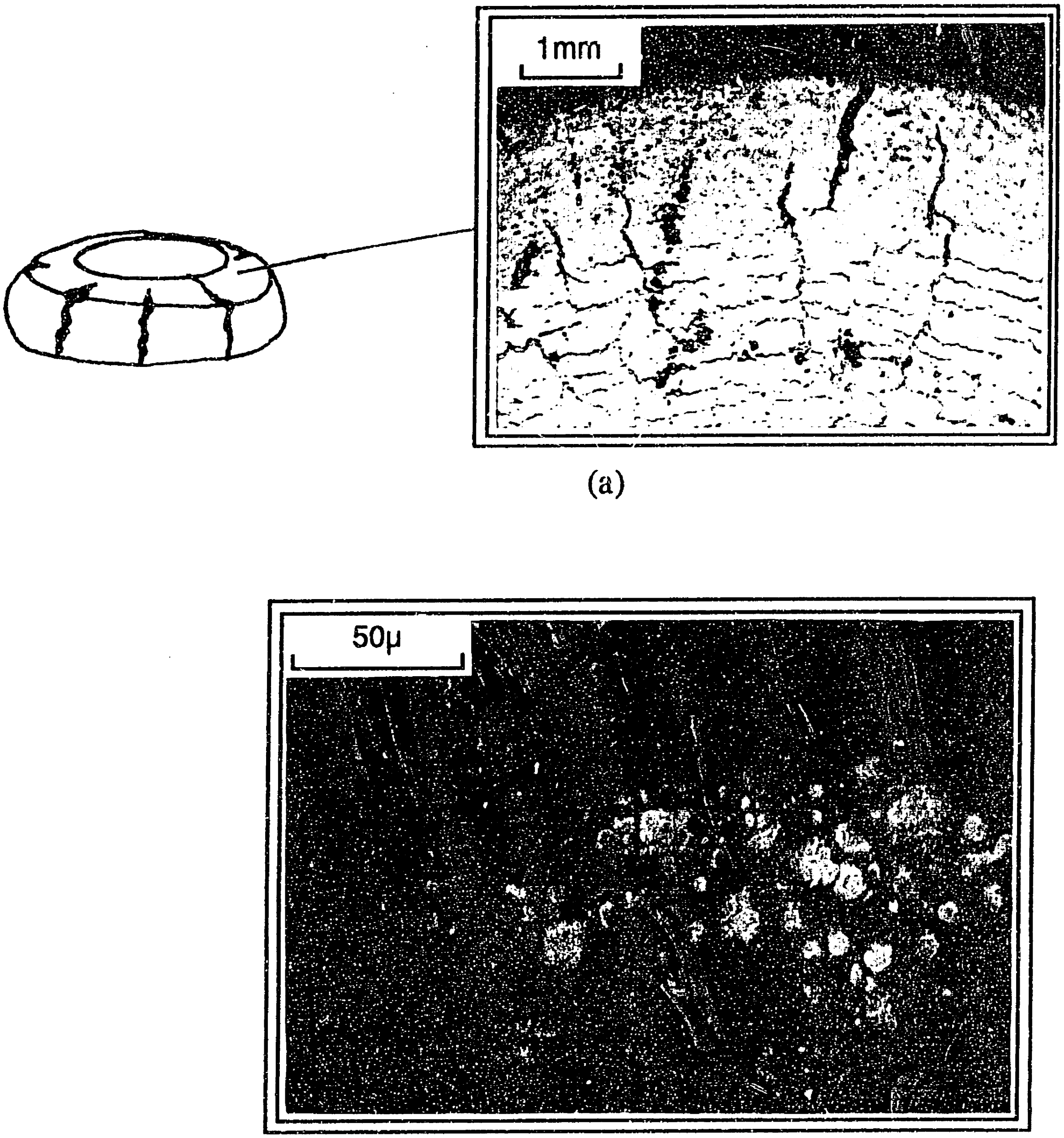

Figure 4.5: Radial and circumferential cracks in a compressed tapered disk (HT1). A close examination of the fractured surface revealed separation along previous particle boundaries.

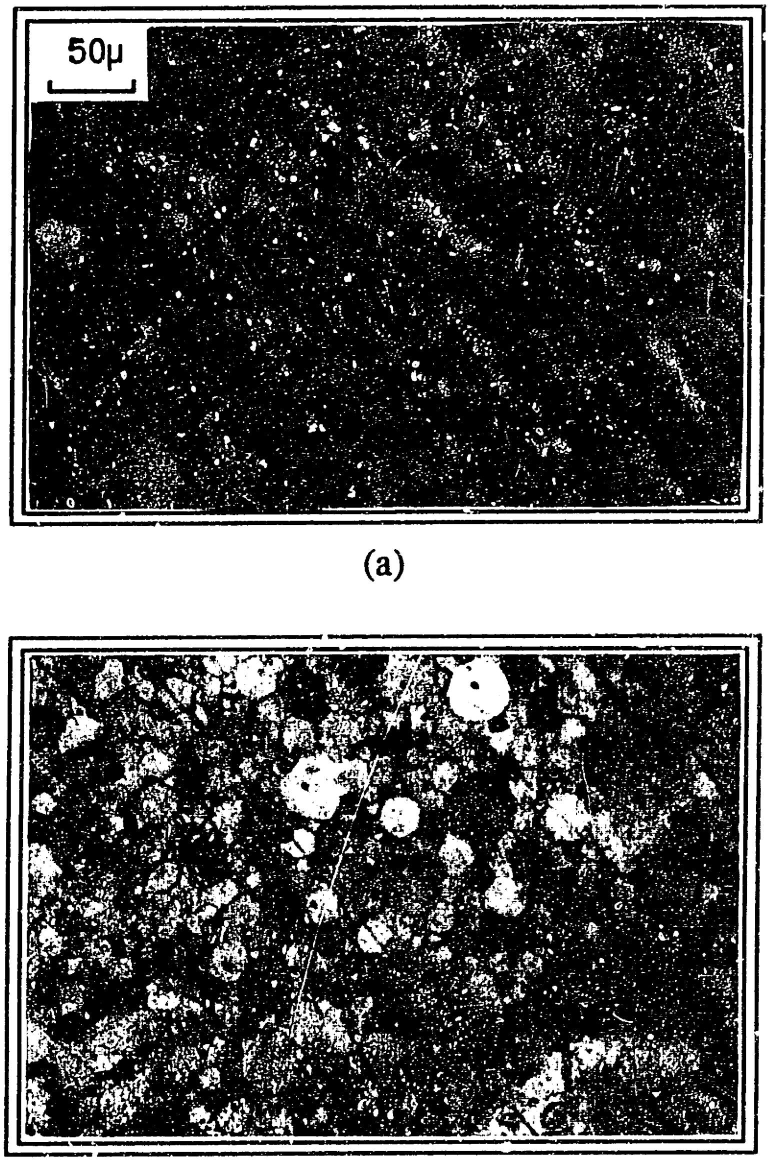

(a)

(b)

Figure 4.6: (a) Near spherical voids in Fe-2%Si powder compacts after sintering for 100 hours at 1100°C. (b) Grain size in HT2 Fe-2%Si. No significant grain growth is observed.

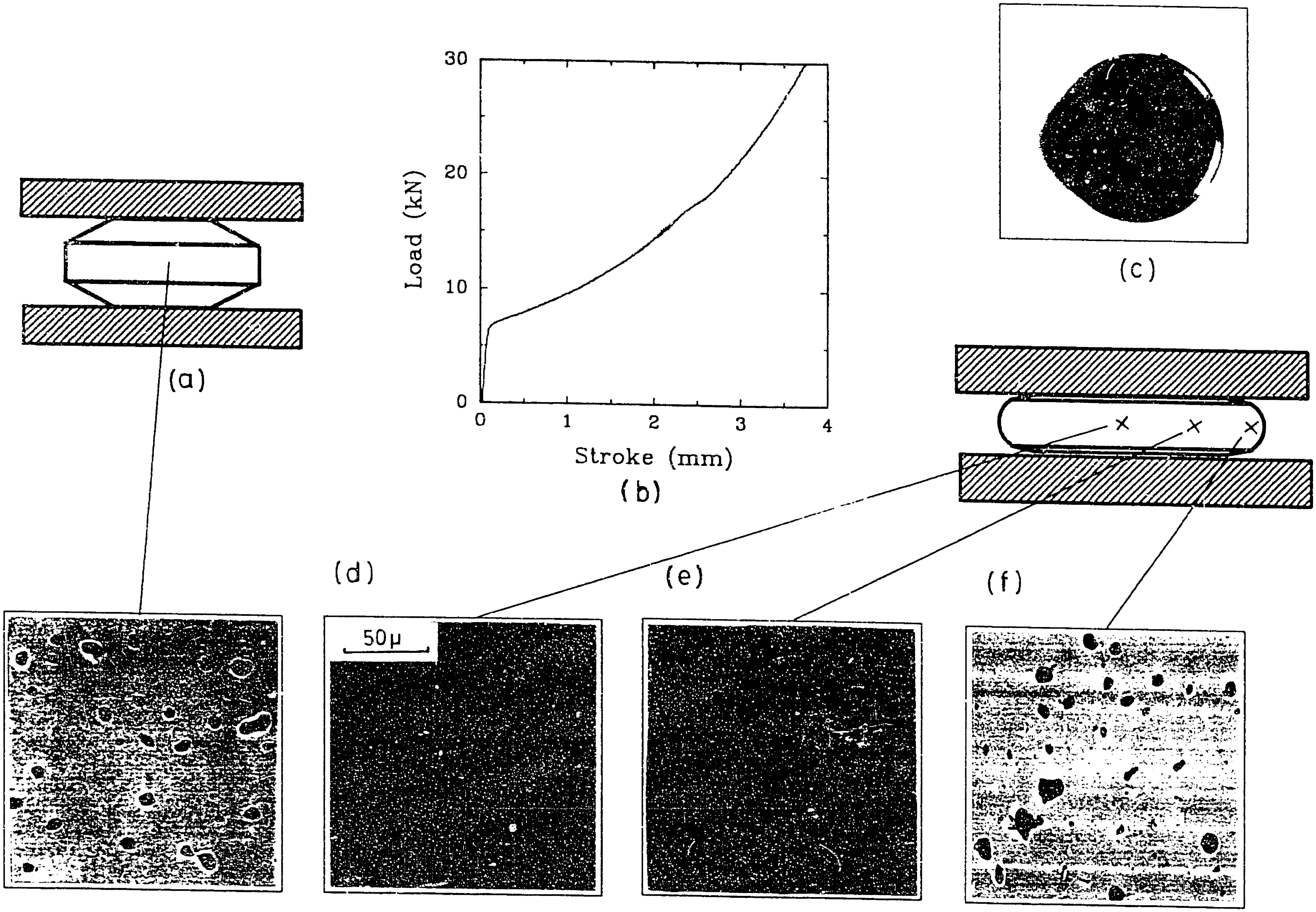

Figure 4.7: Compression of a tapered disk of porous Fe-2%Si at $800^{\circ}C$ at a nominal compressive strain rate 0.008/sec. (a) Initial geometry and porosity (f=4.75%). (b) Load versus stroke curve. (c) Deformed specimen. (d),(e) and (f) Porosity at different radial locations after completion of experiment.

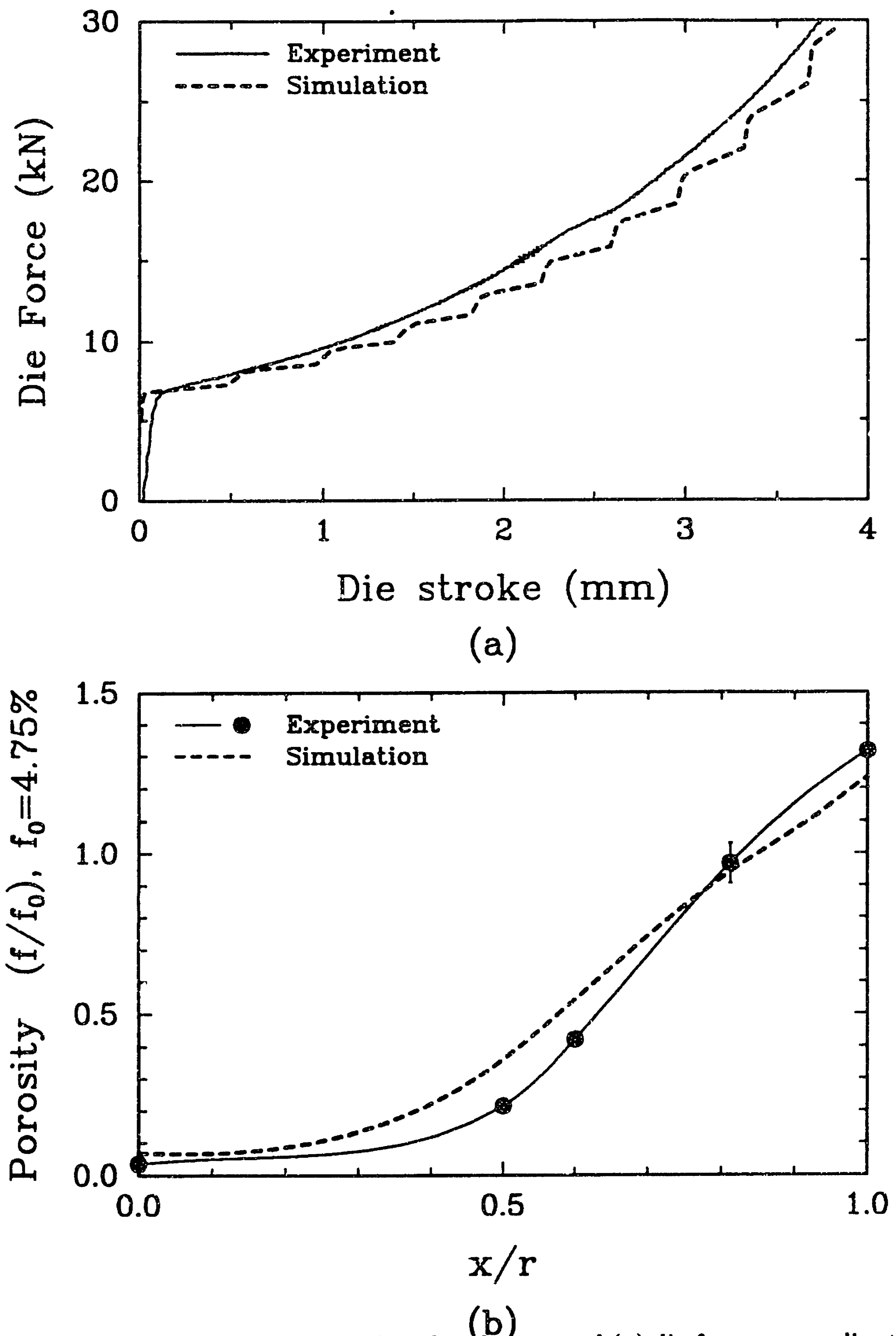

Figure 4.8: Comparison of the predicted and measured (a) die force versus die stroke, and (b) change in porosity versus normalized radial distance in the tapered disk compression experiment.

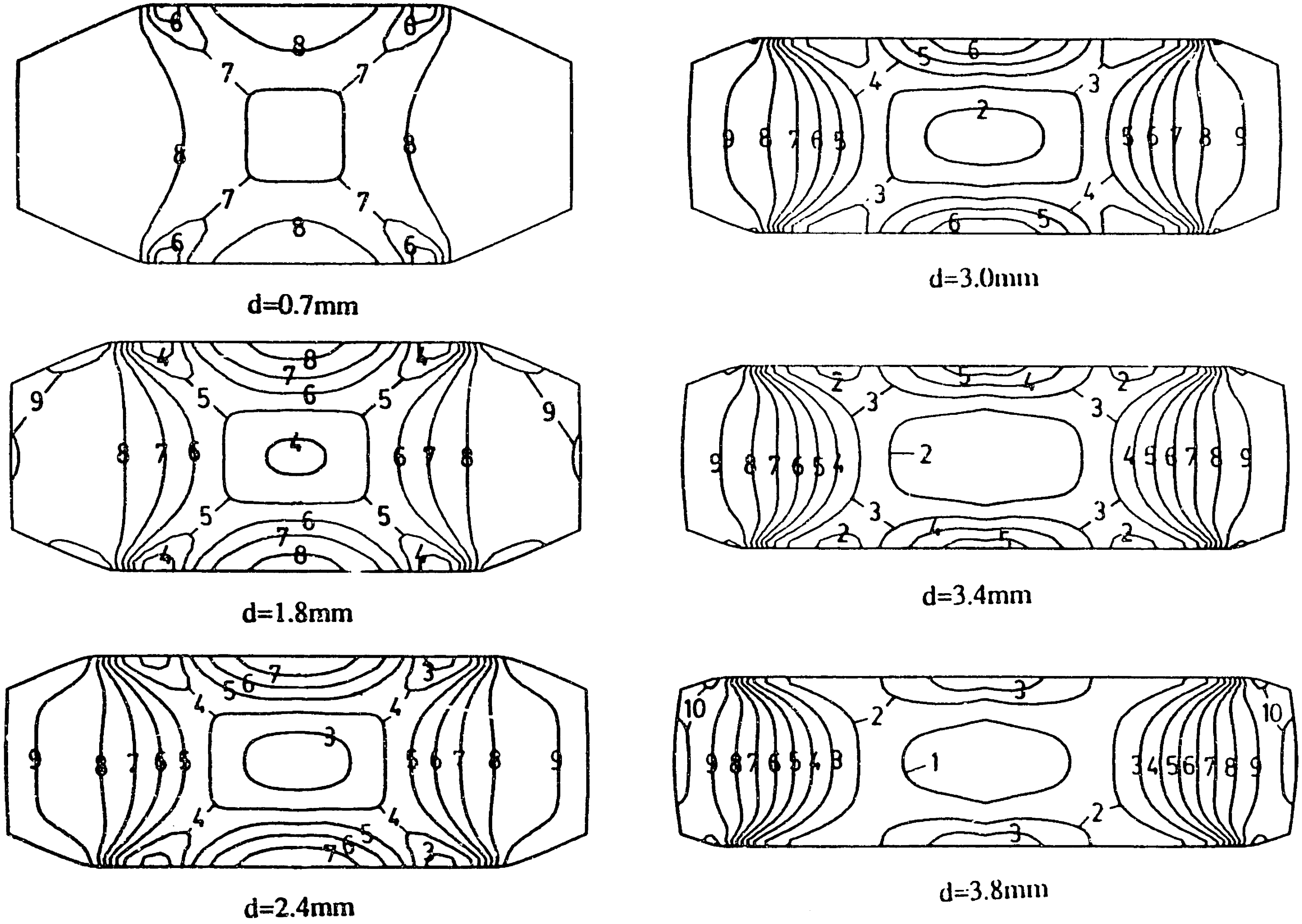

d=0.7mm

d=3.0mm

d=1.8mm

d=3.4mm

d=2.4mm

d=3.8mm

I.D.	f
1	0.0055
2	0.0110
3	0.0165
4	0.0220
5	0.0275
6	0.0330
7	0.0385
8	0.0440
9	0.0495
10	0.0550

Figure 4.9: Evolution of the porosity in the tapered disk experiment ($f_0 = 4.75\%$).

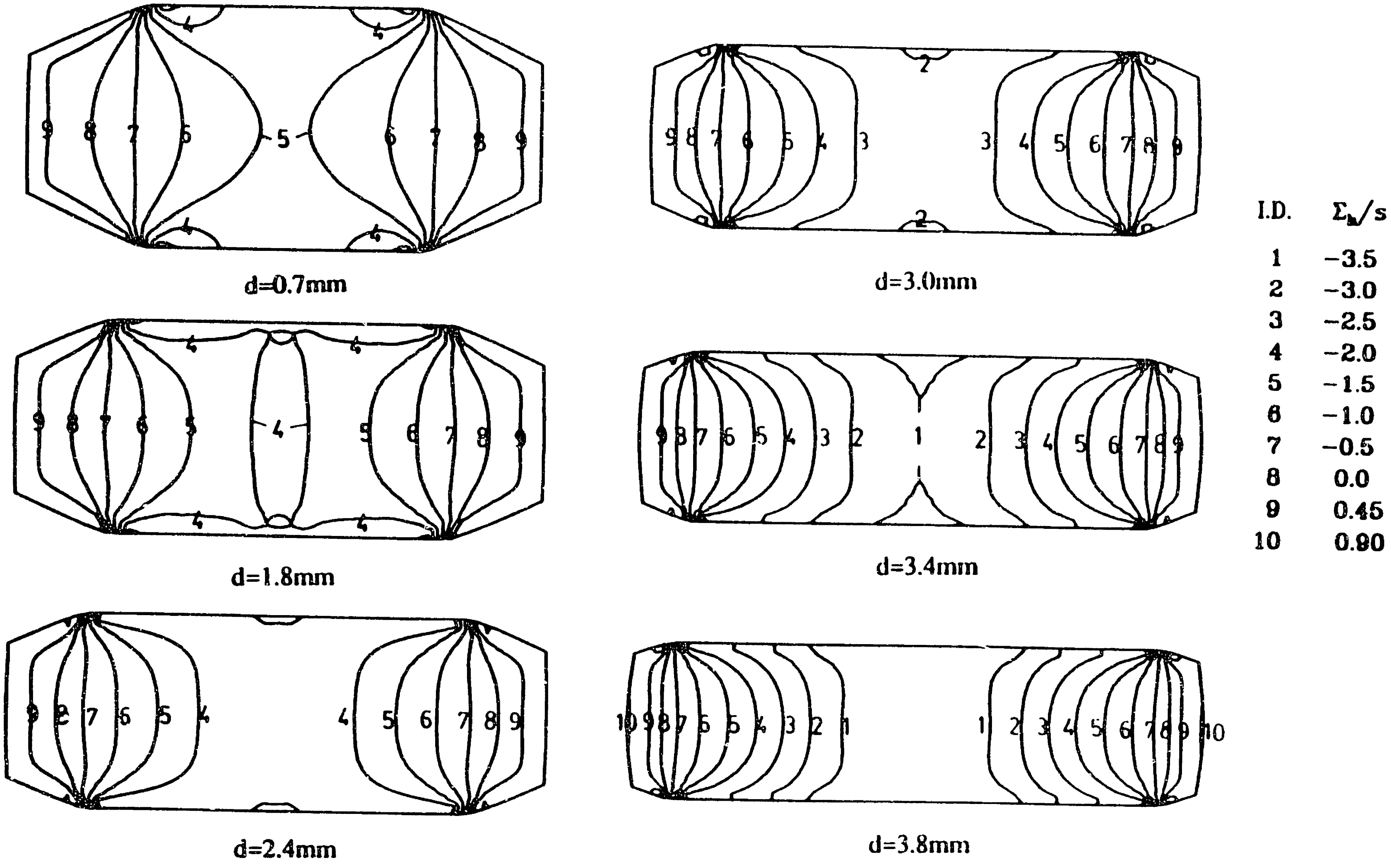

Figure 4.10: Evolution of Σ_h/s in the tapered disk experiment ($f_0 = 4.75\%$).

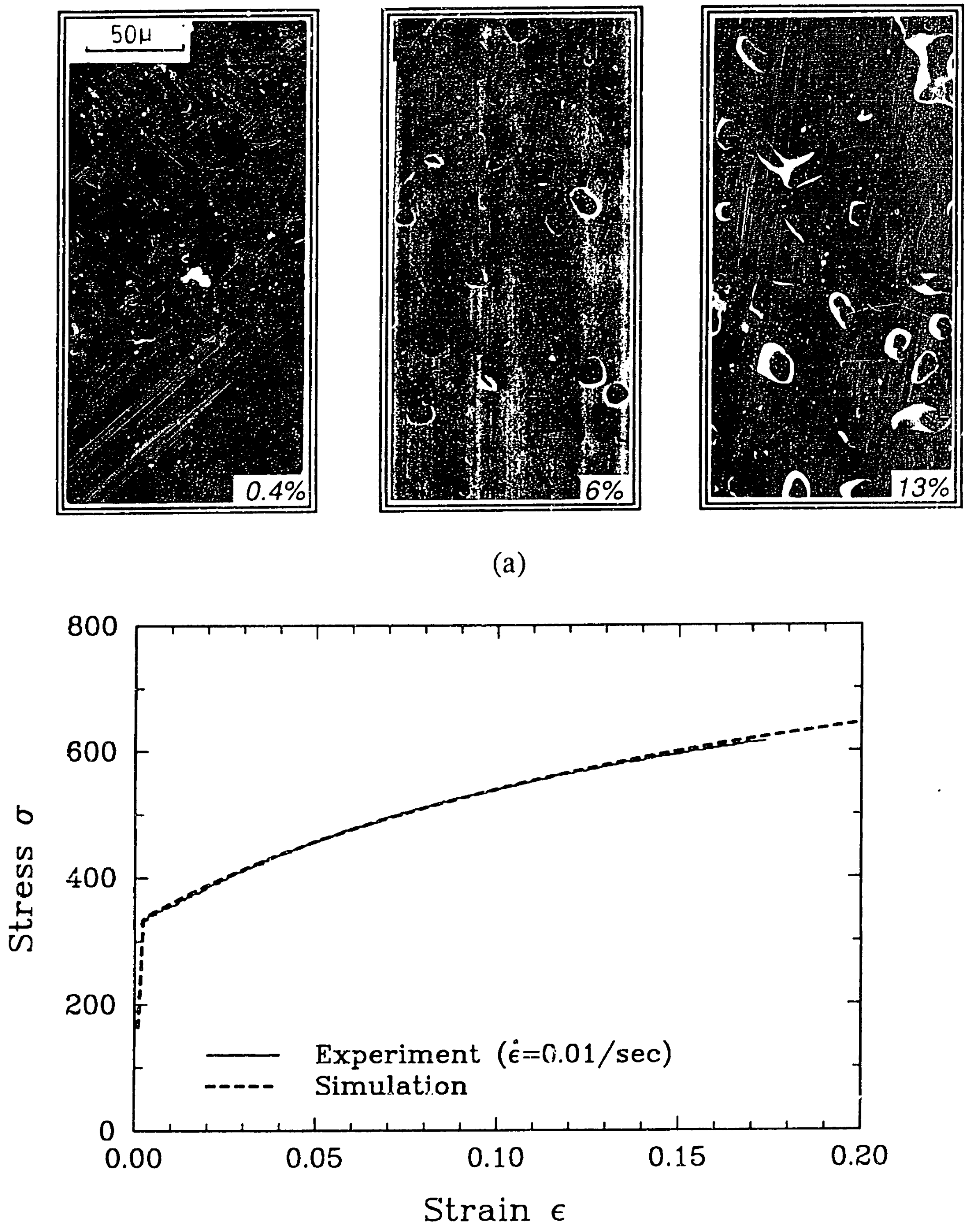

(a)

(b)

Figure 4.11: (a) Micrographs of the initial porosity in the notched tension bars. (b) Room temperature compression test on fully dense Fe-2%Si to determine the constitutive parameters for the matrix material.

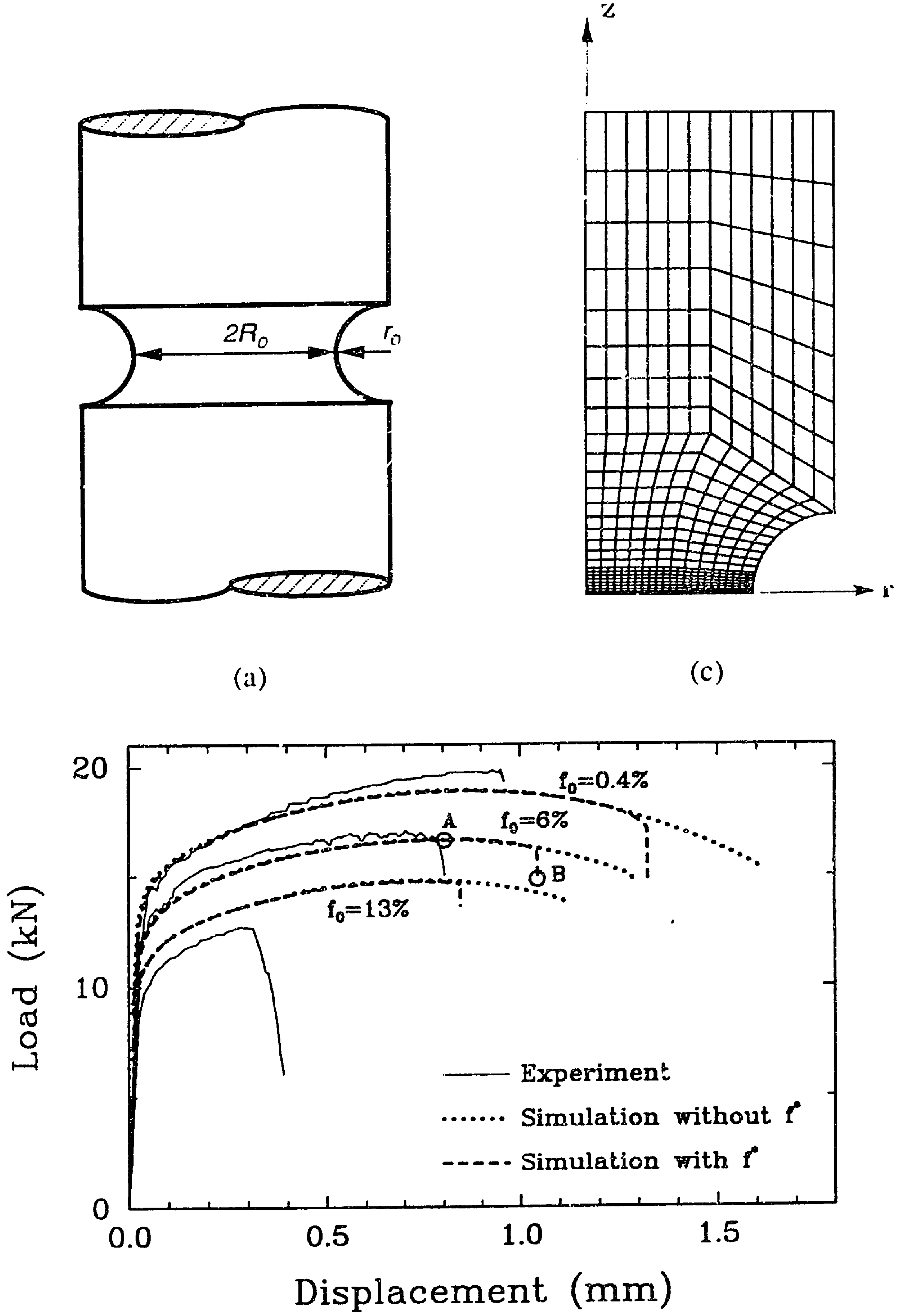

Figure 4.12: Notched bar in tension. (a) Geometry. (b) Load versus displacement curve for various porosities. The simulations with f^* are the ones carried out with the void coalescence model of Tvergaard and Needleman [59] (c) Finite element mesh.

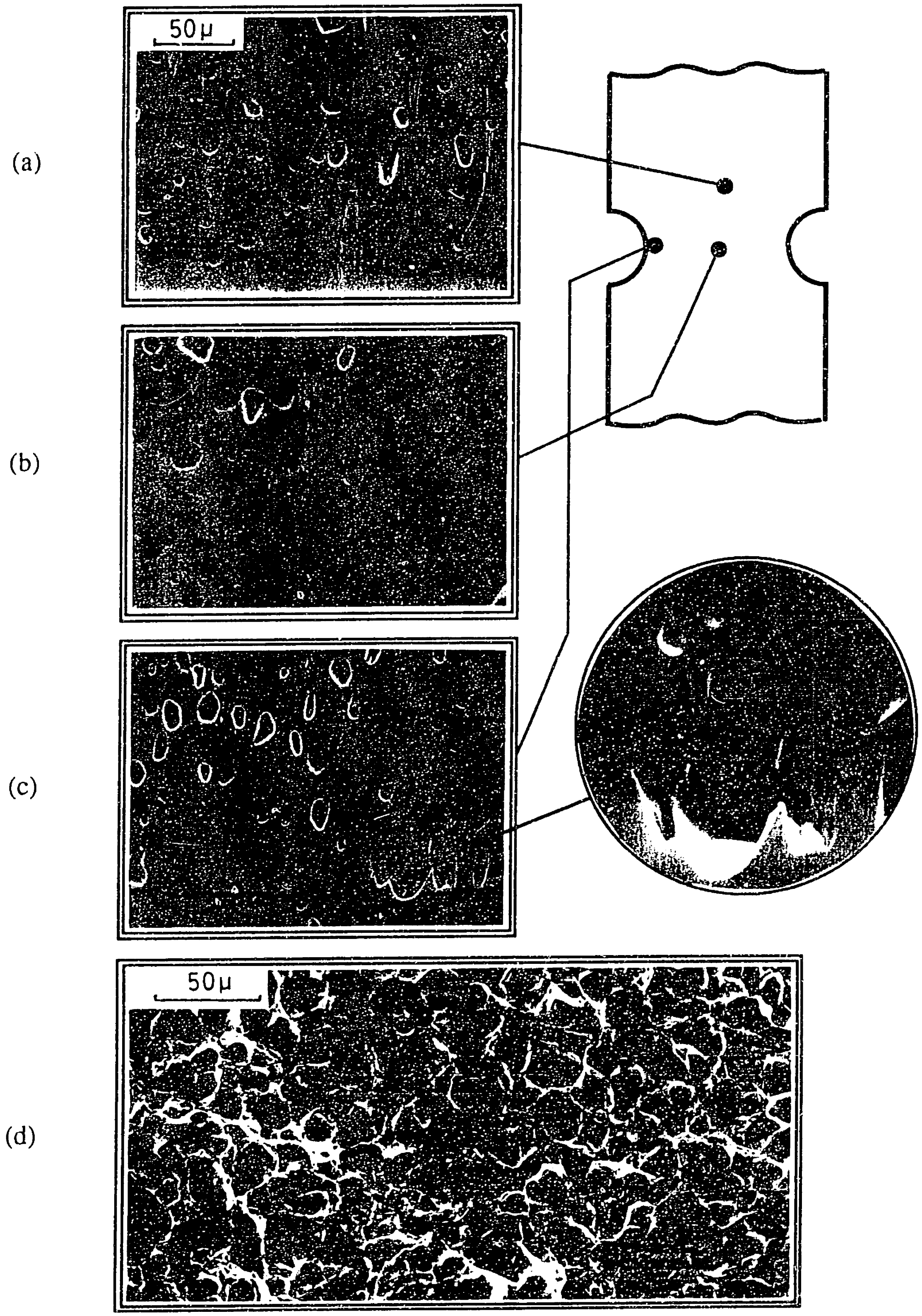

Figure 4.13: Notched bar in tension ($f_0 = 6\%$): (a - c) Porosity at different locations after failure. All three micrographs are at the same magnification. (d) Fracture surface.

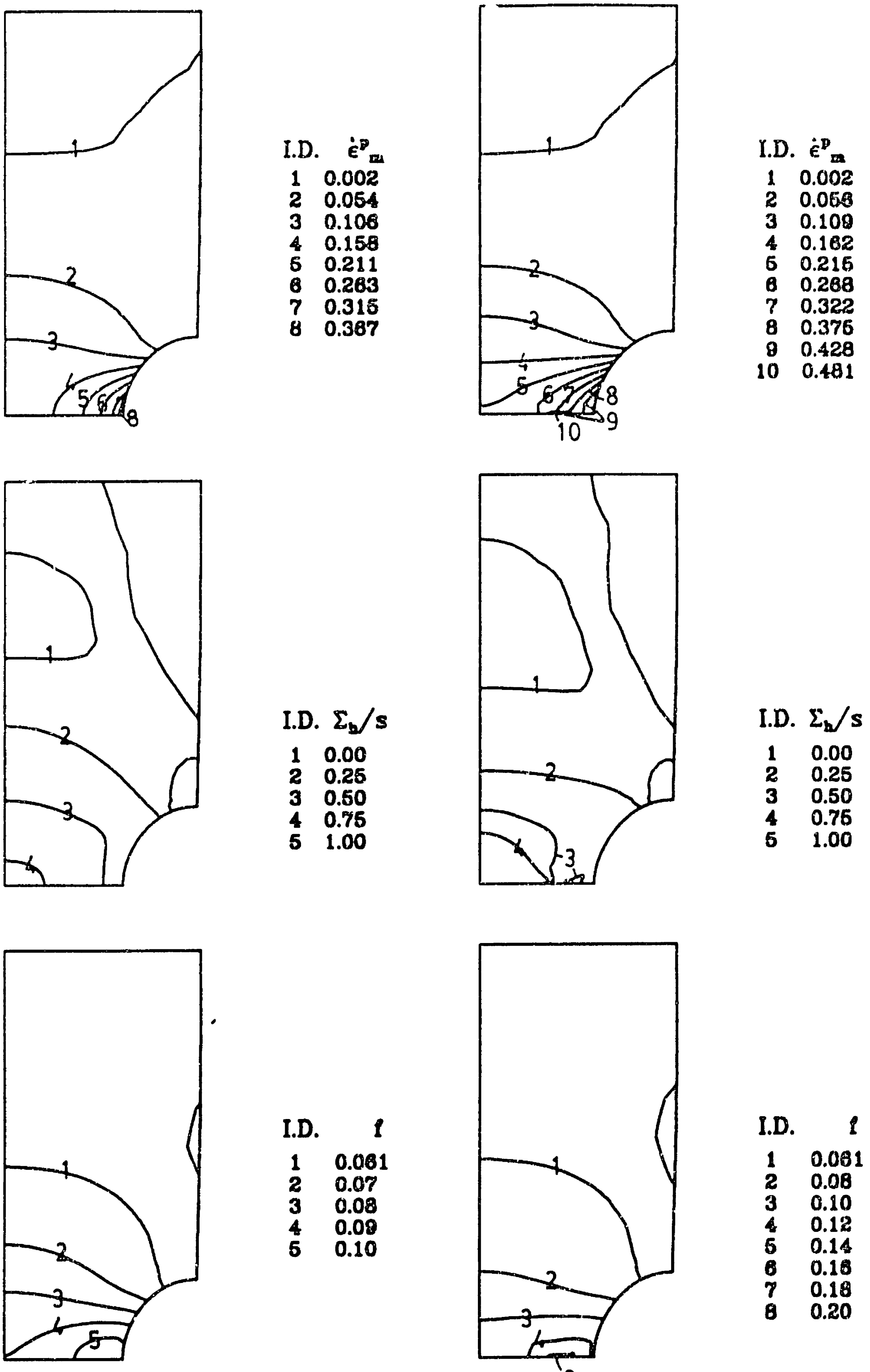

Point A **Point B**

Figure 4.14: Level contours of ϵ^p_m, Σ_h/s, and f for notched specimens with $f_0 = 6\%$ at displacement levels A and B keyed to Fig. 4.12(b).

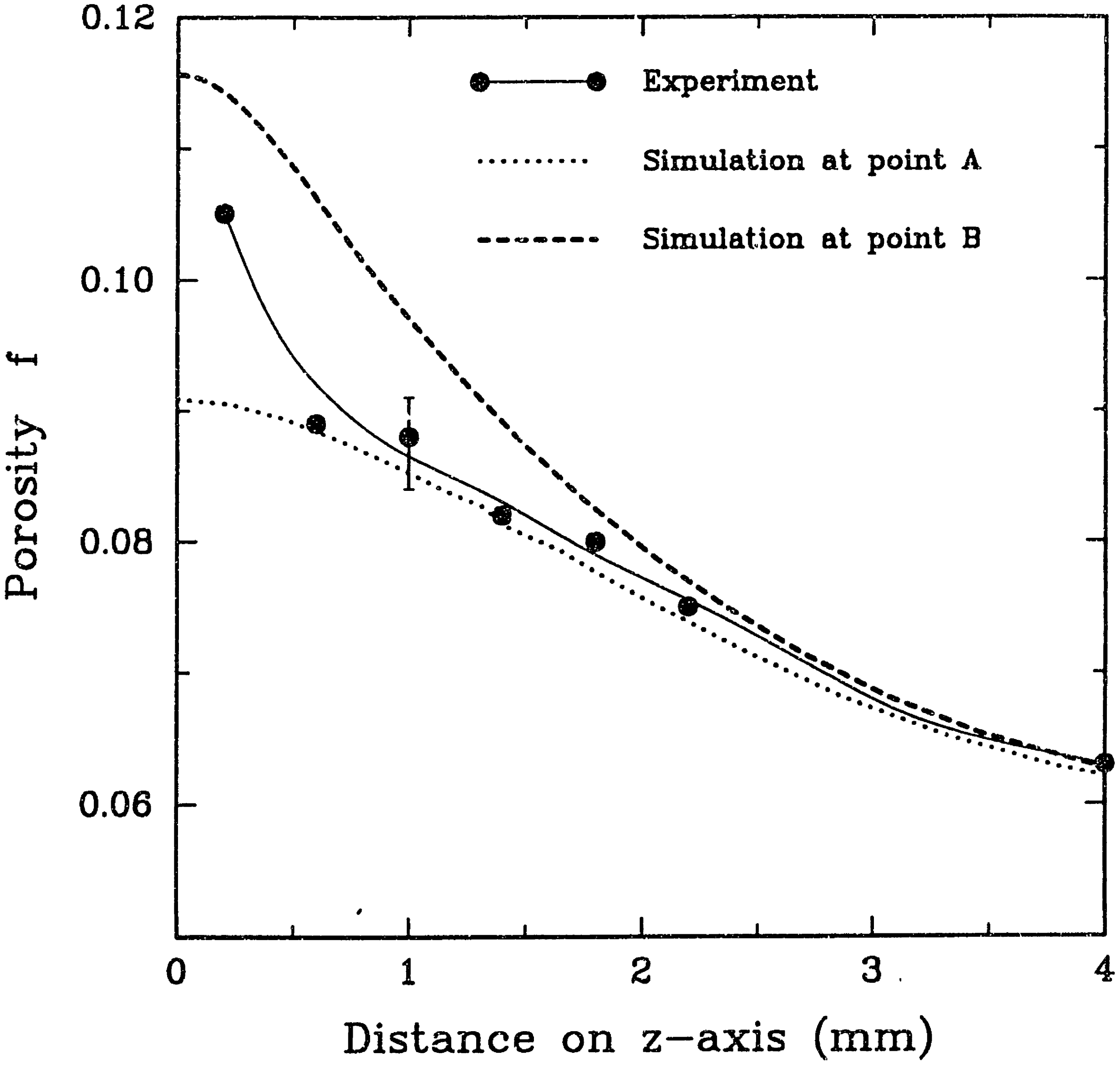

Figure 4.15: Porosity distribution after failure along the centerline of the specimen in the axial z-direction in the notched bar with $f_0 = 6\%$. Points A and B are displacement levels keyed to Fig. 4.12(b).

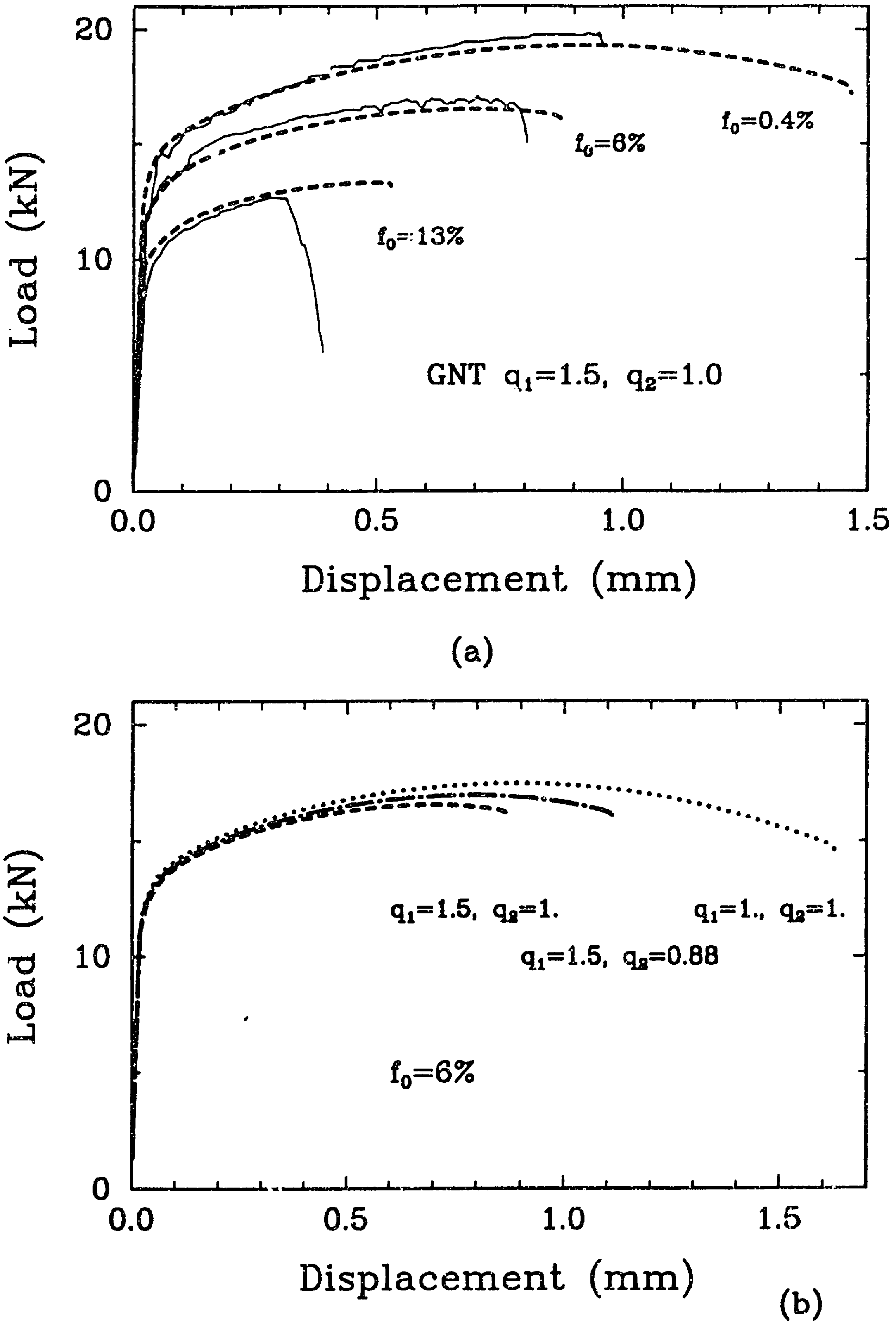

Figure 4.16: (a) Load versus displacement curve for various porosities based on the GNT model with $q_1 = 1.5$ and $q_2 = 1.0$. The void coalescence model of Tvergaard and Needleman [59] has been used. (b) Sensitivity of the predictions of the GNT model on the parameters q_1 and q_2.

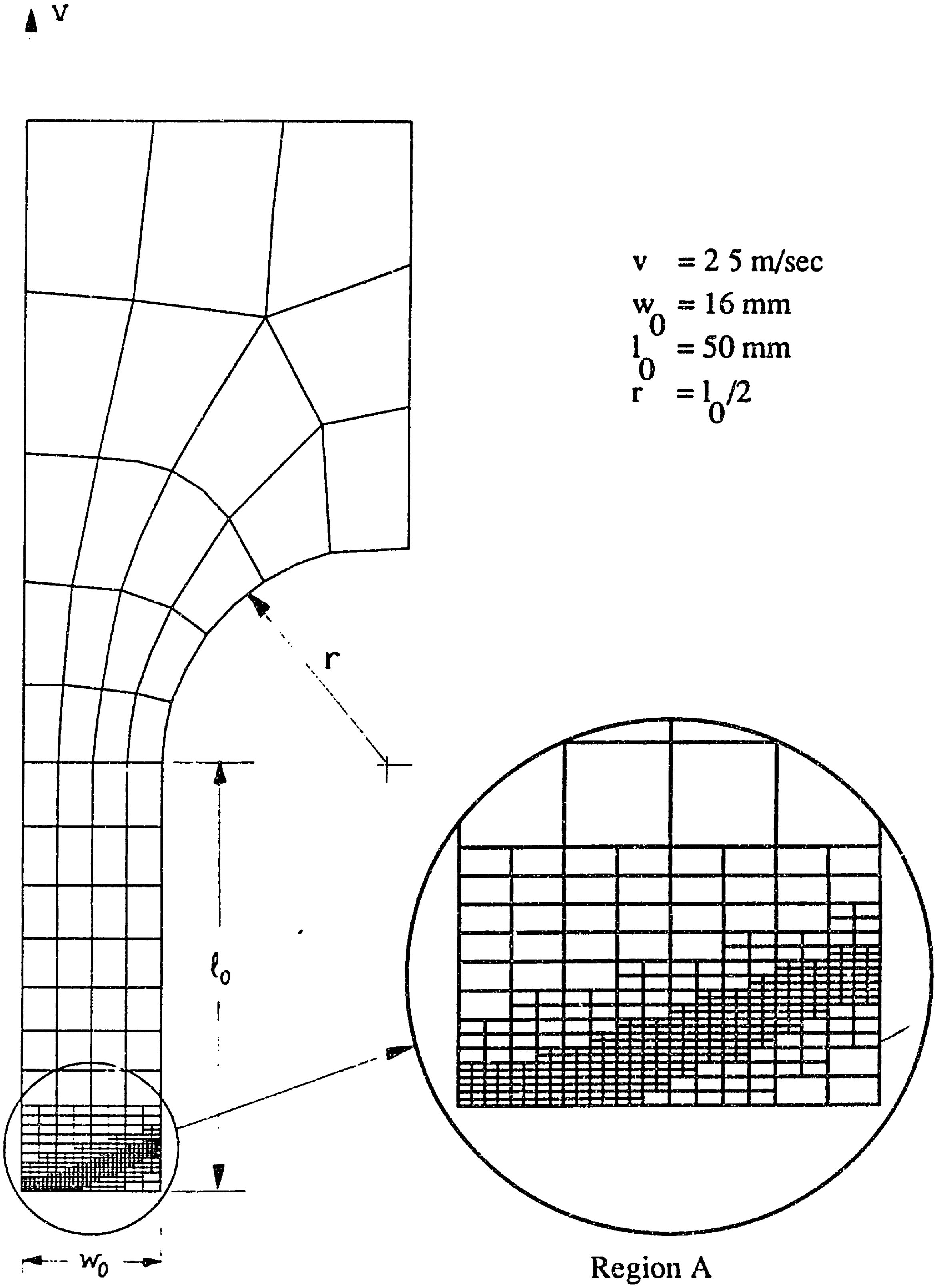

Figure 4.17: Geometry and the finite element mesh for simulation of a plane strain tension test. The mesh represents only one quarter of the specimen. All views of the specimen in subsequent figures show only region A of the complete mesh.

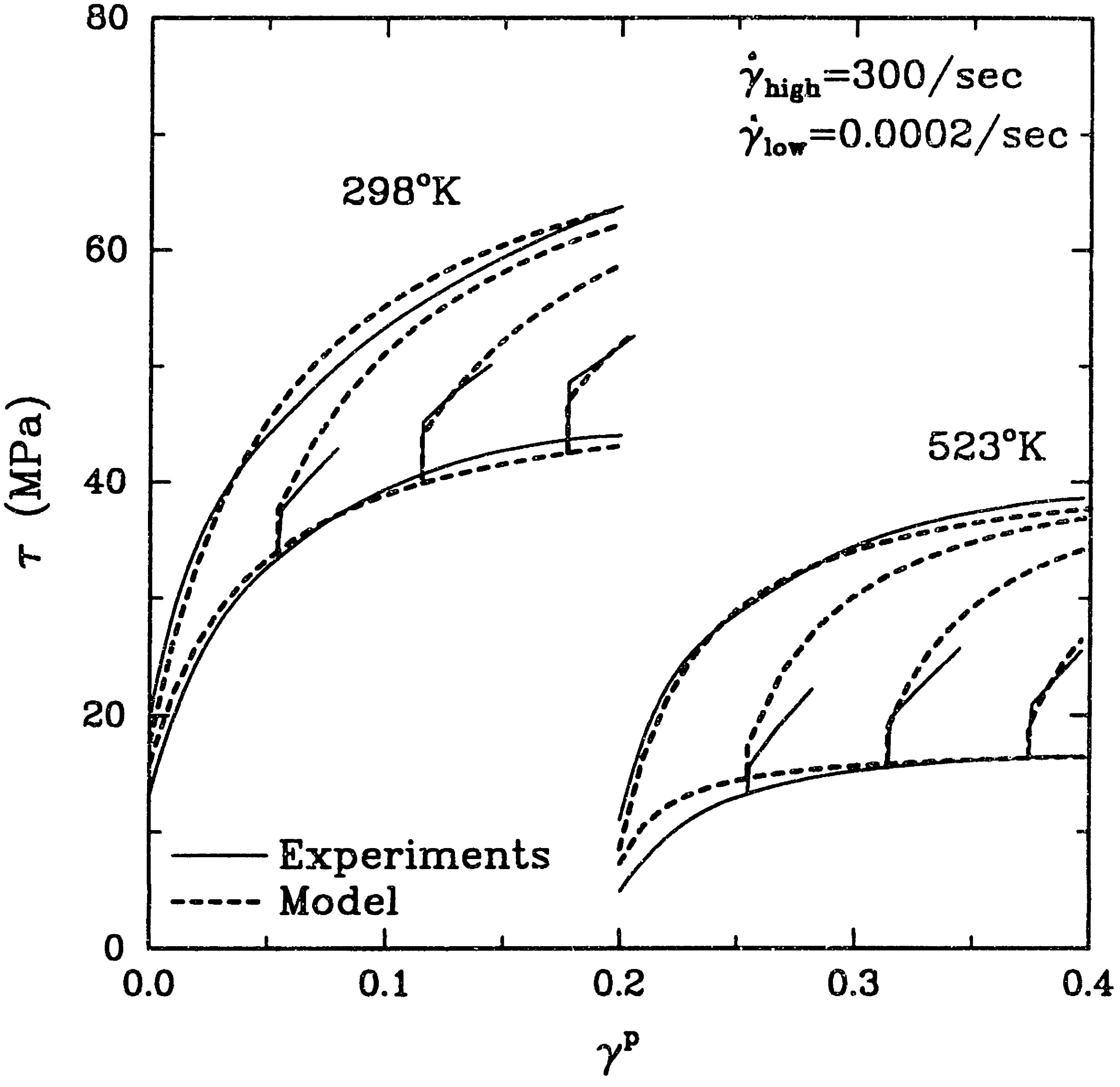

Figure 4.18: Effect of strain rate, strain rate history and temperature on the shear stress versus shear strain behavior of dense 1100 aluminum. The solid lines are experimental data from Senseny, Duffy and Hawley (1978). The dashed lines are the representation of this data using our constitutive model for dense materials.

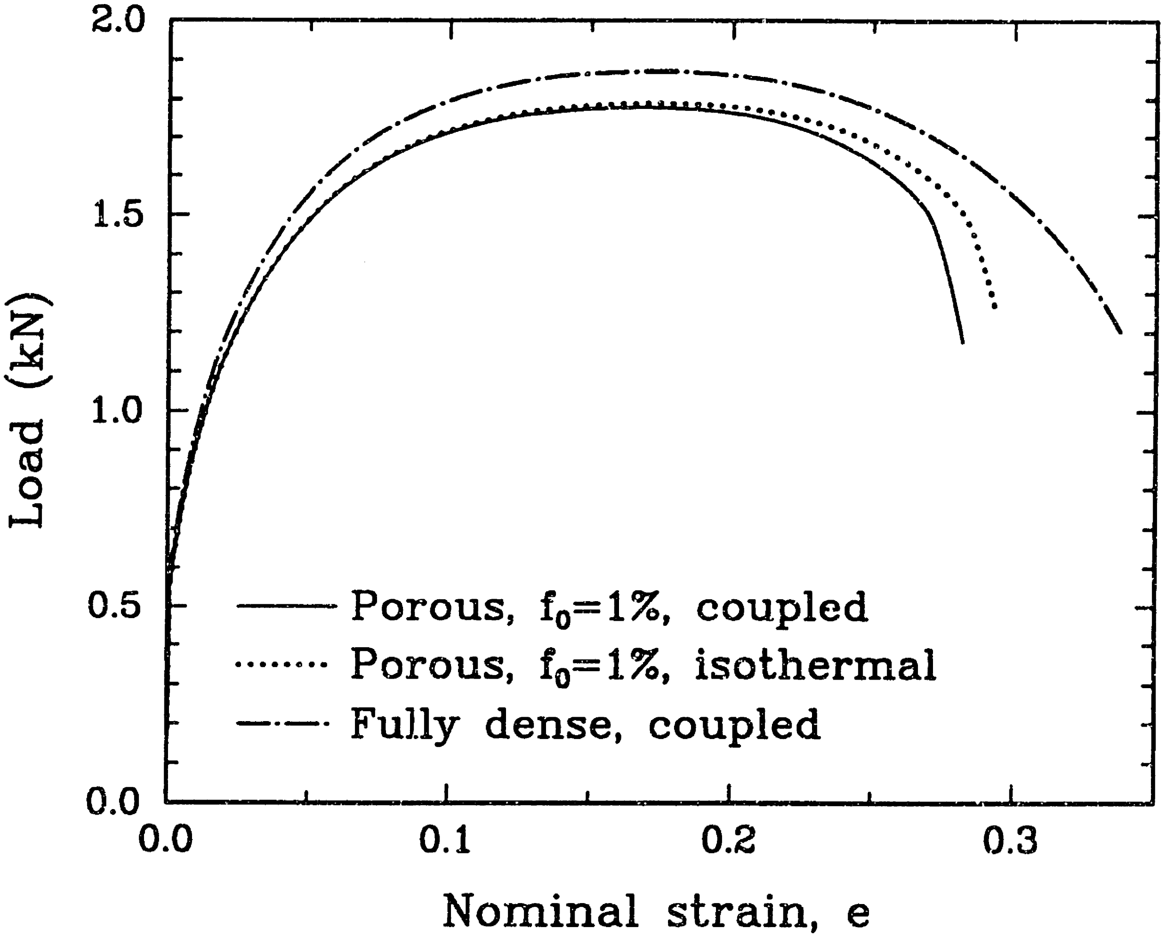

Figure 4.19: Load versus nominal strain, $e = (v/l_0)t$, curves for fully dense and porous aluminum.

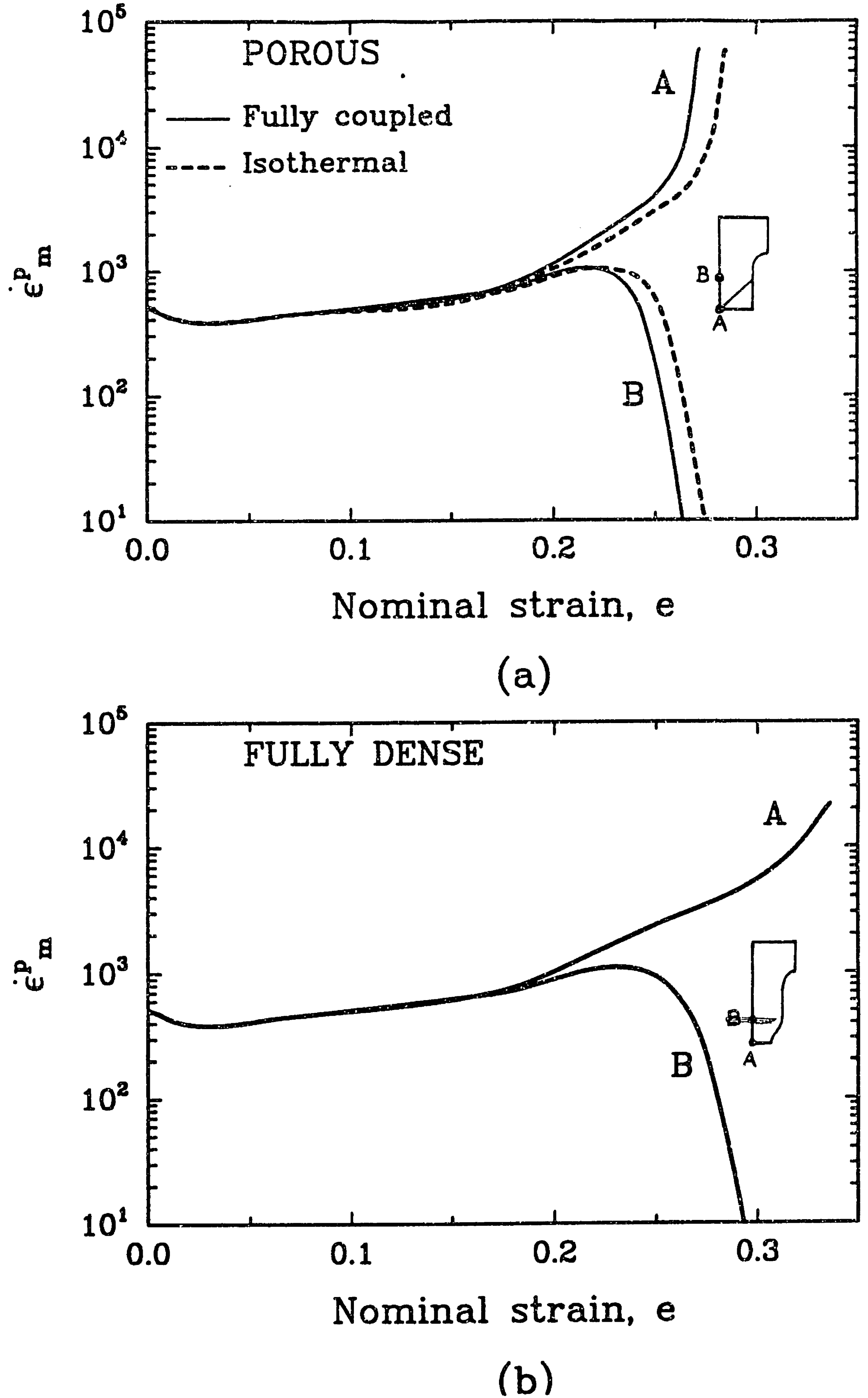

(a)

(b)

Figure 4.20: Evolution of the equivalent tensile plastic strain rate in the matrix in the (a) porous and (b) fully dense specimens during the course of the deformation at two points, one at the center of the specimen, point A, and one outside the central region on the axis of symmetry, point B.

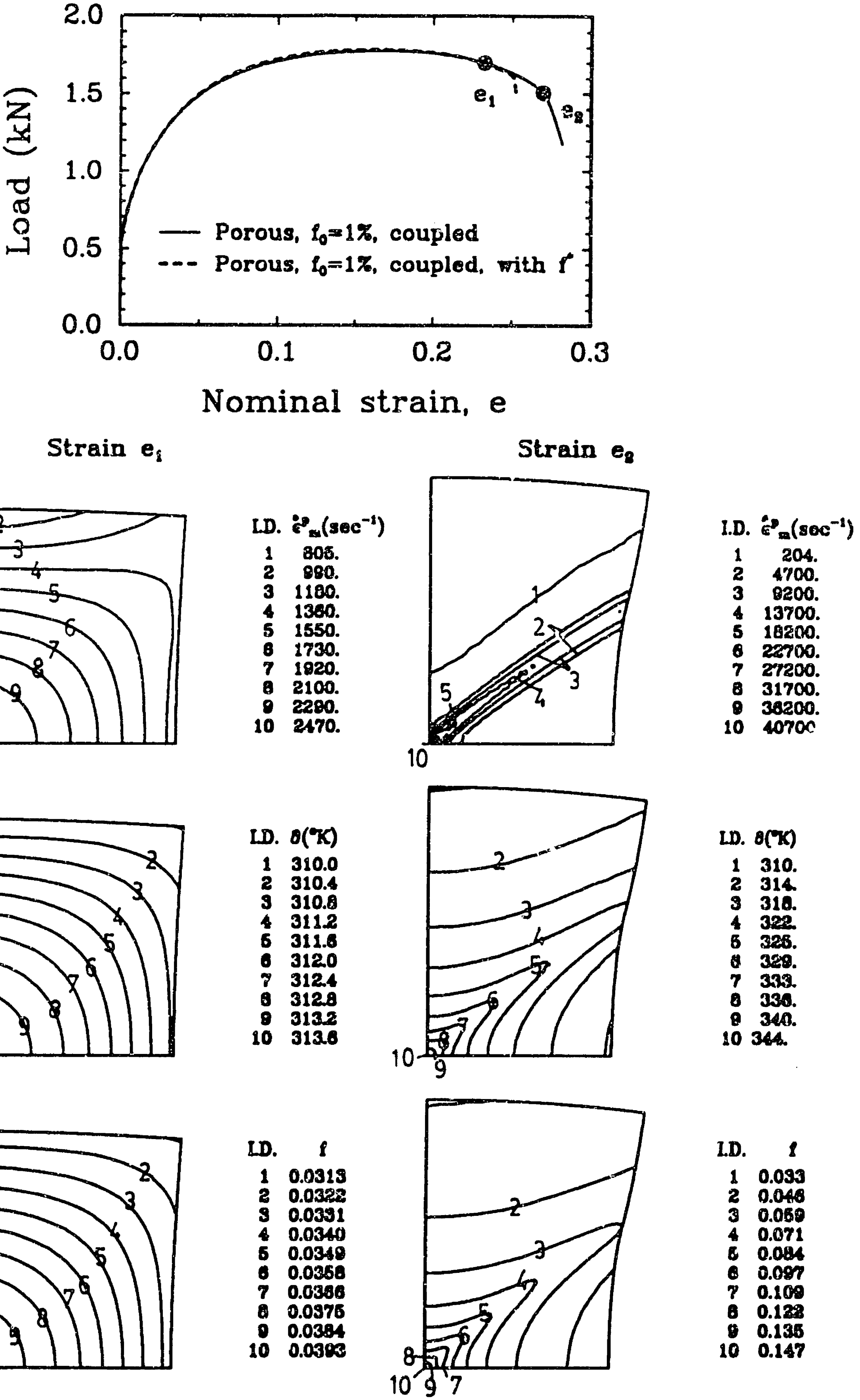

Figure 4.21: Level contours of $\dot{\epsilon}^p_m$, θ and f at two representative nominal strain levels e_1 and e_2 in the vicinity of the rapid load drop in the plane strain tension calculation for an initially porous material, $f_0 = 0.01$.

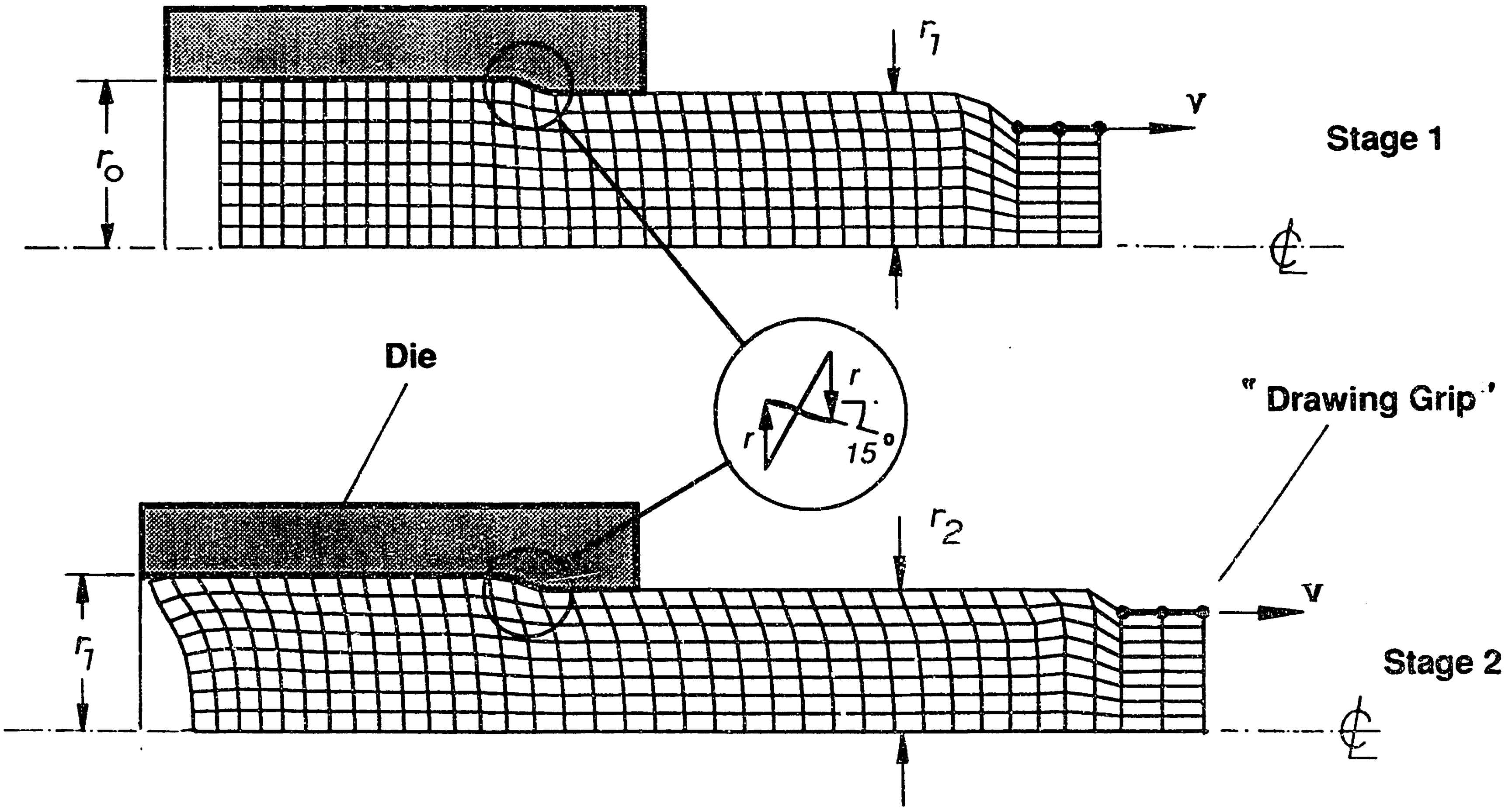

Figure 4.22: Geometry of axisymmetric, two-step, cold drawing simulation with $r_1/r_0 = r_2/r_1 = 0.915$. This reduction in radii corresponds to a reduction in area of 16.3% in each pass. The nodes on the gripping surface were given a horizontal pulling velocity v, to simulate the drawing operation.

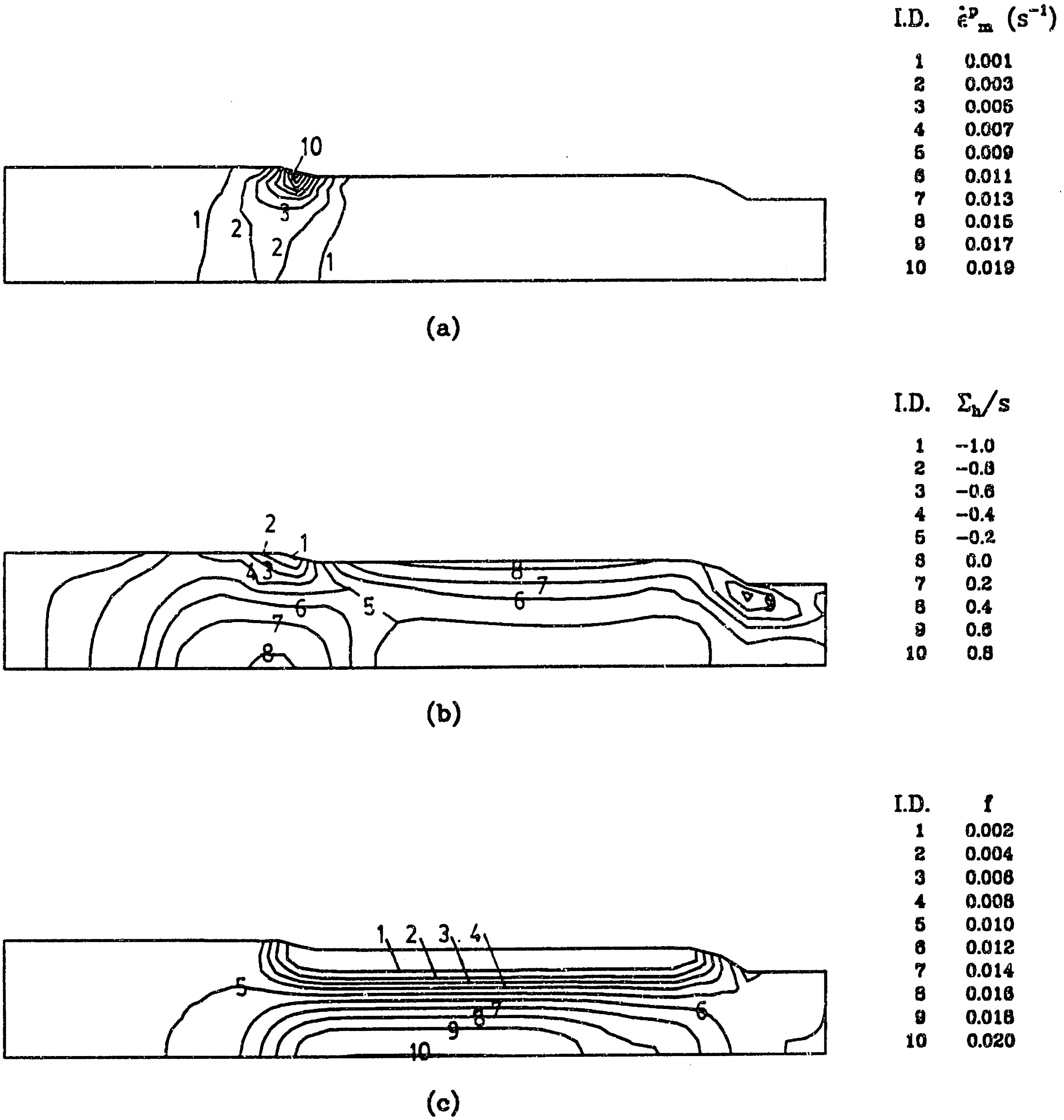

Figure 4.23: Defect formation in multi-step rod drawing. First step: (a) contours of the equivalent tensile plastic strain rate in the matrix $\dot{\epsilon}^{p}_{m}$, (b) pressure contours, and (c) porosity contours.

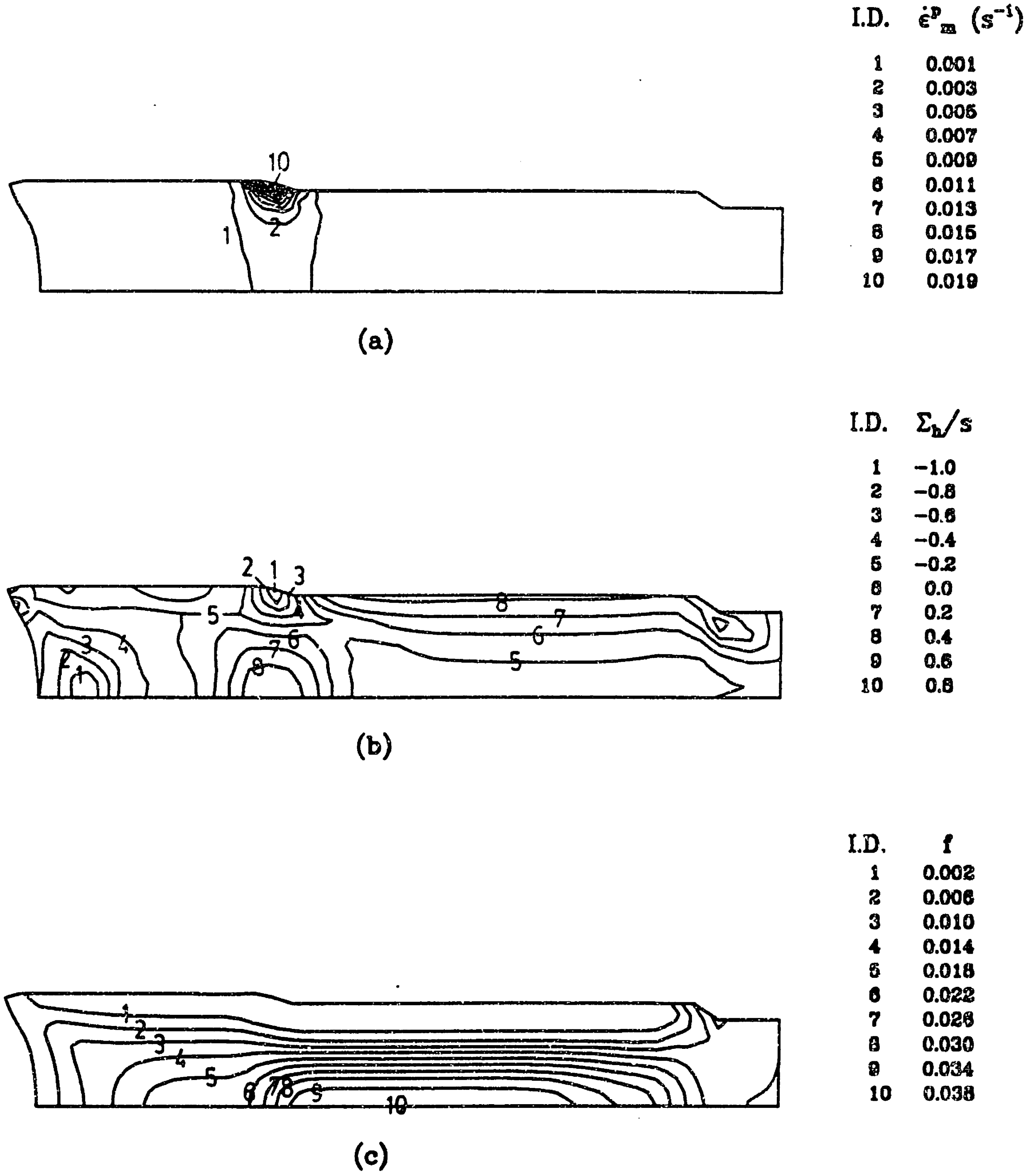

Figure 4.24: Defect formation in multi-step rod drawing. Second step: (a) contours of the equivalent tensile plastic strain rate in the matrix $\dot{\epsilon}^p_m$, (b) pressure contours, and (c) porosity contours.

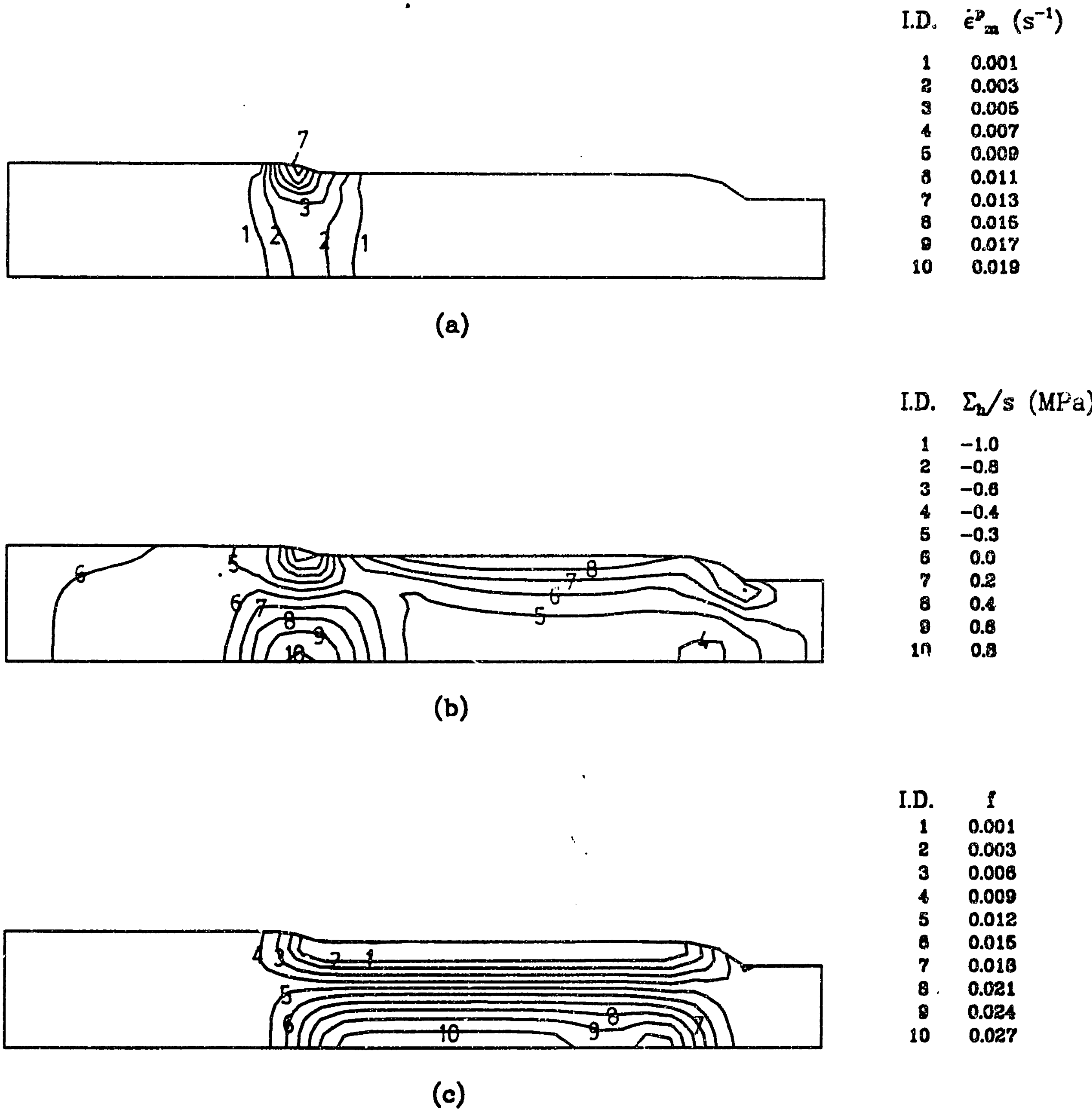

Figure 4.25: Effect of lack of strain hardening, $h_0 = 0$, on drawing: (a) contours of the equivalent tensile plastic strain rate in the matrix $\dot{\epsilon}^p_m$, (b) pressure contours, and (c) porosity contours. Compare with Fig. 4.23.

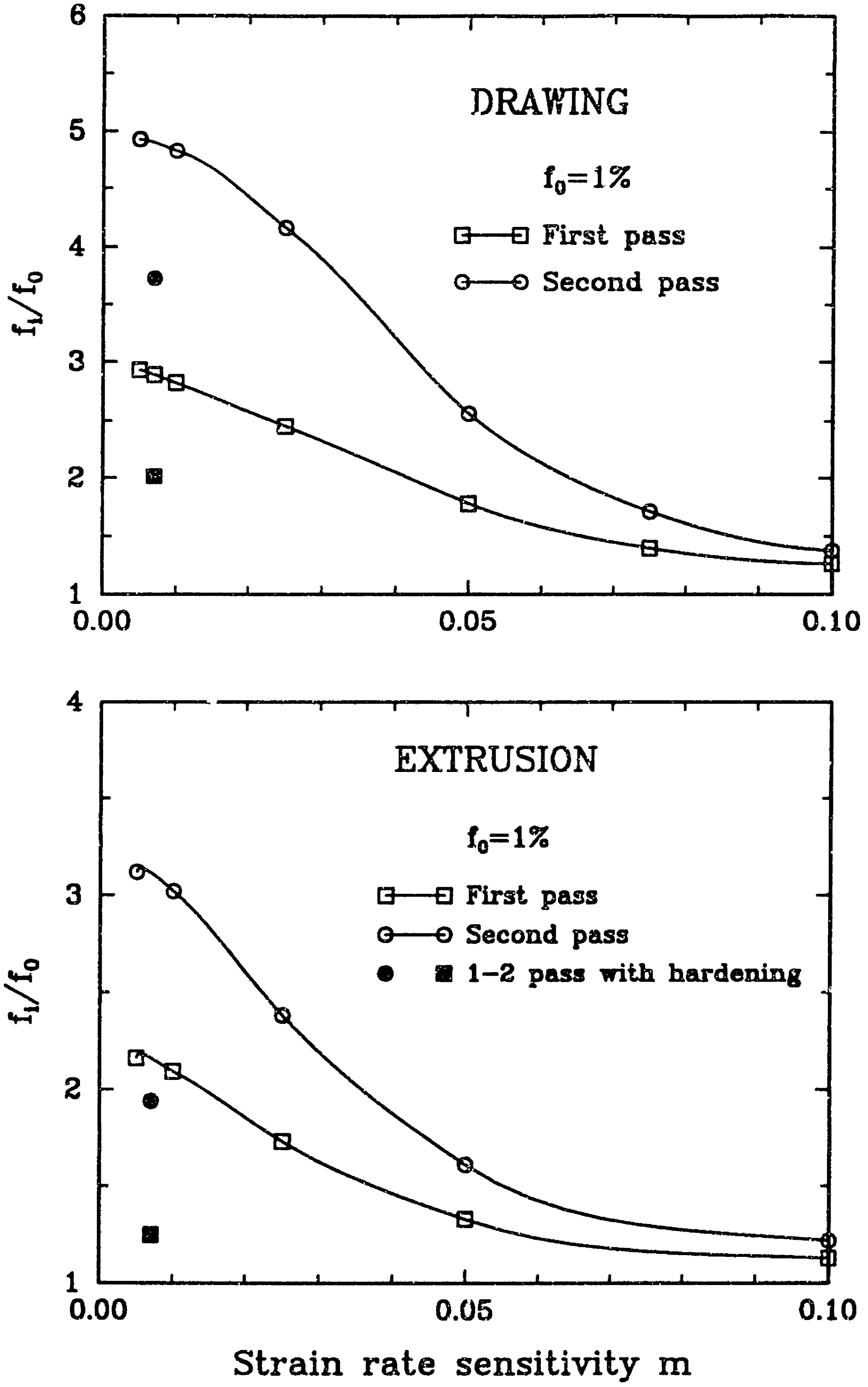

Figure 4.26: Effect of strain rate sensitivity on defect formation during multi-step (a) rod drawing and (b) rod extrusion.

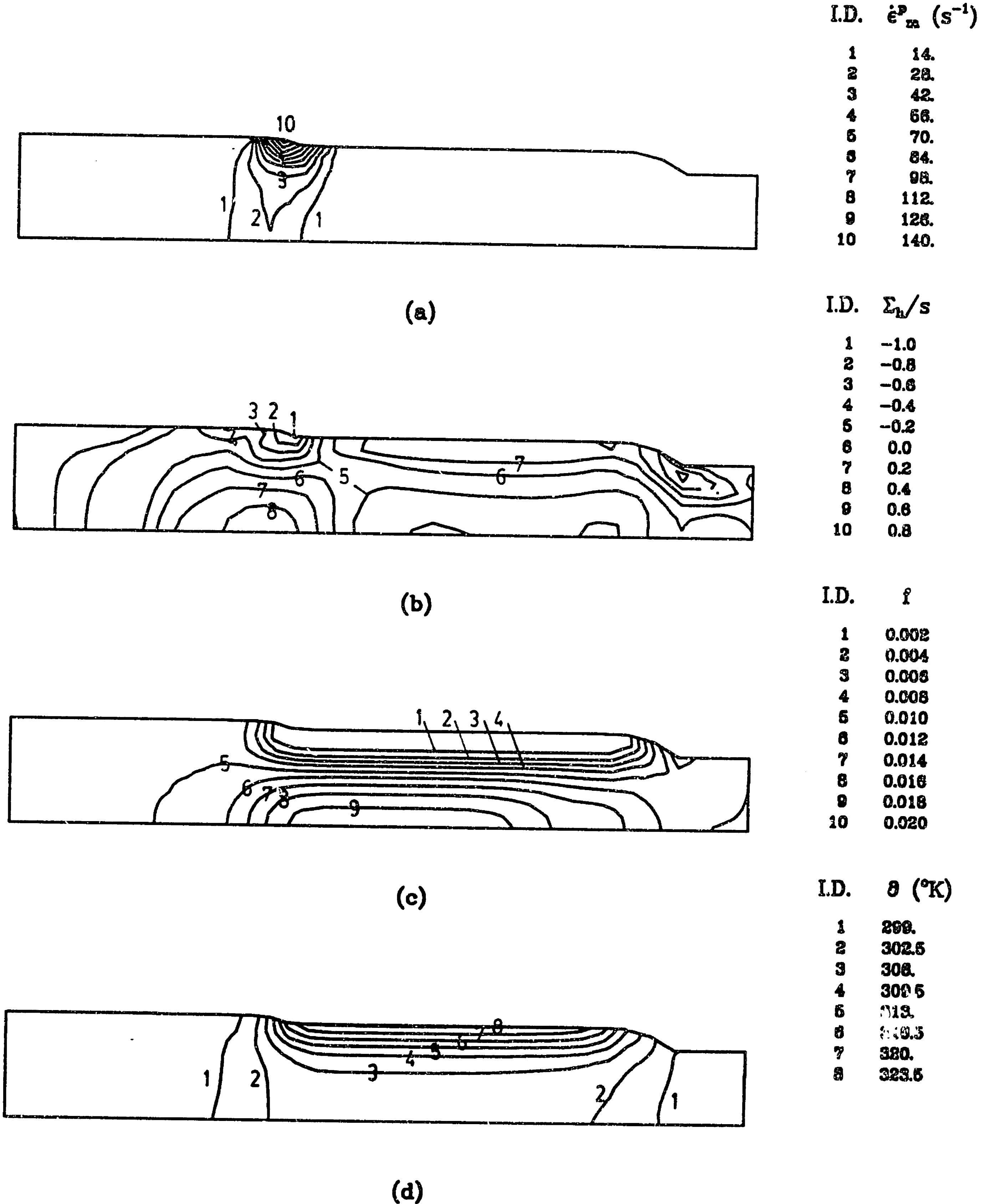

Figure 4.27: Effect of temperature increase due to plastic dissipation: (a) contours of the equivalent tensile plastic strain rate in the matrix $\dot\epsilon^p_m$, (b) pressure contours, (c) porosity contours, and (d) temperature contours. Compare with Fig. 4.23.

Chapter 5

Conclusions

We have formulated a complete rate and temperature dependent macroscopic constitutive framework for isotropic, moderately porous metallic materials. A modified form of the plastic potential function of Haghi and Anand [100] was proposed that interpolates properly the low triaxiality behavior of porous materials at any level of strain rate sensitivity.

The general features of our constitutive framework are similar to the framework introduced by Gurson in that (*i*) porosity is characterized by a single parameter — the void volume fraction; (*ii*) matrix incompressibility is used to obtain the evolution equation for the void volume fraction; and (*iii*) an expression relating the macroscopic plastic power to the plastic power in the matrix is used to determine an averaged effective stress in the matrix, which in turn governs the evolution of an averaged deformation resistance of the matrix.

However, the specific forms of the flow potential and the evolution equation for the matrix deformation resistance in our model are substantially different from the ones in the GTN model. In particular, it is important to note that while material rate-sensitivity was introduced into Gurson's constitutive model by Pan, Saje and Needleman [53] only for slightly rate-sensitive behavior, our constitutive model is for inherently rate dependent materials and is intended for material rate-sensitivities in the entire range spanning from nearly rate-insensitive behavior at low homologous temperatures to highly rate-dependent behavior at high homologous temperatures.

Also, we developed a new fully-implicit, fully thermo-mechanically coupled time-integration procedure for this class of constitutive equations, and implemented it in ABAQUS. This time integration procedure is a generalization of the widely used radial-return algorithm for classical J_2 flow theory for dense metals. It is implicit, robustly stable, and numerically objective. These features of our work make it well suited for large scale computations involving both moderately large elastic deformations and large elastic-plastic deformations of microporous as well as fully dense materials. We presented example calculations which demonstrate the versatility of the proposed constitutive model and the robustness of the time-integration procedure. Predictions from the numerical procedures are shown to agree well with physical experiments both at high and low homologous temperatures.

We have also examined in detail the accuracy of the spherical cell type of models by using calculations on periodic arrays of voids. Moreover, a refined approach to determine the plastic potential has been explored by using the differential self consistent scheme. We found that the main differences between the various models appear to occur at triaxialities higher than ≈ 2. Due to the lack of reliable experimental data in the high triaxiality regime we can not verify the quality of the various models in the triaxiality range $X > 2$.

Our efforts in modeling the effect of porosity on the viscoplastic behavior of materials have been focused on a first-order approach that should be widely applicable. However, the characterization of porosity by only the volume fraction f clearly does not address important issues such as the shape and distribution of pores as well as the non-spherical evolution of porosity. We performed periodic unit cell calculations that demonstrated that our model can be applied with confidence in problems with initially near spherical shaped voids (see Appendix C). There is an error in the prediction of the porosity evolution at small triaxialities when large deformation induce strong changes in the shape of the voids. When the pores are initially non-spherical, the behavior of the material depends more on the shape and orientation of the voids. The evolution of the volume fraction is very sensitive to the shape the voids. Therefore phenomena such as the closure of voids and the coalescence of voids depend strongly on the shape of the voids.

Another limitation is the lack of a fracture criterion. Although the considerations of Tvergaard and Needleman [57] for void coalescence and fracture initiation, equation (4.1), provide an approximate means of incorporating these effects into constitutive models for deformation of porous solids, a physically based model for this important process is still lacking. The development of quantitative and predictive models which account for the statistics of distribution, shape, shape evolution and transition from void growth to fracture remains a formidable challenge. Meanwhile, the constitutive model and the computational procedures presented here, when coupled with a robust finite element package, provide a firm foundation and a powerful capability for the simulation and design of deformation processing operations.

Appendix A

Temperature and Porosity Dependence of Elastic and Thermal Properties

- Elastic moduli:

  The results of theoretical estimates for the dependence of μ, κ on f and the corresponding properties of the matrix material (denoted by a subscript m), based on the "differential self-consistent" calculations for a macroscopically isotropic composite of a random dispersion of roughly spherical holes in a matrix material have been first given in an implicit-analytical form by Norris [63], and are repeated here for convenience.

  Let $\mu_1 = \hat{\mu}_m(\theta)$ and $\kappa_1 = \hat{\kappa}_m(\theta)$ be the temperature dependent moduli of the matrix material.

$$\kappa_1^* = \frac{4}{3}\mu_1$$

$$R_1 = \frac{\kappa_1^*}{\kappa_1}$$

Then the DSC solution is defined implicitly as:

$$\kappa^* = \kappa_1^* \left(\frac{R-1}{R_1-1}\right)^{5/3}$$

$$\kappa = \kappa^*/R$$

$$\left(\frac{R-1}{R_1-1}\right)^5 \left(\frac{R_1+1}{R+1}\right) = (1-f)^6$$

These are a pair of simultaneous equations for the overall effective moduli which need to be solved numerically.

If the matrix is incompressible then $R_1 = 0$, and the solution is simplified:

$$\left(\frac{1}{1-R_1}\right)^5 \left(\frac{1}{R+1}\right) = (1-f)^6$$

and

$$\kappa^* = \kappa_1^* (1-R)^{5/3}$$

For the temperature dependence of the elastic moduli of the matrix, it is found that the temperature variation is linear with respect to the homologous temperature (θ/θ_m) for a reasonably large range about a reference temperature (θ_0/θ_m) (e.g. [19] and [48]):

$$\mu_m = \mu_{m,0} \left[1 - \chi_1 \left\{(\theta/\theta_m) - (\theta_0/\theta_m)\right\}\right], \tag{A.1}$$

$$\kappa_m = \kappa_{m,0} \left[1 - \chi_2 \left\{(\theta/\theta_m) - (\theta_0/\theta_m)\right\}\right], \tag{A.2}$$

where $\mu_{m,0}, \kappa_{m,0}$ are values of the elastic moduli of the matrix at the reference temperature θ_0, χ_1, χ_2 are constants, and θ_m is the melting temperature of the material.

The results of theoretical estimates for the dependence of $\alpha, c,$ and λ on f and the corresponding properties of the matrix material (denoted by a subscript m), based on "self-consistent" calculations for a macroscopically isotropic composite of a random dispersion of roughly spherical holes in a matrix material are listed below [14]:

- Mass density

$$\rho \doteq (1-f)\rho_m, \qquad \rho_m = \rho_m(\theta) \,. \tag{A.3}$$

- Coefficient of thermal expansion:

$$\alpha = \alpha_m, \qquad \alpha_m = \hat{\alpha}_m(\theta). \tag{A.4}$$

For a voided material, the overall bulk thermal expansion coefficient is equal to temperature dependent coefficient of thermal expansion of the matrix material.

- Specific Heat:

$$c \doteq (1-f)\, c_m, \qquad c_m = \hat{c}_m(\theta). \tag{A.5}$$

- Thermal conductivity:

$$\lambda = (1-(3/2)\,f)\;\lambda_m, \qquad \lambda_m = \hat{\lambda}_m(\theta). \tag{A.6}$$

Appendix B

Further examination of the function F(X,m,f)

The proposed forms of the function F (equation 2.44) by Haghi and Anand [100], Duva and Crow [99], Sofronis and McMeeking [105] and Michel and Suquet [103] are interpolations of the limiting behavior at purely deviatoric ($X = 0$) and purely hydrostatic ($X = \infty$) states. However this interpolation is not unique. The proposal of Haghi and Anand [100] differs from the others ($A_1 = 1$ instead of $A_1 = 0$ of the others).

Sofronis and McMeeking [105] derived their potential from finite elements calculations on a hollow sphere. By performing these calculations at intermediate triaxialities, they found that the quality of their interpolation was not good in that range (their Figs. 5 and 6). The error was more significant at low porosities.

In the following sections we employ the periodic media homogenization technique to test various aspects of the quality of the functional form of F (2.44) and to calibrate the A_is. The differential self consistent method is also employed to obtain improved estimates of A_is.

B.1 Periodic Arrays of Voids

The so-called periodic structures have been a popular homogenization technique and one of the earliest approaches (e.g., Needleman [21], Sanchez-Palencia [24]) to the problem of inhomogeneous media. The basic idea is to identify a representative unit cell and examine its behavior which also characterizes the macroscopic behavior of the periodic medium. The method has been popular because:

- Many details of a possibly complicated representative microscopic unit can be accounted for (shape, properties, etc.).
- The solution (whenever it is possible to obtain) is exact for the specific arrangement of the unit cells.
- Some aspects of the anisotropy of the distribution of the inhomogeneities can be addressed.

There are, however, several reservations associated with this technique. Namely:

- The periodic arrangement of a representative cell imposes a strong restriction on the geometry. The specific arrangement is in contradiction with the assumption of random distribution of voids.
- The periodic media are inherently anisotropic. Therefore some ad-hoc averaging scheme must be selected in order to draw conclusions for isotropic non-homogeneous materials.
- There is indeterminacy in the selection of the geometry of the cell (e.g., for a 3-D arrangement, there is an cubic arrangement, a closed packed arrangement etc.).

Previous work on periodic arrays of voids has concentrated on the rate independent behavior. Needleman [21] examined the behavior of a doubly periodic array of circular cylindrical voids under plane-strain conditions in a elastic-perfectly plastic medium. Two-dimensional axisymmetric models have been employed to examine rate-independent or near rate-independent porous material with spherical voids (e.g. Tvergaard [43, 83], Koplik [76]). Three dimensional unit-cell calculations, which represent the more realistic form of this model, have been performed on elasto-plastic hardening porous materials (Worswick and Pick [90], Hom and McMeeking [81], [87]). These results provided important information on the large strain behavior of porous materials. However, when compared with the predictions of isotropic models, it is difficult to identify the source of existing descripencies, since the individual effect of each one of the important variables (such as the matrix properties, the macroscopic stress field, and the geometry of the void and the unit cell) cannot be easily distinguished from the others. The strain rate dependence complicates the situation even more. Here we focus on the *incipient* rate of deformation of 2D and 3D periodic arrays of voids in a power-law matrix. By restricting our attention on the incipient behavior we can clearly present the dependence of the behavior of porous materials on the strain rate sensitivity, the porosity and the macroscopic stress triaxiality.

B.1.1 Geometry and Matrix Model

Two different type of unit cell calculations were performed. First, we examined the axisymmetric model of Fig. 2.1. This model has been widely used in the literature as a convenient approximation of materials containing voids (e.g. Tvergaard [88]). The unit cell consists of a single void of radius r located on the center of a cylinder of height $2R$ and radius R. The volume fraction of voids is given by:

$$f = \frac{2}{3}\left(\frac{r}{R}\right)^3 .$$

Due to symmetry only one quarter of the unit cell is modeled. The sides of the cylinder are constrained to remain straight in order to *approximate* periodic arrangement of hexagonal cells in the void distribution drawn in Fig. 2.1

The imposed load consists of an axial stress Σ_A and a lateral stress Σ_L. hen equivalent and hydrostatic stresses are given by:

$$\Sigma_e = |\Sigma_A - \Sigma_L| \quad \text{and} \quad \Sigma_h = X\,\Sigma_e\,, \tag{B.1}$$

where X is the triaxiality of the stress given by:

$$X = \frac{\Sigma_A + 2\Sigma_L}{3|\Sigma_A - \Sigma_L|}\,. \tag{B.2}$$

Because of the absolute value in the definition of Σ_e, there are two pairs $\{\Sigma_A, \Sigma_L | \Sigma_A < \Sigma_L\}$ and $\{\Sigma_A, \Sigma_L | \Sigma_A > \Sigma_L\}$ which satisfy the desired combination of (Σ_e, X). These pairs correspond to two different values of the third invariant of the stress deviator $(2/9)(\Sigma_A - \Sigma_L)^3$. Under the imposed stress system the response of the unit cell is characterized by a pair of instantaneous stran rates:

$$\dot{E}_A = \lim_{\Delta t \to 0} \frac{\Delta U_A}{\Delta t} \quad \text{and} \quad \dot{E}_L = \lim_{\Delta t \to 0} \frac{\Delta U_L}{\Delta t}\,, \tag{B.3}$$

where ΔU_A and ΔU_L is the axial and lateral displacement of the unit cell within a time interval Δt. The corresponding equivalent and hydrostatic part of the strain rate are given by:

$$\dot{E}_e = \frac{2}{3}|\dot{E}_A - \dot{E}_L| \quad \text{and} \quad \dot{E}_h = \frac{\dot{E}_A + 2\dot{E}_L}{3}\,. \tag{B.4}$$

The loads were applied instantaneously and the strain response was determined over a time increment during which the maximum strain increment in the unit cell was less that 10 microstrain.

The major disadvantage of the axisymmetric geometry is the different behavior along the cylinder axis and along the radius. In other words when a pure hydrostatic pressure is applied the strain rate response contains a non-zero deviatoric component. In our calculations this was evident at higher values of porosity. It is known that periodic media calculations become sensitive to the representative cell selection when the ratio of the radius of the void over the size of the cell increases. For higher values of f, we examined a three-dimensional cubic array of spherical voids (Fig. A.1). The unit cell consists of a single void of radius r located on the center of a cube of edge $2a$.

$$f = \frac{\pi}{6}\left(\frac{r}{a}\right)^3$$

The sides of the cube are constrained to remain straight. One eighth of the unit cell is needed to be modeled due to the symmetry. If axisymmetric loads are considered then modeling one sixteenth of the unit cell suffices. The cubic periodic array of voids is considered to be a better choice for the examination of periodic media than the axisymmetric one. However, it is computationally expensive.

In both cases bifurcation is possible but it will not be considered here. An example of possible buffircation was examined by Tvergaard [49] in the shear band formation in a periodic array of voids.

Finite element calculations were performed to evaluate the incipient behavior of representative unit cells under prescribed load. The matrix material was modeled by a non hardening, incompressible power law material, with plastic potential given by equation (2.26). The incompressibility of the matrix poses a serious numerical problem. This problem is addressed by modeling the mean strain rate response by a penalty term (Zienkiewicz [107]) in the strain rate response is given by:

$$\dot{E}_m = \frac{p}{k_p}\ \frac{\dot{\epsilon}_0}{\sigma_0}\left(\frac{\dot{E}_e}{\dot{\epsilon}_0}\right)^{1-m}$$

where k_p is a large number of the order of 10^{10}. The higher the penalty the more accurate the incompressibility assumption and the more difficult the convergence of the solution. The difficulty is increasing with decreasing strain rate sensitivity. To facilitate the convergence, successful solutions for given values of $1/m$ were used as initial estimates of the solution for a higher value of the power law exponent $1/m + \Delta(1/m)$. To ensure convergence continuously smaller values of $\Delta(1/m)$ must be used as $(1/m)$ increases. In this way we were able to obtain solutions up to $1/m = 20$.

In the axisymmetric case a convergence study was conducted in all cases, while in the 3-dimensional case few selected meshes were checked for convergence, due to the high cost of the 3-D computation. 8-noded and 20 noded isoparametric hybrid reduced integration elements have been used for the axisymmetric and the 3-D calculations respectively.

B.1.2 Results

Using the axisymmetric cell we have obtained a set of results for different strain rate sensitivities, porosities and triaxialities. Representative results from the axisymmetric cell are plotted in Fig. A.2 and Fig. A.3 for f=0.01 and f=0.10 respectively. In these figures we plot the loci of the pair $(\Sigma_{eN}, \Sigma_{hN})$ where

$$\Sigma_{eN} = \frac{\Sigma_e}{s_0 \left(\dot{E}_e/\dot{\epsilon}_0\right)^m} \tag{B.5}$$

and

$$\Sigma_{hN} = \frac{\Sigma_h}{s_0 \left(\dot{E}_h/\dot{\epsilon}_0\right)^m} \tag{B.6}$$

are normalized values of the equivalent and hydrostatic components of the macroscopic stress. Σ_e and Σ_h are the imposed equivalent and hydrostatic components of the macroscopic stress (B.1), $\dot{E}_e$ and $\dot{E}_h$ is the calculated equivalent and hydrostatic components of the strain rate response of the unit cell (B.4). If there is no void in the unit cell ($f = 0$) then $\Sigma_{eN} = 1$ and $\Sigma_{hN} = \infty$ and the locus $(\Sigma_{eN}, \Sigma_{hN})$, a straight line at $\Sigma_{eN} = 1$, represents the behavior of an incompressible power law material. For non zero values the porosity, Σ_{eN} and Σ_{hN} represent the reduction of the stress required to produce certain level of strain rate response in the porous material due to the presence of voids. At the rate independent limit $m \to 0$, the locus of $(\Sigma_{eN}, \Sigma_{hN})$ coincides with the yield surface normalized by the yield stress s_0. [1] At the linear viscous limit $m \to 1$, the two ratios correspond to the values of the shear and bulk moduli of the porous material normalized by the shear modulus of the matrix material. The strong effect of the rate sensitivity is evident. Lower rate sensitivity results a softer response in the porous material. This effect is directly related to the intensity of the void-to-void interaction and is small at $X = 0$ while it increases as the triaxiality increases.

In Fig. A.2(b) and Fig. A.3(b) the "triaxiality" of the strain rate tensor

$$Y = \frac{\dot{E}_h}{\dot{E}_e}$$

is plotted versus the stress triaxiality. Low values of the rate sensitivity for the same value of triaxiality and porosity result in a higher fraction of the mean part of the strain rate over the deviatoric part.

Representative results obtained by the three dimensional unit cell have also been obtained. At low porosity (f=0.01) they do not differ from the axisymmetric ones. However there is difference at higher porosity for intermediate to high values of the triaxiality (see Fig. A.4). The source of the difference is the asymmetry in the behavior of the axisymmetric unit cell along the radial and the axial direction. This introduces the "corner"-like effect at $X = \infty$ in Fig. A.3(a), since the axisymmetric cell when loaded by a hydrostatic stress produces a strain rate response with a non-zero deviatoric component. At the contrary the behavior of the 3D unit cell is the same

---

[1] The results at the rigid plastic limit can be obtained by extrapolation of the non-linear viscous results. An alternative technique based on limit load calculations has been employed by Haghi (1991).

along its three axes of symmetry. The observed difference between the axisymmetric and 3D unit cell is indicating the sensitivity of the results of periodic structures on the selection of the geometry of the unit cell.

It is interesting to note that the axisymmetric and 3D unit cell predict the same values of $(\Sigma_{eN}, \Sigma_{hN})$ at $X = 0$ and $X = \infty$. These values can be used to calibrate the parameters A_2 and A_3 of the function F (equation (2.44).

B.1.3 Calibration of A_3

We have determined the value of the function $A_3(f, m)$ from the results of the previous section. The results for the incipient $\dot{E}^p_e$ at $X = 0$, normalized by the effective stress for a fully dense material, $\dot{E}^p = \partial\phi_{matrix}/\partial\Sigma_e$, caused by the same stress Σ_e are plotted in Fig. A.5 for various values of porosities f and inverse rate sensitivities $1/m$. From equations (2.17) and (2.39):

$$\frac{\dot{E}^p_e}{\dot{E}^p} = F(X = 0) = F_0, \qquad F_0 = \hat{F}_0(f, m) \tag{B.7}$$

In the same figure we plot the lower bound for F_0 [95] and the predicted F_0 by the spherical cell at $X = 0$ of Sofronis and McMeeking [105]). The prediction of the spherical cell at $X = 0$ are much higher than the corresponding predictions of the periodic cell (note that the scale is logarithmic), while the lower bound can be considered as a reasonable approximation (within 10%). We found that the unit cell results can be well approximated by the empirical relation

$$F_0 = \left(\frac{1 + 3.34\, f + 0.25\, f^2}{1 - f^2}\right)^{\frac{1}{2m}}, \tag{B.8}$$

for the range $0 < f < 0.1$ and $0.067 < m < 1$. Equation (B.8) satisfies the dilute limit solution of Duva and Hutchinson. Note that the quadratic dependence of F_0 on f in this expression is necessary to match the results of our numerical experiments.

Also, the specific form for the denominator in this empirical expression is chosen so that the material looses any load carrying capacity as $f \to 1$.

A_3 can be obtained using the interpolation of F_0 by equation (B.8):

$$A_3 = (F_0 - 1)^{\frac{2m}{m+1}} \quad \text{when} \quad A_1 = 1 \tag{B.9}$$

$$A_3 = F_0^{\frac{2m}{m+1}} \quad \text{when} \quad A_1 = 0 \tag{B.10}$$

B.1.4 Calibration of A_2

The parameter A_2, which governs the behavior of the model at $X = \infty$ (see equation 2.46), can be calibrated by the periodic unit cell results at $X = \infty$. Our calculations show that the response predicted by the unit cell calculations differs from the one calculated by the spherical cell. In Fig. A.6(a) we plot the response $\dot{E}_h^p$ of the periodic cell at $X = \infty$, normalized by the corresponding prediction of the spherical cell (2.46) for the same pressure for various rate sensitivities and porosities. The results of the two methods coincide at the linear limit. However with decreasing strain rate sensitivity, the periodic unit cell is substantially softer.

The estimation of A_2 is easier if we replot the results of Fig. A.6(a) in terms of the ratio p_s/p_p of the pressures required to cause the same mean strain rates in the spherical and the periodic unit cell (see Fig. A.6(b)). The ratio p_s/p_p has an asymptotic value as $m \to 0$ corresponding to the ratio of yield pressures p_s^Y/p_p^Y of the spherical and periodic unit cell respectively. These results can be fit well by the following formula:

$$\frac{p_s}{p_p} = 1 + \left(\frac{p_s^Y}{p_p^Y} - 1\right)\left[1 - exp\left\{a\left(1 - \frac{1}{m}\right)\right\}\right] \tag{B.11}$$

with $(p_s^Y/p_p^Y) = 1.03 + 0.67f$, and $a = 0.146$. Using the interpolation (B.11) and equation (2.45) an estimate of A_2 can be obtained:

$$A_{2_p} = A_{2_s} \left(\frac{p_s}{p_p} \right)^{\frac{2}{1+m}} \tag{B.12}$$

with A_{2_s} given by equation (2.47). Using the estimate of $\dot{E}_h^p$ based on this interpolation is plotted in Fig. A.6.

B.1.5 Intermediate Triaxialities

With A_2 and A_3 properly calibrated using eqns (B.9) or (B.10) and B.12) we can now compare the periodic array results and the predictions of the two forms of F with $A_1 = 0$ and $A_2 = 1$ respectively. In Fig. A.7, Fig. A.8, Fig. A.9, and Fig. A.10 we plot (Σ_{en} versus Σ_{hn}) and X versus Y respectively. It is evident that neither the interpolation based on $A_1 = 0$ nor the one based on $A_1 = 1$ match the results at high rate sensitivities and low porosities. The later provides a better correlation at low m and low f. As m and f increase the role of A_1 is not important and the predictions of the two forms are similar.

B.1.6 Discussion

At low porosity where the size of the void is small compared to the dimensions of the unit cell the results of the periodic array of voids reliable As the characteristic size of the void becomes comparable with the size of the unit cell the results become sensitive to the selection of the cell geometry. Therefore, it is preferable to work with a model that avoids this problem without sacrificing the advantage of representing accurately the geometry of the void. The differential self consistent method presents an interesting alternative choice.

B.2 The Differential Self Consistent Method (DSCM)

Self consistent models can provide estimates for the effective properties of multi-phase composite bodies. The basic idea is to approximate the effect of a local inhomogeneity (a void, an inclusion etc.) by employing the dilute solution of this phase in an "equivalent" homogeneous medium with properties same with the (unknown) properties of the composite body. The various models utilize different techniques to sum up the individual effect of all inhomogeneities. The original self consistent schemes ([6], [8]) are symmetric with respect to the material properties of each phase. The predicted effective properties by these schemes are occasionally peculiar when the ratios of the corresponding properties of the various phases are extreme (e.g. voids, rigid inclusions). For example, for a linear material with voids zero moduli are predicted at 50% porosity. Under these conditions the differential self consistent method is considered to be advantageous, since it discriminates between the matrix and the voids. Theoretical predictions of the effective elastic moduli for porous materials based on the DSCM were compared with experiments in a comparative study by Chen et al. [40], and were found to be in agreement for a large range of porosities. Applications of this method for non-linear materials were presented by Duva [55] for a power law matrix reinforced by rigid particles and by Rodin and Parks [78] for a power law matrix weakened by cracks.

The selection of the differential self consistent method for the estimation of the behavior of porous materials offers the following advantages:

- The basic idea seems physically appealing
- The results for linear materials have been favorably compared with experiments
- It is (in principle) as versatile as the periodic structures technique in accounting for the shape of the voids, while it does not pose the problem of the selection of the unit cell.

- It offers a better approximation of the medium strength interactions between voids than the periodic array of voids

Differential Self Consistent Method: The Basic Idea

Consider the body A (Fig. A.11) consisting of a fully dense power-law matrix and a number of voids with volume fraction f. The matrix material is characterized by the strain rate potential ϕ_{matrix} of equation (2.26). Each void corresponds to a differential amount of volume fraction df. The body A is loaded by a macroscopic stress $\mathbf{T}^{\infty}$ and its macroscopic response described by an *unknown* strain rate potential Φ. The introduction of a new void into body A produces a body B with volume fraction of voids $f + df$ and strain rate potential $\Phi + d\Phi$.

Assume that there exists an homogeneous material equivalent to body A characterized by the same strain rate potential Φ. Consider this homogeneous material in two configurations, an infinite body C and a infinite body D with one void, both loaded by the same macroscopic stress $\mathbf{T}^{\infty}$ at infinity. The central assumption of the self consistent methods is that the increase in the potential $d\Phi$ can be calculated from the difference of the potentials of bodies C and D. More precisely:

$$(1-f)\frac{d\Phi}{df} =$$

$$= \Phi_V = \lim_{V_v \to 0} \left[\frac{1}{V_v} \int_{V_m} \Phi\Big(\mathbf{T}(\mathbf{x})\Big) dV - \frac{V_v + V_m}{V_v} \Phi(\mathbf{T}^{\infty}) \right] \tag{B.13}$$

where V_v and V_m are the volumes of the void and the matrix in the body D [2].

---

[2] To derive equation (B.13) the following result obtained by Hutchinson [28] has been employed. For a porous material with volume fraction of voids f and a matrix strain rate potential ϕ_{matrix} the macroscopic response is given by the potential:

$$\Phi = \frac{1-f}{V_m} \int_{V_m} \phi_{matrix}(\mathbf{x}) dV$$

This result is independent of the boundary conditions when the size of the voids is smaller than the dimensions of the porous body.

The calculation of this integral requires the complete solution for the local stress field $\mathbf{T}(\mathbf{x})$, in the ***kernel problem***, i.e. a infinite medium characterized by a strain rate potential Φ with one void, loaded at infinity by $\mathbf{T}^{\infty}$.

The characteristic of the differential self consistent method is that starting from the fully dense matrix, the porosity is introduced in differential amounts in the continuously homogenized material. This process can be expressed in terms of an differential equation for Φ:

$$\frac{d\Phi}{df} = \frac{\Phi_V}{1-f} \quad \text{with} \quad \Phi(f=0) = \phi_{matrix}. \tag{B.14}$$

With Φ given by (2.37) for a power law matrix material: the corresponding form for Φ_V is given by

$$\Phi_V = \frac{\dot{\epsilon}_0 s}{1/m+1} F_V \left(\frac{\Sigma_e}{s}\right)^{1/m+1} . \tag{B.15}$$

Using equation (B.13) the function F_V can be calculated as follows

$$F_V = F_V\left(F(X,m,f);X\right) =$$

$$\lim_{V_v->0}\left[\frac{1}{V_v}\int_{V_m} F\left(\chi(\mathbf{x}),m,f\right)\left(\frac{\sigma(\mathbf{x})}{\Sigma_e}\right)^{1/m+1} - \frac{V_v+V_m}{V_v}F(X,m,f)\right] \tag{B.16}$$

where X is the triaxiality of the macroscopic applied stress $\mathbf{T}^{\infty}$, $\sigma(\mathbf{x})$ and $\chi(\mathbf{x})$ are the equivalent stress and triaxiality of the local stress $\mathbf{T}(\mathbf{x})$. As it can be seen from equation (B.16), F_V depends on the function F and on the triaxiality X of the applied stress filed $\mathbf{T}^{\infty}$. The differential equation (B.13) can be expressed in terms of F and F_V:

$$\frac{\partial F}{\partial f} = \frac{F_V}{1-f} \quad \text{with} \quad F = 1 \text{ at } f = 0 \tag{B.17}$$

By integrating equation (B.17) for a specific material (i.e. fixed value of m) the dependency of F on the porosity can be inferred. However, due to the implicit dependence of F_V on F, direct integration of equation (B.17) is not possible (as it was for the case of rigid particles [55]). Conceptually the DSCM can provide the complete dependence of F on the porosity and the triaxiality. However that task would require the solution of the kernel problem for a very large number of triaxialities, to adequately capture the effect of triaxiality on F. A compromise can be made by selecting a functional form of the triaxiality dependence of F. Since an integration is involved, *the success of the DSCM depends strongly on the proper selection of the functional form for F.*

A possible candidate for F is the general form of the spherical cell models:

$$F = A_1 + (A_2 X^2 + A_3)^{((1/m+1)/2)} \tag{B.18}$$

with $A_i = A_i(m, f)$. This form complies with all the requirements on the asymptotic behavior and meets the convexity requirement if:

$$A_1 \geq - - \frac{1}{2} \left[\frac{(n+1)A_3}{n} \right]^{\frac{n+1}{2}} \tag{B.19}$$

B.2.1 Integration

With F given by equation (B.18), the differential equation (B.17) can be written as:

$$\sum_{i=1}^{3} \frac{\partial F}{\partial A_i} \frac{dA_i}{df} = \frac{F_V}{1-f} \tag{B.20}$$

Using (B.20), the variation of A_is with the porosity can be obtained from the solution of the kernel system at three different values of triaxiality. The solution of the kernel problem can not be obtained analytically for the general case. Therefore we have to resort to numerical techniques.

B.2.2 Solution of the kernel problem

The integration of the differential equation (B.17) requires the solution of the kernel problem i.e. an isolated void in an infinite body characterized by a strain rate potential such as that of equation (B.18) loaded with a stress $\mathbf{T}^{\infty}$ at infinity. Budiansky *et al.* [46] presented an analytical solution for a linear viscous body ($\Phi = \phi_{matrix}$ and $m = 1$) as well as a numerical solution for non-linear (power-law) viscous bodies ($\Phi = \phi_{matrix}$ and $m \neq 1$).

Two different approximate methods can be applied, for problems over infinite domains. The first approximates the unknown field with a finite series of a complete orthogonal basis of functions. The unknown coefficients of each term of the series is then determined by a Rayleigh-Ritz procedure. This method can be very accurate if the form of the solution can be guessed. However, if this is not possible, then a very large number of terms is necessary to obtain reasonable approximations [3]. The second method is to solve the problem over a finite domain, using a numerical technique, e.g., finite-elements, and then track down the infinite limit by increasing the size of the domain. This method is accurate but it may not converge "quickly enough" and may pose some numerical difficulties. Also, when solving the problem on a finite domain, the boundary conditions are prescribed approximately. Referring to the case of a void in an incompressible matrix under pressure at infinity, Budiansky et al. [46] cautioned that numerical calculations carried over a finite block of material may not reflect accurately the behavior of the void in the infinite block unless the void fraction is *extremely* small. In their example for a moderate value of non-linearity ($N = 3$) a 0.1% void gives a 30% error on the rate of change of volume with respect to the true dilute result.

The generic kernel problem of the DSCM involves a compressible matrix since it represents the homogenized porous material. Therefore guessing the solution form is extremely difficult, and that makes the Rayleigh-Ritz minimization technique not to be attractive. The use of the finite-domain technique is more preferable. However the obtained solutions must be carefully checked for convergence. The case of a void in an

---

[3] Note that the original results of [46] were wrong for that reason. Huang [82] showed that at least 50 terms are required in the series proposed by [46] to get accurate results

incompressible matrix, which was given as an alarming example [46], represents two extremes, that of infinite triaxiality and that of incompressibility. When moving away from these extremes the accuracy problems are easing out. Moreover we employ a special technique, which is described below, that enhance the accuracy and efficiency of the calculations.

This technique was first applied by Parks and Rodin for the case of a crack in an infinite matrix. Consider the boundary value problem of an isolated void in an infinite matrix with strain rate potential Φ loaded by the stress $\mathbf{T}^{\infty} = \mathit{constant}$ at infinity (Fig. A.12). The stress $\mathbf{T}(\mathbf{x})$ at every point in the matrix can be written in the following form:

$$\mathbf{T}(\mathbf{x}) = \mathbf{T}^{\infty} + \hat{\mathbf{T}}(\mathbf{x}) \tag{B.21}$$

where $\hat{\mathbf{T}}(\mathbf{x})$ is the perturbation of the homogeneous stress field due to the presence of the void. The stress field $\mathbf{T}(\mathbf{x})$ must satisfy the boundary conditions at infinity and on the surface of the void ∂V:

$$\mathbf{T}(\infty) = \mathbf{T}^{\infty} \quad \text{and} \quad \mathbf{T}\mathbf{n}|_{\partial V} = 0 \tag{B.22}$$

as well as the equilibrium equation.

The solution of the corresponding homogeneous problem (i.e. without void) problem is trivial $\mathbf{T}(\mathbf{x}) = \mathbf{T}^{\infty}$ everywhere.

Note that both stress fields $\mathbf{T}(\mathbf{x})$ and $\mathbf{T}^{\infty}$ are in equilibrium. Due to the linearity of the equilibrium equation, $\hat{\mathbf{T}}(\mathbf{x})$ is in equilibrium too. The stress field $\hat{\mathbf{T}}(\mathbf{x})$ is the solution of a boundary value problem that is the "difference" of the kernel problem and the homogeneous problem. In other words, it corresponds to the problem of an isolated void in an infinite body where the strain rate of the matrix is given by:

$$\dot{\epsilon}(\mathbf{x}) = \frac{\partial \Phi}{\partial \mathbf{T}}\Big|_{\mathbf{T}=\mathbf{T}^{\infty}+\hat{\mathbf{T}}(\mathbf{x})} - \frac{\partial \Phi}{\partial \mathbf{T}}\Big|_{\mathbf{T}=\mathbf{T}^{\infty}} \tag{B.23}$$

and satisfies the following boundary conditions:

$$\mathbf{T}(\infty) = 0 \quad \text{and} \quad \mathbf{t} = -\mathbf{T}\mathbf{n}(\partial V) \tag{B.24}$$

The implementation of this procedure in ABAQUS is shown in A.12. This method significantly increases the accuracy of the calculations since it focuses attention on the important part of the solution, which is the perturbation of the homogeneous stress field by the presense of a void. Moreover, the boundary conditions at infinity are no longer as important as before, since the loading is now applied on the surface of the void.

The finite-element method is used to evaluated the function F_V according to equation (B.16), for finite values of the macroscopic triaxiality. The selection of the mesh is guided by two considerations. The mesh much be fine enough to provide accurate descritization and the size of the model must be much larger that the size of the void to provide an accurate approximation of the infinite body solution. Different meshes were employed depending on the power law exponent $1/m$ and the triaxiality of the macroscopic stress field X. A typical mesh is shown in Fig. A.13. The stress concentration around the void is larger for smaller $1/m$ requiring adequate mesh density around the void. For increasing $1/m$ and X, the size of the required model increases in order to approximate accurately the infinite body solution. Eight noded displacement-based axisymmetric elements (ABAQUS CAX8R elements) with reduced integration since they provide a combination of desired accuracy and economy.

For the kernel problem at $X = \infty$ we have developed accurated numerical techniques to solve the one dimensional equilibrium equation. Recently Michel and Suquet [103] presented an analytical solution to this problem for the general form of equation (2.37). Although our calculations were based on our numerical technique, we do not present the details here since the analytical solution makes them obsolete. We did, however, check the accuracy of our numerical techniques against the solution of Michel and Suquet [103] and found them to be completely accurate.

Integration of the equation

(B.20)

There is no a priori optimal numerical procedure for the solution of a system of differential equations. A popular choice is the fourth order Runge-Kutta scheme. The modified 4th order Runge-Kutta algorithm [72] was used with automatic time stepping. This method requires a number of derivative evaluations per increment but provides an estimate of the error.

There is an additional problem associated with the 1st step of the integration. Let $F = 1 + (A_2X^2 + A_3)^{\frac{N+1}{2}}$. Then:

$$\frac{dF}{df} = \left(\frac{dA_2}{df}X^2 + \frac{dA_3}{df}\right)\left(\frac{N+1}{2}\right)\left(A_2X^2 + A_3\right)^{\frac{N-1}{2}} \tag{B.25}$$

The initial conditions at $f = 0$ are $A2 = A3 = 0$. The integration cannot start with an explicit scheme, since $dF/df = 0$. Therefore, we used an implicit Euler-backward scheme to initialize the integration. The significance of the error associated with the implicit scheme is minimized by choosing a sufficiently small first increment. By using a Euler-backward first step the difficult solution of the fully incompressible problem at $f = 0$ is avoided.

In the next section we turn our attention to the quality of the selection of the functional form of F, which is critical for the accuracy of the predictions of the differential self consistent scheme.

Checking the quality of the selection of F

Three different forms of the potential have been considered:

- Form A: $F = (A_2X^2 + A_3)^{(1/m+1)/2}$, which corresponds to the suggested form by [95], [99] and [105]
- Form B: $F = 1 + (A_2X^2 + A_3)^{(1/m+1)/2}$, which corresponds to the form by [94].
- Form C: $F = A_1 + (A_2X^2 + A_3)^{(1/m+1)/2}$, with variable $A_1(m, f)$, which provides a better description of the behavior in intermediate triaxialities.

For the two first cases the variation of A_2 and A_3 was calculated by solving the kernel problem at $X = 0$ and $X = \infty$. In the third case, one more calculation of the kernel problem is necessary at an intermediate triaxiality. The value $X = 2$ was selected because is corresponds approximately to the value $\sqrt{A_3/A_2}$ for which the contribution of the terms A_2X^2 and A_3 in the value of F are approximately equal.

We selected the form C because preliminary calculations indicated that the forms A and B do not approximate adequately the triaxiality effect at low porosities and high power law exponents 1/m. This is crucial for the differential self consistent scheme due to the required integration where a small error at low porosities can lead the solution to the wrong result.

If the exact functional form of F were known, the evaluation of the kernel problem for 3 different triaxialities would suffice. But the triaxiality dependence of F was assumed by selecting equation (2.37). The best way to solve this problem, is to solve the kernel problem for m-different triaxialities ($m > 3$) and then solve the corresponding system ($m \times 3$) of differential equations in the least square sense. However this procedure requires a large number of evaluations of F_V. As an alternative we can monitor the quality of the approximation of F in an indirect way. By solving the kernel problem for three triaxialities (e.g. $X = 0$, $X = 2$, $X = \infty$), the values of the derivatives $\frac{dA_i}{df}$ can be obtained. Using these values, the derivative dF/df can be calculated for any triaxiality:

$$\frac{dF}{df}\Big|_{formula} = \frac{dF}{df} = \frac{dA_1}{df} + \left(\frac{dA_2}{df}X^2 + \frac{dA_3}{df}\right)\left(\frac{n+1}{2}\right)\left(A_2X^2 + A_3\right)^{\frac{n-1}{2}} \tag{B.26}$$

The derivative $\frac{dA_i}{df}$ can also be obtained directly from the solution of the kernel problem:

$$\frac{dF}{df}\Big|_{kernel} = \frac{F_V}{1-f} \tag{B.27}$$

The results of (B.26) and (B.27) are same for the 3 selected triaxialities (e.g. $X = 0$, $X = 2$, $X = \infty$). If the approximation of F were exact, they should be same for any triaxiality. By comparing the results of (B.26) and (B.27) for triaxialities different than those used to determine the derivatives $\frac{dA_i}{df}$, we can estimate the quality of the selection of the functional form of F.

In Fig. A.14 the predictions for $F(X, f, m = 0.2)$ are plotted against porosity for $X = 0, 2, \infty$, for the 3 different forms. At $X = 0$ there is practically no difference between the predictions of the different functional forms, which are higher than the bound by 20%. However, substantial differences are observed for higher triaxialities. In Fig. A.14 (b) the results of F(X=2) are shown to depend significantly on the selection of the functional form for F. The maximum difference occurs as $X \rightarrow \infty$ (see Fig. A.14(c)). Recall that the parameter A_2 represents the behavior of the materials at infinite triaxiality. In other words

$$F(X \rightarrow \infty) \propto A_2^{(n+1)/2} X^{n+1} \tag{B.28}$$

In Fig. A.14(c), the value of A_2 has been normalized by the predicted value of A_2 by the spherical cell model (eq. (2.47)). The importance of the selection of the specific form for F is evident. In order to evaluate the error associated with it, the following test is performed as mentioned before. The values of dF/df are calculated using equations B.26 and B.27 and are compared against each other for triaxialities different than those used to compute the A_i's.

The ratio of the two values of dF/df calculated from equations (B.26) and (B.27) is plotted versus the triaxiality for $m = 0.2$ and $f = 0.01, 0.10$ in Fig. A.15. This ratio equals one at $X = 0$ and $X = \infty$ for forms A and B and at $X = 0$, $X = 2$ and $X = \infty$ for form C, because these are the triaxialities at which the derivatives dA_i/df are computed. Deviation from one indicates the error in dF/df introduced by the selection of the functional dependence of F on the triaxiality. At $f = 0.01$ the error in both forms A and B is significant, ranging up to 40%. For Form A the error remains significant at the higher porosity $f = 0.10$. Since the prediction of F is based on an integration of dF/df, the accuracy of the calculation is particularly important at lower porosities. From the results of Fig. A.15 it is clear that neither form A nor Form B are appropriate. With form C due to the extra free parameter A_1, the error is minimum. This form will be employed for the rest of the calculations.

Results and Discussion

In Fig. A.16 we plot the predicted variation of the functions A_i, $i = 1, 2, 3$ with the porosity for different values of m. Predictions of the response of a porous power law material based on these results are plotted in Fig. A.17 for $f = 0.01$ and in Fig. A.18 for $f = 0.10$ in the familiar form of $(\Sigma_{eN}, \Sigma_{hN})$ and (X, Y).

In Fig. A.19, Fig. A.20, Fig. A.21, and Fig. A.22 we present a comparison of the predictions of the differential self consistent method with the periodic array of voids.

The main difference between the results of the periodic cell and the DSCM is due to the different approximation of the void to void interactions. For the linear solid, it has been known that for moderate porosities the DSCM predicts a softer response that the periodic cell and is in agreement with the experiment ([40]). For the non-linear matrix material we observe a similar trend. When the interactions are increasing (i.e., increasing porosity, increasing triaxiality or decreasing strain rate sensitivity) the response of predicted by the differential self consistent method is increasingly softer than the one predicted by the periodic array of voids.

The maximum discrepancy among the various models examined occurs at very high triaxialities. Ultimately the only way to judge for the quality of each model is to compare it with experiments. However "clean" high triaxiality experiments that would produce large strains at high temperatures and pressures are very difficult to design and perform.

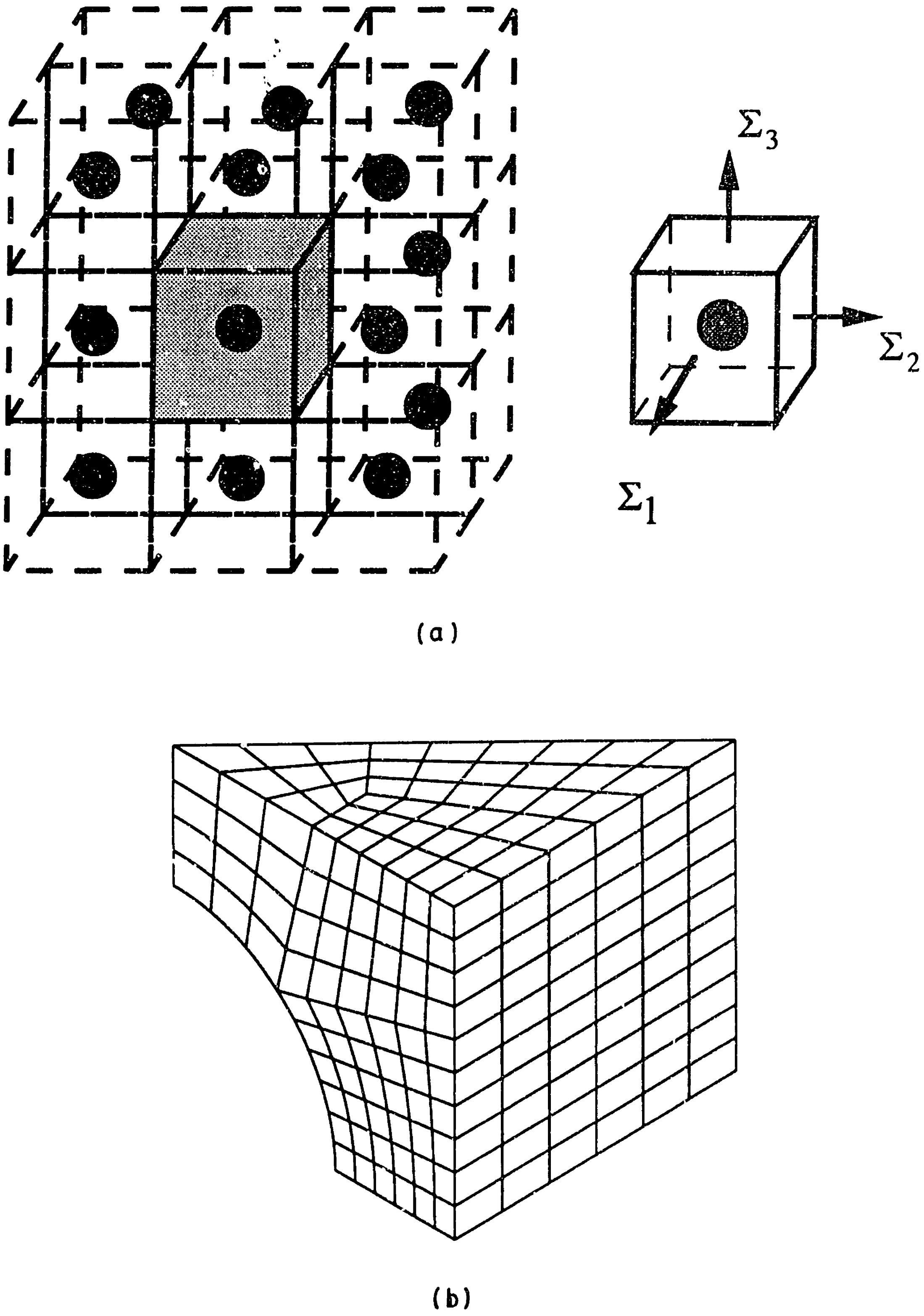

Figure A.1: 3-D periodic unit cell.

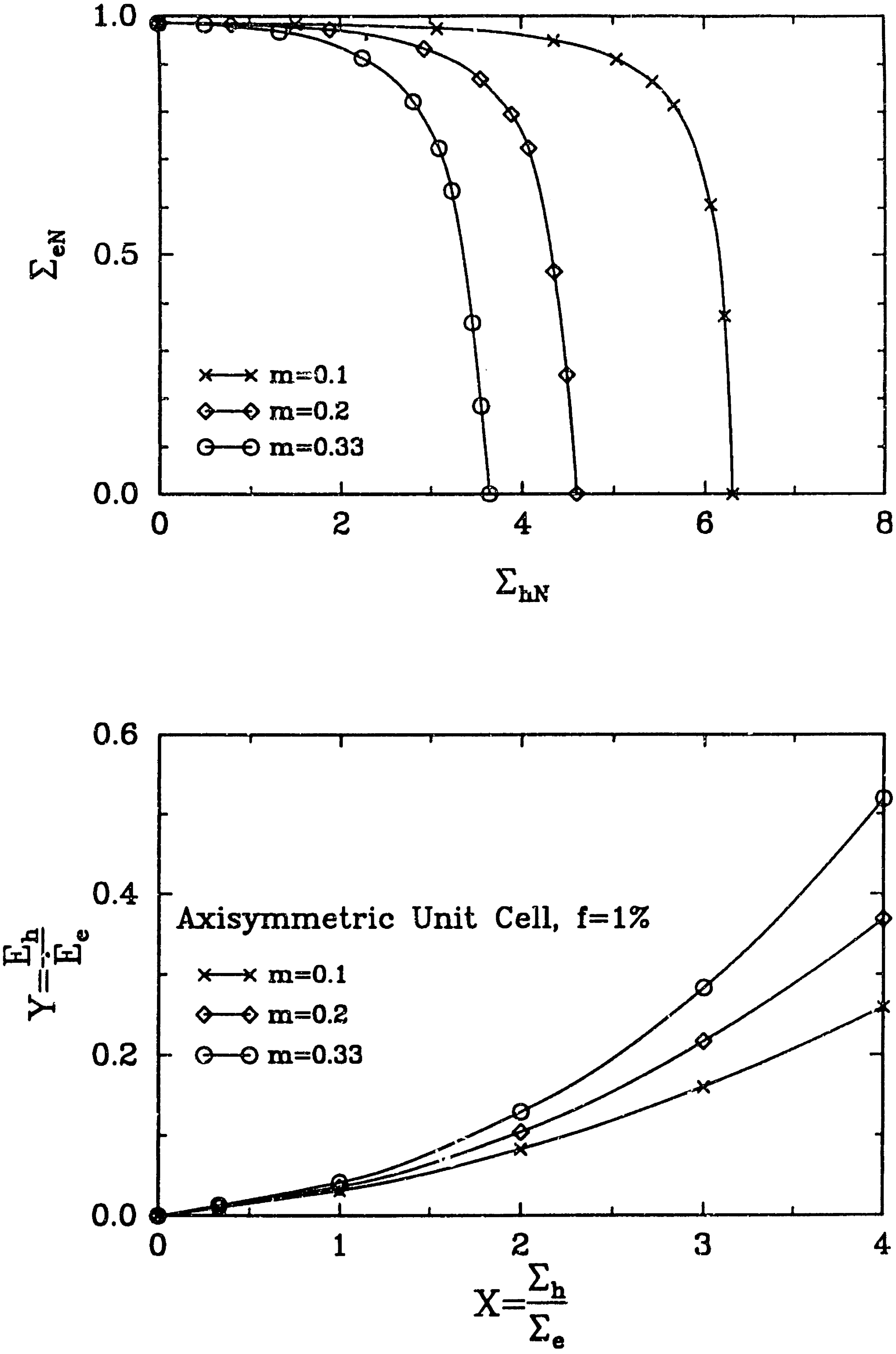

Figure A.2: Predictions of the axisymmetric unit cell calculations for f = 1%, for various values of m.

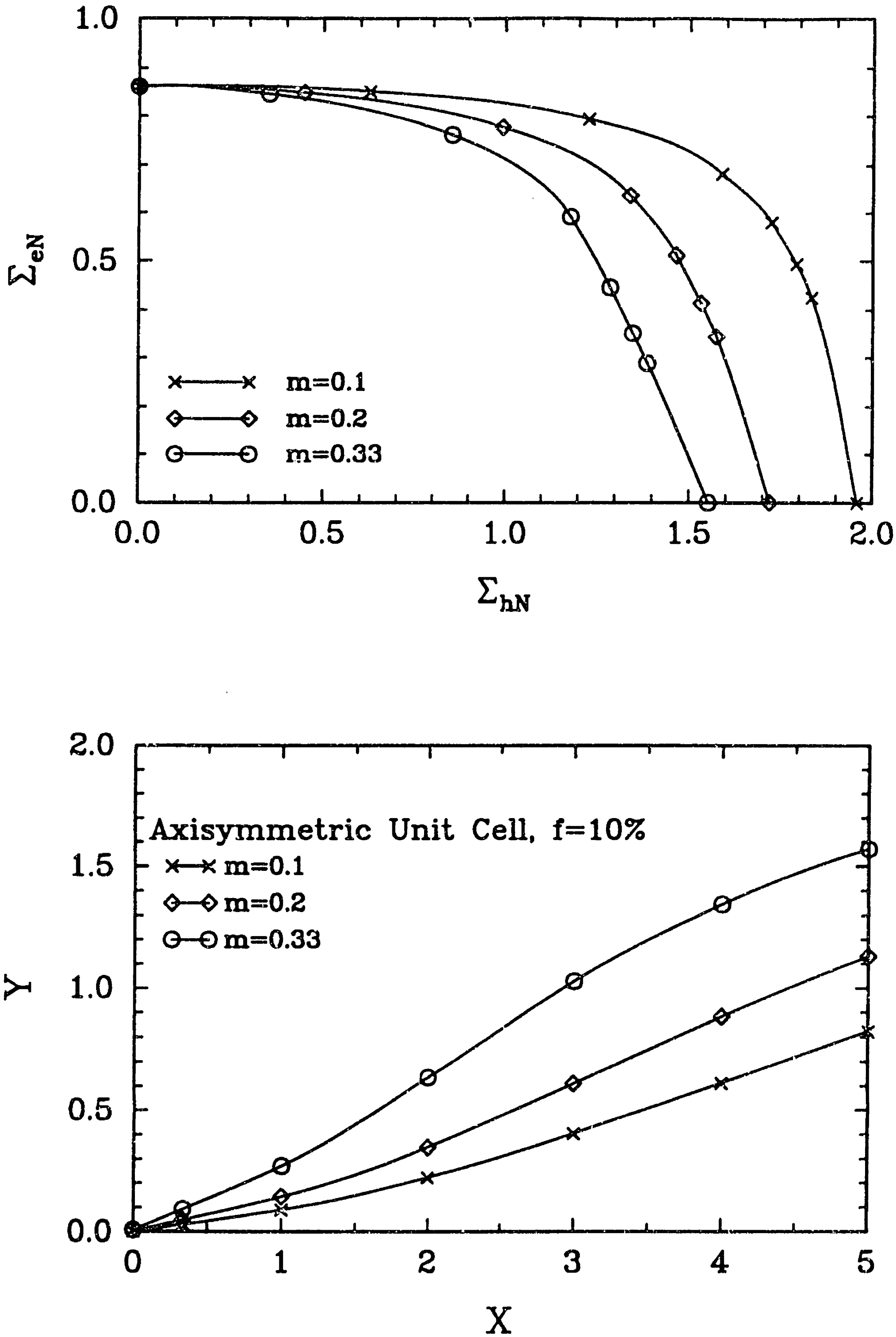

Figure A.3: Predictions of the axisymmetric unit cell calculations for f = 10%, for various values of m.

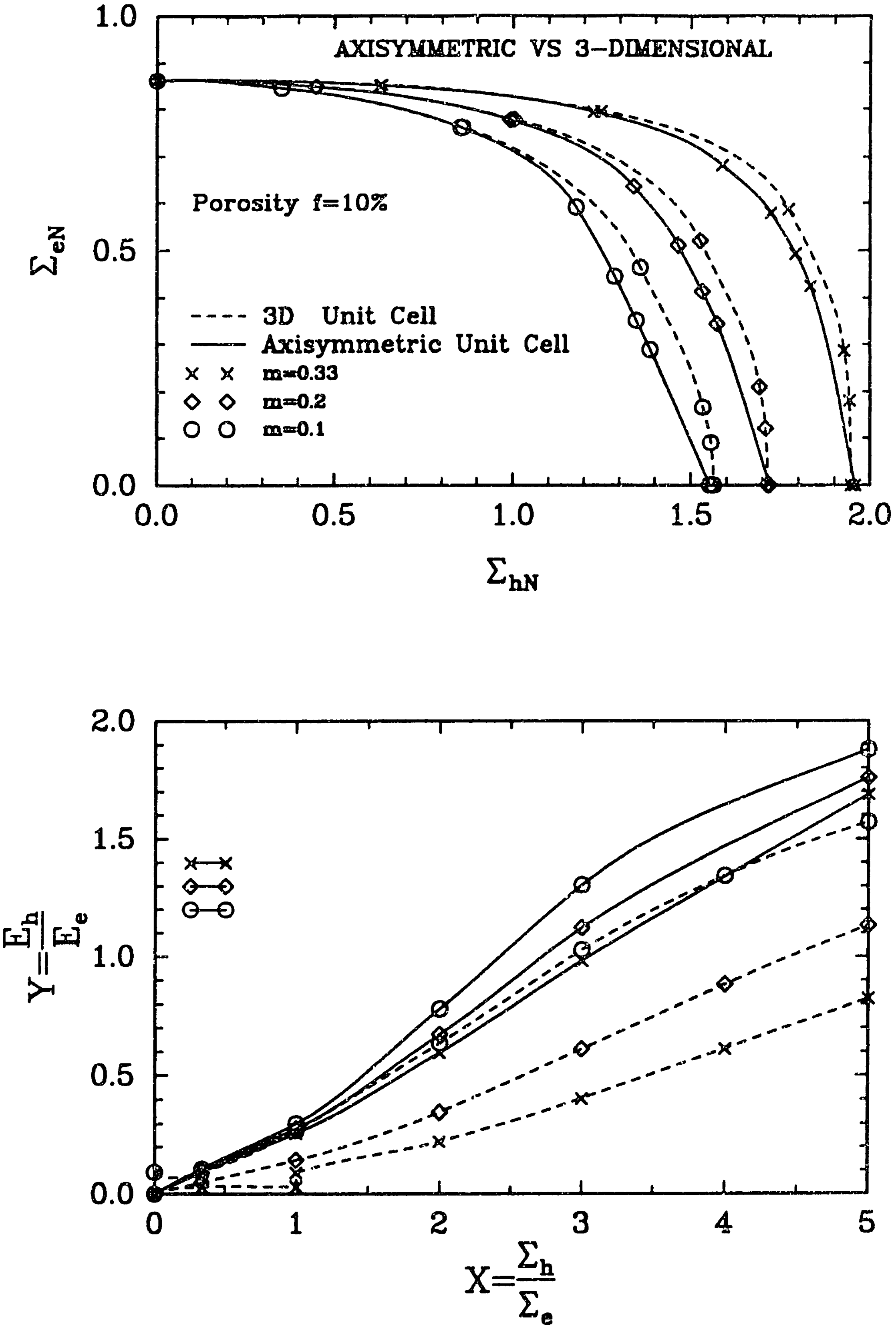

Figure A.4: Comparison of axisymmetric versus 3-D unit cell results at $f = 10\%$.

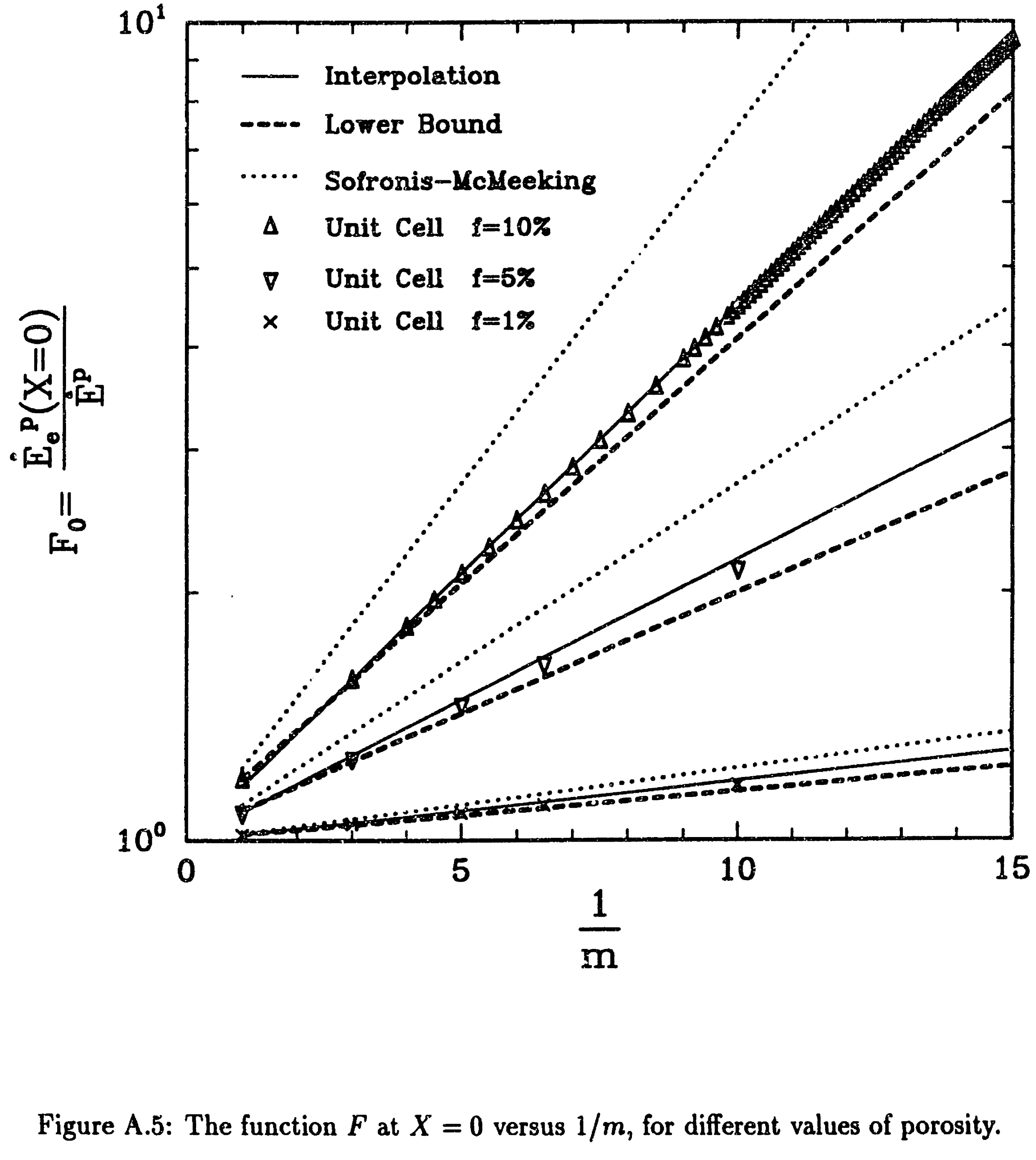

Figure A.5: The function F at $X = 0$ versus $1/m$, for different values of porosity.

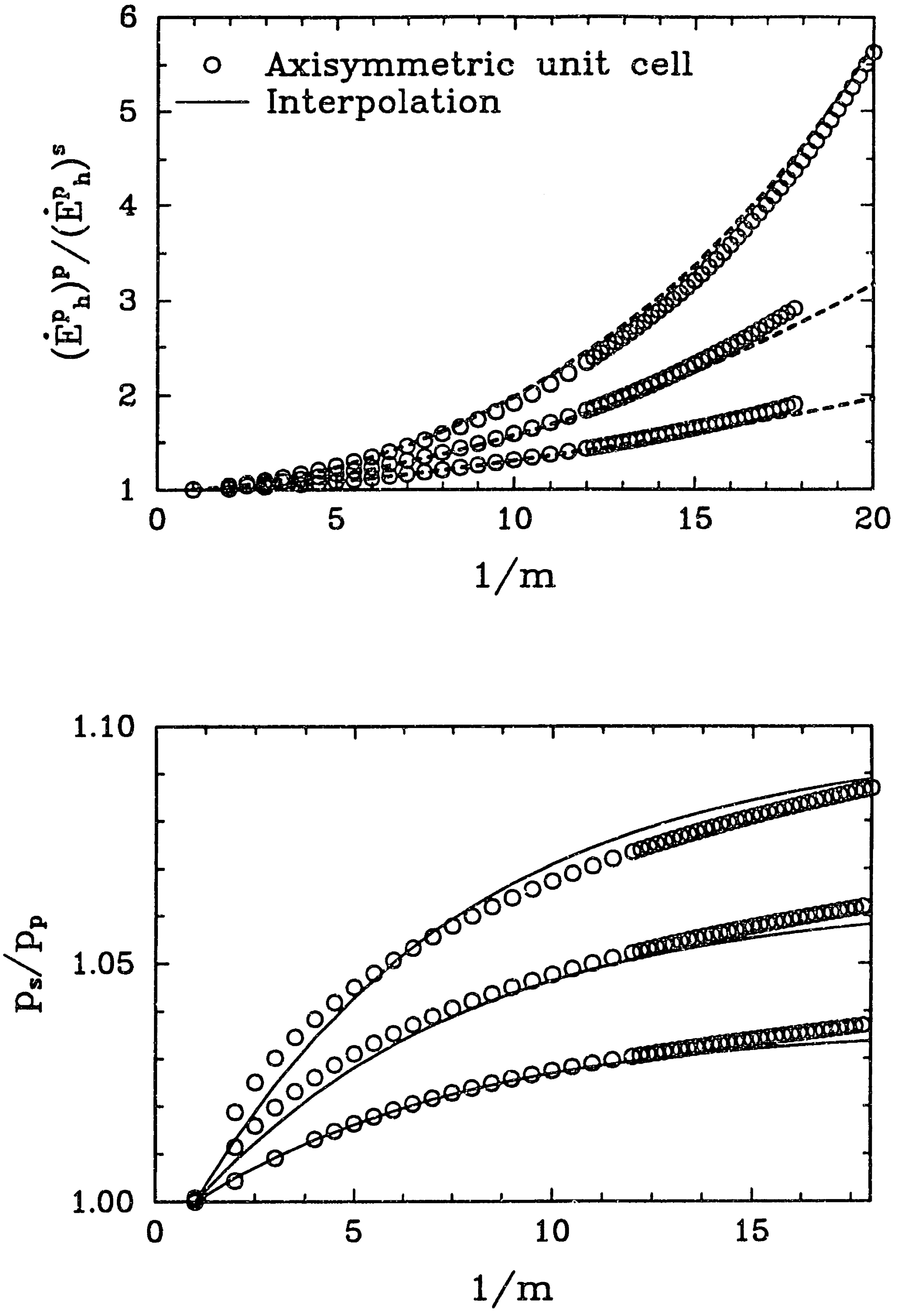

Figure A.6: (a) Prediction of the dilatation rate of the periodic cell normalized by the corresponding predictions of the spherical cell under the same pressure. (b) Same with (a) but plotted in terms of pressures needed to cause the same dilatation rate.

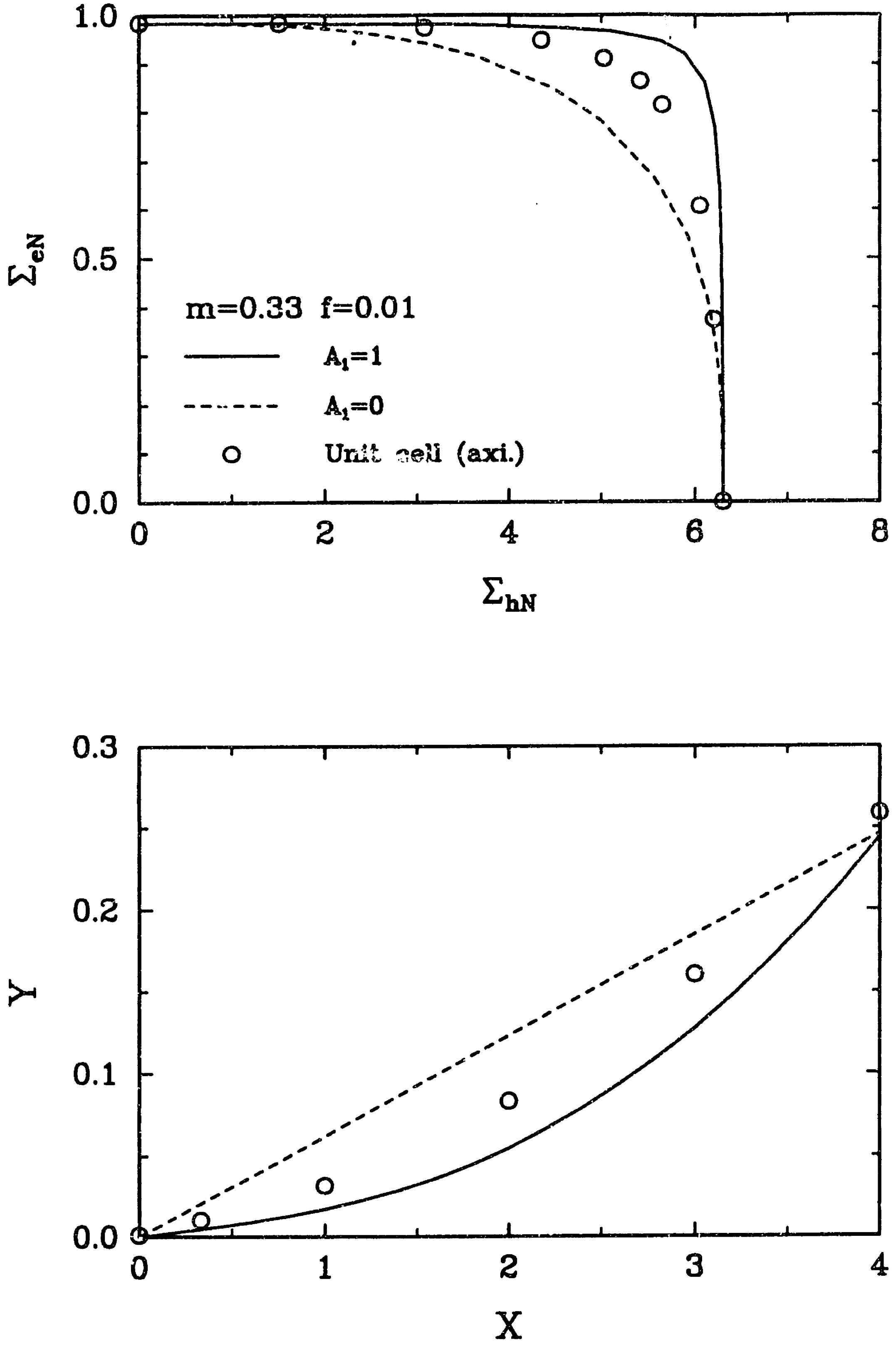

Figure A.7: Interpolations with $A_1 = 1$ and $A_1 = 0$ compared with the results of the periodic array of voids for $f = 0.01$ and $m = 0.33$

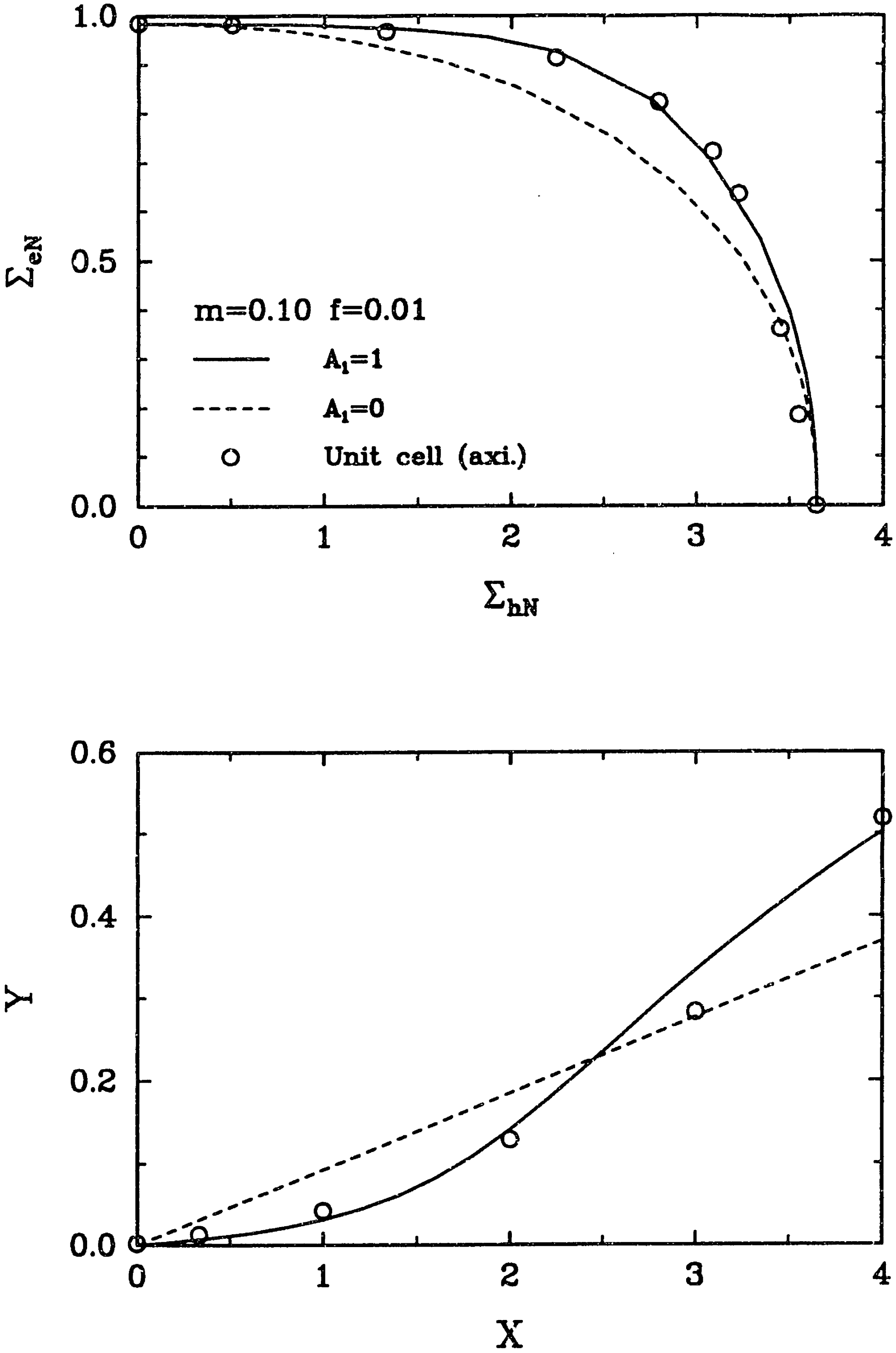

Figure A.8: Interpolations with $A_1 = 1$ and $A_1 = 0$ compared with the results of the periodic array of voids for $f = 0.01$ and $m = 0.1$

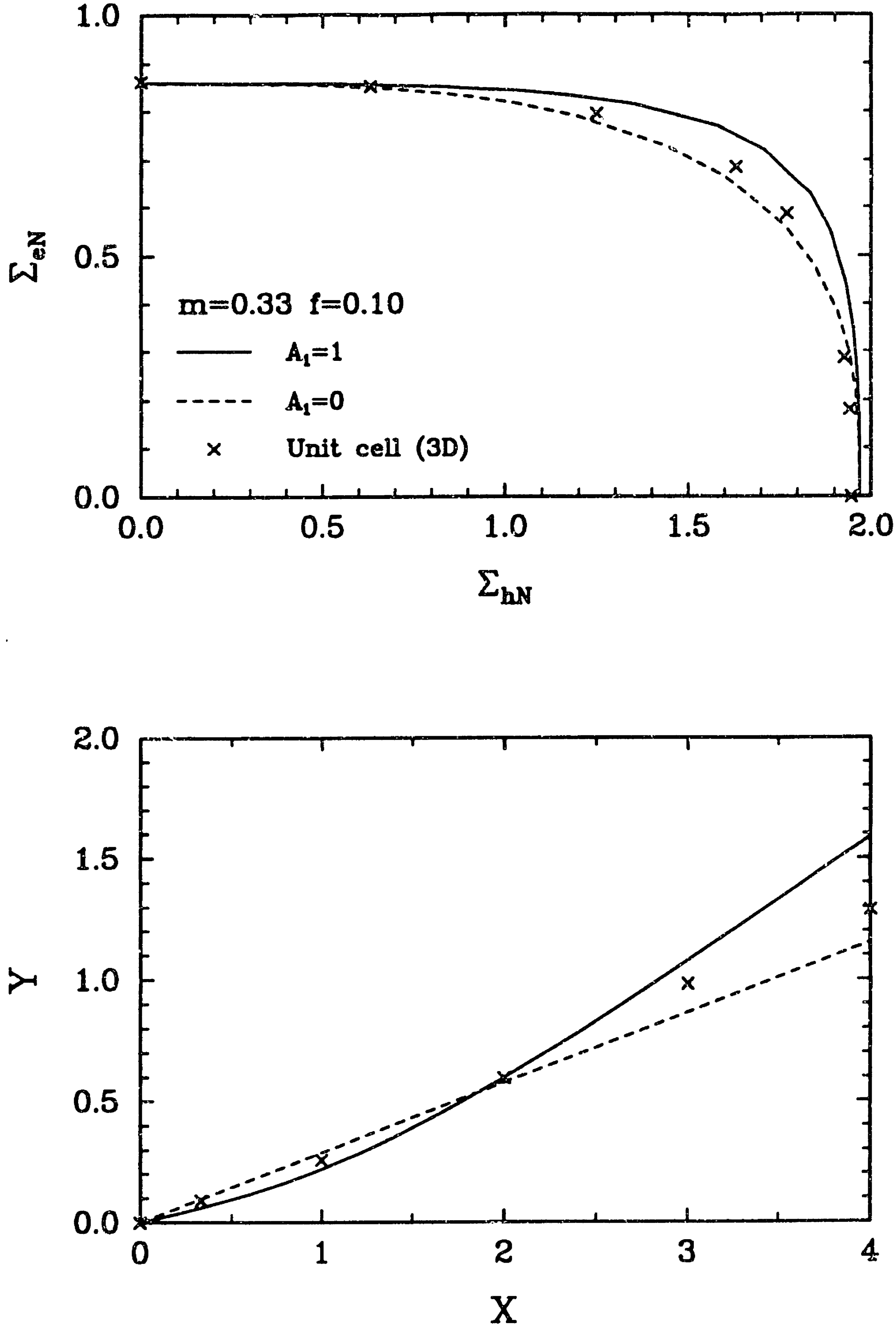

Figure A.9: Interpolations with $A_1 = 1$ and $A_1 = 0$ compared with the results of the periodic array of voids for $f = 0.1$ and $m = 0.33$

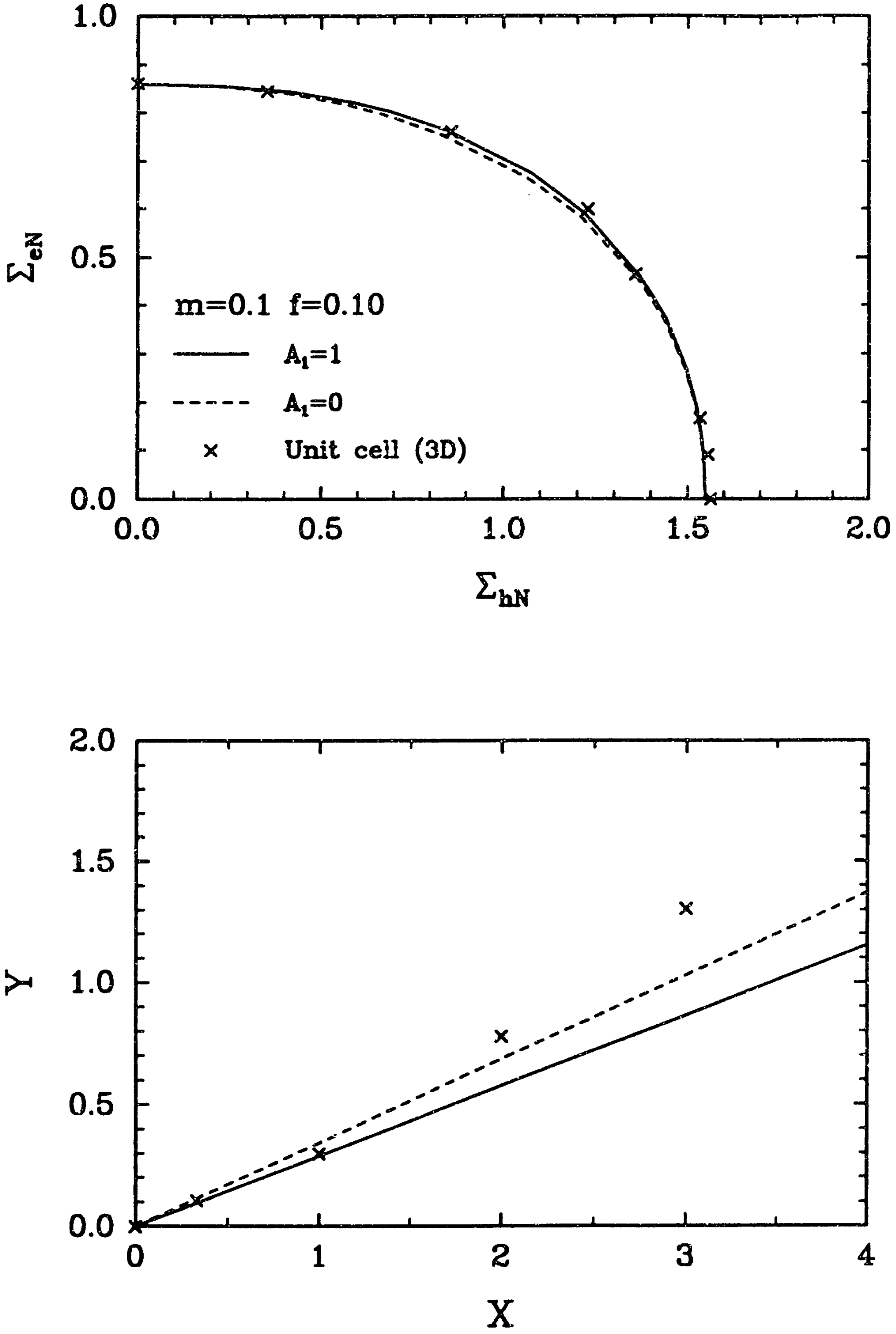

Figure A.10: Interpolations with $A_1 = 1$ and $A_1 = 0$ compared with the results of the periodic array of voids for $f = 0.1$ and $m = 0.1$.

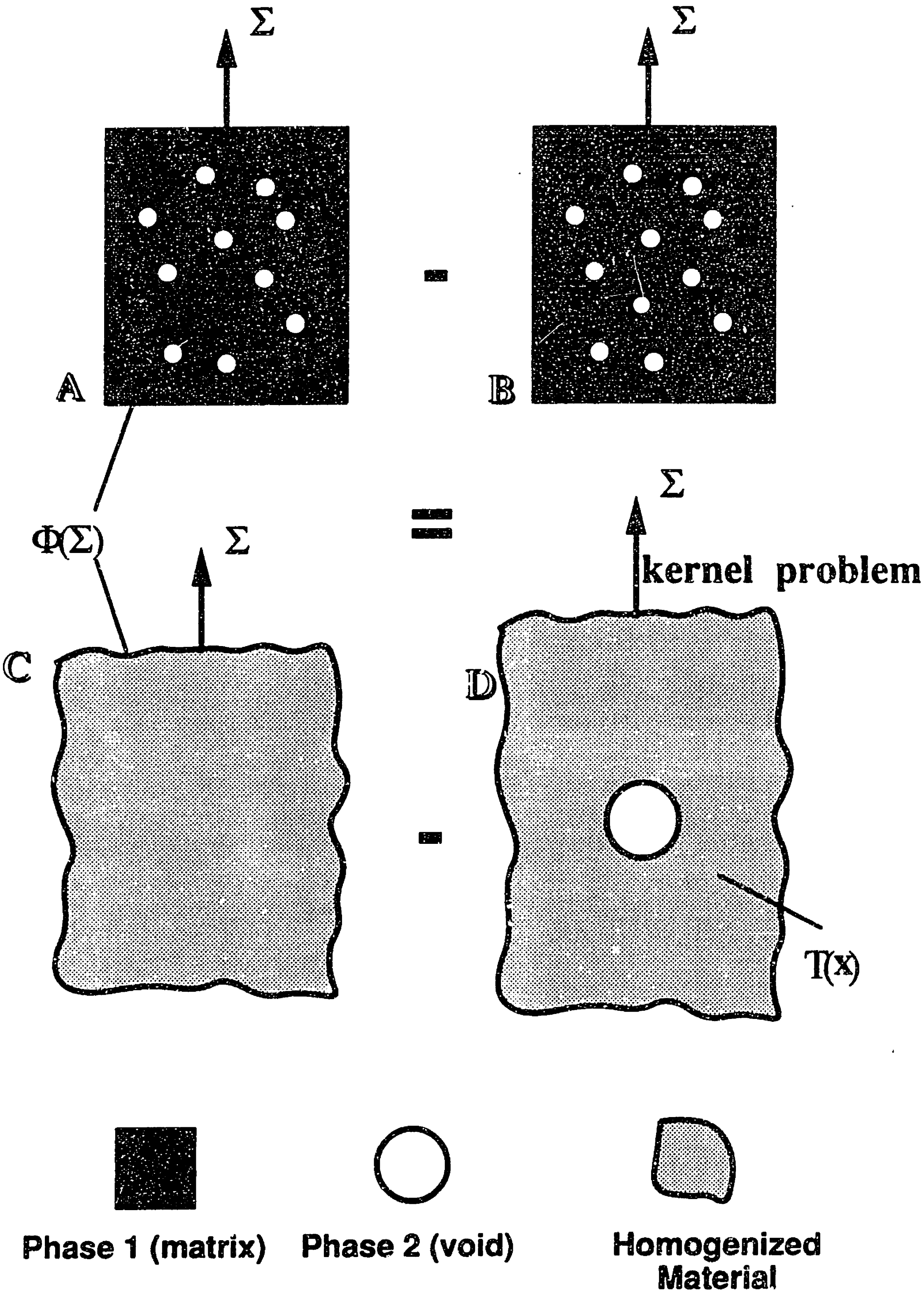

Figure A.11: The Differential Self Consistent Scheme.

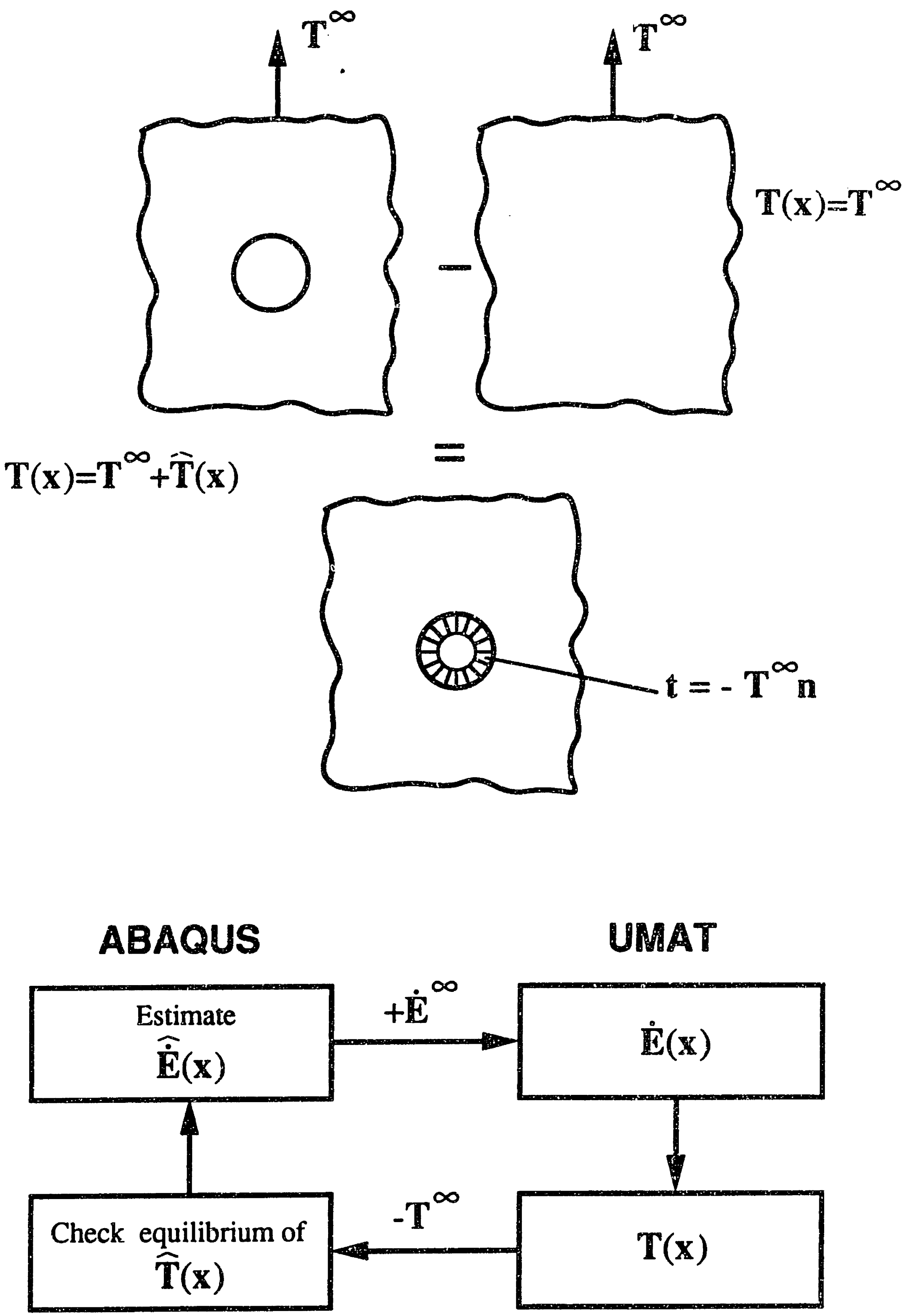

Figure A.12: The perturbation field method.

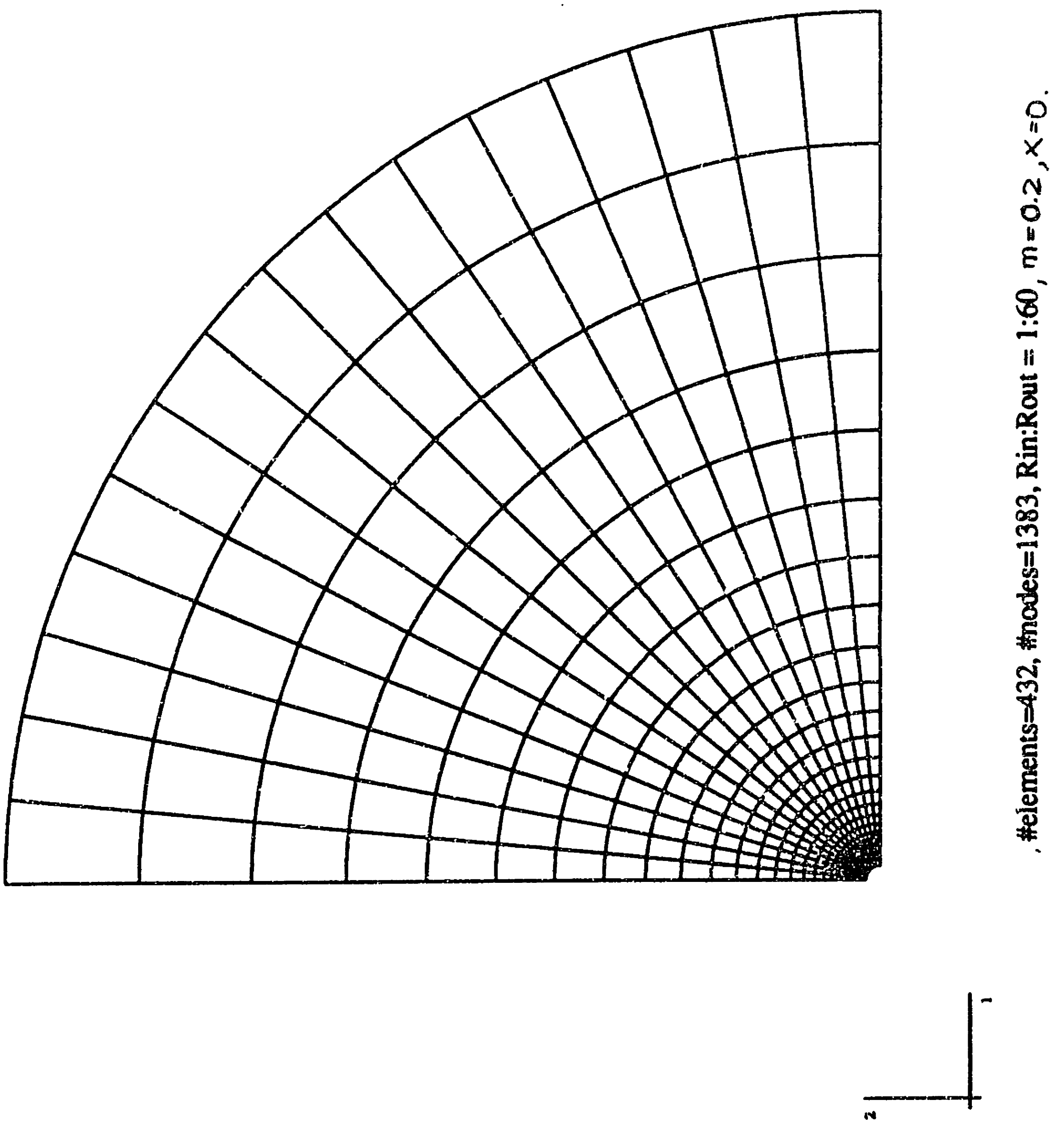

Figure A.13: Finite element mesh for the solution of the kernel problem.

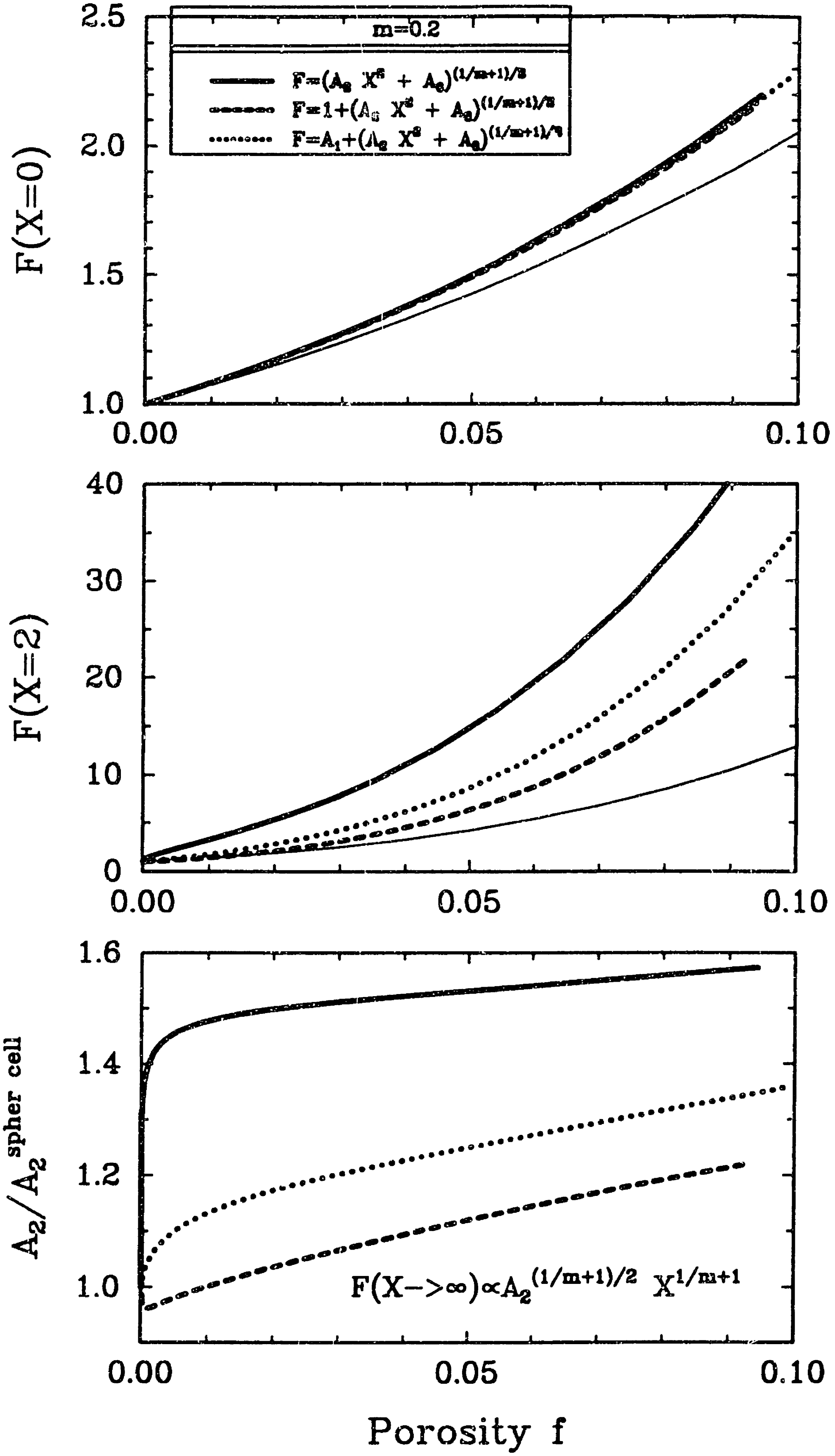

Figure A.14: Effect of the selection of the functional form of F on the results of the DSCM.

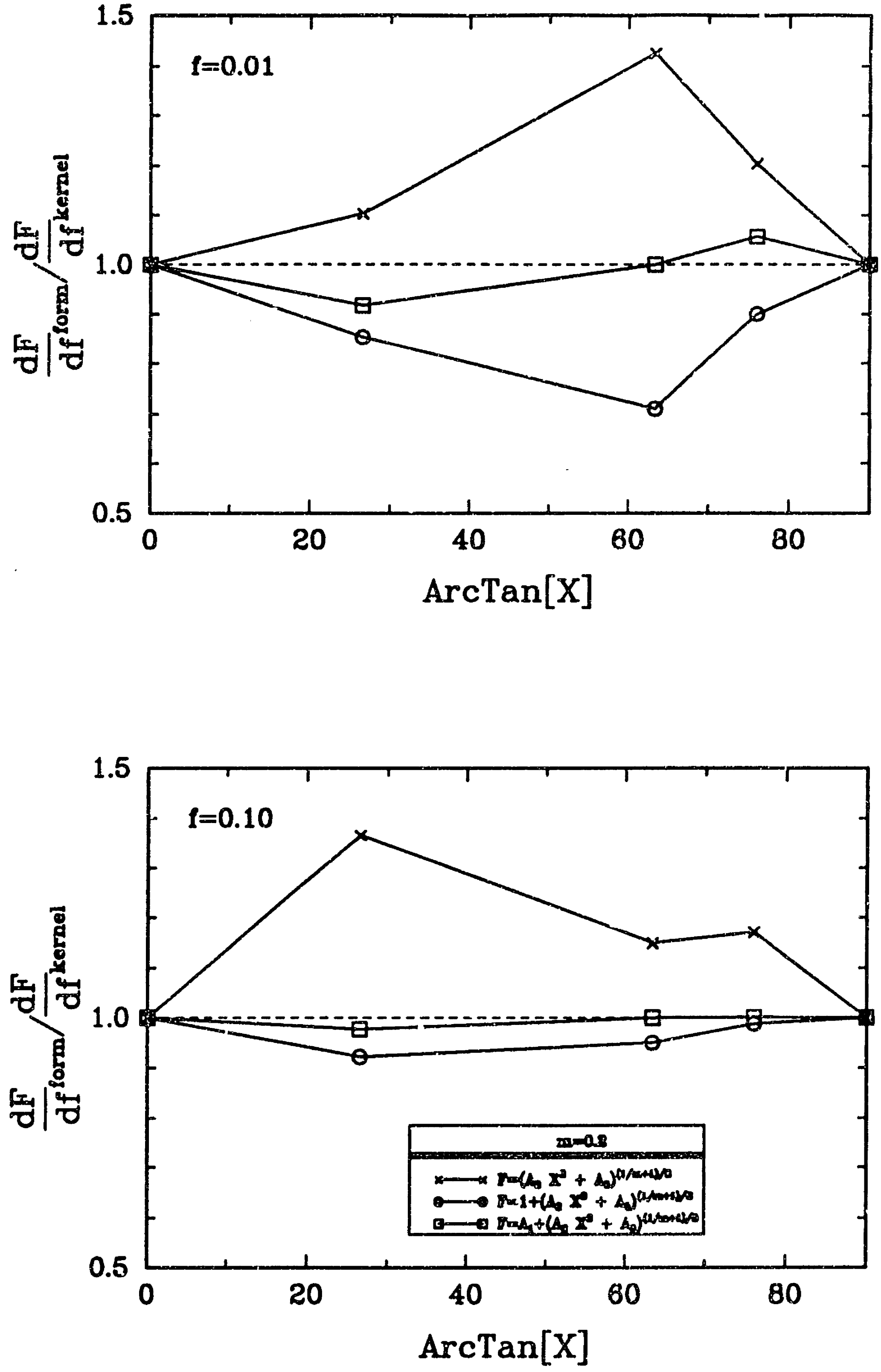

Figure A.15: Error associated with the selection of $F(X, f, m)$.

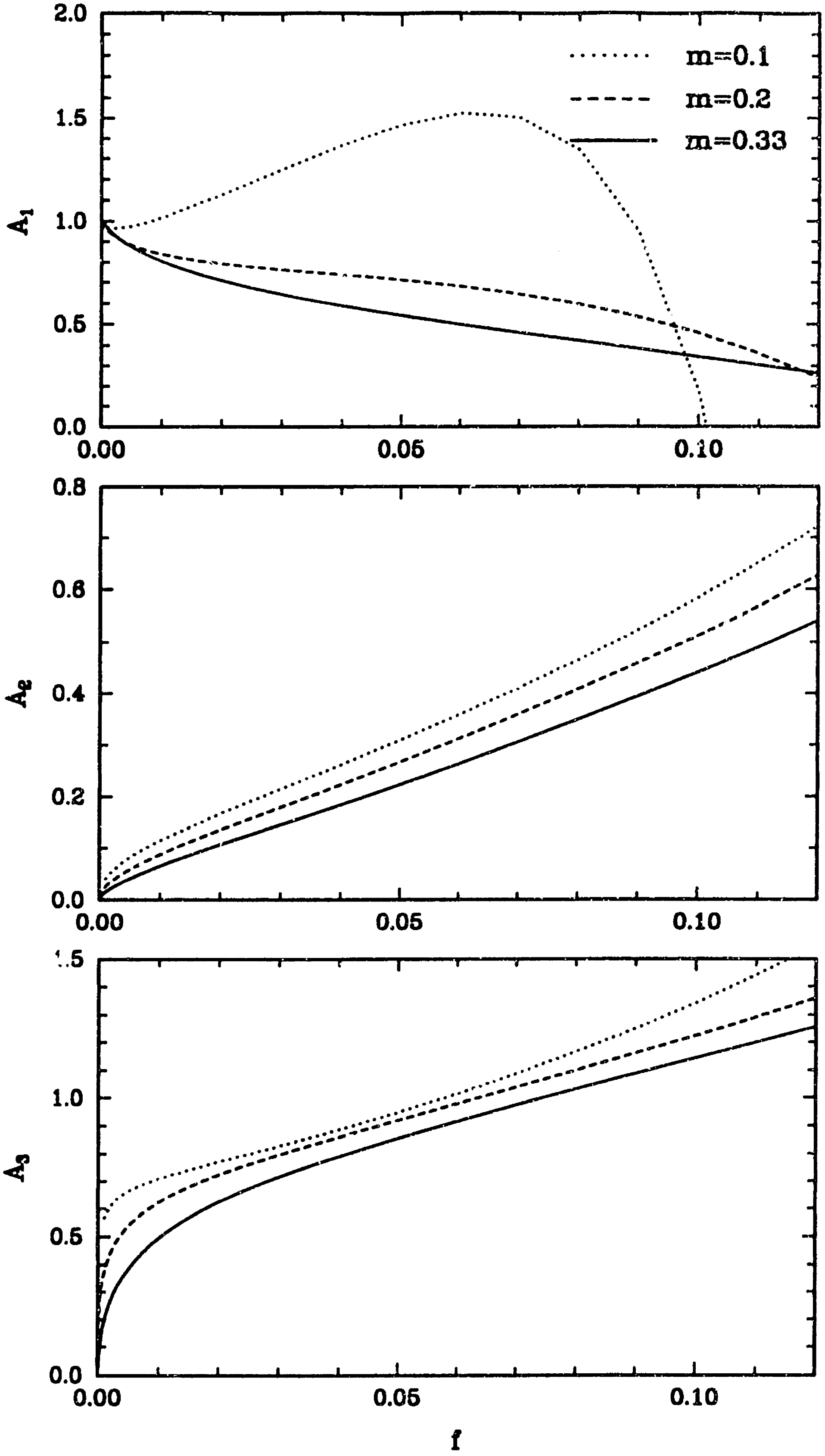

Figure A.16: Variation of A_i's with porosity for $m = 0.1, 0.2, 0.33$.

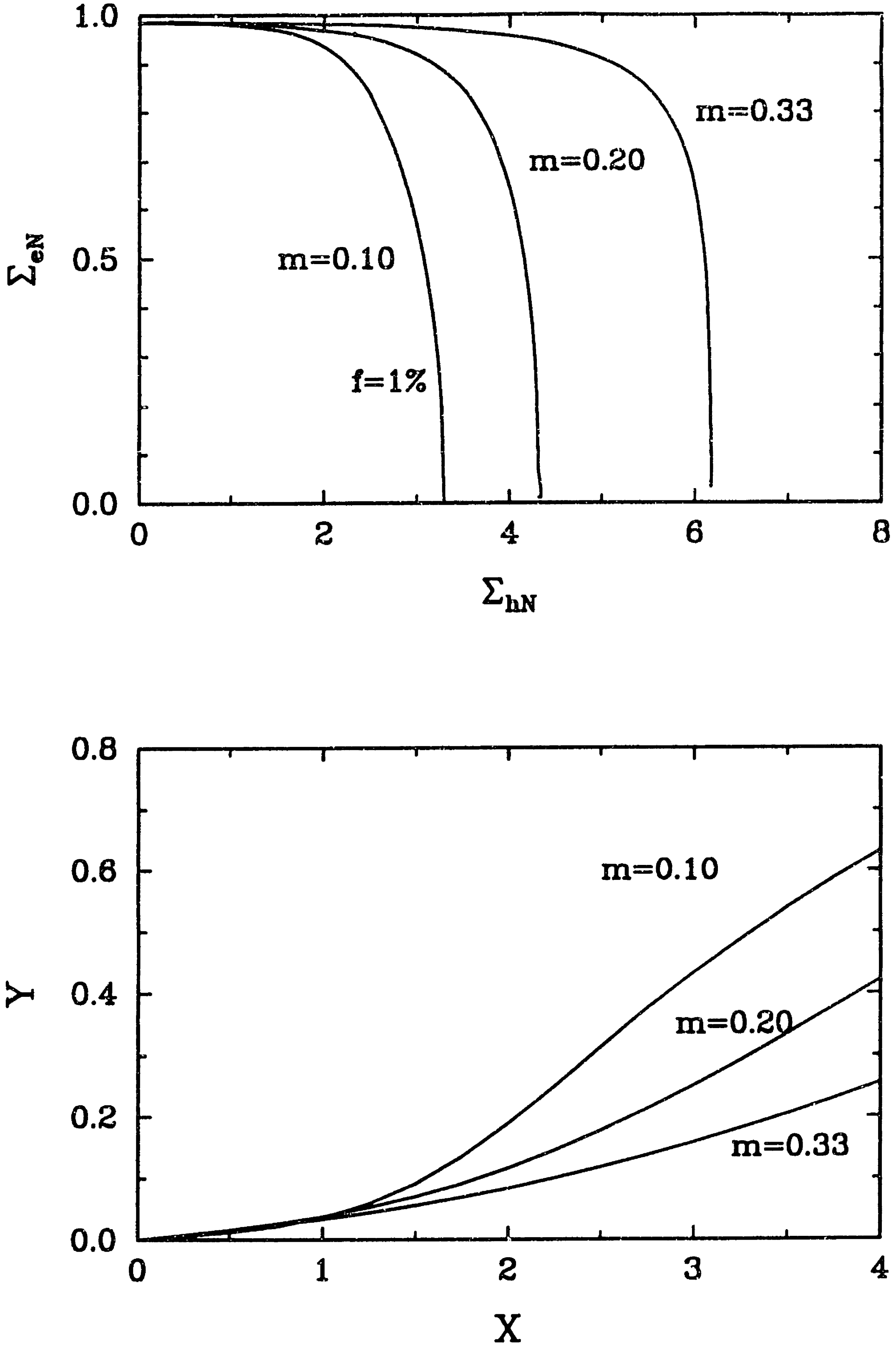

Figure A.17: Predictions of the DSCM, for $f = 0.01$

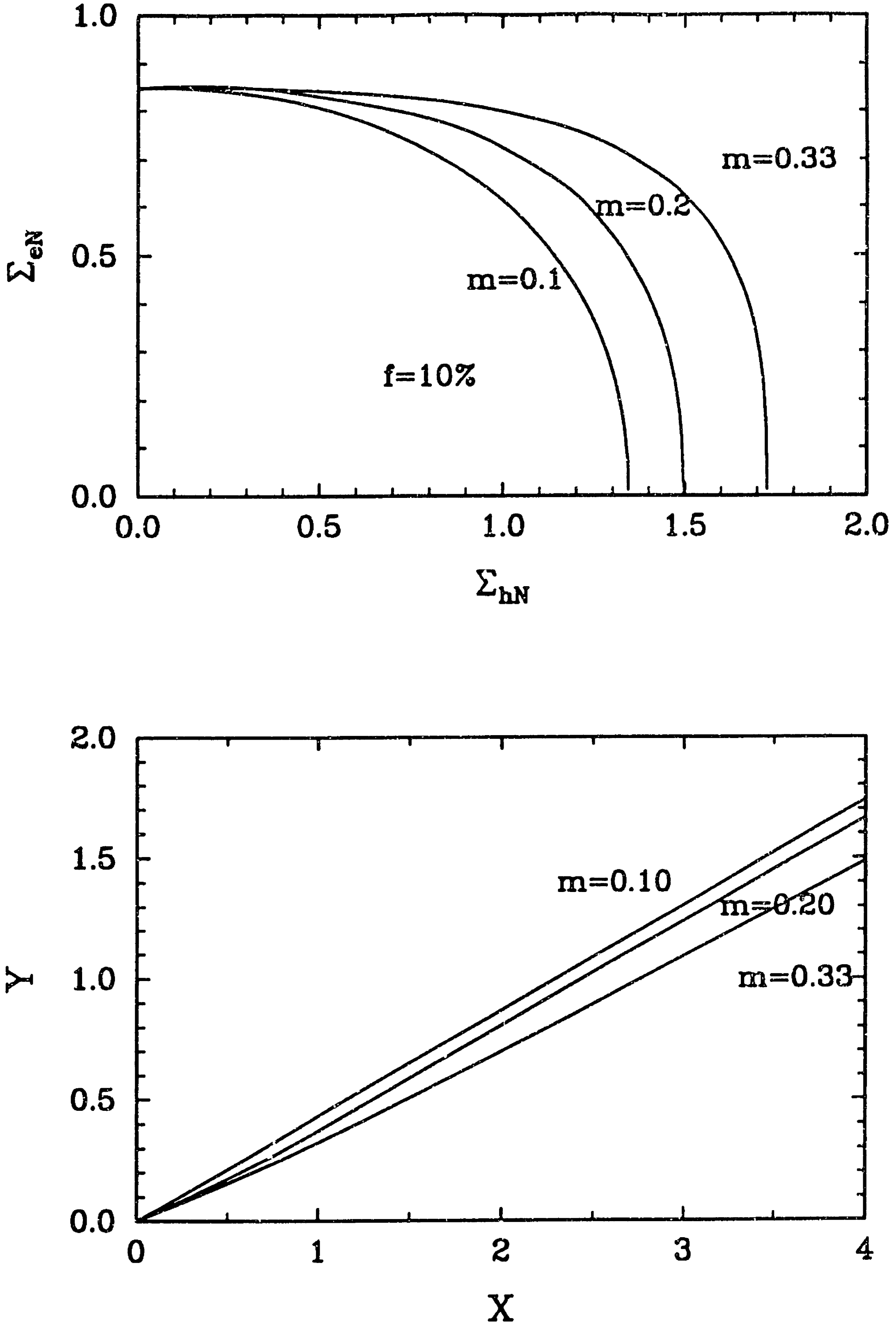

Figure A.18: Predictions of the DSCM, for $f = 0.10$

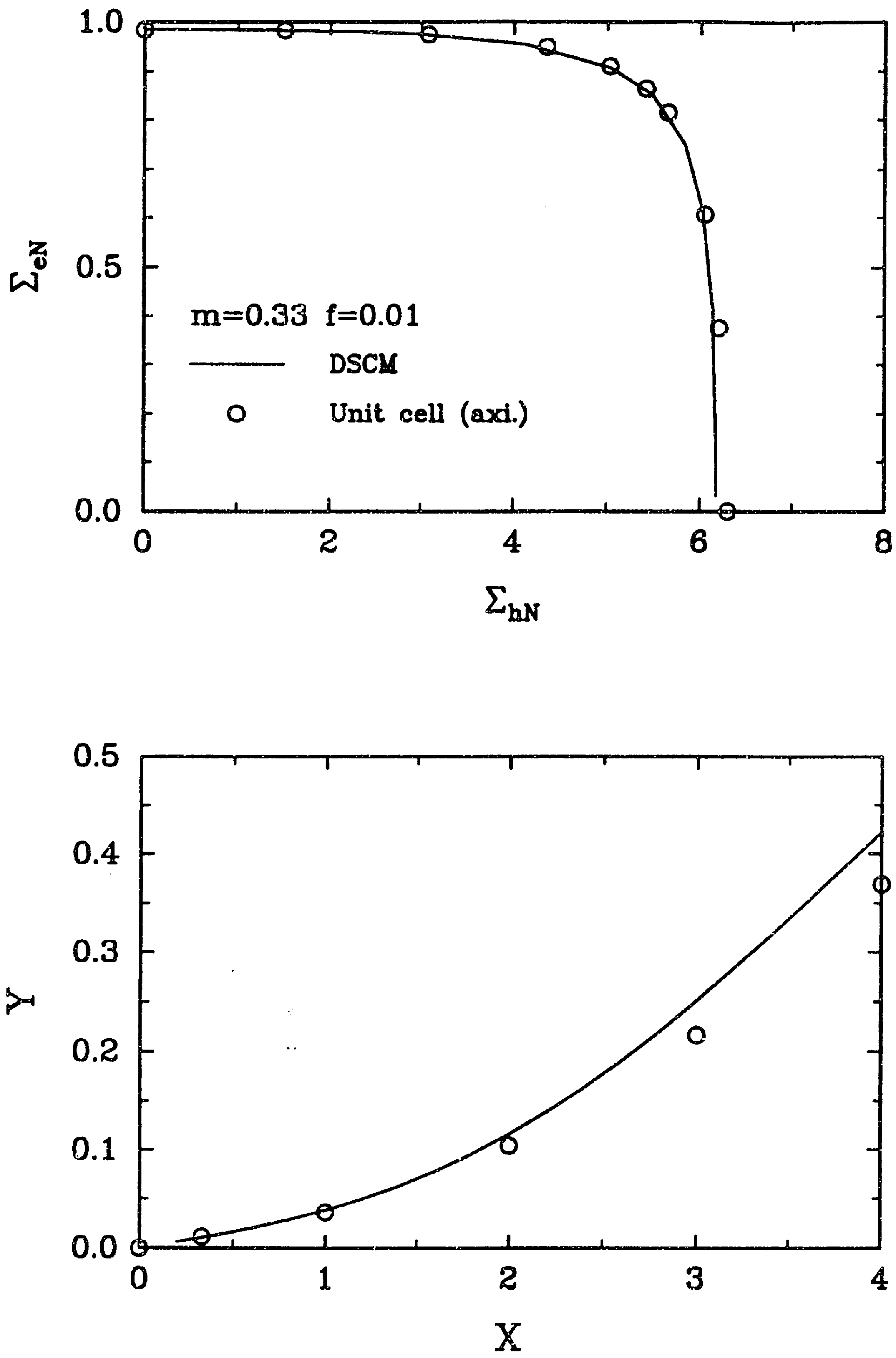

Figure A.19: Comparison of the predictions of the periodic array of voids against those of the DSCM, for $f = 0.01$, and $m = 0.33$

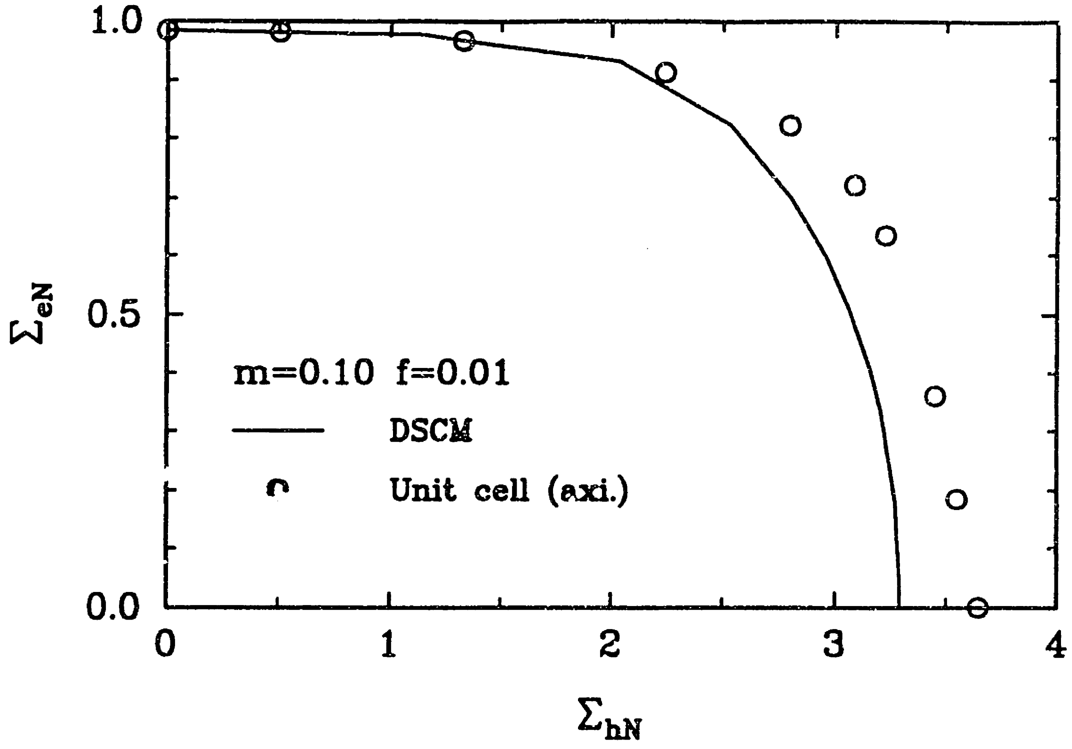

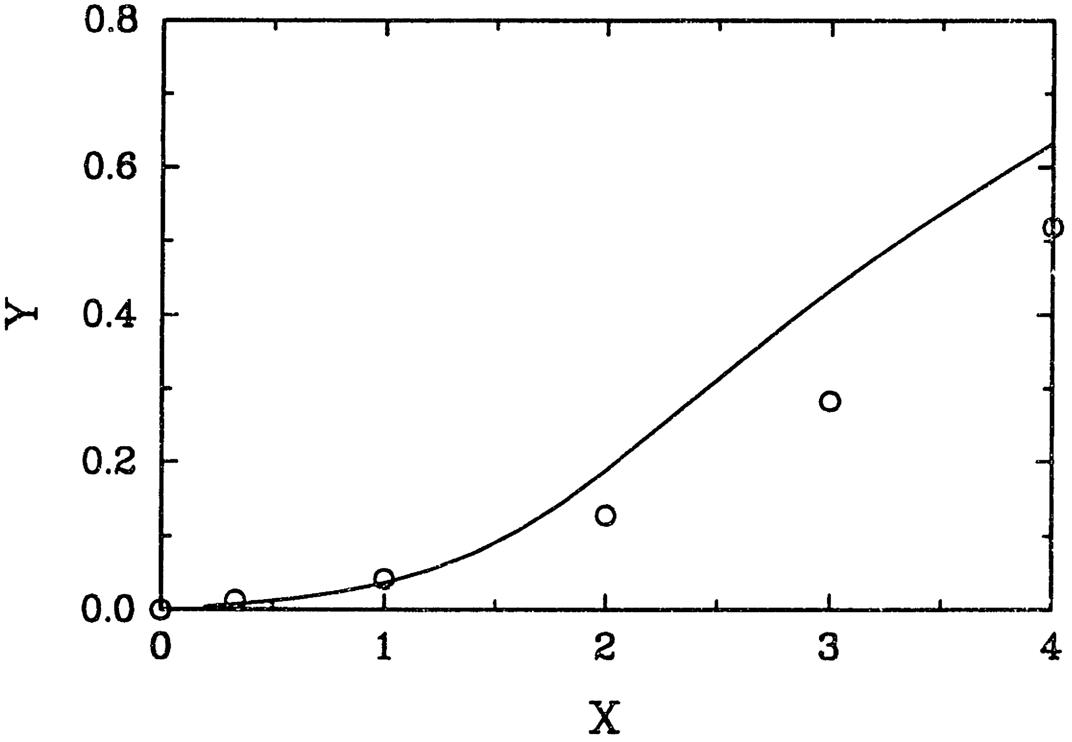

Figure A.20: Comparison of the predictions of the periodic array of voids against those of the DSCM, for $f = 0.01$, and $m = 0.1$

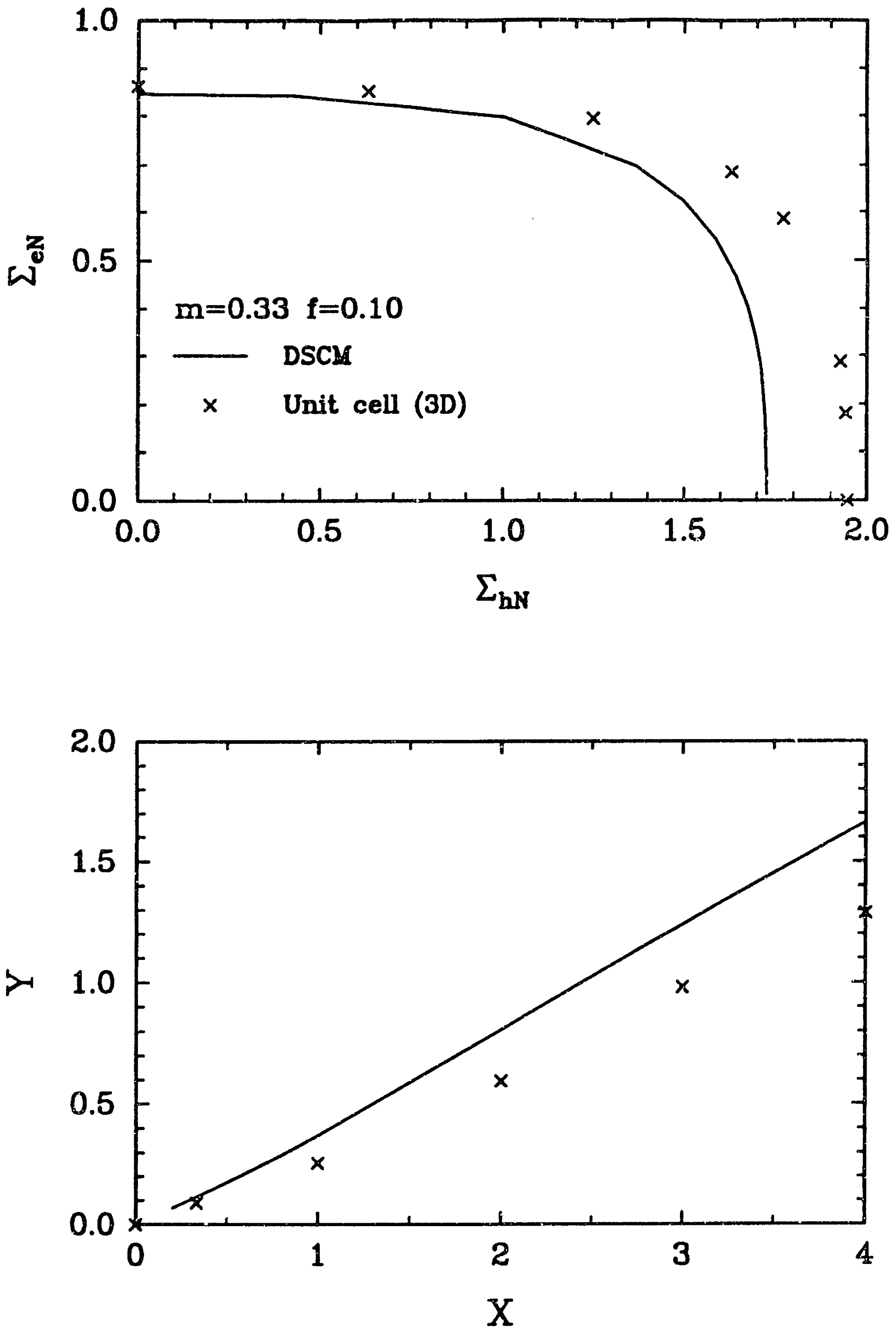

Figure A.21: Comparison of the predictions of the periodic array of voids against those of the DSCM, for $f = 0.10$, and $m = 0.33$

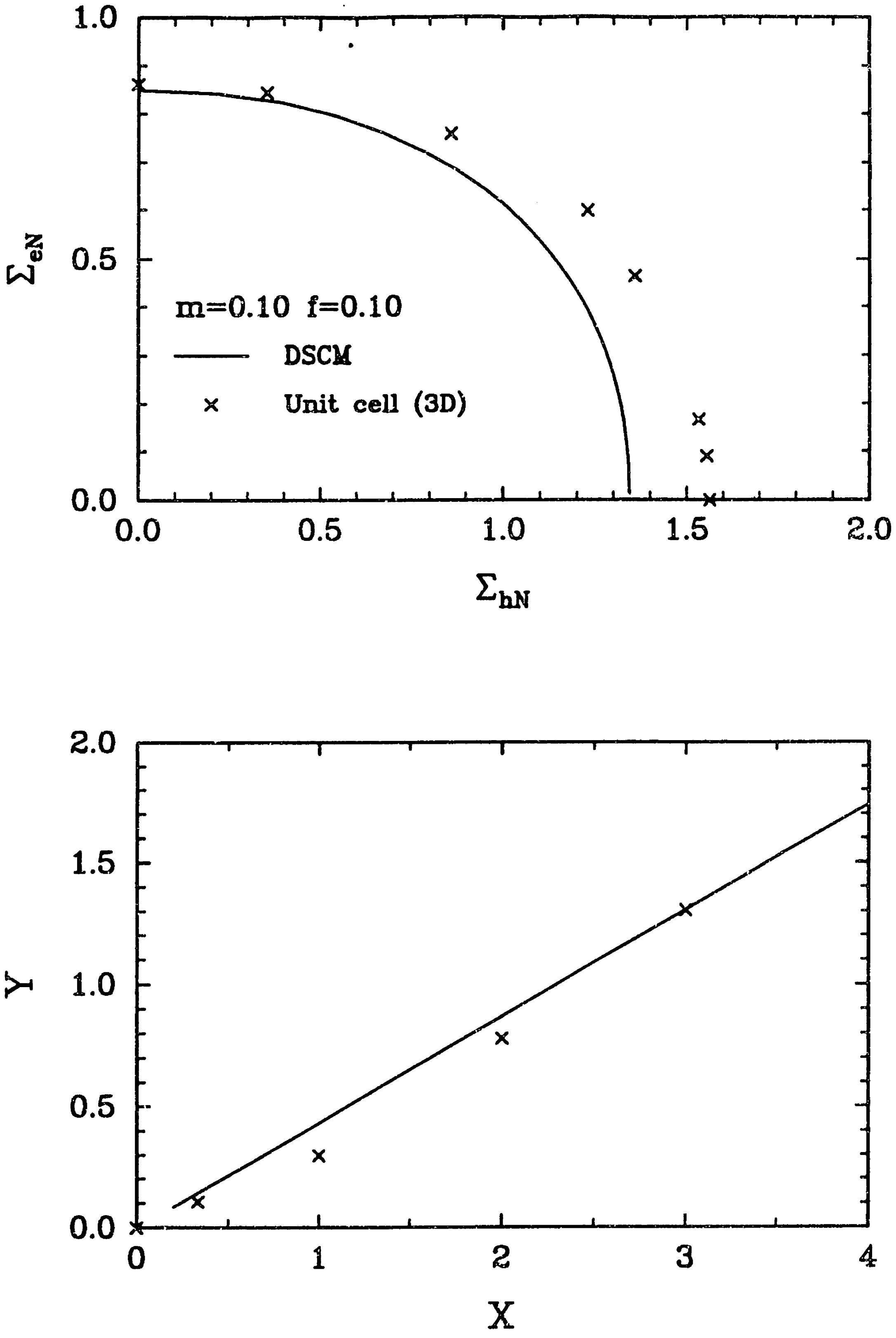

Figure A.22: Comparison of the predictions of the periodic array of voids against those of the DSCM, for $f = 0.10$, and $m = 0.1$

Appendix C

Shape Effects

The use of one scalar variable for the description of the porosity may not be adequate when the shape of the voids is not spherical. The assumption of a spherical non evolving void shape is probably the strongest assumption made so far. Deviations from this idealization may become important in two cases:

1. If the initial shape is near spherical, but changes during deformation of the porous material.
2. When the initial shape is non-spherical.

This is a difficult problem because the non-spherical shape not only calls for a non-scalar measure of the porosity, i.e., at least a second order tensor, but it may also imply a macroscopic anisotropy.

In this appendix we discuss some issues associated with the shape effect, in an effort to probe the limitations of the models that use one scalar parameter to characterize the porosity. Recently Lee and Mear ([101]) examined the effect of the void shape in the macroscopic response of isotropic materials with dilute concentrations of randomly oriented ellipsoidal voids. It is well known that dilute solutions have a impracticably small range of validity due to void-to-void interactions. However, the trends in the dilute results are expected to be similar to those at higher volume fractions of voids. The results of Lee and Mear indicate that the effect of the shape on the stress response is small but increasing with increasing aspect ratio of the voids, while the effect on the rate of growth of voids is more significant. Here we employ the periodic array of voids to demonstrate the effect of the void shape at non-dilute concentrations of voids.

C.1 Initially spherical voids

In order to isolate the effect of the evolving shape of an initially spherical void we compare predictions based on the following two descriptions of a porous material:

1. Finite element simulation of an axisymmetric unit cell loaded by an axisymmetric macroscopic stress field of *constant triaxiality*, deformed to large strains. During the deformation the shape of the initially spherical void changes to a spheroid.

2. Using the results of the incipient strain rate response of the periodic arrays of voids (see Appendix B.1) to a constant triaxiality loading, one can construct a model describing:

   $$\dot{E}_e = F_1(f)\left(\frac{\Sigma_e}{s_0}\right)^{1/m} ,$$

   and

   $$\dot{E}_h = F_2(f)\left(\frac{\Sigma_e}{s_0}\right)^{1/m} .$$

   F_1 and F_2 would correspond to $F - XF'/(1/m+1)$ and $F'/(1/m+1)$ respectively in a potential of the form (2.37) and are obtained by numerically interpolating the results of Appendix B.1. Using the above prescription we obtain the response of a periodic unit cell with a void that remains spherical. We shall refer to this calculation as unit cell calculation without shape evolution. We use this method instead of the macroscopic model developed in chapter 2 because that model does not predict accurately the periodic unit cell behavior at the intermediate triaxialities (see Appendix B.1).

Results obtained by these two methods are plotted in Fig. A.24 for two tensile triaxialities $X = 1/3$ and $X = 2$ for a non-hardening power law porous material with $m = 0.2$. In the case of simple tension the effect of the change of void shape is small, and is due to the overprediction of the void growth when the shape evolution is ignored. At the higher triaxiality $X = 2$, the effect of the changing void shape is also small. The deviation at the end is probably due to a localization of the plastic flow in the ligaments between the pores, similar to that observed by Budiansky et al. ([46]) and Koplik and Needleman ([76]). With a compressive macroscopic stress at $X = -1/3$, the full unit cell calculation predicts quick densification (see Fig. A.25, which is achieved by the approach of the opposite sides of the voids along the compression axis. This leads to *void closure* at a strain of ≈ -0.60 (which is in agreement with experimental findings), while if the evolution of the shape is not taken into account void closure is predicted at unreallistically large strains. The dramatic increase in the stress response in the full unit cell calculation is due to the folding and contact of the root of the void. At triaxiality $X = -2$, it is shown that under compressive macroscopic stress an originally spherical void will remain almost spherical.

C.2 Initially non spherical voids

Again, using the method of periodic arrays of voids we try to explore the magnitude of the effect of the initially non spherical void shape. Fig. A.26 shows the evolution of the shape of voids of the same initial porosity but different initial shapes during a uniaxial compression simulation. The first of the three cases represents a conical void similar to those observed in compacts of spherical powder with little sintering. The sides of this void roll on each other as the void closes and the densification rate initially is faster than that of a spherical void. However, it takes more strain to close completely this kind of voids than round voids. Fig. A.27 shows the evolution of the volume fraction of the voids versus strain. Large variation of the densification rates is observed. The conical void starts to densify faster than the others, while the initially spherical void closes first when the top and bottom of the void come into contact. Underprediction of the densification rate is observed when the evolution of the void shape is not taken into account. The experimental results plotted in Fig. A.27 correspond to initially spherical voids in a Fe-2%Si powder compact compressed at 800^oC (see Chapter 4 for material properties). In that material the voids do not close as quickly as the unit cell predicts because of additional porosity generated by local fracture at previous particle boundaries at the root of the void where the top and bottom sides of the void fold one onto the other (see Fig 6.70(b) in Haghi's thesis [94]). Fig. A.28 shows the stress response for the different void shapes. Abrupt changes in the stress response are due to elements on the surface of the void coming into contact.

Our calculations indicate that the model presented in this chapter can be used with some confidence in problems with initially spherical voids. At small triaxialities when large deformations induces strong changes in the shape of he voids, there is an error in the prediction of the porosity evolution. If the pores are initially non-spherical, the behavior of the material depends more on the shape and orientation of the voids. The evolution of the volume fraction is very sensitive to the shape of the voids. Therefore phenomena such as the closure of voids and the coalescence of voids depend strongly on the shape of the voids.

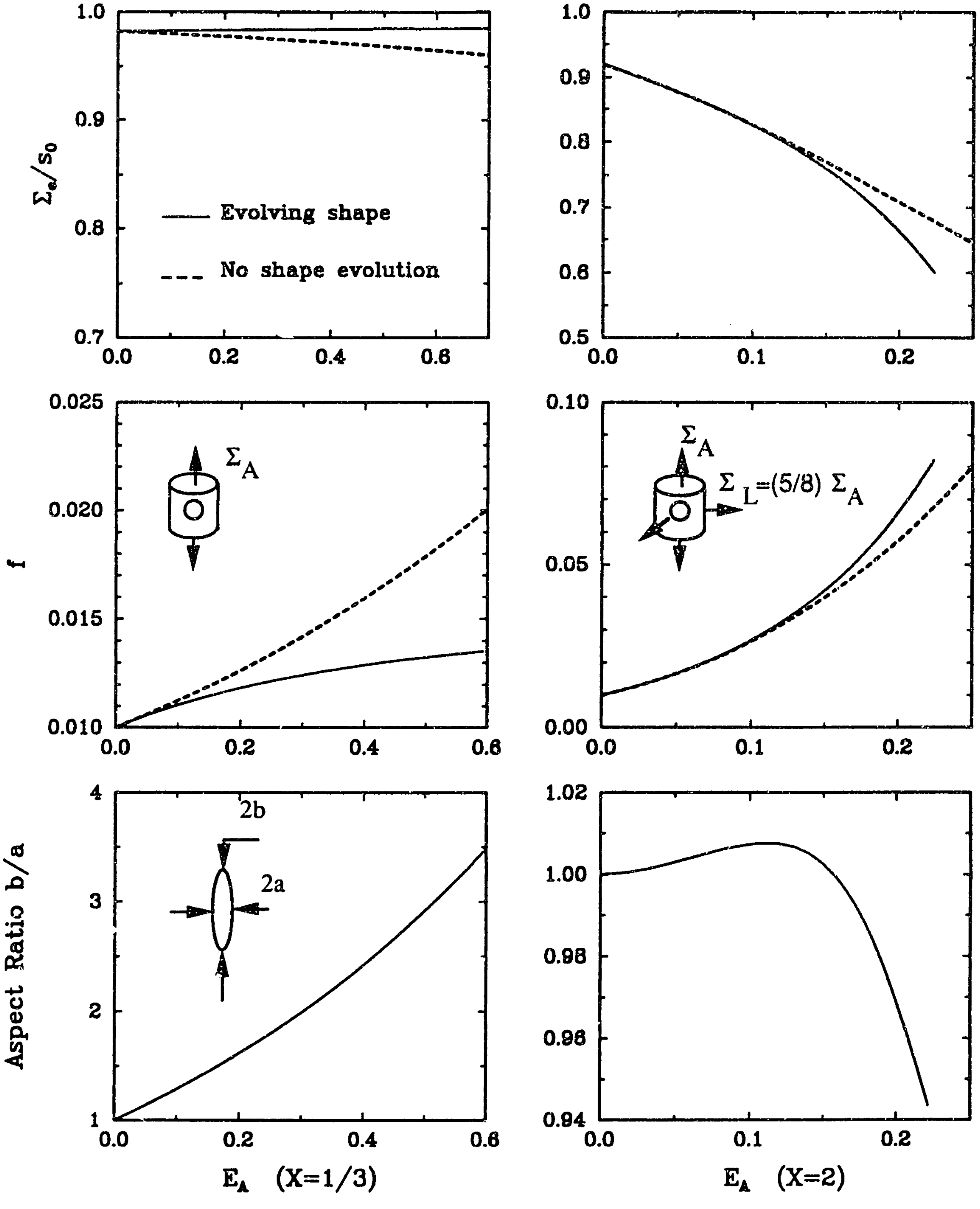

Figure A.24: Effect of the void evolution during the deformation of a porous material, subjected to tensile triaxiality loading.

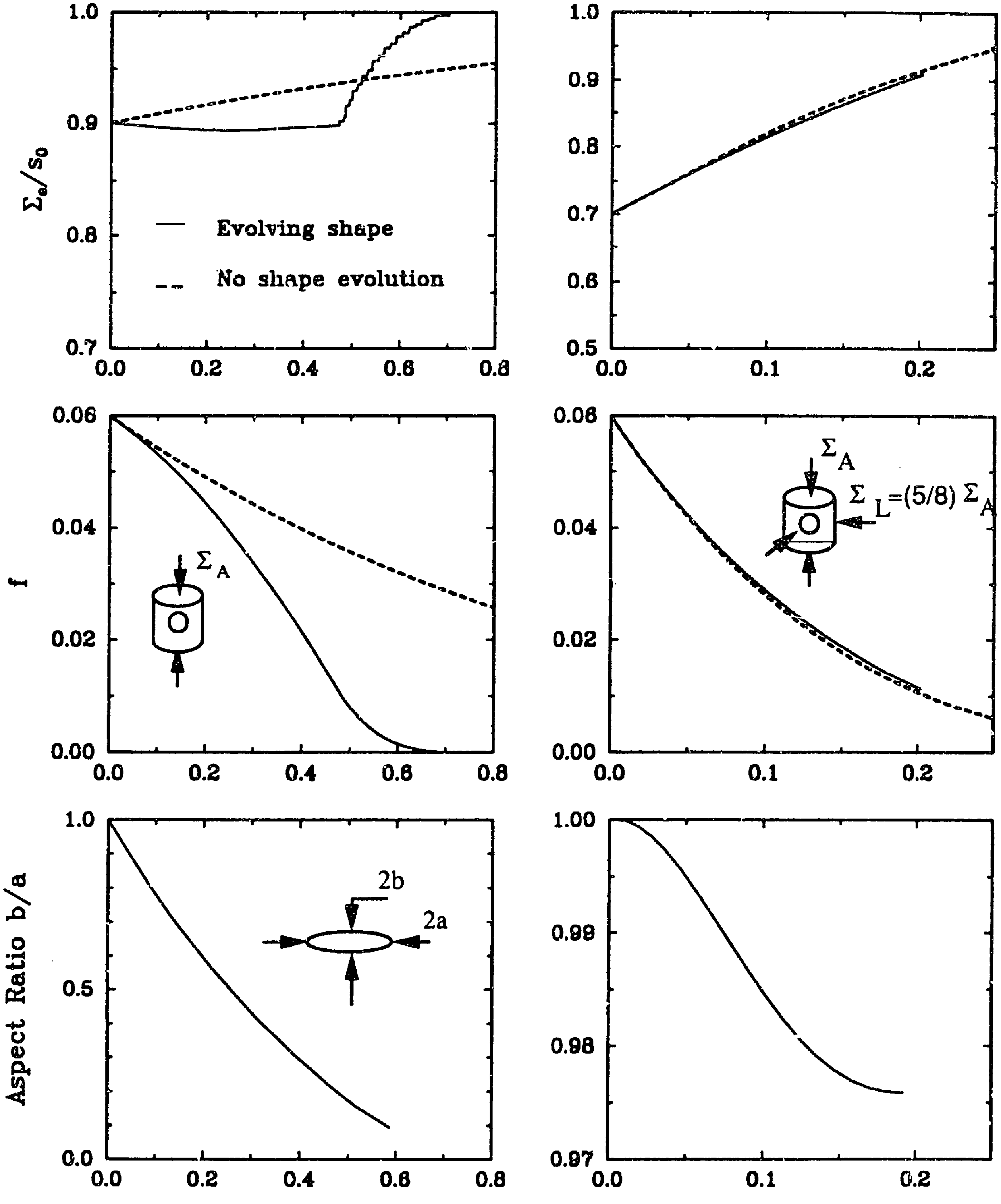

Figure A.2b: Effect of the void evolution during the deformation of a porous material, subjected to compressive triaxiality loading.

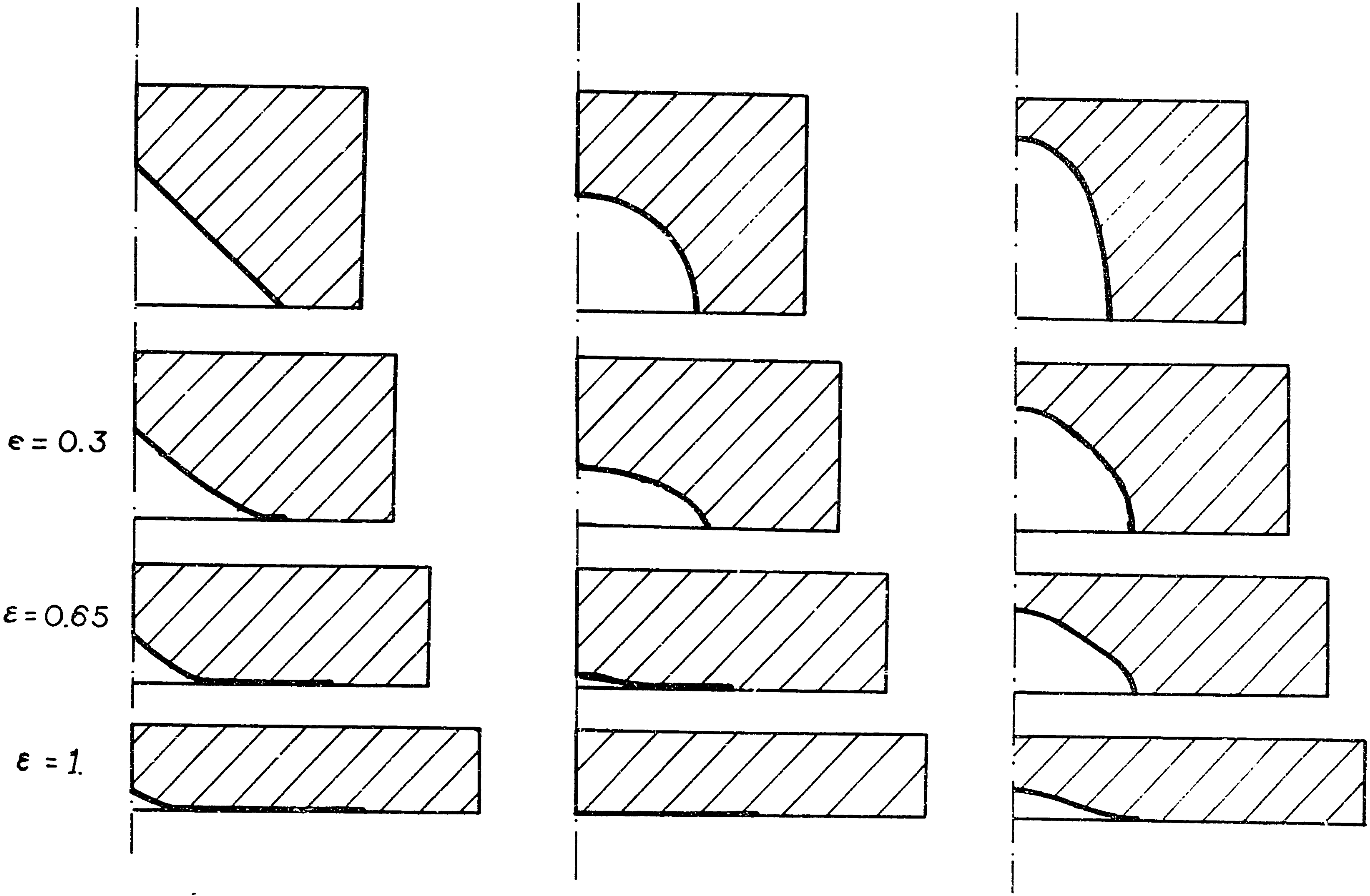

Figure A.26: Evolution of the shape of voids with different initial shapes. (finite element analysis of periodic axisymmetric unit cell).

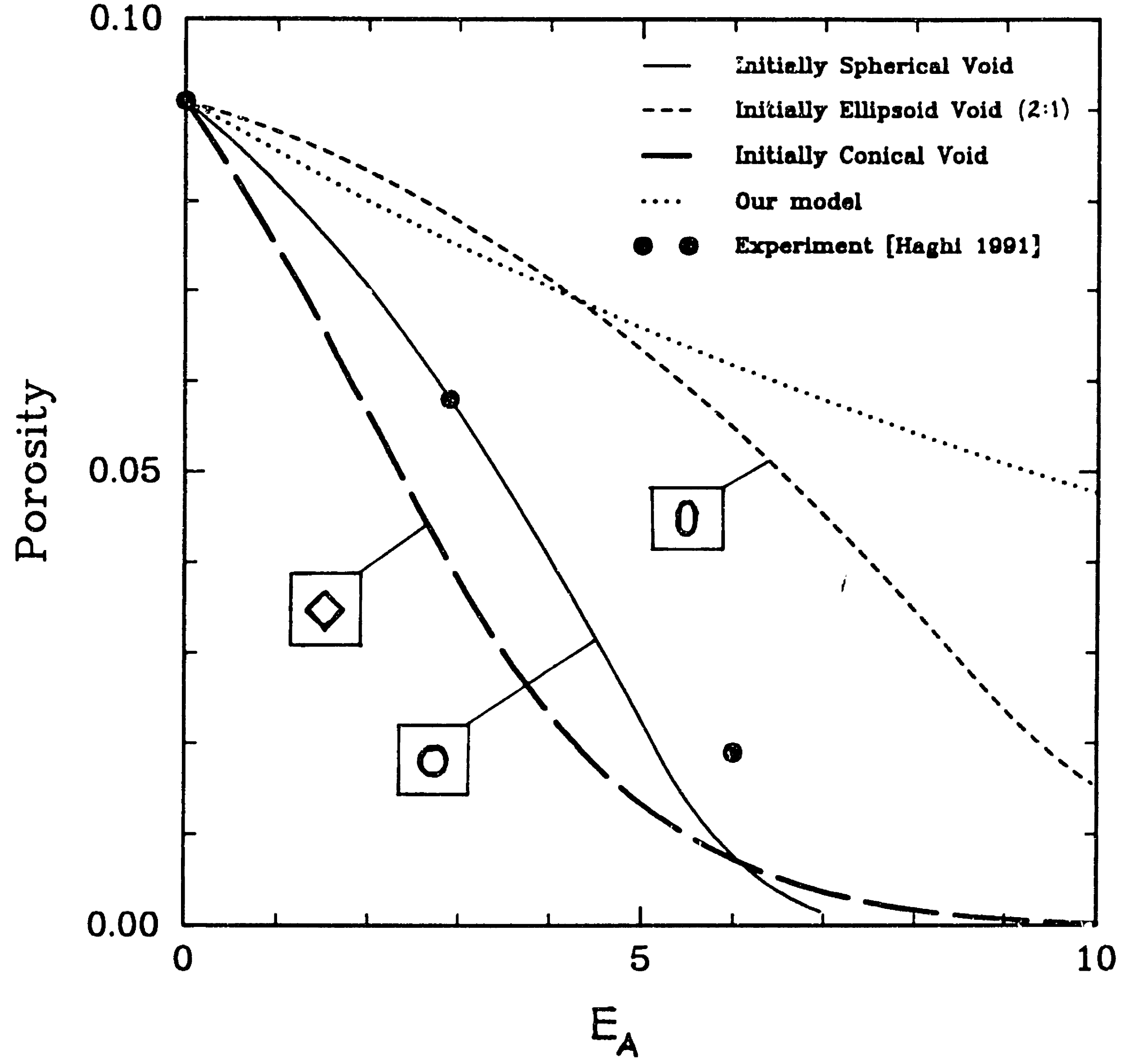

Figure A.27: Porosity evolution during compression of axisymmetric unit cells with initial voids of different geometries.

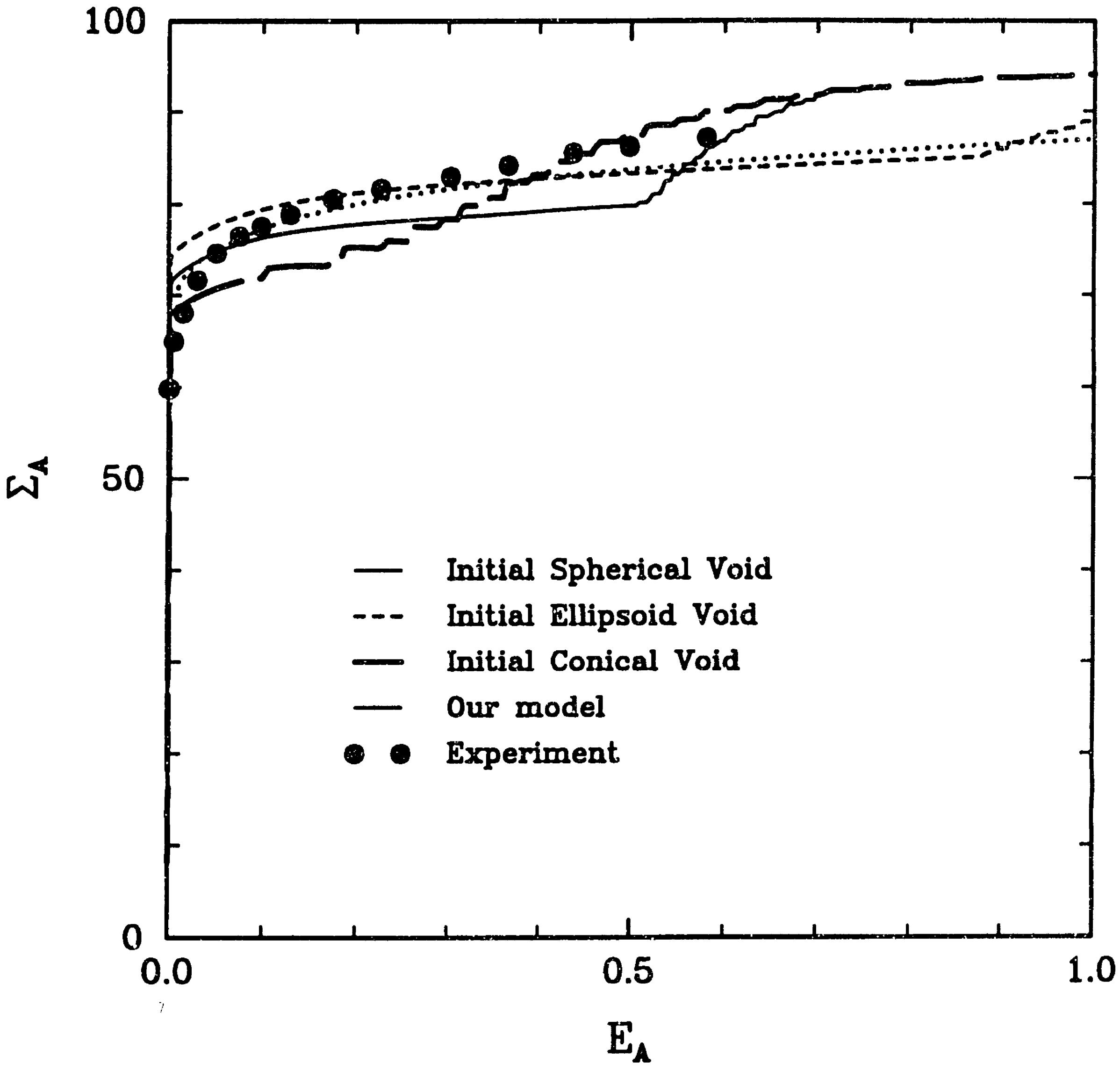

Figure A.28: Stress response of periodic axisymmetric unit cells with initial voids of different geometries, in simple compression.

Appendix D

FORTRAN code

```
C
C*****************************************************************
C
C                    ABAQUS USER MATERIAL FOR
C
C      RATE AND TEMPERATURE DEPENDENT ISOTROPIC POROUS PLASTICITY
C **
C  TO BE USED WITH ABAQUS VERSION 4.9
C **
C  THIS UMAT IS NOT FOR USE IN PLANE STRESS OR IN ANY OTHER
C  SITUATION WHEN THERE ARE MORE STRAIN TERMS THAN STRESS TERMS
C **
C  SUBROUTINES SDOT, FUNCPHI, FUNCF AND EDOTPM  ARE PARTICULAR TO THE
C  FORM OF THE POTENTIAL FUNCTION AND THE CONSTITUTIVE FUNCTIONS FOR
C  THE EQUIVALENT TENSILE PLASTIC STRAIN RATE IN THE MATRIX AND THE
C  EVOLUTION EQUATION FOR THE DEFORMATION RESISTANCE.
C*****************************************************************
C CONTENTS OF PROPS VECTOR (*USER MATERIAL, CONSTANTS = 22):
C I      PROPS(I)
C
C 1      MFLAG; MFLAG = 1.D0 --- THERMO-ELASTIC
C                   MFLAG = 2.D0 --- THERMO-ELASTIC-VISCOPLASTIC
C 2      KFLAG; KFLAG = 1.D0 --- ISOTHERMAL
C                   KFLAG = 2.D0 --- COUPLED
C 3      EYOUNG
C 4      ANU
C 5      APREEXP
C 6      QACT
C 7      RGAS
C 8      AM
C 9      S0
C 10     H0
C 11     SBAR
C 12     QHARD
C 13       AN
C 14     VFRAC0
C 15     THETA0
C 16     THETAM
C 17     CHI1
C 18     CHI2
C 19     ALPHA
C 20     RHO
C 21     SPHEAT
C 22     OMEGA
C
C          TO SIMULATE INCOMPRESSIBLE MATERIALS SET VFRAC0 = 1.D-10
C
C          TO SIMULATE NEAR RATE-INDEPENDENT BEHAVIOR SET AM = 0.01
C          OR LOWER, BUT FOR AM < 0.01 BE CAREFUL OF NUMERICAL
C          OVERFLOW/UNDERFLOW PROBLEMS ON SOME MACHINES.
C
C          TO SIMULATE NON-HARDENING BEHAVIOR SET
C          H0 = 0., SBAR = 0., QHARD = 0.,AN = 0.
C
C **
C STATE VARIABLES
C (*DEPVAR
C  11)             :
C
C       STATEV(1) = S      --  MATRIX DEFORMATION RESISTANCE
C       STATEV(2) = VFRAC  --  VOLUME FRACTION OF POROSITY
C       STATEV(3) = FP(1,1) -- PLASTIC DEFORMATION GRADIENT, (1,1) COMP.
C       STATEV(4) = FP(1,2) -- PLASTIC DEFORMATION GRADIENT, (1,2) COMP.
C       STATEV(5) = FP(1,3) -- PLASTIC DEFORMATION GRADIENT, (1,3) COMP.
```

```
C       STATEV(6) = FP(2,1) -- PLASTIC DEFORMATION GRADIENT, (2,1) COMP.
C       STATEV(7) = FP(2,2) -- PLASTIC DEFORMATION GRADIENT, (2,2) COMP.
C       STATEV(8) = FP(2,3) -- PLASTIC DEFORMATION GRADIENT, (2,3) COMP.
C       STATEV(9) = FP(3,1) -- PLASTIC DEFORMATION GRADIENT, (3,1) COMP.
C       STATEV(10)= FP(3,2) -- PLASTIC DEFORMATION GRADIENT, (3,2) COMP.
C       STATEV(11)= FP(3,3) -- PLASTIC DEFORMATION GRADIENT, (3,3) COMP.
C       STATEV(12)= EFFTAU
C       STATEV(13)= SIGHTAU/SIGETAU
C       STATEV(14)= DPHIDSE
C       STATEV(15)= Strain in the matrix
C       STATEV(16)= Macroscopic Strain
C
C
C *****************************************************************

        SUBROUTINE UMAT(STRESS,STATEV,DDSDDE,SSE,SPD,SCD,RPL,DDSDDT,
     1 DRPLDE,DRPLDT,STRAN,DSTRAN,TIME,DTIME,TEMP,DTEMP,PREDEF,DPRED,
     2 CMNAME,NDI,NSHR,NTENS,NSTATV,PROPS,NPROPS,COORDS,DROT)

          IMPLICIT REAL*8(A-H,O-Z)

      CHARACTER*8 CMNAME
      DIMENSION STRESS(NTENS),STATEV(NSTATV),
     1 DDSDDE(NTENS,NTENS),
     2 DDSDDT(NTENS),DRPLDE(NTENS),
     3 STRAN(NTENS),DSTRAN(NTENS),PREDEF(1),DPRED(1),
     4 PROPS(NPROPS),COORDS(3),DROT(3,3),DROTTRANS(3,3)


        REAL*8  FT(3,3),STRESST(3,3),FPT(3,3),ST,VFRACT,THETAT,
     1        FTAU(3,3),STRESSTAU(3,3),FPTAU(3,3),STAU,VFRACTAU,
     2    THETATAU,SIGETAU,SIGHTAU,
     3    AUX(3,3),STRESSTAUD(3,3),STRESSTAUV(6),STRESSTAUDV(6),
     4    STRESSTD(3,3),STRESSTDV(6),ALPHAM(4,4),ASTAR(4,4),INDX(4),
     5    DGFDTHETA(4,1),DXDTHETA(4,1),DETTAU(3,3),FTAUP(3,3),
     6        STRESSTAUP(3,3),DETTAUV(6),STRESSTAUPV(6)

      COMMON/DEFGRAD/FT,FTAU
      COMMON/LUSH1/UMEROR,TIMELU,ITGEN
      COMMON/LUSH2/LEVEL1,LEVEL2,MAXL1,MAXL2

        COMMON/FLAG/MFLAG,KFLAG,LFLAG
        COMMON/MATPEL/EYOUNG,ANU,AMU,AKAPPA,ALAMBDA
        COMMON/MATPRD/APREEXP,QACT,RGAS,AM,S0,H0,SBAR,QHARD,AN,VFRAC0
        COMMON/MATPTP/THETA0,THETAM,ALPHA,RHO,SPHEAT,OMEGA,THETADOT
        COMMON/MATPTQ/CHI1,CHI2

C
C       MFLAG                      -- FLAG FOR MATERIAL MODEL:
C                                     MFLAG = 1 -- THERMO-ELASTIC
C                                     MFLAG = 2 -- THERMO-ELASTIC-VISCOPLASTIC
C       KFLAG                      -- FLAG FOR ISOTHERMAL OR COUPLED CALCULATION
C                                     KFLAG = 1 -- ISOTHERMAL
C                                     KFLAG = 2 -- COUPLED
C       T                          -- CURRENT TIME
C       TAU                        -- NEXT TIME
C       DT                         -- (TAU - T) -- TIME INCREMENT
C       FT(3,3)         -- DEF. GRADIENT AT TIME T
C       FPT(3,3)                   -- PLASTIC DEF. GRAD. AT TIME T
C       STRESST(3,3)    -- CAUCHY STRESS  AT TIME T
C       S0                         -- DEF. RESISTANCE AT TIME 0
C       ST                         -- DEF. RESISTANCE AT TIME T
C       VFRAC0          -- VALUE OF POROSITY AT TIME 0
C       VFRACT          -- VALUE OF POROSITY AT TIME T
```

```
C       THETA0           -- REF. VALUE OF TEMPERATURE AT TIME 0
C       THETAM           -- VALUE OF MELTING TEMPERATURE
C       CHI1,CHI2                -- FACTORS IN TEMP. DEPENDENCE OF
C                                   ELASTIC MODULI
C       THETAT           -- VALUE OF TEMPERATURE AT TIME T
C       FTAU(3,3)                -- DEF. GRADIENT AT TIME TAU
C       FPTAU(3,3)               -- PLASTIC DEF. GRAD AT TIME T
C       STRESSTAU(3,3)   -- CAUCHY STRESS DEVIATOR AT TIME TAU
C       STAU                     -- DEF. RESISTANCE AT TIME TAU
C       VFRACTAU                 -- VALUE OF POROSITY AT TIME TAU
C       THETATAU                 -- VALUE OF TEMPERATURE AT TIME TAU
C
C       AMUMO                    -- SHEAR MODULUS OF MATRIX AT REF. TEMP
C       AKAPPAMO                 -- BULK  MODULUS OF MATRIX AT REF. TEMP
C
C       APREEXP,QACT,RGAS,AM     -- MAT. PARAMS IN THE STRAIN RATE
C       S0,H0,SBAR,QHARD,AN      -- MATERIAL PARAMETERS IN THE EVOLUTION
C                                         EQUATION FOR S, FOR THE RATE
C                                         DEPENDENT MATERIAL.
C
C NOTE THAT ABAQUS STORES SYMMETRIC 3 BY 3 MATRICES AS VECTOR OF
C DIMENSION 6. THE SUBROUTINE WHICH HELPS CONVERT FROM ONE FROM TO
C ANOTHER IS CALLED PUSHSV WHICH IS INVOKED BY CALLING:
C
C        CALL PUSHSV(SYM,VECT,IFLAG,NDI,NTENS)
C
C WHERE
C
C        IFLAG=1   CONVERTS A SYMMETRIC MATRIX WRITTEN AS A
C                  VECTOR VECT(6) TO A MATRIX SYM(3,3)
C        IFLAG=2   CONVERTS A SYMMETRIC MATRIX SYM(3,3) TO
C                  THE CORRESPONDING VECTOR VECT(6)
C ----------------------------------------------------------------------
C
C               INITIALIZATION
C
C ----------------------------------------------------------------------
C       I=IEEE_HANDLER("set","common",SIGFPE_ABORT)

        OPEN(31,FILE='UMAT_MESSAGES')
C        OPEN( 32,FILE='randl.dat')


        IF( PROPS(1) .EQ. 1.D0     ) THEN
C               THERMO-ELASTIC CALCULATION
            MFLAG  = 1
      ELSE IF(PROPS(1) .EQ. 2.D0) THEN
C               THERMO-ELASTIC-VISCOPLASTIC CALCULATION
            MFLAG  = 2
      END IF

        IF( PROPS(2) .EQ. 1.D0     ) THEN
                ISOTHERMAL CALCULATION
            KFLAG  = 1
      ELSE IF(PROPS(2) .EQ. 2.D0) THEN
C               COUPLED CALCULATION
            KFLAG  = 2
      END IF


        EYOUNG = PROPS(3)
        ANU    = PROPS(4)
        APREEXP= PROPS(5)
        QACT   = PROPS(6)
```

```
      RGAS   = PROPS(7)
      AM     = PROPS(8)
      S0     = PROPS(9)
      H0     = PROPS(10)
      SBAR   = PROPS(11)
      QHARD  = PROPS(12)
      AN     = PROPS(13)
      VFRACO = PROPS(14)
      THETA0 = PROPS(15)
      THETAM = PROPS(16)
      CHI1   = PROPS(17)
      CHI2   = PROPS(18)
      ALPHA  = PROPS(19)
      RHO    = PROPS(20)
      SPHEAT = PROPS(21)
      OMEGA  = PROPS(22)


      IF(VFRACO .LT. 1.D-10) THEN
C       WRITE(*,*) 'VFRACO TOO SMALL! SETTING VFRACO = 1.D-10'
        VFRACO = 1.D-10
      END IF

C
C             AT THE START OF AN ABAQUS CALCULATION THE STATE
C             VARIABLES ARE PASSED INTO UMAT WITH ZERO VALUES.
C             INTIALIZE THE STATE VARIABLES.
C
      IF( STATEV(1) .LE. 0.D0) THEN
         STATEV(1)   = S0
C        READ(32,*) STATEV(2)
         STATEV(2)   = VFRACO
         STATEV(3)   = 1.D0
         STATEV(4)   = 0.D0
         STATEV(5)   = 0.D0
         STATEV(6)   = 0.D0
         STATEV(7)   = 1.D0
         STATEV(8)   = 0.D0
         STATEV(9)   = 0.D0
         STATEV(10)  = 0.D0
         STATEV(11)  = 1.D0
         STATEV(14)  = 0.
         STATEV(15)  = 0.
         STATEV(16)  = 0.
      END IF
C
C             STORE THE VALUE OF THE DEFORMATION RESISTANCE AT
C             THE BEGINNING OF THE TIME STEP IN ST
C             AND POROSITY IN VFRACT
C
      ST     = STATEV(1)
      VFRACT = STATEV(2)

C
C             STORE THE VALUE OF THE PLASTIC DEFORMATION GRADIENT
C             AT THE BEGINNING OF THE TIME STEP IN FPT
C
      FPT(1,1) = STATEV(3)
      FPT(1,2) = STATEV(4)
      FPT(1,3) = STATEV(5)
      FPT(2,1) = STATEV(6)
      FPT(2,2) = STATEV(7)
      FPT(2,3) = STATEV(8)
      FPT(3,1) = STATEV(9)
```

```
      FPT(3,2) = STATEV(10)
      FPT(3,3) = STATEV(11)

C
C     SET THETAT = TEMP, AND THETATAU = TEMP + DTEMP
C
      THETAT   = TEMP
      THETATAU = TEMP + DTEMP


C     AM  =  0.007 + (THETATAU-298.)/235.*(0.011-0.007)
C     AN  =  0.024 + (THETATAU-298.)/[illegible].*(0.052-0.024)

C
C     SET DT = DTIME
C
      DT = DTIME

     THETACRIT = 0.99*THETAM
     IF (THETATAU .GE. THETACRIT) THEN
        WRITE(31,*)'TEMPERATURE GREATER THAN CRITICAL VALUE!STOPPING'
        WRITE(31,*) 'Tm=',THETAM,' THETATAU=',THETATAU
          CALL XIT
     END IF

      VFRACCRIT = 0.49D0
      IF (VFRACT .GE. VFRACCRIT) THEN
       WRITE(31,*)'POROSITY GREATER THAN CRITICAL VALUE!STOPPING'
          CALL XIT
     END IF

      AMUM0    = EYOUNG/2.D0/(1.D0 + ANU)
      AKAPPAM0 = EYOUNG/3.D0/(1.D0 - 2.D0*ANU)
      CALL ELASCON(AMUM0,AKAPPAM0,THETAT,VFRACT,AMU,AKAPPA,ALAMBDA)
C
C
C     WHEN UMAT IS CALLED FOR THE FIRST ITERATION IN AN
C             INCREMENT, ABAQUS DOES NOT UPDATE  THE DEFORMATION
C             GRADIENT, AND IT PASSES IN A ZERO STRAIN INCREMENT.
C             IN THIS CASE DO NOT PERFORM THE INTEGRATION.
C             COMPUTE THE ELASTIC JACOBIAN AND RETURN.
C
C             STRFLG -- STRFLG = 0.D0 IF STRAIN INCREMENT
C                                        INTO UMAT IS PASSED IN AS ZERO.
C                        STRFLG = 1.D0 IF STRAIN INCREMENT IS
C                                        NONZERO.
C
C             IF THE MONOTONIC FLAG IS USED IN THE PROCEDURE, THEN
C             THE STRAIN INCREMENT IS ALWAYS NONZERO.
C

      STRFLG=0.D0
      DO 5 I=1,NTENS
         STRFLG = STRFLG + DABS(DSTRAN(I))
5     CONTINUE
      IF (UMEROR.GE.2.) THEN
         STRFLG = 0.D0
         GO TO 45
      END IF
C     IF (STRFLG .LT. 1.D-15) THEN
      IF (ITGEN.EQ.1) THEN
              IF (STATEV(21).EQ.0.D0) THEN
                  STRFLG=0.D0
                  GOTO 45
                  ELSE
                  DDSDDE(1,1) = STATEV(21)
                  DDSDDE(1,2) = STATEV(22)
                  DDSDDE(1,3) = STATEV(23)
                  DDSDDE(1,4) = STATEV(24)
                  DDSDDE(2,1) = STATEV(25)
                  DDSDDE(2,2) = STATEV(26)
                  DDSDDE(2,3) = STATEV(27)
                  DDSDDE(2,4) = STATEV(28)
                  DDSDDE(3,1) = STATEV(29)
                  DDSDDE(3,2) = STATEV(30)
                  DDSDDE(3,3) = STATEV(31)
                  DDSDDE(3,4) = STATEV(32)
                  DDSDDE(4,1) = STATEV(33)
                  DDSDDE(4,2) = STATEV(34)
                  DDSDDE(4,3) = STATEV(35)
                  DDSDDE(4,4) = STATEV(36)
                  DDSDDT(1)   = STATEV(37)
                  DDSDDT(2)   = STATEV(38)
                  DDSDDT(3)   = STATEV(39)
                  DDSDDT(4)   = STATEV(40)
                  DRPLDT      = STATEV(41)
                  DRPLDE(1)   = STATEV(42)
                  DRPLDE(2)   = STATEV(43)
                  DRPLDE(3)   = STATEV(44)
                  DRPLDE(4)   = STATEV(45)
                  RETURN
                  ENDIF
      ENDIF

      IF (STRFLG .LT. 1.D-15) THEN
              STRFLG=0.D0
              GOTO 45
      ENDIF
C
C             STORE THE STRESS AT THE BEGINNING OF THE TIME  STEP
C             INTO THE MATRIX STRESST
C
     CALL PUSHSV(STRESST,STRESS,1,NDI,NTENS)
C
C             THIS STRESS MATRIX IS NOT THE CAUCHY STRESS AT TIME T,
C             BUT ACTUALLY DROT * STRESST * DROT^T. CALCULATE THE
C             CAUCHY STRESS AT TIME T
C
     CALL ZEROM(AUX)
     CALL MTRANS(DROT,DROTTRANS)
     CALL MPROD(DROTTRANS,STRESST,AUX)
     CALL MPROD(AUX,DROT,STRESST)
C ----------------------------------------------------------------------
C
C             TIME INTEGRATION PROCEDURE FOLLOWS
C
C ----------------------------------------------------------------------
C
C             INCREMENT THE STRESS, THE PLASTIC DEFORMATION
C             GRADIENT, THE DEFORMATION RESISTANCE AND THE POROSITY
C
C
         ITERX = 0
         ITERERR = 0
         CALL INTEG(MFLAG,FT,STRESST,FPT,ST,VFRACT,THETAT,
     +        DT,FTAU,THETATAU,STRESSTAU,FPTAU,
     +        SIGETAU,SIGHTAU,STAU,VFRACTAU,ETA,
```

```
     +           ITERK,ITERERR,EFFTAU)

           IF (ITERERR .EQ. 1) THEN
C
C                     INTEG HAS NOT CONVERGED. THE VALUES OF VARIABLES
C                     AT THE END OF THE STEP ARE NOT CORRECT.
C                     CUT BACK THE TIME STEP AND RECALCULATE.
C
               WRITE(31,*)'ITERERR = 1!',UMEROR
             UMEROR = 2.D0
               STATEV(1)   = ST
               STATEV(2)   = VFRACT
               STATEV(3)   = FPT(1,1)
               STATEV(4)   = FPT(1,2)
               STATEV(5)   = FPT(1,3)
               STATEV(6)   = FPT(2,1)
               STATEV(7)   = FPT(2,2)
               STATEV(8)   = FPT(2,3)
               STATEV(9)   = FPT(3,1)
               STATEV(10)  = FPT(3,2)
               STATEV(11)  = FPT(3,3)
               GO TO 45
           END IF

               LEVEL1=LEVEL1+ITERK
               MAXL1=DMAX1(MAXL1,ITERK)
C
C              THE SOLUTION IS ACCEPTABLE
C              WRITE THE RESULTS TO FILE. RESET, AND SELECT A NEW TIME
C              STEP, AND CONTINUE.
C
C
C              CALCULATE THE STRESS DEVIATOR AT TIME TAU
C
      CALL DEVM(STRESSTAU,STRESSTAUD)
C
C              CONVERT THE MATRIX STRESSTAU TO THE VECTOR STRESSTAUV
C              AND THE MATRIX STRESSTAUD TO THE VECTOR STRESSTAUDV
C
      CALL PUSHSV(STRESSTAU,STRESSTAUV,2,NDI,NTENS)
      CALL PUSHSV(STRESSTAUD,STRESSTAUDV,2,NDI,NTENS)


C
C              UPDATE THE STRESS, THE DEFORMATION RESISTANCE
C              THE EQUIV. TENSILE PLASTIC STRAIN, THE
C              THE EQUIV. TENSILE PLASTIC STRAIN RATE, AND
C              THE PLASTIC DEFORMATION GRADIENT.
C
      DO  10 I=1,NTENS
             STRESS(I)=STRESSTAUV(I)
10      CONTINUE
      IF( MFLAG .EQ. 2) THEN
           STATEV(1)   = STAU
           STATEV(2)   = VFRACTAU
           STATEV(3)   = FPTAU(1,1)
           STATEV(4)   = FPTAU(1,2)
           STATEV(5)   = FPTAU(1,3)
           STATEV(6)   = FPTAU(2,1)
           STATEV(7)   = FPTAU(2,2)
           STATEV(8)   = FPTAU(2,3)
           STATEV(9)   = FPTAU(3,1)
           STATEV(10)  = FPTAU(3,2)
           STATEV(11)  = FPTAU(3,3)
```

```
           STATEV(12) = EFFTAU
           STATEV(13) = SIGHTAU/SIGETAU
      END IF
C---------------------------------------------------------------------
C
C              AUTOMATIC TIME STEPPING ALOGORITHM FOLLOWS
C
C ---------------------------------------------------------------------
C
C              THE USER SPECIFIED LIMITS EPSLMT ON THE
C              EQUIVALENT TENSILE PLASTIC STRAIN IN THE MATRIX IS USED
C              TO CALCULATE AN ERROR RATIO
C
C              UMEROR  -- PARAMETER WHICH CONTROLS THE
C                                AUTOMATIC TIME-STEPPING PROCEDURE.
C
C              UMAT IS CODED SO THAT THE LARGEST "ERROR" FROM ANY
C              INTEGRATION POINT IN THE MODEL IS USED FOR THE TIME STEP
C              CONTROL ALGORITHM.
C
C              IF UMEROR IS LARGER THAN 1.5 THEN THE TIME INCREMENT
C              IS REPEATED WITH A TIME INCREMENT WHICH IS SMALLER BY
C              50%: DT = 0.5*DT.
C              ELSE, THE NEXT INCREMENT IS PERFORMED WITH A SUITABLY LARGER C
IME STEP:
C
C           IF((UMEROR.GT.0.8D0) .AND. (UMEROR .LE. 1.5)) THEN
C              DT =DT/UMEROR
C           ELSE IF (UMEROR.GT.0.5D0) THEN
C              DT=1.25D0*DT
C           ELSE
C              DT=1.5D0*DT
C           END IF
C

            CALL SDOT(SIGETAU,SIGHTAU,STAU,VFRACTAU,THETATAU,
     +             PHI,DPHIDSE,DPHIDSH,DPHIDS,DPHIDF,DPHIDTHETA,
     +             D2PHIDSE2,D2PHIDSEDSH,D2PHIDSEDS,D2PHIDSEDF,
     +             D2PHIDSH2,D2PHIDSHDS,D2PHIDSHDF,D2PHIDSDF,
     +             G,DGDSE,DGDSH,DGDS,DGDF,DGDTHETA)

        EPSLMT = 0.03D0
        UMEROR1 = (DPHIDSE+2.*DABS(DPHIDSH))*DT/EPSLMT

            STATEV(15)=STATEV(15)+EFFTAU*DT


      IF (ITERK .GT. 10) THEN
       UMEROR2 = 0.8+(ITERK-10.)/40.*0.45
      ELSE IF (ITERK .GT. 5) THEN
       UMEROR2 = 0.6
      ELSE
       UMEROR2 = 0.25
      END IF


        UMEROR1 = DMAX1(UMEROR1,UMEROR2)
        UMEROR  = DMAX1(UMEROR1,UMEROR)

        IF (UMEROR .LT. 0.25) THEN
           UMEROR = 0.25
        ELSE IF (UMEROR .GT. 2.D0) THEN
           UMEROR = 2.D0
        END IF
```

```
C
C              TO SUPPRESS AUTOMATIC TIME INCREMENTATION SET
C              UMEROR = 1.D0.
C
C       UMEROR = 1.D0
C
C ---------------------------------------------------------------------
C
C              CALCULATION OF  THE JACOBIAN FOLLOWS
C
C ---------------------------------------------------------------------
45     CONTINUE
C--------------------------------------------------------------------
C              INTIALIZE MATRICES
C--------------------------------------------------------------------
        DO 50 I = 1,NTENS
      DO 50 J = 1,NTENS
              DDSDDE(I,J) = 0.D0
50      CONTINUE

        DO 60 I = 1,NTENS
              DDSDDT(I) = 0.D0
60      CONTINUE

        RPL = 0.D0

        DRPLDT=0.D0

        DO 70 I = 1, NTENS
              DRPLDE(I) = 0.D0
70      CONTINUE
C ---------------------------------------------------------------------
      IF (STRFLG .EQ. 0.D0) THEN

           C1 = 2.D0*AMU
         C2 = AKAPPA - C1/3.D0

         DO 100 I = 1, NDI
                   DDSDDE(I,I)=C1
100      CONTINUE

           DO 110 I = NDI+1, NTENS
                   DDSDDE(I,I)=C1/2.D0
110       CONTINUE

           DO 120 I = 1,NDI
         DO 120 J = 1, NDI
                   DDSDDE(I,J) = DDSDDE(I,J) + C2
120       CONTINUE


           RETURN
        END IF
C ---------------------------------------------------------------------
122      IF(ITERERR .EQ. 1) THEN
           CALL DEVM(STRESST,STRESSTD)
           CALL PUSHSV(STRESSTD,STRESSTDV,2,NDI,NTENS)
         CALL TRACEM(STRESST,SIGHT)
         SIGHT = SIGHT/3.D0
         CALL EQUIVS(STRESST,SIGET)
         SIGETAU=SIGET
         SIGHTAU=SIGHT
         STAU=ST
         VFRACTAU=VFRACT
```

```
         THETATAU=THETAT
         DO 125 JJ=1,NDI
           STRESSTAUDV(JJ)=STRESSTDV(JJ)
125        CONTINUE
        ENDIF
C ---------------------------------------
C                     DDSDDE
C ---------------------------------------
         DO 129 I = 1,NTENS
       DO 129 J = 1,NTENS
            DDSDDE(I,J) = 0.D0
129      CONTINUE

           IF(SIGETAU .LT. 1.D-10 ) SIGETAU = 1.D-10

            CALL SDOT(SIGETAU,SIGHTAU,STAU,VFRACTAU,THETATAU,
     +              PHI,DPHIDSE,DPHIDSH,DPHIDS,DPHIDF,DPHIDTHETA,
     +              D2PHIDSE2,D2PHIDSEDSH,D2PHIDSEDS,D2PHIDSEDF,
     +              D2PHIDSH2,D2PHIDSHDS,D2PHIDSHDF,D2PHIDSDF,
     +              G,DGDSE,DGDSH,DGDS,DGDF,DGDTHETA)

            STATEV(14) = DPHIDSE
            STATEV(16) = STATEV(16)+DPHIDSE*DT

            ALPHAM(1,1) = 1. + 3. * AMU * DT * D2PHIDSE2
            ALPHAM(1,2) =      3. * AMU * DT * D2PHIDSEDSH
            ALPHAM(1,3) =      3. * AMU * DT * D2PHIDSEDS
            ALPHAM(1,4) =      3. * AMU * DT * D2PHIDSEDF

            ALPHAM(2,1) =        AKAPPA * DT * D2PHIDSEDSH
            ALPHAM(2,2) = 1. +   AKAPPA * DT * D2PHIDSH2
            ALPHAM(2,3) =        AKAPPA * DT * D2PHIDSHDS
            ALPHAM(2,4) =        AKAPPA * DT * D2PHIDSHDF

            ALPHAM(3,1) =               - DT * DGDSE
            ALPHAM(3,2) =               - DT * DGDSH
            ALPHAM(3,3) = 1.            - DT * DGDS
            ALPHAM(3,4) =               - DT * DGDF

            ALPHAM(4,1) =   -(1.- VFRACTAU) * DT * D2PHIDSEDSH
            ALPHAM(4,2) =   -(1.- VFRACTAU) * DT * D2PHIDSH2
            ALPHAM(4,3) =   -(1.- VFRACTAU) * DT * D2PHIDSHDS
          ALPHAM(4,4) =1.-(1-VFRACTAU)*DT*D2PHIDSHDF+DT*DPHIDSH

C
C       Perform the matrix inversion
C
            CALL MATINV(ALPHAM,4,4,INDX,ASTAR)

            D1 = ASTAR(1,1)
            D2 = ASTAR(1,2)
            D3 = ASTAR(2,1)
            D4 = ASTAR(2,2)
            D5 = ASTAR(3,1)
            D6 = ASTAR(3,2)
            D7 = ASTAR(4,1)
            D8 = ASTAR(4,2)

          IF(ITERERR.EQ.1) THEN
             ETA=SIGETAU/(SIGETAU+3.*DT*AMU*DPHIDSE)
          END IF

          AMUTILDE    = AMU * ETA
          AKAPPATILDE = D4 * AKAPPA
```

```
      C1          = 2.D0 * AMUTILDE
      C2          = AKAPPATILDE - C1 / 3.D0
      C3          = -3.D0*AMU*(ETA-D1)/(SIGETAU * SIGETAU)
      C4          = 3.D0*AMU*D3/SIGETAU
      C5          = AKAPPA*D2/SIGETAU

      DO 200 I = 1, NDI
             DDSDDE(I,I)=C1
200   CONTINUE
        DO 210 I = NDI+1, NTENS
             DDSDDE(I,I)=C1/2.D0
210   CONTINUE
        DO 220 I = 1, NDI
      DO 220 J = 1, NDI
             DDSDDE(I,J) = DDSDDE(I,J) + C2
220   CONTINUE
        DO 230 I = 1, NTENS
      DO 230 J = 1, NTENS
             DDSDDE(I,J) = DDSDDE(I,J) +
     +       C3*STRESSTAUDV(I)*STRESSTAUDV(J)
230   CONTINUE
        DO 240 I = 1, NDI
      DO 240 J = 1, NTENS
             DDSDDE(I,J) = DDSDDE(I,J) +
     +       C4*STRESSTAUDV(J)
240   CONTINUE
        DO 250 I = 1, NTENS
      DO 250 J = 1, NDI
             DDSDDE(I,J) = DDSDDE(I,J) +
     +       C5*STRESSTAUDV(I)
250   CONTINUE

      DDSDDE(1,2)=0.5*(DDSDDE(1,2)+DDSDDE(2,1))
      DDSDDE(2,1)=DDSDDE(1,2)
      DDSDDE(1,3)=0.5*(DDSDDE(1,3)+DDSDDE(3,1))
      DDSDDE(3,1)=DDSDDE(1,3)
      DDSDDE(2,3)=0.5*(DDSDDE(2,3)+DDSDDE(3,2))
      DDSDDE(3,2)=DDSDDE(2,3)


C
C           IF THIS IS AN ISOTHERMAL CALCULATION, KFLAG = 1,
C           THEN DONT CALCULATE THE OTHER DERIVATIVES. RETURN
C
      STATEV(21)=DDSDDE(1,1)
      STATEV(22)=DDSDDE(1,2)
      STATEV(23)=DDSDDE(1,3)
      STATEV(24)=DDSDDE(1,4)
      STATEV(25)=DDSDDE(2,1)
      STATEV(26)=DDSDDE(2,2)
      STATEV(27)=DDSDDE(2,3)
      STATEV(28)=DDSDDE(2,4)
      STATEV(29)=DDSDDE(3,1)
      STATEV(30)=DDSDDE(3,2)
      STATEV(31)=DDSDDE(3,3)
      STATEV(32)=DDSDDE(3,4)
      STATEV(33)=DDSDDE(4,1)
      STATEV(34)=DDSDDE(4,2)
      STATEV(35)=DDSDDE(4,3)
      STATEV(36)=DDSDDE(4,4)

        IF (KFLAG .EQ. 1) THEN
            RETURN
        END IF
```

```
C ----------------------------------
C                    DDSDDT
C ----------------------------------
         QRT = (QACT/RGAS)/(THETATAU*0.6*THETAM
         D2PHIDSEDTHETA = DPHIDSE*QRT
         D2PHIDSHDTHETA = DPHIDSH*QRT
         DGFDTHETA(1,1)=-3.D0 * AMU * DTIME * D2PHIDSEDTHETA
      DGFDTHETA(2,1)=-3.D0*AKAPPA*ALPHA-AKAPPA*DTIME*D2PHIDSHDTHETA
      DGFDTHETA(3,1)=  DTIME * DGDTHETA
         DGFDTHETA(4,1)=  DTIME*(1.D0 - VFRACTAU)*D2PHIDSHDTHETA
         DO 260 I = 1,4
            DXDTHETA(I,1) = 0.D0
            DO 255 J = 1,4
              DXDTHETA(I,1)=DXDTHETA(I,1)+ASTAR(I,J)*DGFDTHETA(J,1)
255         CONTINUE
260   CONTINUE
      DSEDTHETA = DXDTHETA(1,1)
      DSHDTHETA = DXDTHETA(2,1)
      DSDTHETA  = DXDTHETA(3,1)
      DFDTHETA  = DXDTHETA(4,1)

         DO 300 I = 1,NDI
            DDSDDT(I) = (DSEDTHETA/SIGETAU)*STRESSTAUDV(I)+DSHDTHETA
300      CONTINUE
         DO 310 I = NDI+1, NTENS
               DDSDDT(I) = (DSEDTHETA/SIGETAU)*STRESSTAUDV(I)
310      CONTINUE


         STATEV(37)=DDSDDT(1)
         STATEV(38)=DDSDDT(2)
         STATEV(39)=DDSDDT(3)
         STATEV(40)=DDSDDT(4)
C ---------------------------------
C                    RPL
C ---------------------------------
         ANPL = 1.D0/AM
         RPL = OMEGA*(1.D0 + ANPL )*PHI/(1.-VFRACTAU)**2
C ---------------------------------
C                    DRPLDT
C ---------------------------------
         DPHIDTHETAC = DPHIDTHETA + DPHIDSE*DSEDTHETA+
     &       DPHIDSH*DSHDTHETA+DPHIDS*DSDTHETA+DPHIDF*DFDTHETA

         DRPLDT=OMEGA*(1.D0+ANPL)*DPHIDTHETAC/(1.-VFRACTAU)**2+
     &       2.*RPL/(1.-VFRACTAU)* DFDTHETA
         STATEV(41)=DRPLDT
C ------------------------------------
C                    DRPLDE
C ------------------------------------
         FAC1=DPHIDSE*D1+DPHIDSH*D3+DPHIDS*D5+DPHIDF*D7
         FAC2=DPHIDSE*D2+DPHIDSH*D4+DPHIDS*D6+DPHIDF*D8
         XI  =OMEGA*(1.D0+ANPL)*3.D0*AMU*FAC1/SIGETAU/(1.-VFRACTAU)**2
     &        +2.*RPL/(1.-VFRACTAU)*D7/SIGETAU
         BETA=OMEGA*(1.D0+ANPL)*AKAPPA*FAC2/(1.-VFRACTAU)**2
     &        +2.*RPL/(1.-VFRACTAU)*D8/SIGETAU

         DO 400 I = 1,NDI
            DRPLDE(I) =XI*STRESSTAUDV(I) + BETA
400      CONTINUE
         DO 410 I = NDI+1, NTENS
           DRPLDE(I) =XI*STRESSTAUDV(I)
410      CONTINUE
         STATEV(42)=DRPLDE(1)
```

```
         STATEV(43)=DRPLDE(2)
         STATEV(44)=DRPLDE(3)
         STATEV(45)=DRPLDE(4)
C ------------------------
      RETURN
      END
C ********************************************************************
      SUBROUTINE INTEG(MFLAG,FT,STRESST,FPT,ST,VFRACT,THETAT,
     +                 DT,FTAU,THETATAU,STRESSTAU,FPTAU,
     +                 SIGETAU,SIGHTAU,STAU,VFRACTAU,ETA,
     +                 ITERK,ITERERR,EFFTAU)
C
C     THIS SUBROUTINE UPDATES THE STATE VARIABLES FOR A GIVEN TIME
C     INCREMENT
C -------------------------------------------------------------------
      IMPLICIT REAL*8 (A-H,O-Z)

      COMMON/MATPEL/EYOUNG,ANU,AMU,AKAPPA,ALAMBDA
      COMMON/MATPRD/APREEXP,QACT,RGAS,AM,S0,H0,SBAR,QHARD,AN,VFRAC0
      COMMON/MATPTP/THETA0,THETAM,ALPHA,RHO,SPHEAT,OMEGA,THETADOT
      COMMON/LUSH1/UMEROR,TIMELU,ITGEN

      INTEGER MFLAG
      REAL*8  FT(3,3),STRESST(3,3),FPT(3,3),FPTINV(3,3),ST,VFRACT,DT,
     +        FTAU(3,3),RTAU(3,3),UTAU(3,3),UEIGVAL(3),UEIGVEC(3,3),
     +        ETAU(3,3),
     +        FESTAR(3,3), RESTAR(3,3),UESTAR(3,3),
     +        UESTAREIGVAL(3),UESTAREIGVEC(3,3),UESTAREIGVECT(3,3)
       REAL*8 EESTAR(3,3),TSTRESS(3,3),TSIGH,TSTRESSD(3,3),TSIGE,
     +    SIGETAU,SIGHTAU,STAU,VFRACTAU,THETATAU,
     +        STRESSBTAU(3,3),STRESSBTAUD(3,3),
     +        EETAU(3,3),
     +        STRESSTAU(3,3),FPTAU(3,3),
     +        IDEN(3,3),TEMP1(3,3), TEMP2(3,3),FTEMP(3,3)

C
C     MFLAG                  -- FLAG FOR MATERIAL MODEL:
C                               MFLAG = 1--POROUS-ELASTIC
C                               MFLAG = 2--POROUS-ELASTIC-VISCOPLASTIC
C     STRESST(3,3)    -- CAUCHY STRESS AT TIME T
C     FPT(3,3)               -- PLASTIC DEF. GRAD. AT TIME T
C     FPTINV(3,3)            -- INVERSE OF FPT
C     ST                     -- DEFORMATION RESISTANCE AT T
C     VFRACT          -- VOID VOLUME FRACTION AT T
C     THETAT          -- TEMPERATURE AT T
C     DT                     -- TIME INCREMENT
C     FTAU(3,3)              -- DEFORMATION GRADIENT
C     RTAU(3,3)              -- ROTATION PART OF FTAU
C     UTAU(3,3)              -- RIGHT STRETCH PART OF FTAU
C     UEIGVAL(3)             -- EIGENVALUES OF UTAU
C     UEIGVEC(3,3)    -- EIGENVECTORS OF UTAU
C     UEIGVECT(3,3)   -- TRANSPOSE OF ABOVE
C     ETAU(3,3)              -- ELASTIC STRAIN
C     FESTAR(3,3)            -- TRIAL ELASTIC DEF. GRAD.
C     RESTAR(3,3)            -- ROTATION PART OF FESTAR
C     UESTAR(3,3)            -- RIGHT STRETCH PART OF FESTAR
C     UESTAREIGVAL(3) -- EIGENVALUES OF UESTAR
C     UESTAREIGVEC(3,3)      -- EIGENVECTORS OF UESTAR
C     UESTAREIGVECT(3,3)-- TRANSPOSE OF ABOVE
C     EESTAR(3,3)            -- TRIAL ELASTIC STRAIN
C     TSTRESS(3,3)    -- TRIAL STRESS
C     TSIGH                  -- MEAN NORMAL PART OF TSTRESS
C     TSTRESSD(3,3)   -- DEVIATORIC PART OF TSTRESS
```

```
C     TSIGE                  -- TRIAL EQUIV. TENSILE STRESS
C     SIGETAU         -- EQUIV. TENSILE STRESS AT TAU
C     SIGHTAU         -- MEAN NORMAL STRESS AT TAU
C     STAU                   -- DEFORMATION RESISTANCE AT TAU
C     VFRACTAU               -- VOID VOLUME FRACTION AT TAU
C     THETATAU               -- TEMPEARTURE AT TAU
C     STRESSBTAU(3,3) -- BAR STRESS AT TAU
C     EETAU(3,3)             -- ELASTIC STRAIN AT TAU
C     EEEIGVAL(3)            -- EIGENVALUES OF ABOVE
C     UEEIGVAL(3)            -- EIGENVALUES OF ELASTIC STRETCH AT TAU
C     FPTAU                  -- PLASTIC DEF. FRAD AT TAU
C     STRESSTAU(3,3)  -- CHAUCHY STRESS AT TAU
C
C     IDEN(3,3)              -- IDENTITY MATRIX
C     TEMP1, TEMP2    -- TEMPORARY MATRICES
C -------------------------------------------------------------------
C            INITIALIZE
C
      CALL TRACEM(STRESST,SIGHT)
      SIGHT = SIGHT/3.D0
      CALL EQUIVS(STRESST,SIGET)
      CALL ZEROM(TSTRESS)
      CALL ONEM(FPTINV)
      CALL ONEM(FESTAR)
      CALL ONEM(RESTAR)
      CALL ONEM(UESTAR)
      CALL ZEROM(EESTAR)
      CALL ZEROM(TSTRESS)
      CALL ZEROM(TSTRESSD)
      CALL ONEM(UESTAREIGVEC)
      CALL ONEM(UESTAREIGVECT)
      CALL ZEROM(STRESSBTAU)
      CALL ZEROM(STRESSBTAUD)
      CALL ZEROM(EETAU)
      CALL ONEM(FPTAU)
      CALL ZEROM(STRESSTAU)
      STAU = ST
      VFRACTAU = VFRACT
      CALL ZEROM(TEMP1)
      CALL ZEROM(TEMP2)
      CALL ONEM(IDEN)
      CALL ONEM(FTEMP)
C
C                     PURELY ELASTIC CASE
C
      IF(MFLAG. EQ. 1) THEN

C
C                     STEP 1. FROM THE  DEFORMATION GRADIENT
C                             CALCULATE THE  ROTATION, STRETCH
C                             AND LOGARITHMIC STRAIN TENSORS
C
         CALL SKINEM(FTAU,RTAU,UTAU,UEIGVAL,UEIGVEC,ETAU)

C
C                     STEP 2. CALCULATE THE BAR STRESS, STRESSBTAU, AT
C                             TIME TAU
C
         DO 10 I = 1,3
         DO 10 J = 1,3
               STRESSBTAU(I,J) = 2.0D0*AMU*ETAU(I,J)
     +         +ALAMBDA*(ETAU(1,1)+ETAU(2,2)+ETAU(3,3))*IDEN(I,J)
     +         -  3.D0*AKAPPA*ALPHA*(THETATAU - THETA0)*IDEN(I,J)
10        CONTINUE
```

```
C
C                 STEP 3. CALCULATE THE CAUCHY STRESS AT TIME TAU
C
        DETU = UEIGVAL(1)*UEIGVAL(2)*UEIGVAL(3)
        DO 15 I = 1,3
        DO 15 J = 1,3
             STRESSBTAU(I,J) = STRESSBTAU(I,J)/DETU
15      CONTINUE
        CALL  MTRANS(RTAU,TEMP1)
       CALL  MPROD(STRESSBTAU,TEMP1,TEMP2)
       CALL  MPROD(RTAU,TEMP2,STRESSTAU)
        RETURN
      END IF
C
C                 ELASTIC-VISCOPLASTIC CASE
C
      IF (MFLAG .EQ. 2) THEN
C
C                 STEP 1. CALCULATE THE TRIAL ELASTIC DEF. GRAD
C
        CALL M3INV(FPT,FPTINV)
        CALL MPROD(FTAU,FPTINV,FESTAR)
C
C                 STEP 2. CALCULATE KINEMATICAL QUANTITIES
C                           CORRESPONDING TO FESTAR
C
        CALL SKINEM(FESTAR,RESTAR,UESTAR,UESTAREIGVAL,
     +            UESTAREIGVEC,EESTAR)

        IF (UMEROR.EQ.5.) THEN
C          error from skinem ->  cutback
                      ITERERR=1
                      RETURN
        ENDIF
C
C                 STEP 3. CALCULATE THE TRIAL STRESS AND
C                           ASSOCIATED QUANTITIES
C
        DO 20 I = 1,3
        DO 20 J = 1,3
              TSTRESS(I,J) = 2.0D0*AMU*EESTAR(I,J)
     +   +ALAMBDA * (EESTAR(1,1)+EESTAR(2,2)+EESTAR(3,3)) *IDEN(I,J)
20      CONTINUE

       CALL TRACEM(TSTRESS,TSIGH)
       TSIGH = TSIGH/3.D0

        CALL DEVM(TSTRESS,TSTRESSD)
        CALL EQUIVS(TSTRESS,TSIGE)

        IF (SIGET .LE. 1.D-10)       SIGET  = 1.D-10
        IF (DABS(SIGHT) .LE. 1.D-10) SIGHT  = 1.D-10
        IF (ST .LE. 1.D-10)          ST     = 1.D-10
        IF (VFRACT .LE. 1.D-10)      VFRACT = 1.D-10
C
C                 STEP 4. CALCULATE THE VALUE OF THE SIGE, SIGH, S,
C                           AND VFRAC AT THE END OF THE INCREMENT
C
        ITERK = 0
        ITERERR = 0
       CALL SOLVPORO(SIGET,SIGHT,ST,VFRACT,THETAT,
     +                DT,TSIGE,TSIGH, THETATAU,
     +                SIGETAU,SIGHTAU,STAU,VFRACTAU,
     +                ITERK,ITERERR,EETAU)

       IF (ITERERR .EQ. 1) THEN
C
C                 SOLVPORO HAS NOT CONVERGED IN MAXIT ITERATIONS.
C                 CUT BACK THE TIME STEP AND RECALCULATE.
C                 RETURN TO MAIN TO CUT BACK TIME-STEP, AND RECALCULATE.
C
           RETURN
       END IF
C
C                 STEP 5. UPDATE THE BAR STRESS
C
       IF (TSIGE+DABS(TSIGH).LT.1.D-15) THEN
           ETA=1.D0
       ELSE
           ETA = SIGETAU / TSIGE
       ENDIF
       DO 25 I = 1,3
      DO 25 J = 1,3
          STRESSBTAU(I,J)=ETA*TSTRESSD(I,J)+ SIGHTAU*IDEN(I,J)
25     CONTINUE
C
C                 STEP 6. UPDATE THE PLASTIC DEF. GRADIENT
C
       CALL ZEROM(EETAU)
       DO 30 I = 1,3
      DO 30 J = 1,3
       EETAU(I,J)= (ETA*TSTRESSD(I,J))/(2.D0*AMU) +
     +           (SIGHTAU/(3.D0*AKAPPA))* IDEN(I,J) +
     +            ALPHA *(THETATAU - THETA0)* IDEN(I,J)
30     CONTINUE

       CALL ZEROM(TEMP1)
       CALL MTRANS(UESTAREIGVEC,UESTAREIGVECT)
       CALL MPROD(UESTAREIGVECT,EETAU,TEMP1)
       CALL ZEROM(EETAU)
       CALL MPROD(TEMP1,UESTAREIGVEC,EETAU)

      ALAMBDAE1 = DEXP(EETAU(1,1))
      ALAMBDAE2 = DEXP(EETAU(2,2))
      ALAMBDAE3 = DEXP(EETAU(3,3))

       CALL ONEM(FTEMP)
      FTEMP(1,1) = UESTAREIGVAL(1) / ALAMBDAE1
      FTEMP(2,2) = UESTAREIGVAL(2) / ALAMBDAE2
      FTEMP(3,3) = UESTAREIGVAL(3) / ALAMBDAE3

       CALL ZEROM(TEMP1)
       CALL ZEROM(TEMP2)
       CALL MPROD(UESTAREIGVEC,FTEMP,TEMP1)
       CALL MPROD(TEMP1,UESTAREIGVECT,TEMP2)
       CALL MPROD(TEMP2,FPT,FPTAU)
C
C                 STEP 9. CALCULATE THE CAUCHY  STRESS AT THE END
C                           OF THE  INCREMENT
C
       CALL ZEROM(TEMP1)
       CALL ZEROM(TEMP2)
       CALL  MTRANS(RESTAR,TEMP1)
      CALL  MPROD(STRESSBTAU,TEMP1,TEMP2)
      CALL  MPROD(RESTAR,TEMP2,STRESSTAU)
      FACTOR = 1.D0/( ALAMBDAE1*ALAMBDAE2*ALAMBDAE3 )
      DO 35 I = 1,3
      DO 35 J = 1,3
```

```
              STRESSTAU(I,J) = FACTOR*STRESSTAU(I,J)
 35         CONTINUE


          RETURN
        END IF

        END
C *********************************************************************
        SUBROUTINE SOLVPORO(SIGET,SIGHT,ST,VFRACT,THETAT,
     +                  DT,TSIGE,TSIGH, THETATAU,
     +                  SIGETAU,SIGHTAU,STAU,VFRACTAU,
     +                  ITERK,ITERERR,EFFTAU)


C       THIS SUBROUTINE SOLVES FOR  (SIGETAU,SIGHTAU,STAU,VFRACTAU) WHICH
C       SATISFY THE SET OF FOUR SCALAR EQUATIONS.
C ---------------------------------------------------------------------
        IMPLICIT REAL*8 (A-H,O-Z)
        PARAMETER (MAXIT=100,NP=4,N=4,TOLEP =0.1)
        DIMENSION ALPHAM(NP,NP),BETA(NP),INDX(NP)
        DIMENSION FT(3,3),FTAU(3,3)

        COMMON/MATPEL/EYOUNG,ANU,AMU,AKAPPA,ALAMBDA
        COMMON/MATPRD/APREEXP,QACT,RGAS,AM,SO,HO,SBAR,QHARD,AN,VFRACO
        COMMON/MATPTP/THETAO,THETAM,ALPHA,RHO,SPHEAT,OMEGA,THETADOT
        COMMON/LUSH1/UMEROR,TIMELU,ITGEN
        COMMON/DEFGRAD/FT,FTAU

C       INITIAL ESTIMATES FOR THE ROOTS:

        SE    = SIGET
        SH    = SIGHT
        S     = ST
        F     = VFRACT
        THETA = THETATAU
        ITERK =0
        ITERERR = 0

        IF (SE.LT.0.) PRINT*,'Should not happen SE=',SE
        IF (SE.LT.0.) SE=1.D-10
        IF (F .LT.0.) PRINT*,'Should not happen F =',F
        IF (F .LT.0.) F =1.D-10
        IF (F .GT.0.999) PRINT*,'Should not happen F =',F
        IF (F .GT.1.) F =0.999

        DO 16  K=1,MAXIT


           CALL SDOT(SE,SH,S,F,THETA,
     +           PHI,DPHIDSE,DPHIDSH,DPHIDS,DPHIDF,DPHIDTHETA,
     +           D2PHIDSE2,D2PHIDSEDSH,D2PHIDSEDS,D2PHIDSEDF,
     +           D2PHIDSH2,D2PHIDSHDS,D2PHIDSHDF,D2PHIDSDF,
     +           G,DGDSE,DGDSH,DGDS,DGDF,DGDTHETA)


           CALL EDOTPM(SE,SH,S,F,THETA,EFFT)
C
C                    Calculate BETA_i --- the negative of the values of
C                    the functions f_i(x_k)
C
           BETA(1) =  - (SE -  TSIGE + 3. * AMU * DT * DPHIDSE)
           BETA(2) =  - (SH- TSIGH +3.* AKAPPA*ALPHA*(THETA - THETAO) +
     +             AKAPPA *DT * DPHIDSH)
           BETA(3) =  - (S - ST - DT * G)
           BETA(4) =  - (F - VFRACT - DT*(1.D0 - F)*DPHIDSH )
C
C                    Calculate the Jacobian for the Newton corrections
C
           ALPHAM(1,1) = 1. + 3. * AMU * DT * D2PHIDSE2
           ALPHAM(1,2) =      3. * AMU * DT * D2PHIDSEDSH
           ALPHAM(1,3) =      3. * AMU * DT * D2PHIDSEDS
           ALPHAM(1,4) =      3. * AMU * DT * D2PHIDSEDF

           ALPHAM(2,1) =        AKAPPA * DT * D2PHIDSEDSH
           ALPHAM(2,2) = 1. +   AKAPPA * DT * D2PHIDSH
           ALPHAM(2,3) =        AKAPPA * DT * D2PHIDSHDS
           ALPHAM(2,4) =        AKAPPA * DT * D2PHIDSHDF

           ALPHAM(3,1) =                 - DT * DGDSE
           ALPHAM(3,2) =                 - DT * DGDSH
           ALPHAM(3,3) = 1.              - DT * DGDS
           ALPHAM(3,4) =                 - DT * DGDF

           ALPHAM(4,1) =      -(1.- F) * DT * D2PHIDSEDSH
           ALPHAM(4,2) =      -(1.- F) * DT * D2PHIDSH2
           ALPHAM(4,3) =      -(1.- F) * DT * D2PHIDSHDS
           ALPHAM(4,4) = 1.   -(1.- F) * DT * D2PHIDSHDF + DT*DPHIDSH


           if(alpham(1,1)*0.d0.ne.0.d0) then
                print*,K,'alpham(1,1) = NaN'
                print*,se,sh,s,f, (se/s)**am,theta,s
                print*, 'FT'
                print*, (FT(1,JJJ), JJJ=1,3)
                print*, (FT(2,JJJ), JJJ=1,3)
                print*, (FT(3,JJJ), JJJ=1,3)
                print*, 'FTAU'
                print*, (FTAU(1,JJJ), JJJ=1,3)
                print*, (FTAU(2,JJJ), JJJ=1,3)
                print*, (FTAU(3,JJJ), JJJ=1,3)
                goto 18
           endif

C
C               Calculate the Newton corrections
C
         CALL LUDCMP(ALPHAM,N,NP,INDX,D)
C            something wrong (at low m)
         IF (UMEROR.EQ.1.D0) GOTO 18

         CALL   LUBKSB(ALPHAM,N,NP,INDX,BETA)
C
C                BETA  NOW CONTAINS THE NEWTON CORRECTIONS.
C                  CHECK TO SEE IF THE NEWTON CORRECTIONS ARE
C                WITHIN SPECIFIED TOLERANCES. IF YES, THEN
C                  PROCESS HAS CONVERGED. UPDATE AND RETURN.
C                  IF NOT, THEN CONTINUE ITERATING.

           JCHECK = 0

           IF ((AM.LT.0.05).AND.(K.LE.2)) THEN
                   BETA(1)=BETA(1)/2.
                   BETA(2)=BETA(2)/2.
                   BETA(3)=BETA(3)/2.
                   BETA(4)=BETA(4)/2.
           ENDIF
           IF ((AM.LT.0.01).AND.(K.LE.4)) THEN
```

```
                  BETA(1)=BETA(1)/3.
                  BETA(2)=BETA(2)/3.
                  BETA(3)=BETA(3)/3.
                  BETA(4)=BETA(4)/3.
         ENDIF

         IRKUT=0
123      IF (SE + BETA(1).LT.1.D-10) BETA(1)=1.D-10-SE
         SETEMP =  SE + BETA(1)
         SHTEMP =  SH + BETA(2)
         STEMP  =  S  + BETA(3)
         IF (F+BETA(4).LT.0.) BETA(4)=F/3.
         IF (F+BETA(4).GT.1.0) BETA(4)=(0.999-F)
         FTEMP  =  F  + BETA(4)


         CALL EDOTPM(SETEMP,SHTEMP,STEMP,FTEMP,THETA,EFFTEMP)
C        EPSTOL = 0.1D0*S0/EYOUNG
C        EPSTOL = S0/EYOUNG*AM
C        ERROR1 = (DT * DABS(EFFTEMP - EFFT) )/EPSTOL
C        ERROR2 = DT * EFFTEMP / 0.005
C        ERROR = DMAX1 (ERROR1,ERROR2)
C
C        IF ((K .EQ. 1).AND.(ERROR .LE.1.D0))THEN
C           JCHECK = 1
C        END IF

         TOL = S0*1.D-8
        IF (    ( DABS( BETA(1) ) .LE. TOL ) .AND.
     +          ( DABS( BETA(2) ) .LE. TOL ) .AND.
     +          ( DABS( BETA(3) ) .LE. TOL ) .AND.
     +     ( DABS( BETA(4) ) .LE. 1.D-5)    )  THEN
            JCHECK = 1
         END IF

         IF (JCHECK  .EQ. 1) THEN
C
C                 ITERATIVE PROCEDURE HAS CONVERGED. UPDATE AND RETURN.
C
           SIGETAU  = SETEMP
           SIGHTAU  = SHTEMP
           STAU     = STEMP
           VFRACTAU = FTEMP
           CALL EDOTPM(SIGETAU,SIGHTAU,STAU,VFRACTAU,THETATAU,EFFTAU)
          ITERK = K
          RETURN
         END IF

           DIFF = EFFTEMP - EFFT
           IF ((DABS(DIFF) * DT) .GE. TOLEP) THEN
C                Scale back the Newton corrections by RKUT
              IF (DIFF .GT. 0.) THEN
                   RKUT = DABS(EFFTEMP/((TOLEP/DT) + EFFT))**AM
              ELSE
                  RKUT=DABS(((TOLEP/DT) + EFFT)/EFFTEMP)**AM
              ENDIF
              RKUT = DMAX1(RKUT,1.02D0)
              RKUT = DMIN1(RKUT,5.0D0 )
              IRKUT=IRKUT+1
              IF (IRKUT.GT.50.) GOTO 18
              DO 12 I=1,N
                 BETA(I) = BETA(I)/RKUT
12          CONTINUE
            GOTO 123
```

```
            ENDIF
C
C                 ADD THE CORRECTIONS TO THE VARIABLES
C
            SE = SE + BETA(1)
            SH = SH + BETA(2)
            S  = S  + BETA(3)
            F  = F  + BETA(4)
C
C                 CHECK TO SEE IF THE NEWTON CORRECTIONS ARE TOO
C                 WILD. CORRECT THE SITUATION IF THEY ARE.
C
           IF (SE.LT.1.D-10)  SE=1.D-10
           IF (S .LT.1.D-10)  S =1.D-10
           IF (F .LT.1.D-10)   F =1.D-10
           IF (F .GT.0.999)   F =0.999
16      CONTINUE

18      ITERK = MAXIT + 1
        ITERERR = 1
C
C                 ITERATIVE PROCEDURE
C                 HAS NOT CONVERGED IN MAXIT ITERATIONS.
C                 RETURN TO CUT BACK TIME-STEP, AND RECALCULATE.
            UMEROR=6.

       RETURN
        END
C ********************************************************************
        SUBROUTINE SDOT(SE,SH,S,F,THETA,
     +             PHI,DPHIDSE,DPHIDSH,DPHIDS,DPHIDF,DPHIDTHETA,
     +             D2PHIDSE2,D2PHIDSEDSH,D2PHIDSEDS,D2PHIDSEDF,
     +             D2PHIDSH2,D2PHIDSHDS,D2PHIDSHDF,D2PHIDSDF,
     +             G,DGDSE,DGDSH,DGDS,DGDF,DGDTHETA)

        IMPLICIT REAL*8(A-H,O-Z)

        COMMON/MATPEL/EYOUNG,ANU,AMU,AKAPPA,ALAMBDA
        COMMON/MATPRD/APREEXP,QACT,RGAS,AM,S0,H0,SBAR,QHARD,AN,VFRAC0
        COMMON/MATPTP/THETA0,THETAM,ALPHA,RHO,SPHEAT,OMEGA,THETADOT

        CALL FUNCPHI(SE,SH,S,F,THETA,
     +                     PHI,DPHIDSE,DPHIDSH,DPHIDS,DPHIDF,DPHIDTHETA,
     +                     D2PHIDSE2,D2PHIDSEDSH,D2PHIDSEDS,D2PHIDSEDF,
     +                     D2PHIDSH2,D2PHIDSHDS,D2PHIDSHDF,D2PHIDSDF)



        ANPL    = 1./ AM
        ANPLONE = ANPL + 1.

        THETA06M=0.6*THETAM
        QRT    = QACT/(RGAS*THETA06M)
        EDOT0  = APREEXP * DEXP(-QRT*(DLOG(THETA06M/THETA)+1) )

C
C             CALCULATE THE EQUIVOLENT STRESS IN THE MATRIX, SEM
C

        BRAK   = ( (ANPLONE*PHI)/(EDOT0*S*(1.D0 - F)) )
        SEMS   = BRAK**(1.D0/ANPLONE)
        SEM    = S*SEMS
```

```
      IF ((SEMS .LT.1.D-12).OR.(H0.EQ.0.D0).OR.(PHI.LT.1.D-15)) THEN
          G = 0.D0
          DGDSE = 0.D0
          DGDSH = 0.D0
          DGDS  = 0.D0
          DGDF  = 0.D0
          DGDTHETA = 0.D0
          RETURN
      ENDIF
C
C             CALCULATE THE PLASTIC STRAIN RATE FUNCTION EFF
C             AND ITS DERIVATIVES
C

      EFF = EDOTO * SEMS ** ANPL
      DEFFDSEM = EFF/(AM*SEM)
      DEFFDS   = - EFF/(AM*S)
      DEFFDTHETA = EFF * QRT /THETA
C
C             CALCULATE THE HARDENING FUNCTION AND ITS DERIVATIES
C
      SSTAR = SBAR * (EFF/EDOTO)**AN
      SFAC = 1.D0 - S/SSTAR
      IF(SFAC .GE. 0.D0) THEN
          SIGN = 1.D0
      ELSE
         SIGN = -1.D0
      ENDIF



      H = H0* ( DABS(SFAC)**QHARD ) * SIGN
      HFACT = H0 * QHARD * DABS(SFAC)**(QHARD-1.D0)
      DHDSEM = HFACT * (1.D0 - SFAC)*(AN/AM)/SEM
      DHDS = HFACT * (SFAC - 1.D0)*(1.D0 + (AN/AM))/S
C*************  EFF/E0 indep of THETA  ********************
      DHDTHETA = 0.D0



C
C             CALCULATE THE DERIVATIVES OF G WRT SEM, S,THETA
C             AT FIXED SEM
C
      DGDSEM    = DHDSEM   *EFF  + H*DEFFDSEM
      DGDS1     = DHDS     *EFF  + H*DEFFDS
      DGDTHETA1 = DHDTHETA*EFF   + H*DEFFDTHETA
C
C             CALCULATE DERIVATIVES OF SEM WRT SE,SEH,S,F,THETA
C
      GFACT = SEM/(PHI*ANPLONE)
      DSEMDSE =  GFACT * DPHIDSE
      DSEMDSH =  GFACT * DPHIDSH
      DSEMDS  =  GFACT*(DPHIDS - PHI/S) + SEMS
      DSEMDF        =  GFACT*(DPHIDF + PHI/(1.D0 - F))
      DSEMDTHETA  =  GFACT*(DPHIDTHETA - PHI*QRT/THETA)
C
C             CALCULATE THE FUNCTION G AND ITS DERIVATIVES WRT
C             SE,SH,S,F,THETA
C
      G              = H * EFF
      DGDSE          = DGDSEM * DSEMDSE
      DGDSH          = DGDSEM * DSEMDSH
      DGDS       = DGDSEM * DSEMDS    + DGDS1
```

```
      DGDF          = DGDSEM * DSEMDF
      DGDTHETA      = DGDSEM * DSEMDTHETA + DGDTHETA1



      RETURN
      END
C ********************************************************************
      SUBROUTINE FUNCPHI(SE,SH,S,F,THETA,
     +                 PHI,DPHIDSE,DPHIDSH,DPHIDS,DPHIDF,DPHIDTHETA,
     +                 D2PHIDSE2,D2PHIDSEDSH,D2PHIDSEDS,D2PHIDSEDF,
     +                 D2PHIDSH2,D2PHIDSHDS,D2PHIDSHDF,D2PHIDSDF)

     IMPLICIT REAL*8(A-H,O-Z)

      COMMON/MATPEL/EYOUNG,ANU,AMU,AKAPPA,ALAMBDA
      COMMON/MATPRD/APREEXP,QACT,RGAS,AM,S0,H0,SBAR,QHARD,AN,VFRAC0
      COMMON/MATPTP/THETA0,THETAM,ALPHA,RHO,SPHEAT,OMEGA,THETADOT

      ANPL     = 1./ AM
      AMONE    = AM + 1.
      ANPLONE = ANPL + 1.
      ANPLMONE = ANPL -1.

      IF (SE+DABS(SH).LT.1.D-15) THEN
                PHI=0.D0
                DPHIDSE =0.D0
                DPHIDSH =0.D0
                DPHIDS =0.D0
                DPHIDF =0.D0
                DPHIDTHETA =0.D0
                D2PHIDSE2 =0.D0
                D2PHIDSEDSH =0.D0
                D2PHIDSEDS =0.D0
                D2PHIDSEDF =0.D0
                D2PHIDSH2 =0.D0
                D2PHIDSHDS =0.D0
                D2PHIDSHDF =0.D0
                D2PHIDSDF=0.D0
                RETURN
       ENDIF


      CALL FUNCF(F,AM,
     +          A1,A2,A3,
     +          DA1DF,DA2DF,DA3DF)

      THETA06M=0.6*THETAM
      QRT   = QACT/(RGAS*THETA06M)
      EDOTO = APREEXP * DEXP(-QRT * (DLOG(THETA06M/THETA)+1.) )

      SES  = SE/S
      SES2 = SES*SES
      SHS  = SH/S
      SHS2 = SHS*SHS
      BRAK = A2*SHS2 + A3*SES2
      BRAK1 = BRAK**((ANPL-1.)/2.)
      BRAK3 = BRAK**((ANPL-3.)/2.)

      IF (SE.LT.0.) PRINT*,'Warning SE=',SE
      IF (F .LT.0.) PRINT*,'Warning F =',F
      IF (F .GT.0.99) PRINT*,'Warning F =',F
```

```
      PHI  = (EDOTO*S/ANPLONE)*(A1*SES**ANPLONE + BRAK**(ANPLONE/2.))

      IF (PHI.LT.1.D-15) THEN
                DPHIDSE =0.D0
                DPHIDSH =0.D0
                DPHIDS =0.D0
                DPHIDF =0.D0
                DPHIDTHETA =0.D0
                D2PHIDSE2 =0.D0
                D2PHIDSEDSH =0.D0
                D2PHIDSEDS =0.D0
                D2PHIDSEDF =0.D0
                D2PHIDSH2 =0.D0
                D2PHIDSHDS =0.D0
                D2PHIDSHDF =0.D0
                D2PHIDSDF=0.D0
                RETURN
       ENDIF



      DPHIDSE = EDOTO*(A1*SES**ANPL +A3*SES*BRAK1)

      DPHIDSH = EDOTO*A2*SHS*BRAK1

      DPHIDS = -PHI*ANPL/S
C             DPHIDS  = PHI/S
C    +        -EDOTO*(A1*SES**ANPLONE + BRAK**(ANPLONE/2.))


      DPHIDF =  (EDOTO*S/ANPLONE)*(DA1DF*SES**ANPLONE) +
     +          (EDOTO*S/2.)*BRAK1*(DA2DF*SHS2 + DA3DF*SES2)

     DPHIDTHETA = PHI*QRT/THETA


      D2PHIDSE2 = EDOTO*((A1*ANPL/SE)*SES**ANPL + (A3/S)*BRAK1 +
     +              (A3*A3*(ANPL-1.)/S)*SES2*BRAK3)

     D2PHIDSEDSH = (EDOTO*A2*A3*(ANPL-1.)/S)*SES*SHS*BRAK3

       D2PHIDSEDS= -DPHIDSE*ANPL/S
C        D2PHIDSEDS = -EDOTO*(A1*ANPL/S)*SES**ANPL
C    +               -EDOTO*(A3*ANPL/S)*SES*BRAK1

     D2PHIDSEDF=EDOTO*(DA1DF*SES**ANPL+DA3DF*SES*BRAK1+
     +                       A3*SES*((ANPL-1.)/2.)*BRAK3*
     +                       (DA2DF*SHS2 + DA3DF*SES2) )

      D2PHIDSH2 =(EDOTO*A2)*((1./S)*BRAK1+
     +             (ANPL-1.)*(A2/S)*SHS*SHS*BRAK3)

       D2PHIDSHDS= -DPHIDSH*ANPL/S
C      D2PHIDSHDS = -(EDOTO*A2*ANPL/S)*SHS*BRAK1

      D2PHIDSHDF = EDOTO*SHS*(DA2DF*BRAK1+
     +              A2*((ANPL-1.)/2.)*BRAK3*
     +              (DA2DF*SHS2 + DA3DF*SES2))

        D2PHIDSDF = (DPHIDF/S) -
     +  EDOTO*(DA1DF*SES**ANPLONE + (ANPLONE/2.)*BRAK1*
```

```
     +   (DA2DF*SHS2 + DA3DF*SES2))

      RETURN
        END
C ********************************************************************
        SUBROUTINE FUNCF(F,AM,
     +                 A1,A2,A3,
     +                 DA1DF,DA2DF,DA3DF)
        IMPLICIT REAL*8(A-H,O-Z)
        DATA FCRIT,FFAIL,FF/0.055,0.25,1./

        IF(F .LE. 1.5D-10) THEN
           A1 = 1.D0
           A2 = 0.D0
           A3 = 0.D0
           DA1DF = 0.D0
           DA2DF = 0.D0
           DA3DF = 0.D0
           RETURN
        END IF

        IFCRITFLAG=0
        IF  (F.GT.FCRIT) THEN
             IF (F.GT.FFAIL) F=0.999*FFAIL
             IFCRITFLAG=1
             FORIG=F
             FAMPL=(FF-FCRIT)/(FFAIL-FCRIT)
             F=FCRIT+FAMPL*(FORIG-FCRIT)
        ENDIF

        ANPL    = 1./ AM
        AMONE   = AM + 1.
        ANPLONE = ANPL + 1.
        AMEXP   = (3. + AM)/(AMONE)

        IF (F.LT.0.) PRINT*,'WARNING F=',F
        IF (F.GT.1.) PRINT*,'WARNING F=',F

        A1 = 1.
        DA1DF = 0.
C
        A2 = (9./4.)*( ANPL * ( F**(-AM) - 1.) )**(-2./AMONE)_
        DA2DF = 4.5*((ANPL*(F**(-AM)-1 ))**(-AMEXP))*F**(-AMONE)/AMONE
C   Haghi
C       G  = 1.27
C       A3 = (F*ANPL)**(2./ANPLONE)*G
C       DA3DF = 2.*A3/F/ANPLONE
C   AZ 1
        A3 = (-1.+(1.+3.34*f+1.25*f**2)**(ANPL/2))**(2/ANPLONE)
        DA3DF =ANPL*(-1.23112 + 1.25*(1.336 + f)**2)**(-1 + ANPL/2)*
     @            (-1 + (-1.23112 + 1.25*(1.336 + f)**2)**(ANPL/2))**
     @             (-1 + 2/ANPLONE)*(3.34 + 2.5*f)/ANPLONE
C   AZ 1
        AFACT=(1.+3.34*f+0.25*f**2)**(ANPL/2)
        BFACT=(1.-f**2)**(ANPL/2)
        A3=(-1.+AFACT/BFACT)**(2/ANPLONE)
        DA3DF=2*(-1.+ AFACT/BFACT)**(-1.+ 2/ANPLONE)*
     @          (AFACT*BFACT**(-1.-2./ANPL)*f*ANPL +
     @    AFACT**(1 - 2/ANPL)*ANPL*(3.34 + 0.5*f)/(2*BFACT))/ANPLONE


C   McMeeking
C       A3=( (1.0+F)/(1.0-F) )**(2.0 * ANPL/(1.0+ANPL))
```

```
C       DA3DF=4.*ANPL*(1. - F)**(-1. - 2.*ANPL/(1.+ANPL))*
C    &    (1.+F)**((-1.+ANPL)/(1.+ANPL))/(1.+ANPL)

        IF(IFCRITFLAG.EQ.1) THEN
          DA1DF=DA1DF*FAMPL
          DA2DF=DA2DF*FAMPL
          DA3DF=DA3DF*FAMPL
          F=FORIG
        ENDIF


        RETURN
        END
C ******************************************************************

        SUBROUTINE EDOTPM(SE,SH,S,F,THETA,EFF)

        IMPLICIT REAL*8(A-H,O-Z)

        COMMON/MATPEL/EYOUNG,ANU,AMU,AKAPPA,ALAMBDA
        COMMON/MATPRD/APREEXP,QACT,RGAS,AM,S0,H0,SBAR,QHARD,AN,VFRAC0
        COMMON/MATPTP/THETA0,THETAM,ALPHA,RHO,SPHEAT,OMEGA,THETADOT

        ANPL    = 1.D0/ AM
        ANPLONE = ANPL + 1.D0

        CALL FUNCF(F,AM,
     +            A1,A2,A3,
     +            DA1DF,DA2DF,DA3DF)

        THETA06M=0.6*THETAM
        QRT   = QACT/(RGAS*THETA06M)
        EDOT0 = APREEXP * DEXP(-QRT * (DLOG(THETA06M/THETA)+1.) )


        if (se.lt.1.D-10) se=1.D-10

        SES  = SE/S
        SES2 = SES*SES
        SHS  = SH/S
        SHS2 = SHS*SHS
        BRAK = A2*SHS2 + A3*SES2


        PHI= (EDOT0*S/ANPLONE)*(A1*SES**ANPLONE + BRAK**(ANPLONE/2.D0))

C
C              CALCULATE THE EQUIVALENT STRAIN RATE IN THE MATRIX, EFF
C

        BRAK1  = ( (ANPLONE*PHI)/(EDOT0*S*(1.D0 - F)) )


        SEMS  = BRAK1**(1.D0/ANPLONE)
        SEM   = S*SEMS

        IF (SEMS .LT.1.D-12) THEN
            EFF = 1.0D-12
        ELSE
            EFF = EDOT0 * SEMS ** ANPL
        END IF

        RETURN
        END
```

```
C******************************************************************

        SUBROUTINE ELASCON(AMUM0,AKAPPAM0,THETA,F,AMU,AKAPPA,ALAMBDA)
C
C  This subroutine calculates the temperature dependent elastic moduli
C  of porous materials.
C
        IMPLICIT REAL*8 (A-H,O-Z)

        COMMON/MATPTP/THETA0,THETAM,ALPHA,RHO,SPHEAT,OMEGA,THETADOT
        COMMON/MATPTQ/CHI1,CHI2

        THETAFAC1  = THETA/THETAM
        THETAFAC0  = THETA0/THETAM
        DTHETA = THETAFAC1 - THETAFAC0
        AMUM    = AMUM0*(1.D0 - CHI1*DTHETA)
        AKAPPAM = AKAPPAM0*(1.D0 - CHI2*DTHETA)

        IF (AMUM .LE. 0.D0) THEN
           PRINT *,'ERROR IN ELASCON! AMUM = 0.D0'
           WRITE(31,*)'ERROR IN ELASCON! AMUM = 0.D0'
           CALL XIT
        END IF
        IF(AKAPPAM .LE. 0.D0) THEN
          PRINT *,'ERROR IN ELASCON! AKAPPAM = 0.D0'
          WRITE(31,*) 'ERROR IN ELASCON! AKAPPAM = 0.D0'
          CALL XIT
        END IF


      IF(F.LE.1.D-5) THEN
           AMU = AMUM
           AKAPPA = AKAPPAM
           ALAMBDA = AKAPPA - (2.D0/3.D0)*AMU
           RETURN
      ENDIF

            SKAPPA1=4./3.*AMUM
            R1=SKAPPA1/AKAPPAM

C  initial guess
            R=R1

            DO 1 K=1,100
            ERROR=(-1.+R)**5*(1.+R1)/(-1.+R1)**5-(1.+R)*(1.-f)**6
            DERIV=5*(-1.+R)**4*(1.+R1)/(-1.+R1)**5-(1.-f)**6
            DR=-ERROR/DERIV
            IF (R+DR.LT.0.) THEN
                  R=R/2.
            ELSE
                  R=R+DR
            ENDIF
            IF (DABS(DR).GT.1.D-5)  GOTO 1
            SKAPPA=SKAPPA1*( (R-1.D0)/(R1-1.D0) )**(5.D0/3.D0)
            AMU=3.D0/4.D0*SKAPPA
            AKAPPA=SKAPPA/R
            ALAMBDA = AKAPPA - (2.D0/3.D0)*AMU
            RETURN
1           CONTINUE

C
C                      ITERATIVE PROCEDURE
C                      HAS NOT CONVERGED IN MAXIT ITERATIONS.
```

```
          IF (ERROR.LT.1.D-6) THEN
          SKAPPA=SKAPPA1*( (R-1.D0)/(R1-1.D0) )**(5.D0/3.D0)
          AMU=3.D0/4.D0*SKAPPA
          AKAPPA=SKAPPA/R
          ALAMBDA = AKAPPA - (2.D0/3.D0)*AMU
          RETURN
          ELSE
             PRINT*,'ERROR:ELASCON NO CONV:F = ',F,'ERROR=',ERROR
          ENDIF

             RETURN
             END
C*************************************************************
     SUBROUTINE LUDCMP(A,N,NP,INDX,D)
C
C       Given an NxN matrix [A], with physical dimension NP, this
C       routine replaces it by the LU decomposition of a row-wise
C       permutation of itself. [A] and N are input. [A] is output,
C       arranged in LU form. INDX is an output vector which records
C       the row permutation effected by the partial pivoting;
C       D is output as +1 or -1 depending on wheter the nuber of
C       row interchanges was even or odd, respectively. This routine
C       is used in combination with LUBKSB to solve linear equations
C       or invert a matrix.
C
        IMPLICIT REAL*8 (A-H,O-Z)
        PARAMETER (NMAX=100,TINY=1.0E-20)
        COMMON/LUSH1/UMEROR,TIMELU,ITGEN
        DIMENSION A(NP,NP),INDX(N),VV(NMAX)
        D=1.
        DO 12 I=1,N
        AAMAX=0.
        DO 11 J=1,N
          IF (ABS(A(I,J)).GT.AAMAX) AAMAX=ABS(A(I,J))
11      CONTINUE
        IF (AAMAX.EQ.0.) THEN
           PRINT *, 'Singular matrix in LUDCMP'
            DO 234 KK=1,NP
234         PRINT*, (A(KK,J),J=1,NP)
            UMEROR=20.
            RETURN
        END IF
        VV(I)=1./AAMAX
12      CONTINUE
        DO 19 J=1,N
        IF (J.GT.1) THEN
          DO 14 I=1,J-1
            SUM=A(I,J)
            IF (I.GT.1)THEN
              DO 13 K=1,I-1
                SUM=SUM-A(I,K)*A(K,J)
13            CONTINUE
              A(I,J)=SUM
            ENDIF
14        CONTINUE
        ENDIF
        AAMAX=0.
        DO 16 I=J,N
          SUM=A(I,J)
          IF (J.GT.1)THEN
            DO 15 K=1,J-1
              SUM=SUM-A(I,K)*A(K,J)
15          CONTINUE
            A(I,J)=SUM
          ENDIF
          DUM=VV(I)*ABS(SUM)
          IF (DUM.GE.AAMAX) THEN
            IMAX=I
            AAMAX=DUM
          ENDIF
16      CONTINUE
        IF (J.NE.IMAX)THEN
          DO 17 K=1,N
            DUM=A(IMAX,K)
            A(IMAX,K)=A(J,K)
            A(J,K)=DUM
17        CONTINUE
          D=-D
          VV(IMAX)=VV(J)
        ENDIF
        INDX(J)=IMAX
        IF(J.NE.N)THEN
          IF(A(J,J).EQ.0.)A(J,J)=TINY
          DUM=1./A(J,J)
          DO 18 I=J+1,N
            A(I,J)=A(I,J)*DUM
18        CONTINUE
        ENDIF
19      CONTINUE
        IF(A(N,N).EQ.0.)A(N,N)=TINY
        RETURN
        END
C*************************************************************
       SUBROUTINE LUBKSB(A,N,NP,INDX,B)
C
C       Solves the set of N linear equations [A](X} = (B).
C       Here [A] is input, not as the matrix [A], but as its LU
C       decomposition, determined by the routine LUDCMP. INDX
C       is input as the permutation vector returned by LUDCMP. {B}
C       is input as the right-hand side vector {B}, and returns
C       with the solution vector {X}. [A], N, NP, INDX are not
C       modified by this routine, and can be left in place
C       for succesive calls with different right-hand sides {B}.
C       This routine takes into account that {B} will begin with
C       many zero elements, so it is efficient for use in matrix
C       inversion.
C
        IMPLICIT REAL*8 (A-H,O-Z)
        DIMENSION A(NP,NP),INDX(N),B(N)
       II=0
       DO 12 I=1,N
        LL=INDX(I)
        SUM=B(LL)
        B(LL)=B(I)
        IF (II.NE.0)THEN
          DO 11 J=II,I-1
            SUM=SUM-A(I,J)*B(J)
11        CONTINUE
        ELSE IF (SUM.NE.0.) THEN
          II=I
        ENDIF
        B(I)=SUM
12     CONTINUE
       DO 14 I=N,1,-1
        SUM=B(I)
        IF(I.LT.N)THEN
          DO 13 J=I+1,N
            SUM=SUM-A(I,J)*B(J)
```

```
13        CONTINUE
        ENDIF
        B(I)=SUM/A(I,I)
14      CONTINUE
        RETURN
        END
C ****************************************************************
      SUBROUTINE MATINV(A,N,NP,INDX,Y)
C
C       Given an NxN matrix [A], with physical dimension NP, this
C       routine replaces it by the LU decomposition of a rowwise
C       permutation of itself. [A] and N are input. [A] is output,
C       arranged in LU form. INDX is an output vector which records
C       the row permutation effected by the partial pivoting;
C       D is output as +1 or -1 depending on wheter the number of
C       row interchanges was even or odd, respectively.
C
C       Once the LU decomposition is performed, this routine
C       calculates the inverse of [A] by using subroutine LUBKSB.
C       Note that INDX is input as the permutation vector returned by
C       LUDCMP. {B} is input as the right-hand side vector {B}, and
C       returns with the solution vector {X}. [A], N, NP, INDX are not
C       modified by this routine, and are left in place
C       for succesive calls with different right-hand sides {B}.
C       This routine takes into account that {B} will begin with
C       many zero elements, so it is efficient for use in matrix
C       inversion.
C
C       The inverse of [A] is calculated using as many unit vectors
C       {B} needed as right hand side vectors. The result is
C       returned as the matrix [Y].
C
        IMPLICIT REAL*8 (A-H,O-Z)
      DIMENSION A(NP,NP), Y(NP,NP), INDX(NP)
C
C       Set up the identity matrix
C
        DO 12 I = 1,N
            DO 11  J = 1,N
                Y(I,J) = 0.0
11          CONTINUE
          Y(I,I) = 1.
12      CONTINUE
C
C       Decompose the matrix just once
C
        CALL LUDCMP(A,N,NP,INDX,D)
C
C       Find the inverse by columns. It is necessary to recognize
C       that FORTRAN stores two dimensional matrices by column, so
C       so that Y(1,J) is the address of the Jth column of Y.
C
        DO 13 J=1,N
            CALL LUBKSB(A,N,NP,INDX,Y(1,J))
13      CONTINUE
        RETURN
        END

C ****************************************************************
C
C       THE NEXT SUBROUTINE CALCULATES VARIOUS KINEMATICAL QUANTITIES
C       ASSOCIATED WITH THE DEFORMATION GRADIENT
```

```
C
C ****************************************************************
       SUBROUTINE SKINEM(F,R,U,UEIGVAL,EIGVEC,E)
C
C              THIS SUBROUTINE PERFORMS THE RIGHT POLAR DECOMPOSITION
C              [F]=[R][U] OF THE DEFORMATION GRADIENT [F] INTO
C              A ROTATION [R] AND THE RIGHT  STRETCH TENSOR [U].
C              THE EIGENVALUES AND EIGENVECTORS OF [U] AND
C              THE  LOGARITHMIC STRAIN [E] = LN [U]
C              ARE ALSO RETURNED.
C ---------------------------------------------------------------
C       VARIABLES
C
        IMPLICIT REAL*8 (A-H,O-Z)
        REAL*8 F(3,3),DETF,FTRANS(3,3),
     +       C(3,3), OMEGA(3),
     +   UEIGVAL(3),EIGVEC(3,3), EIGVECT(3,3),
     +   U(3,3),E(3,3),UINV(3,3),R(3,3),TEMP(3,3)
         COMMON/LUSH1/UMEROR,TIMELU,ITGEN

C
C       F(3,3)  -- THE DEFORMATION GRADIENT MATRIX WHOSE
C                         POLAR DECOMPOSITION IS DESIRED.
C       DETF             -- THE DETRMINANT OF [F]; DETF > 0.
C       FTRANS(3,3)      -- THE TRANSPOSE OF [F].
C       R(3,3)  -- THE ROTATION MATRIX; [R]^T [R] = [I];
C                         OUTPUT.
C       U(3,3)  -- THE RIGHT STRETCH TENSOR; SYMMETRIC
C                         AND POSITIVE DEFINITE; OUTPUT.
C       UINV(3,3)        -- THE INVERSE OF [U].
C       C(3,3)  -- THE RIGHT CAUCHY-GREEN TENSOR = [U][U];
C                         SYMMETRIC AND POSITIVE DEFINITE.
C       OMEGA(3)         -- THE SQUARES OF THE PRINCIPAL STRETCHES.
C       UEIGVAL(3)       -- THE PRINCIPAL STRETCHES; OUTPUT.
C       EIGVEC(3,3)      -- MATRIX OF EIGENVECTORS OF [U];OUTPUT.
C       EIGVECT(3,3)-- TRANSPOSE OF THE ABOVE.
C       E(3,3)  -- THE LOGARITHMIC STRAIN TENSOR, [E]=LN[U];
C                         OUTPUT.
C ---------------------------------------------------------------
C       COMPUTATION
C

C
C               STORE THE IDENTITY MATRIX IN  [R], [U], AND [UINV]
C
        CALL ONEM(R)
        CALL ONEM(U)
        CALL ONEM(UINV)
C
C               STORE THE ZERO MATRIX IN [E]
C
        CALL ZEROM(E)

C
C       CHECK IF THE DETERMINANT OF [F] IS GREATER THAN ZERO.
C               IF NOT, THEN PRINT DIAGGNOSTIC AND STOP.
C
        CALL MDET(F,DETF)

        IF (DETF .LE. 0.D0) THEN
           WRITE(31,100)
           UMEROR=5.
           RETURN
C          CALL XIT
```

```
      END IF
C
C      CALCULATE THE RIGHT CAUCHY GREEN STRAIN TENSOR [C]
C
      CALL  MTRANS(F,FTRANS)
      CALL  MPROD(FTRANS,F,C)

C
C             CALCULATE THE EIGENVALUES AND EIGENVECTORS OF  [C]
C

       CALL SPECTRAL(C,OMEGA,EIGVEC)

C
C             CALCULATE THE PRINCIPAL VALUES OF [U] AND [E]
C

       UEIGVAL(1) = DSQRT(OMEGA(1))
       UEIGVAL(2) = DSQRT(OMEGA(2))
       UEIGVAL(3) = DSQRT(OMEGA(3))

       U(1,1) = UEIGVAL(1)
       U(2,2) = UEIGVAL(2)
       U(3,3) = UEIGVAL(3)

       E(1,1) = DLOG( UEIGVAL(1) )
       E(2,2) = DLOG( UEIGVAL(2) )
       E(3,3) = DLOG( UEIGVAL(3) )

C
C      CALCULATE THE COMPLETE TENSORS [U] AND [E]
C

      CALL MTRANS(EIGVEC,EIGVECT)
      CALL MPROD(EIGVEC,U,TEMP)
      CALL MPROD(TEMP,EIGVECT,U)
      CALL MPROD(EIGVEC,E,TEMP)
      CALL MPROD(TEMP,EIGVECT,E)

C
C             CALCULATE [UINV]
C

      CALL  M3INV(U,UINV)

C
C             CACULATE [R]

C
      CALL MPROD(F,UINV,R)
C ------------------------------------------------------------------
C     FORMATS
C
 100  FORMAT(5X,'--ERROR IN KINEMATICS-- THE DETERMINANT OF [F]',
     +       ' IS NOT GREATER THAN 0',/,
     +       10X,'PROGRAM TERMINATED')
C ------------------------------------------------------------------
      RETURN
      END
C *****************************************************************
C
C     THE FOLLOWING SUBROUTINES CALCULATE THE SPECTRAL
C     DECOMPOSITION OF A SYMMETRIC THREE BY THREE MATRIX
C
```

```
C ******************************************************************
      SUBROUTINE SPECTRAL(A,D,V)

C     THIS SUBROUTINE CALCULATES THE EIGENVALUES AND EIGENVECTORS OF
C     A SYMMETRIC 3 BY 3 MATRIX [A].
C
C     THE OUTPUT CONSISTS OF A VECTOR D CONTAINING THE THREE
C     EIGENVALUES IN ASCENDING ORDER, AND
C     A MATRIX [V] WHOSE COLUMNS CONTAIN THE CORRESPONDING
C     EIGENVECTORS.
C ------------------------------------------------------------------
      IMPLICIT REAL*8 (A-H,O-Z)
      PARAMETER(NP=3)
      DIMENSION D(NP),V(NP,NP)
      DIMENSION A(3,3),E(NP,NP)

      DO 2 I = 1,3
        DO 1 J= 1,3
           E(I,J) = A(I,J)
 1       CONTINUE
 2    CONTINUE

      CALL JACOBI(E,3,NP,D,V,NROT)
      CALL EIGSRT(D,V,3,NP)

      RETURN
      END
C ******************************************************************
      SUBROUTINE JACOBI(A,N,NP,D,V,NROT)

C
C     COMPUTES ALL EIGENVALUES AND EIGENVECTORS OF A REAL SYMMETRIC
C     MATRIX [A], WHICH IS OF SIZE N BY N, STORED IN A PHYSICAL
C     NP BY BP ARRAY. ON OUTPUT, ELEMENTS OF [A] ABOVE THE DIAGONAL
C     ARE DESTROYED, BUT THE DIAGONAL AND SUB-DIAGONAL ARE UNCHANGED
C     AND GIVE FULL INFORMATION ABOUT THE ORIGINAL SYMMETRIC MATRIX.
C     VECTOR D RETURNS THE EIGENVALUES OF [A] IN ITS FIRST N ELEMENTS.
C     [V] IS A MATRIX WITH THE SAME LOGICAL AND PHYSICAL DIMENSIONS AS
C     [A] WHOSE COLUMNS CONTAIN, ON OUTPUT, THE NORMALIZED
C     EIGENVECTORSOF [A]. NROT RETURNS THE NUMBER OF JACOBI ROTATIONS
C     WHICH WERE REQUIRED.
C
C     THIS SUBROUTINE IS TAKEN FROM "NUMERICAL RECIPES", PAGE 346.
C ------------------------------------------------------------------
      IMPLICIT REAL*8 (A-H,O-Z)
      PARAMETER (NMAX =100)
      DIMENSION A(NP,NP),D(NP),V(NP,NP),B(NMAX),Z(NMAX)

C
C      INITIALIZE [V] TO THE IDENTITY MATRIX
C

      DO 12 IP = 1,N
            DO 11 IQ = 1,N
                  V(IP,IQ) = 0.D0
 11         CONTINUE
            V(IP,IP) = 1.D0
 12   CONTINUE

C
C     INITIALIZE B AND D TO THE DIAGONAL OF [A], AND Z TO ZERO. THE
C     VECTOR Z WILL ACCUMULATE TERMS OF THE FORM T*A_PQ AS
C     IN EQUATION (11.1.14)
C
```

```
      DO 13 IP = 1,N
        B(IP) = A(IP,IP)
        D(IP) = B(IP)
        Z(IP) = 0.D0
 13   CONTINUE

      NROT = 0

      DO 24 I = 1,50

C
C         SUM OFF-DIAGONAL ELEMENTS
C
        SM = 0.D0
        DO 15 IP = 1, N-1
           DO 14 IQ = IP + 1, N

             SM = SM + DABS ( A(IP,IQ ))

 14         CONTINUE
 15     CONTINUE
C
C         IF SUM = 0., THEN RETURN. THIS IS THE NORMAL RETURN
C         WHICH RELIES ON QUADRATIC CONVERGENCE TO MACHINE
C         UNDERFLOW.
C
         IF( SM .EQ. 0.D0) RETURN
C
C         IF( SM .LT. 1.0D-15) RETURN
C
C         IN THE FIRST THREE SWEEPS CARRY OUT THE PQ ROTATION ONLY IF
C         |A_PQ| > TRESH, WHERE TRESH IS SOME THRESHOLD VALUE, C  C
SEE EQUATION (11.1.25).  THEREAFTER TRESH = 0.
C
       IF( I .LT. 4) THEN
          TRESH = 0.2D0*SM/N**2
       ELSE
          TRESH = 0.D0
       END IF

       DO 22 IP = 1, N-1
          DO 21 IQ = IP+1,N
             G = 100.D0*DABS(A(IP,IQ))
C
C                 AFTER FOUR SWEEPS, SKIP THE ROTATION IF THE
C                 OFF-DIAGONAL ELEMENT IS SMALL.
C

      IF( (I .GT. 4) .AND. ( DABS(D(IP))+G  .EQ.  DABS( D(IP)) )
     +             .AND. ( DABS(D(IQ))+G  .EQ.  DABS( D(IQ)) ) )THEN

              A(IP,IQ) = 0.D0
            ELSE IF( DABS(A(IP,IQ)) .GT. TRESH) THEN
              H = D(IQ) - D(IP)
              IF(DABS(H)+G .EQ. DABS(H)) THEN
C
C                 T= 1./(2.*THETA), EQUATION(11.1.10)
C
                  T =A(IP,IQ)/H
                 ELSE
                   THETA = 0.5D0*H/A(IP,IQ)
                 T =1.D0/(DABS(THETA)+DSQRT(1.D0+THETA**2))
                   IF(THETA .LT. 0.D0) T = -T
```

```
                 END IF
                 C = 1.D0/DSQRT(1.D0 + T**2)
                 S = T*C
                 TAU = S/(1.D0 + C)
                  H = T*A(IP,IQ)
                  Z(IP) = Z(IP) - H
                  Z(IQ) = Z(IQ) + H
                  D(IP) = D(IP) - H
                  D(IQ) = D(IQ) + H
                  A(IP,IQ) = 0.D0
C
C                 CASE OF ROTATIONS 1<= J < P
C
                  DO 16 J = 1, IP-1
                     G = A(J,IP)
                     H = A(J,IQ)
                     A(J,IP) = G - S*(H + G*TAU)
                     A(J,IQ) = H + S*(G - H*TAU)
 16               CONTINUE
C
C                 CASE OF ROTATIONS P < J < Q
C
                  DO 17 J = IP+1, IQ-1
                     G = A(IP,J)
                     H = A(J,IQ)
                     A(IP,J) = G - S*(H + G*TAU)
                     A(J,IQ) = H + S*(G - H*TAU)
 17               CONTINUE
C
C                 CASE OF ROTATIONS Q < J <= N
C
                  DO 18 J = IQ+1, N
                     G = A(IP,J)
                     H = A(IQ,J)
                     A(IP,J) = G - S*(H + G*TAU)
                     A(IQ,J) = H + S*(G - H*TAU)
 18               CONTINUE
                  DO 19 J = 1,N
                     G = V(J,IP)
                     H = V(J,IQ)
                     V(J,IP) = G - S*(H + G*TAU)
                     V(J,IQ) = H + S*(G - H*TAU)
 19               CONTINUE
                NROT = NROT + 1
           END IF
 21        CONTINUE
 22     CONTINUE
C
C         UPDATE D WITH THE SUM OF T*A_PQ, AND REINITIALIZE Z
C
       DO 23 IP = 1, N
         B(IP) = B(IP) + Z(IP)
         D(IP) = B(IP)
         Z(IP) = 0.D0
 23    CONTINUE
 24   CONTINUE
C
C         IF THE ALGORITHM HAS REACHED THIS STAGE, THEN
C         THERE ARE TOO MANY SWEEPS, PRINT A DIAGNOSTIC
C         AND STOP
      WRITE(31,'(/1X,A/)') '50 ITERS IN JACOBI SHOULD NEVER HAPPEN'
      RETURN
      END
C *********************************************************************
```

```
      SUBROUTINE EIGSRT(D,V,N,NP)
C
C     GIVEN THE EIGENVALUES D AND EIGENVECTORS [V] AS OUTPUT FROM
C     JACOBI, THIS ROUTINE SORTS THE EIGENVALUES INTO ASCENDING ORDER,
C     AND REARRANGES THE COLUMNS OF [V] ACCORDINGLY.
C
C     THIS SUBROUTINE IS TAKEN FROM "NUMERICAL RECIPES", P. 348.
C -----------------------------------------------------------------
      IMPLICIT REAL*8 (A-H,O-Z)
      DIMENSION D(NP),V(NP,NP)

      DO 13 I = 1,N-1
            K = I
            P = D(I)
            DO 11 J = I+1,N
                 IF(D(J) .GE. P) THEN
                      K = J
                      P = D(J)
                 END IF
 11         CONTINUE
            IF(K .NE. I) THEN
               D(K) = D(I)
               D(I) = P
               DO 12 J = 1,N
                    P = V(J,I)
                    V(J,I) = V(J,K)
                    V(J,K) = P
 12          CONTINUE
            END IF
 13   CONTINUE
      RETURN
      END
C **************************************************************
C
C     THE FOLLOWING SUBROUTINES ARE UTILITY ROUTINES
C
C ******************************************************************
      SUBROUTINE ZEROV(V,SIZE)
C
C     THIS SUBROUTINE STORES THE ZERO VECTOR IN A VECTOR V
C -----------------------------------------------------------------
      IMPLICIT REAL*8 (A-H,O-Z)
      INTEGER SIZE
      REAL*8 V(0:SIZE-1)

      I = 0
10    IF (I .LE. SIZE-1) THEN
         V(I) = 0.D0
         I = I+1
      GO TO 10
      END IF

      RETURN
      END
C ********************************************************************
      SUBROUTINE ZEROM(A)
C
C     THIS SUBROUTINE SETS ALL ENTRIES OF A 3 BY 3 MATRIX TO 0.D0
C ----------------------------------------------------------------
      REAL*8 A(3,3)
      DATA ZERO/0.D0/

       A(1,1) = ZERO
       A(1,2) = ZERO
       A(1,3) = ZERO
       A(2,1) = ZERO
       A(2,2) = ZERO
       A(2,3) = ZERO
       A(3,1) = ZERO
       A(3,2) = ZERO
       A(3,3) = ZERO

      RETURN
      END
C ******************************************************************
      SUBROUTINE ONEM(A)
C
C     THIS SUBROUTINE STORES THE IDENTITY MATRIX IN THE
C     3 BY 3 MATRIX [A]
C -----------------------------------------------------------------
      REAL*8 A(3,3)
      DATA ZERO/0.D0/
      DATA  ONE/1.D0/

       A(1,1) = ONE
       A(1,2) = ZERO
       A(1,3) = ZERO
       A(2,1) = ZERO
       A(2,2) = ONE
       A(2,3) = ZERO
       A(3,1) = ZERO
       A(3,2) = ZERO
       A(3,3) = ONE

      RETURN
      END
C ******************************************************************
      SUBROUTINE MTRANS(A,ATRANS)
C --
C --  THIS SUBROUTINE CALCULATES THE TRANSPOSE OF AN 3 BY 3
C --  MATRIX [A], AND PLACES THE RESULT IN ATRANS.
C ----------------------------------------------------------------
C     VARIABLES
C
      REAL*8  A(3,3), ATRANS(3,3)
C -----------------------------------------------------------------
C     COMPUTATION
C
              ATRANS(1,1) = A(1,1)
              ATRANS(1,2) = A(2,1)
              ATRANS(1,3) = A(3,1)
              ATRANS(2,1) = A(1,2)
              ATRANS(2,2) = A(2,2)
              ATRANS(2,3) = A(3,2)
              ATRANS(3,1) = A(1,3)
              ATRANS(3,2) = A(2,3)
              ATRANS(3,3) = A(3,3)
      RETURN
      END
C ****************************************************************
      SUBROUTINE MPROD(A,B,C)
C --
C --  THIS SUBROUTINE MULTIPLIES TWO 3 BY 3 MATRICES [A] AND [B],
C --  AND PLACE THEIR PRODUCT IN MATRIX [C].
C ----------------------------------------------------------------
C     VARIABLES
C
      REAL*8 A(3,3), B(3,3), C(3,3)
```

```
C ------------------------------------------------------------------
C       COMPUTATION
C
        DO 2 I = 1, 3
        DO 2 J = 1, 3
                C(I,J) = 0.D0
                DO 1 K = 1, 3
                        C(I,J) = C(I,J) + A(I,K) * B(K,J)
 1              CONTINUE
 2      CONTINUE
        RETURN
        END
C **************************************************************
        SUBROUTINE MPROD4(A,B,C)
C --
C --    THIS SUBROUTINE MULTIPLIES TWO 3 BY 3 MATRICES [A] AND [B],
C --    AND PLACE THEIR PRODUCT IN MATRIX [C].
C -----------------------------------------------------------------
C       VARIABLES
C
        REAL*8 A(4,4), B(4,4), C(4,4)
C ------------------------------------------------------------------
C       COMPUTATION
C
        DO 2 I = 1, 4
        DO 2 J = 1, 4
                C(I,J) = 0.D0
                DO 1 K = 1, 4
                        C(I,J) = C(I,J) + A(I,K) * B(K,J)
 1              CONTINUE
 2      CONTINUE
        RETURN
        END
C ******************************************************************
        SUBROUTINE  DOTPM(A,B,C)
C
C       THIS SUBROUTINE CALCULATES THE SCALAR PRODUCT OF TWO
C       3 BY 3 MATRICES [A] AND [B] AND STORES THE RESULT IN THE
C       SCALAR C.
C -----------------------------------------------------------------
C       VARIABLES
C
        REAL*8 A(3,3),B(3,3),C

        C= 0.D0
        DO 1 I = 1,3
        DO 1 J = 1,3
            C = C + A(I,J)*B(I,J)
 1      CONTINUE

        RETURN
        END
C ******************************************************************
        SUBROUTINE MDET(A,DET)
C --
C --    THIS SUBROUTINE CALCULATES THE DETERMINANT
C --    OF A 3 BY 3 MATRIX [A].
C ------------------------------------------------------------------
C       VARIABLES
C
        REAL*8  A(3,3), DET
C ------------------------------------------------------------------
C       COMPUTATION
C
        DET =      A(1,1)*A(2,2)*A(3,3)
     +  + A(1,2)*A(2,3)*A(3,1)
     +  + A(1,3)*A(2,1)*A(3,2)
     +  - A(3,1)*A(2,2)*A(1,3)
     +  - A(3,2)*A(2,3)*A(1,1)
     +  - A(3,3)*A(2,1)*A(1,2)

        RETURN
        END
C ******************************************************************
        SUBROUTINE M3INV(A,AINV)

C --    THIS SUBROUTINE CALCULATES THE THE INVERSE OF A 3 BY 3 MATRIX [A]
C --    AND PLACES THE RESULT IN [AINV].
C --    IF DET(A) IS ZERO, THE CALCULATION
C --    IS TERMINATED AND A DIAGNOSTIC STATEMENT IS PRINTED.
C ------------------------------------------------------------------
C       VARIABLES
C

        REAL*8  A(3,3), AINV(3,3), DET, ACOFAC(3,3), AADJ(3,3)
C
C               A(3,3)   -- THE MATRIX WHOSE INVERSE IS DESIRED.
C               DET             -- THE COMPUTED DETERMINANT OF [A].
C               ACOFAC(3,3)     -- THE MATRIX OF COFACTORS OF A(I,J).
C                                  THE SIGNED MINOR (-1)**(I+J)*M_IJ
C                                  IS CALLED THE COFACTOR OF A(I,J).
C               AADJ(3,3)       -- THE ADJOINT OF [A]. IT IS THE MATRIX
C                                  OBTAINED BY REPLACING EACH ELEMENT OF
C                                  [A] BY ITS COFACTOR, AND THEN TAKING
C                                  TRANSPOSE OF THE RESULTING MATRIX.
C               AINV(3,3)       -- RETURNED AS INVERSE OF [A].
C                                  [AINV] = [AADJ]/DET.
C ------------------------------------------------------------------

        CALL MDET(A,DET)

        IF ( DET .EQ. 0.D0 ) THEN
            WRITE(31,10)
            CALL XIT
        END IF

        CALL MCOFAC(A,ACOFAC)
        CALL MTRANS(ACOFAC,AADJ)
        DO 1 I = 1,3
        DO 1 J = 1,3
            AINV(I,J) = AADJ(I,J)/DET
 1      CONTINUE

C ------------------------------------------------------------------
C       FORMAT
C

 10     FORMAT(5X,'--ERROR IN M3INV--- THE MATRIX IS SINGULAR',/,
     +          10X,'PROGRAM TERMINATED')
C-----------------------------------------------------------------
        RETURN
        END
C ******************************************************************
        SUBROUTINE MCOFAC(A,ACOFAC)
C --
C --    THIS SUBROUTINE CALCULATES THE COFACTOR OF A 3 BY 3 MATRIX [A],
C --    AND PLACES THE RESULT IN ACOFAC.
C -------------------------------------------------------------
```

```
C       VARIABLES
C
        REAL*8  A(3,3), ACOFAC(3,3)
C ----------------------------------------------------------------
C       COMPUTATION
C
        ACOFAC(1,1) = A(2,2)*A(3,3) - A(3,2)*A(2,3)
        ACOFAC(1,2) = -(A(2,1)*A(3,3) - A(3,1)*A(2,3))
        ACOFAC(1,3) = A(2,1)*A(3,2) - A(3,1)*A(2,2)
        ACOFAC(2,1) = -(A(1,2)*A(3,3) - A(3,2)*A(1,3))
        ACOFAC(2,2) = A(1,1)*A(3,3) - A(3,1)*A(1,3)
        ACOFAC(2,3) = -(A(1,1)*A(3,2) - A(3,1)*A(1,2))
        ACOFAC(3,1) = A(1,2)*A(2,3)  - A(2,2)*A(1,3)
        ACOFAC(3,2) = -(A(1,1)*A(2,3) - A(2,1)*A(1,3))
        ACOFAC(3,3) = A(1,1)*A(2,2) - A(2,1)*A(1,2)

        RETURN
        END
C ***************************************************************
        SUBROUTINE INVAR(A,IA,IIA,IIIA)
C
C       THIS  SUBROUTINE CALCULATES THE PRINCIPAL INVARIANTS
C       IA, IIA, IIIA OF       A  TENSOR [A].
C ------------------------------------------------------------------
C       VARIABLES
C
        REAL*8 A(3,3), AD(3,3),AD2(3,3), DETA, IA,IIA,IIIA
C ------------------------------------------------------------------
C       COMPUTATION
C
       DO 1 I=1,3
       DO 1 J=1,3
            AD(I,J) = A(I,J)
 1     CONTINUE

       IA = AD(1,1) + AD(2,2) + AD(3,3)
C
C                      CALCULATE THE SQUARE OF [AD]
C
       CALL MPROD(AD,AD,AD2)
C
       IIA =0.5D0 * ( IA*IA - ( AD2(1,1) + AD2(2,2) + AD2(3,3) ) )
C
       CALL  MDET(AD,DETA)

       IIIA = DETA

C
       RETURN
       END
C ******************************************************************
        SUBROUTINE TRACEM(A,TRA)
C
C       THIS SUBROUTINE CALCULATES THE TRACE OF A 3 BY 3 MATRIX [A]
C       AND STORES THE RESULT IN THE SCALAR TRA
C ------------------------------------------------------------------
C       VARIABLES
C
        REAL*8 A(3,3),TRA

        TRA = A(1,1) + A(2,2) + A(3,3)
```

```
        RETURN
        END
C ******************************************************************
        SUBROUTINE DEVM(A,ADEV)
C
C       THIS SUBROUTINE CALCULATES THE DEVIATORIC PART OF A
C       3 BY 3 MATRIX [A]
C ------------------------------------------------------------------
C       VARIABLES
C
        REAL*8 A(3,3),TRA,ADEV(3,3),IDEN(3,3)

        CALL TRACEM(A,TRA)
        CALL ONEM(IDEN)
        CALL ZEROM(ADEV)

        DO 1 I = 1,3
        DO 1 J = 1,3
             ADEV(I,J) = A(I,J) - (1.D0/3.D0)*TRA*IDEN(I,J)
 1      CONTINUE

        RETURN
        END
C ******************************************************************
        SUBROUTINE EQUIVS(S,SB)
C
C       THIS SUBROUTINE CALCULATES THE EQUIVALENT TENSILE STRESS SB
C       CORESSPONDING TO A 3 BY 3 STRESS MATRIX [S]
C ------------------------------------------------------------------
C       VARIABLES
C
        REAL*8 S(3,3),SDEV(3,3),SDOTS,SB

        SB = 0.D0
        SDOTS = 0.D0

        CALL DEVM(S,SDEV)
        CALL DOTPM(SDEV,SDEV,SDOTS)
        SB = DSQRT(1.5D0* SDOTS)

        RETURN
        END
C**************************************************************
          SUBROUTINE PRTMAT(A,M,N)
          INTEGER M,N
          REAL*8 A(M,N)
          DO 10 K=1,M
            WRITE(31,'(2X,6E12.4,2X)') (A(K,L), L=1,N)
10      CONTINUE
        RETURN
        END
C ******************************************************************
C
C       THE FOLLOWING 3  SUBROUTINES ARE NEEDED FOR INTERFACING WITH
C       ABAQUS
C
C ******************************************************************
          SUBROUTINE PUSHSV(SYM,VECT,IFLAG,NDI,NTENS)
          IMPLICIT REAL*8 (A-H,O-Z)

C        IFLAG=1   CONVERTS A SYMMETRIC MATRIX WRITTEN AS A
C                  VECTOR VECT(6) TO A MATRIX SYM(3,3)
C        IFLAG=2   CONVERTS A SYMMETRIC MATRIX SYM(3,3) TO
C                  THE CORRESPONDING VECTOR VECT(6)
```

```
C ------------------------------------------------------------------
      DIMENSION SYM(3,3),VECT(NTENS)
      NSHR=NTENS-NDI
      IF (IFLAG.EQ.1) THEN
            CALL ZEROM(SYM)
            DO 15 I=1,NDI
15          SYM(I,I)=VECT(I)
            IF (NSHR.NE.0)     THEN
                SYM(1,2)=VECT(NDI+1)
                SYM(2,1)=VECT(NDI+1)
                     IF  (NSHR.NE.1)   THEN
                     SYM(1,3)=VECT(NDI+2)
                     SYM(3,1)=VECT(NDI+2)
                            IF  (NSHR.NE.2)  THEN
                            SYM(2,3)=VECT(NDI+3)
                            SYM(3,2)=VECT(NDI+3)
                            ENDIF
                     ENDIF
            ENDIF
      ELSE
          IF (IFLAG.EQ.2) THEN
              DO 24 I=1,NTENS
24            VECT(I)=0.D0
              DO 25 I=1,NDI
25            VECT(I)=SYM(I,I)
              IF (NSHR.NE.0) THEN
                    VECT(NDI+1)=SYM(1,2)
                    IF (NSHR.NE.1) THEN
                          VECT(NDI+2)=SYM(1,3)
                          IF (NSHR.NE.2) VECT(NDI+3)=SYM(2,3)
                    ENDIF
              ENDIF
          ELSE
          WRITE(6,*) '** ERROR IN PUSHSV WRONG IFLAG  '
          ENDIF
       ENDIF

       RETURN
       END
C ********************************************************************
      SUBROUTINE MATDC(AMTE18,AMTE19,XX1)
C
C     THIS ROUTINE BELONGS IN MAIN           LAST UPDATE 4-6-165
C
C     THIS  SUBROUTINE EXTRACTS THE DEFORMATION GRADIENTS
C     FT AND FTAU
C     AT THE BEGINNING AND THE END OF THE
C     STEP  FROM ABAQUS AND PASSES IT THROUGH THE COMMON BLOCK DEFGRAD
C     FOR USE IN UMAT
C

      IMPLICIT REAL*8(A-H,O-Z)
      DIMENSION AMTE18(1),AMTE19(1),XX1(3,3)
      DIMENSION FT(3,3),FTAU(3,3)

      COMMON/DEFGRAD/FT,FTAU

      COMMON/CEL/LELOP,JETP,JETP1,KEL,KINTK,KINTL,KINTSL,KSPT,NEMCRD,
     1 JINTYP,JEXTYP,JEXTY2,
     2 JLIB,NAN24,MDOF,MCRD,NNODE,NNODU,NTENS,NDI,NSHR,NPR,
     3 NINTK,NINTM,NINTSL,NINTLL,NMP,NPARS,NSHL,NBM,NELZM,NINTTS,
     4 NEINT,NDOFEL,JUNSYM,NEGEOM,LNODEK,NNODEP,LBASIS,NNODET,NTENST,
     5 NTDOFN,
     6 LLUMPM,NOFFT,NNODI,JELHYP,NDGRAD,LELLIN,LELUNS,NELSTV,IETAT1,
     7 IETAT2,
     8 NXDIM,JCNVCT,JSHAP,JEGRP,NELSPR(6),
     9 NSPT,NNOD2,NNOD3,NNOD4,NTDOFE,KSPTT,NINR,NBMB,JUNSEL,NDIP1,
     1 NEGEOP,LENREV,KLPT
C ------------------------------------------------------------------
C        CHANGE JINTYP TO AN EVEN WORD BOUNDARY AT NEXT RECOMPILE
C ------------------------------------------------------------------
C LA
C


         DO 2 I=1,NDI
             FT(I,I)=AMTE18(I)
 2       CONTINUE

      IF(NSHR.NE.0)THEN
         FT(1,2)=AMTE18(NDI+1)
         FT(2,1)=AMTE19(NDI+1)
         IF(NSHR.NE.1)THEN
            FT(1,3)=AMTE18(NDI+2)
            FT(3,1)=AMTE19(NDI+2)
            IF(NSHR.NE.2)THEN
               FT(2,3)=AMTE18(NDI+3)
               FT(3,2)=AMTE19(NDI+3)
            END IF
         END IF
      END IF

         DO 4 I=1,3
         DO 4 J=1,3
             FTAU(I,J)=XX1(I,J)
 4       CONTINUE
C
C LA
C ------------------------------------------------------------------
      DO 10 K1=1,NDI
      AMTE18(K1)=XX1(K1,K1)
   10 CONTINUE
      IF(NSHR.NE.0)THEN
         AMTE18(NDI+1)=XX1(1,2)
         AMTE19(NDI+1)=XX1(2,1)
         IF(NSHR.NE.1)THEN
            AMTE18(NDI+2)=XX1(1,3)
            AMTE19(NDI+2)=XX1(3,1)
            IF(NSHR.NE.2)THEN
               AMTE18(NDI+3)=XX1(2,3)
               AMTE19(NDI+3)=XX1(3,2)
            END IF
         END IF
      END IF
C ------------------------------------------------------------------
C LA
C
C        CORRECTLY INITIALIZE THE DEFORMATION  GRADIENT
C
      CHECK1=0.D0
      CHECK2=0.D0
      DO 90 I=1,3
      DO 90 J=1,3
            CHECK1=CHECK1+ABS(FT(I,J))
            CHECK2=CHECK2+ABS(FTAU(I,J))
 90   CONTINUE
      IF  (CHECK1.EQ.0.D0) THEN
         CALL ONEM(FT)
```

```
      ENDIF
      IF (CHECK2.EQ.0.D0) THEN
         CALL ONEM(FTAU)
      ENDIF
      IF (CHECK2*0.D0.NE.0.D0) THEN
C       FTAU NaN
          DO 91 I=1,3
          DO 91 J=1,3
91        FTAU(I,J)=FT(I,J)
      ENDIF



      RETURN
      END
C ********************************************************************
      SUBROUTINE EXECS
C     THIS ROUTINE BELONGS IN MAIN                         LAST UPDATE 4-6-141
      IMPLICIT REAL*8(A-H,O-Z)
C
C  SUPERVISE STATICS
C  MODIFIED BY ALLEN M. LUSH TO PROVIDE AUTOMATIC TIMESTEP CONTROL
C  USING THE PARAMETER UMEROR.
C  IN ADDITION, THE TIME CALCULATION HAS BEEN REDONE AND THE EXTRAPCLATE
C  FLAG HAS BEEN TURNED OFF. THIS SUPPRESSES THE CALCULATION OF STRAIN
C  INCREMENTS FOR KITGEN=1.
C
      COMMON/LUSH1/UMEROR,TIMELU,ITGEN
      COMMON/LUSH2/LEVEL1,LEVEL2,MAXL1,MAXL2
      COMMON/CEL/LELOP,JETP,JETP1,KEL,KINTK,KINTL,KINTSL,KSPT,NEMCRD,
C
     1 JINTYP,JEXTYP,JEXTY2,
C
     2 JLIB,NAN24,MDOF,MCRD,NNODE,NNODU,NTENS,NDI,NSHR,NPR,
     3 NINTK,NINTM,NINTSL,NINTLL,NMP,NPARS,NSHL,NBM,NELZM,NINTTS,
     4 NEINT,NDOFEL,JUNSYM,NEGEOM,LNODEK,NNODEP,LBASIS,NNODET,NTENST,
     5 NTDOFN,
     6 LLUMPM,NOFFT,NNODI,JELHYP,NDGRAD,LELLIN,LELUNS,NELSTV,IETAT1,
     7 IETAT2,
     8 NXDIM,NELSPR(9),
C
     9 NSPT,NNOD2,NNOD3,NNOD4,NTDOFE,KSPTT,NINR,NBMB,JUNSEL,NDIP1,
     1 NEGEOP,LENREV,KLPT
C        CHANGE JINTYP TO AN EVEN WORD BOUNDARY AT NEXT RECOMPILE
      COMMON/CELGI/IETZYX,IETYP,IENORI,IMTYP,IWAMP,IEFR,IMPK,
     1 IEDBR,INDR,IENICR,IENIC,IEU,IEDU,IEV,IEA,IER,IETEMP,IEJAC,IEXX1,
     2 IEXPU,IEOR,IEO,IESYM,IEAN24,IEOSET,IEOREC,IEOSP,IEB,IEMCRD,
     3 IEINTS,IED,IESK,IESRS,IESIS,IESTR,IESTRD,IESFV,IEDBSB,IEDBB,
     4 IEDBS,IESRSS,IMSTR,IMSTRD,IMDBR,IEDB,IEFRI,IEM,IEDRHS,IESR,IEN,
     5 INFR,INSR,IETRA3,IETRA,IENICL,IENNCR,IEILHS,IEKOLH,IEKOLR,IEGX1,
     6 IBNIC,IMODES,IEDT,IEST,IESTD,IESTDX,IEINTP,IESBT,IESRCT,IESRT1,
     7 IESRT2,IESKT,IESSCT,IEBT,IEINTT,IEBTNC,IMTT,IMDTT,IESTSC,
     8 IEMCD0,IEBASI,IEOEST,IEOESP,IEOV6,IEINTR,IEDUDX,IEDVRD,
     9 IEDBRS,ISLM,IEOINX,IEREDV,INOREC,IEMC,IEIXX1,IEMPCN,
     A IPPCTR,IPPCTL,IPPSHV,IPPTRI,IPPXXT,IESTFE,IECRY1,IEOVAR,IEOVAL,
     B IEOLSS,IEOEXT,IEOIN1,IES56T,IEMORI,IESTS,IELSRC,IEV1,IEDMV1,
     C IEDMV2
      COMMON/CERROR/RESMAX(30),JNREMX(30),ERRMAX(2),CETOL,CSLIM,
     1 CEMAX,PCTOL,TLIMIT,PSUBIN,RESMIN,DUMAX(30),JNDUMX(30),
     2 ERRPRE,UDELSS,PTOL,AMTOL,DMKET,DMRETL,SIGTOL,DSIGMX,
     3 UTOL,UMAX,U4MAX,VMAX,V4MAX,AMAX,A4MAX,TMAX,EPPMAX,RMAX,R4MAX,
     4 NGOPEN,NGCLOS,ROTTOL,ROTFAC,JRIKND,NINCCS,RIKUB,RIKUMX,RIKMU,
     5 RIKLAM,RIKDLA,RIKRO,RIKOLD,RIKLMX,QMAX,DUMAXP,STRRAT,PCUT,
     6 RIKDLO,TERRPR,JCIT1,JCITER,NELFP,NELFPT,AELFPL,MAXVIO,MAXCHP,
     7 KAXVIO,KAXCHP,PTOLVI(2),PERRMX,UERRMX,STOLFA,NSOLBD,NSHLBD,
     8 COMERR,UERRI,PERRI

      COMMON/CGM/LCGM,MNOD,MELS,MMATP,MMNDOF,MSETEX,MENT,MENMAX,
     1 MENSAV,MLNODE,MNODEP,MLVARB,MELDOF,MDOFET,MELZ,MELZM,
     2 MMTENS,MTENST,MMVARB,MSVARB,MSVART,MINTK,MINR,MMPC,MMPCE,
     3 MMMSC,MMSTVR,MTFV,MNTFV,MMINDV,MMEVAL,MTABZ,MNCRD,MNCRD3,
     4 MMITKQ,MUDOFN,MTDOFN,MPDOFN,MNFREF,MNSREF,MDN,MNRL,MAN24,
     5 MSLODS,MEFREF,MELSET,MESREF,MDE,MERL,MDMP,MDSLV(15),MVARBZ,
     6 NALLDF,MAXPA,MMODES,MRHS,MNLDC,MEIGV,MMNIXL,NLNIKN,MLEVEL,
     7 MESET,MNSET,MMCONN,MATTS,MBLKRF,MLTSBM,MOVCR,MNPSD,MNAMP,
     8 MJFRNT,MPPCON,MSPREC,MNLAGR,MREBEL,MEIGV3,MJCONT,MNSCOL,
     9 MRSURF
      COMMON/CGN/LCGN,NNOD,NELS,NNLAGR,NMATP,NNDOF,MMSC,MSTVAR,NTFV,
     1 NNTFV,NNCRD,NNCRD3,NNFREF,NNSREF,NNRL,NEFREF,NESREF,NAXPA,NSEAR,
     2 NESET,NNSET,MCONN,MOXXX,MNIXL,NRMSW,NERL,MEGEOM,MEN,NNSCOL
      COMMON/CLINES/VERSN,DAT(2),TIM,NLPAGE,KLINE,KPAGE,JINP,JOUTP
      COMMON/CMFWA/LMFWA,IMFWA,MCOREM,LCMMAX
      COMMON/CNOGI/INOZYX,INODBR,INODFR,INFILE,INOV7,INOV11,INOV12,
     1 INOV14,INOV15,INEJAC,INJNOD,INVAL,INTITL,
     2 IXDNPD,IXDU,IXDDU,IXDPMI,IXDA,IXDVH,IXDV,IXDMI,IXDUBA,IGLOBV,
     3 IGLOBX
      COMMON/CONSTS/PI,SIN60,COS60,ZERO,ONE,TWO,HALF,THIRD,SIXTY,ABIG,
     1 ASMALL,BCBIG,PRECIS,BLANK,COMMA,LZERO,LONE,KCROS2(3),KCROS3(3),
     2 LOCSHR(2,3),MPDOF,MADOF,MNDOFM,MAXNEL,NETYPD,MJEDOF,SABIG,
     3 IOFFST
      COMMON/CONTRO/LINITL,LARGE,LINEAR,LCREEP,LDYN,LHEAT,LSTAT,LOK,
     2 LEFOND,LMOLOD,LMASS,LREST,LFILE,LUNSYM,LRHSW,LMODST,LELMOD,
     3 LCORT,LTRAMA,LEIGEN,NRHSV,LMESSG,LLHS,LLHSK,LLHSM,LRHS,LSTRN,
     4 LINMAT,LGAPFL,LMDBW,LSUPGN,LGAPS,LGAPEL,LSHELL,LSUPEL,LGEO,
     5 LCONS,LSSS,LSSI,LEXTRP,LDYNC,LEIPRE,LCTU,LPROC,LADDM,LDAA,
     6 LSOLID,LRIKS,LREBAR,LSUBMX,LREBAS,LRHSI,LHYBBM,LEQUIL,LSTEND,
     7 LWPEN,LPORPS,LWPENE,LNOSTP,LSEQU,LAUTO,LITFRE,LITFRP,LGAPPR,
     8 LHYBOK,LMODYN,NRHSI,NRHSP,LCOMPD,LPOUT,LDYNE,LSTRN1,LSTRNE,
     9 LGRAV,LSOLVT,LFPLOK,LREBA1,LVIO,LACOUS,LSSDIR,LPRFNT,LQUASN,
     1 LGLOBR,LCMPLX,NRHSB,LPPEN,LMESS,NSUPEL,KSUPEL,LSRCH,LSRCHA,
     2 LCORTC,LEIGMS
      COMMON/COUNT/KINC,MINC,KITER,MITER,FATIME,ATIME,DATIME,
     1 CTIME,DCTIME,DTIME,DDTIME,HTIME,DHTIME,DDTPRE,DATPRE,HTIM1,
     2 DHTIM2,EXFAC,KSTEP,KCUTS,MCUTS,NUMBER,LSHAF1,LCUTBK,DTNEWS,
     3 KITGEN,KMDINC,TTIME,DTMIN,DTMAX,MITEIG,LTIME0,STIME,DSTIME
     4,TPREV,TNEW,TOLD,TEND,MITRK,KITRK,KTOTIT,KSOLIT,KSOLM,KTINC,
     5 KACUT,MITLSA,FREQR,FREQC,DELFRQ(2),KITLS,MITLS,DTNEW,DTOLD,
     6 ODTOLD
      COMMON/CSP/SINT(1)
C1  INSERTED TEXT
C     PRINT*,'ENTER EXECS'
C     IF (KSTEP.EQ.1) OPEN (UNIT=30,FILE='STATISTICS')
      TIMELU=TTIME
C2
C
C  NEW INCREMENT
      N1=0
      N2=0
      N3=0
      A1=ZERO
  200 CONTINUE
      KITRK=0
      KREFK=0
      IF(LCUTBK.NE.0.AND.LQUASN.NE.0) LINITL=1
C     PRINT*,'CALLING INC'
      CALL INC
C1  INSERTED TEXT
      IF (LCUTBK.EQ.0) THEN
```

```
       TIMEBU=TIMELU
        TIMELU=TIMELU+DATIME
       ELSE
        TIMELU=TIMEBU+DATIME
       END IF
       UMEROR=ZERO
C1
C TO TAKE ADVANTAGE OF THE  MONOTONIC FLAG
C
C      LEXTRP=0
       LEXTRP=1
C2
C
C
       LMOLOD=0
C2
       LSTRN=LSTRN1
       IF(LEXTRP.NE.0) LSTRN=1
C1
C      LSTRN=0
C2
       IF(LPORPS.EQ.0)GO TO 210
       CALL EXECPP
  210  CONTINUE
       IF(MLEVEL.NE.0)CALL SUPUI1
       IF(LCONS.NE.0) LSS1=1
       LOK=1
       LLHS=LINITL
       LLHSK=LLHS
       LLHSM=0
       LRHS=1
       LGLOBR=0
       IF(LINITL.EQ.0.AND.IGLOBV.NE.IGLOBX) LGLOBR=1
       LINMAT=LINEAR
       LMDBW=0
C1  INSERTED TEXT
       LEVEL1=0
       LEVEL2=0
       MAXL1=0
       MAXL2=0
       UMEROR=ZERO
       ITGEN=KITGEN
C2
C      PRINT*,'CALLING ELGEN'
       CALL ELGEN(SINT(IEDBR))
C      PRINT*,'AFTER ELGEN'
       IF(LOK.EQ.1) GO TO 299
       IF(KINC.EQ.1.AND.KSTEP.EQ.1) CALL XIT
       GO TO 45
  299  CONTINUE
  300  CONTINUE
       LFLAG1=0
       IF(KITER.LE.MITER)GO TO 310
       IF(LSTAT.EQ.1)GO TO 310
       IF(LNOSTP.EQ.0)GO TO 305
       IF(LITFRP.EQ.0) GO TO 304
       LFLAGX=1
       CALL ERMESS(LFLAGX,N1,N2,N3,A1)
  304  CONTINUE
       LOK=1
       GO TO 650
  305  CONTINUE
       LFLAG1=1
       LFLAGX=2
       CALL ERMESS(LFLAGX,N1,N2,N3,A1)
       LOK=0
       GO TO 650
  310  CONTINUE
       IF(LQUASN.EQ.1.AND.KITRK.EQ.MITRK) THEN
       LFLAGX=3
       CALL ERMESS(LFLAGX,N1,N2,N3,A1)
       KREFK=KREFK+1
       ENDIF
       LOK=1
C      PRINT*,'CALLING SOLVE1'
       CALL SOLVE1
C      PRINT*,'AFTER SOLVE1'
       CALL FLUSH(6)
       IF(LOK.EQ.1)GO TO 320
       LINITL=1
       PCUT=HALF
       CALL ERROCB
       IF(LOK.NE.2) GO TO 200
       LOK=0
       IF(KINC.EQ.1) CALL XIT
       GO TO 660
  320  CONTINUE
       KITRK=KITER-(KREFK*MITRK)
       LINITL=1
       IF(LINEAR.NE.0) LINITL=0
       IF((LCREEP.EQ.1.OR.LCREEP.EQ.3).AND.LARGE.EQ.0)LINITL=0
       IF(LQUASN.EQ.1.AND.KITRK.LT.MITRK) LINITL=0
  330  CONTINUE
       LLHS=LINITL
       LLHSK=LLHS
       LLHSM=0
       LELOP=2
C      PRINT*,'CALLING ELMPC2'
       CALL ELMPC2
C      PRINT*,'AFTER ELMPC2'
       IF(LRIKS.EQ.1)CALL RIKDU1
       KITGEN=KITGEN+1
       LINMAT=LINEAR
       LSTRN=1
       LMDBW=0
       IF(LPORPS.EQ.0)GO TO 40
       CALL EXECPP
   40  CONTINUE
       LOK=1
       LSTRN=1
       LRHS=1
       LGLOBR=0
       IF(LINITL.EQ.0.AND.IGLOBV.NE.IGLOBX) LGLOBR=1
       LINMAT=LINEAR
       LMDBW=1
       LHYBOX=1
C1  INSERTED TEXT
       LEVEL1=0
       LEVEL2=0
       MAXL1=0
       MAXL2=0
       UMEROR=ZERO
       ITGEN=KITGEN
C      PRINT*,'CALLING ELGEN WITH ITGEN=',ITGEN
C2
       CALL ELGEN(SINT(IEDBR))
C1  INSERTED TEXT
C      PRINT*,'AFTER ELGEN'
```

```
      PRINT*,'TOTAL NUMBER OF LEVEL 1 ITERATIONS=',LEVEL1
C     PRINT*,'TOTAL NUMBER OF LEVEL 2 ITERATIONS=',LEVEL2
      PRINT*,'MAXIMUM NUMBER OF LEVEL 1 ITERATIONS=',MAXL1
C     PRINT*,'MAXIMUM NUMBER OF LEVEL 2 ITERATIONS=',MAXL2
C     CALL PAGING (4)
C     WRITE (30,999) KINC,KITER,LEVEL1,LEVEL2,MAXL1,MAXL2
  999 FORMAT(6I10)
C LA
C
C      IF (KITER.GE.4.AND.UMEROR.GT.1.5D0) THEN
C       LSHAF1=0
C       LCUTBK=1
C       PCUT=.85/UMEROR
C       PCUT=0.8D0
C       PRINT*,'CUTBACK BECAUSE UMEROR.GT.1.5D0'
C       CALL PAGING (1)
C       CALL ERROCB
C       IF (LOK.NE.2) GO TO 200
C       LOK=0
C       IF (KINC.EQ.1) CALL XIT
C       GO TO 660
C      END IF
C2
      IF(LOK.EQ.1)GO TO 400
   45 CONTINUE
      IF(LCUTBK.EQ.0) GO TO 50
C1  INSERTED TEXT
      PRINT*,'CUTBACK BECAUSE LCUTBK.NE.0.AND.LOK.NE.1 FROM ELGEN'
      CALL PAGING (1)
C2
      LSHAF1=0
      PCUT=.25
      CALL ERROCB
      IF(LOK.NE.2) GO TO 200
      LOK=0
      IF(KINC.EQ.1) CALL XIT
      GO TO 660
   50 CONTINUE
      IF(LITFRP.EQ.0) GO TO 395
      LFLAGX=4
      N1=KITER
      N2=NGCLOS
      N3=NGOPEN
      CALL ERMESS(LFLAGX,N1,N2,N3,A1)
  395 CONTINUE
      IF(LINITL.NE.0)GO TO 396
      LINITL=1
      GO TO 330
  396 CONTINUE
      KITER=KITER+1
      IF(KITER.LE.MITER) GO TO 300
      IF(LSTAT.NE.1.AND.LCREEP.EQ.0) GO TO 300
      IF(LITFRP.EQ.0) GO TO 397
      LFLAGX=5
      CALL ERMESS(LFLAGX,N1,N2,N3,A1)
  397 CONTINUE
      LSHAF1=0
      LCUTBK=1
      DTNEWS=DMAX1(0.25*DATIME,DTMIN)
      IF(DATIME.GT.1.1*DTMIN)GO TO 200
      LFLAGX=6
      CALL ERMESS(LFLAGX,N1,N2,N3,A1)
  400 CONTINUE
C  RESIDUAL CHECK
      CALL ERROR
      IF(LOK.EQ.1)GO TO 650
      IF(LOK.NE.2)GO TO 410
      LOK=0
      GO TO 660
  410 CONTINUE
      IF(LINEAR.EQ.0)GO TO 500
      LFLAGX=7
      CALL ERMESS(LFLAGX,N1,N2,N3,A1)
      GO TO 660
  500 CONTINUE
      KITER=KITER+1
C1  INSERTED TEXT
      IF (LCUTBK.EQ.1) PRINT*,'CUTBACK BECAUSE LCUTBK.EQ.1 FROM ERROR'
      IF (LCUTBK.EQ.1) CALL PAGING (1)
C2
      IF(LCUTBK.EQ.1) GO TO 200
      GO TO 300
  650 CONTINUE
      IF(MLEVEL.NE.0)CALL SUPREC(SINT(IEDBR),SINT(IEFR))
      IF(LCREEP.EQ.0) GO TO 660
      CALL CRPSCL
      IF(LOK.EQ.1)GO TO 660
      IF(LCUTBK.EQ.1)GO TO 200
      IF(KITER.GT.MITER)GO TO 200
      KITER=KITER+1
      GO TO 320
  660 CONTINUE
      LFLAG=0
      IF(LFLAG1.NE.0) GO TO 668
      IF(MAXVIO.EQ.0) GO TO 662
      IF(KAXVIO.EQ.0) GO TO 662
      LFLAGX=8
      N1=KAXVIO
      CALL ERMESS(LFLAGX,N1,N2,N3,A1)
      LFLAG=1
  662 CONTINUE
      IF(MAXCHP.EQ.0) GO TO 664
      IF(KAXCHP.EQ.0) GO TO 664
      LFLAGX=9
      N1=KAXCHP
      CALL ERMESS(LFLAGX,N1,N2,N3,A1)
      LFLAG=1
  664 CONTINUE
      IF(LFLAG.EQ.0) GO TO 666
      LFLAGX=10
      CALL ERMESS(LFLAGX,N1,N2,N3,A1)
  668 CONTINUE
C1  INSERTED TEXT
      PRINT*,'UMEROR=',UMEROR
      CALL PAGING (1)
      IF (UMEROR.GT.1.25) THEN
       LSHAF1=0
       LCUTBK=1
       IF (DATIME.LE.DTMIN) THEN
        PRINT*,'TOO MUCH SUBDIVISION - ANALYSIS TERMINATED'
        CALL XIT
       END IF
       DTNEWS=0.85*DATIME/UMEROR
       if ((kiter.gt.5).and.(UMEROR.LT.1.)) then
             DTNEWS=DATIME*(1.+(1./UMEROR-1.)*(1-RESMAX(1)/PTOL))
       endif
       DTNEWS=DMAX1(DTNEWS,DTMIN)
       UMEROR=ZERO
```

```
       PRINT*,'CUTBACK BECAUSE CONSTITUTIVE ERROR TOO LARGE'
       CALL PAGING (1)
       GO TO 200
      ELSE IF (UMEROR.GT.0.8D0) THEN
       DTNEWS=DATIME/UMEROR
      ELSE IF (UMEROR.GT.0.5D0) THEN
       DTNEWS=1.25D0*DATIME
      ELSE
       DTNEWS=1.5D0*DATIME
      END IF
      DTNEWS=DMAX1(DTNEWS,DTMIN)
      DTNEWS=DMIN1(DTNEWS,DTMAX)
      IF (KITER.GT.4) THEN
C     if (kiter.gt.5) then
       PRINT*,'TIME STEP NOT INCREASED BECAUSE THIS INCREMENT TOOK ',
     1 KITER,' ITERATIONS'
       CALL PAGING (1)
       DTNEWS=DATIME
       IF (UMEROR.GT.1) DTNEWS=DTNEWS/UMEROR
       IF (KITER.GT.6) THEN
        DTNEWS=DATIME/TWO
        DTNEWS=DMAX1(DTNEWS,DTMIN)
        PRINT*,'TIME STEP HALVED, DTNEWS=',DTNEWS
        CALL PAGING (1)
       END IF
      ELSE
       PRINT*,'NEXT TIME STEP=',DTNEWS
       CALL PAGING (1)
      END IF
C2
      CALL DBSWAP(7,8,JRCD)
      JRCD=1
      CALL DBALOC(2,8,JRCD)
      CALL TIMEUP
      CALL TIMOUT
      CALL NODUP(SINT(IMDR))
      CALL OUT1
      IF(MLEVEL.NE.0)CALL SUPO1
      KCUTS=0
      IF(LREST.NE.0) CALL RESTAR(SINT(IMDR),SINT(INSR))
      IF(LFILE.NE.0) CALL DBFILE(10,SINT(IMFWA),JRCD)
      LFILE=0
      IF(LOK.EQ.0) CALL XIT
      KINC=KINC+1
      LTRAMA=0
C1  INSERTED TEXT
      UMEROR=ZERO
C2
      IF(LSTEND.EQ.0) GO TO 200
C     PRINT*,'LEAVING EXECS'
      RETURN
      END
      SUBROUTINE HETVAL(JMTYPE,T,TIME,DTIME,SVAR,FLUX,PREDEF)
C     THIS ROUTINE BELONGS IN MAIN
      IMPLICIT REAL*8(A-H,O-Z)
C     COMMON/CLINES/VERSN,DAT(2),TIM,NLPAGE,KLINE,KPAGE,JINP,JOUTP
C     DIMENSION SVAR(1),PREDEF(1)
C     WRITE(JOUTP,100)
C 100 FORMAT(10X,'***ERROR -- USER SUBROUTINE HETVAL IS MISSING')
C     CALL XIT
      RETURN
      END
```

Appendix E

Paper 1

Thermal Aspects Of Shear Localization In Microporous Viscoplastic Solids

by

A. ZAVALIANGOS & L. ANAND

Submitted to *International Journal of Numerical Methods in Engineering*, July 1990
Appeared January 1992

I. INTRODUCTION

Numerous experimental observations (e.g., Tipper[1], Puttick[2,3], Rogers[4], Bluhm and Morrisey[5]) have confirmed that void nucleation, growth and coalescence is a central characteristic of ductile fracture. These experimental observations in turn have led to several theoretical studies of the growth of isolated voids in plastically deforming materials (e.g., McClintock[6,7]; Rice and Tracey[8]; Budiansky, Hutchinson and Slutsky[9]), and to the formulation of phenomenological constitutive models for microporous ductile solids (e.g., Kuhn and Downey[10], Green[11], Gurson[12], Shima and Oyane[13]). Gurson's constitutive model is probably the most widely used model of its type available for the rate-independent, isothermal, idealization of plastic flow at low homologous temperatures. This model was modified slightly by Tvergaard[14,15] to push it towards agreement with certain aspects of his two-dimensional finite element calculations of shear localization in a square array of cylindrical holes. For a recent comparison of predictions from Gurson-Tvergaard type constitutive equations and corresponding three-dimensional computations of void growth of initially spherical voids in periodic cubic arrays, see Hom and McMeeking[16]. The rate-independent idealization of Gurson's model was relaxed by Pan, Saje and Needleman[17] who took the response of the matrix material to be power-law viscoplastic, and proposed a flow potential for the macroscopic plastic stretching based on Gurson's yield function, as modified by Tvergaard. Later, Tvergaard and Needleman[18] proposed a modification of the Gurson model to account for the effects of rapid void coalescence at failure.

For purposes of numerical implementation in finite element programs, Needleman and co-workers (e.g., Peirce, Shih, and Needleman[19] , Becker and Needleman[20]) have developed a semi-implicit "forward gradient" type time-integration procedure for the rate-dependent* case. Using their constitutive models and computational procedures Needleman, Tvergaard and co-workers have developed a computational capability for dealing with the mechanics of void growth as a basic failure mechanism. They have performed numerical analyses of various "standard test specimens" (e.g., Tvergaard and Needleman[18,22] , Becker, Needleman, Richmond, and Tvergaard[23]) to illustrate the ability of the constitutive models of porous ductile solids to simulate tensile ductile fracture in structural materials; for a recent review see Tvergaard[24].

The studies of Needleman, Tvergaard and co-workers have clearly shown that localization of deformation into shear bands plays an important role in the ductile fracture process governed by flow softening due to hole growth. At high rates of deformation softening may also result due to thermal effects. The results of the work of Needleman *et al.* are encouraging to the point that it is important to extend their work to include the effects of temperature.

The purpose of this paper is to report on the framework of a simple phenomenological, state variable constitutive model for large deformations of isotropic, thermo-elastic-viscoplastic, porous materials, and a new semi-implicit, incrementally objective time-integration procedure for these constitutive equations. The constitutive equations and time-integration procedure have been implemented in the commercial finite element program ABAQUS[25], and used to

---

*A fully implicit Euler backward algorithm for the isothermal, rate-independent Gurson model has been recently formulated by Aravas[21].

study shear band formation and ductile fracture initiation triggered by flow softening due to the effects of void growth and/or deformation heating.

The plan of this paper is as follows. After introducing our notation in Section II, we review the basic structure of an isotropic, temperature dependent constitutive model for elastic-viscoplastic porous materials in Section III. The evolution equation for stress in this model employs the Jaumann derivative which renders the model properly frame-indifferent. This entails the use of a hypoelastic relation to model elasticity. It is well known that in the absence of plastic flow, hypoelastic equations for stress lead to dissipation. However, it is easy to show (e.g., Anand[26]) that the hypoelastic form of the constitutive equation for stress is a good approximation to a proper hyperelastic equation under situations where elastic stretches remain infinitesimal. This is a good approximation for most metals.

In Section IV we provide details of our one-step, semi-implicit time-integration procedure for the constitutive model. An important characteristic of a time-integration algorithm for formulations which use a hypoelastic relation to model elasticity, is that it should be "incrementally objective". The formulation of time-integration schemes which ensure objectivity during computations has been bothersome. Important contributions to the formulation of objective time-integration algorithms have been made, for example, by Hughes and Winget[27] , Rubinstein and Atluri[28], Reed and Atluri[29,30], Nagtegaal and Veldpaus[31] , Hughes[32] and Nagtegaal and Rebelo[33] . A detailed examination of this issue has recently been made by Weber, Lush, Zavaliangos and Anand[34], and the discussion of incremental objectivity presented here are taken from this paper. To ensure stability and accuracy of our semi-implicit time-integration procedure, it is necessary to take variable time-steps; a variable time-stepping algorithm is also detailed in Section IV.

In Section V we briefly discuss certain aspects of the implementation of our constitutive equations and time-integration algorithm in the finite element program ABAQUS[25], and we present a few examples of calculations concerning shear band formation which illustrate the physical effects of softening due to void growth and thermal effects in shear band formation and ductile failure initiation in a plane strain tension test. We conclude the paper in Section VI, with some closing remarks.

II. NOTATION

For the most part we shall use notation which is standard in modern continuum mechanics :

$\mathbf{p}$	material point of a body in a reference configuration $\mathcal{B}_0$ at time 0;
$\mathbf{x} = \bar{\mathbf{x}}(\mathbf{p}, t)$	motion;
$\mathcal{B}_t = \bar{\mathbf{x}}(\mathcal{B}_0, t)$	configuration of the body at t ;
$\mathbf{p} = \bar{\mathbf{p}}(\mathbf{x}, t)$	reference map;
$\mathbf{F}(\mathbf{x}, t) \equiv \frac{\partial}{\partial \mathbf{p}}\bar{\mathbf{x}}(\mathbf{p}, t), \qquad \det \mathbf{F}(\mathbf{x}, t) > 0$	deformation gradient;
$\dot{\mathbf{x}}(\mathbf{p}, t) \equiv \frac{\partial}{\partial t}\bar{\mathbf{x}}(\mathbf{p}, t)$	velocity;
$\mathbf{v} \equiv \dot{\mathbf{x}}(\bar{\mathbf{p}}(\mathbf{x}, t), t)$	spatial description of velocity;
$\mathbf{L}(\mathbf{x}, t) \equiv \frac{\partial}{\partial \mathbf{x}}\mathbf{v}(\mathbf{x}, t)$	velocity gradient;
$\mathbf{D}(\mathbf{x}, t) \equiv \mathrm{sym}\ \mathbf{L} = (1/2)(\mathbf{L} + \mathbf{L}^T)$	stretching;
$\mathbf{W}(\mathbf{x}, t) \equiv \mathrm{skw}\ \mathbf{L} = (1/2)(\mathbf{L} - \mathbf{L}^T)$	spin;
θ	absolute temperature;
$\mathbf{T}$	Cauchy stress
$p = -(1/3)\ \mathrm{tr}\ \mathbf{T}$	mean normal pressure;
$\mathbf{S} = \mathbf{T} + p\mathbf{1}$	Cauchy stress deviator;
$S = \sqrt{\mathbf{S} \cdot \mathbf{S}}$	magnitude of stress deviator;
$\mathbf{N} = \mathbf{S}/S$	direction of the stress deviator;
$\mathbf{T}^{\nabla} \equiv \dot{\mathbf{T}} - \mathbf{W}\mathbf{T} + \mathbf{T}\mathbf{W}$	Jaumann derivative of stress;
$\mathbf{z} = \bar{\mathbf{x}}(\mathbf{p}, \tau)$	place occupied by $\mathbf{p}$ at time $\tau > t$;
$\mathbf{z} = \bar{\mathbf{x}}(\bar{\mathbf{p}}(\mathbf{x}, t), \tau) \equiv \bar{\mathbf{x}}_t(\mathbf{x}, \tau)$	relative motion;
$\mathbf{F}_t(\mathbf{x}, \tau) = \frac{\partial}{\partial \mathbf{x}}\bar{\mathbf{x}}_t(\mathbf{x}, \tau), \qquad \det \mathbf{F}_t(\mathbf{x}, \tau) > 0$	relative deformation gradient;
$\mathcal{B}_\tau = \bar{\mathbf{x}}(\mathcal{B}_0, \tau)$	configuration of the body at time τ.

For brevity, and whenever there is no danger of confusion, we will omit the arguments $(\mathbf{x}, t)$, $(\mathbf{p}, \tau)$ etc., for the various field quantities listed above.

III. CONSTITUTIVE MODEL

We confine our attention to voided materials which may be reasonably considered to be isotropic in their overall macroscopic response. The external state variables for the constitutive model are taken to be the pair $(\mathbf{T}, \theta)$, where $\mathbf{T}$ is the applied Cauchy stress and θ is the absolute temperature. The internal state variables are taken to be the scalars (f, s). The variable f is the volume fraction of voids. The variable s has the physical dimensions of stress, it represents an isotropic resistance to plastic flow offered by the matrix material. Changes in the value of s account for isotropic strain hardening of the matrix.

Further, an equivalent tensile stress in the matrix, σ_m, is implicitly defined by the solution to an equation of the form:

$$\Phi = \hat{\Phi}(\mathbf{T}, f, \sigma_m) = 0. \qquad (1)$$

The function $\hat{\Phi}$ is isotropic, and hence it depends on $\mathbf{T}$ only through its invariants. Neglecting the effect of the third invariant of $\mathbf{T}$ we have:

$$\Phi = \hat{\Phi}(S, p, f, \sigma_m) = 0, \tag{2}$$

where S is the magnitude of the stress deviator $\mathbf{S}$, and p is the mean normal pressure. In the limit of fully dense solid, we assume that the function $\hat{\Phi}$ has the Mises form:

$$\lim_{f \to 0} \hat{\Phi} = \left\{ \frac{(3/2)\, S^2}{\sigma_m^2} - 1 \right\}. \tag{3}$$

The rate-dependent constitutive model that we shall consider consists of coupled differential evolution equations for the state variables $(\mathbf{T}, s, f)$. The evolution equation for θ is provided by the equation for balance of energy. The "direction" of plastic flow is taken to be directed normal to a plastic potential surface which is taken to be defined by the same equation (2) which defines σ_m. No yield condition and switching rules are employed. Plastic flow is assumed to occur for all non-zero values of stress, although at low stresses the rate of flow may be immeasurably small. This rate-dependent model belongs to the so-called class of 'unified constitutive equations' in which 'plasticity' and 'creep' are unified, in that they are described by the same set of flow and evolutionary equations.

The evolution equations of the governing variables $(\mathbf{T}, s, f, \theta)$ are:

- Evolution equation for the stress $\mathbf{T}$:

  $$\mathbf{T}^{\nabla} = \mathcal{L}[\mathbf{D} - \mathbf{D}^p - \alpha\, \dot{\theta} \mathbf{1}], \tag{4}$$

  where $\mathbf{T}^{\nabla}$ is the Jaumann derivative of $\mathbf{T}$; $\mathcal{L} \equiv 2\mu\mathcal{I} + \{\kappa - (2/3)\mu\}\mathbf{1}\otimes\mathbf{1}$, with $\mu = \hat{\mu}(\theta, f)$, $\kappa = \hat{\kappa}(\theta, f)$, $\mathbf{1}$, and $\mathcal{I}$, the shear modulus, the bulk modulus, the second order identity, and the fourth order identity, respectively, is the elasticity tensor; $\mathbf{D}^p$ is the plastic stretching tensor; and $\alpha = \hat{\alpha}(\theta, f)$ the coefficient of thermal expansion.

  The plastic stretching tensor $\mathbf{D}^p$ is given by a normality flow rule:

  $$\mathbf{D}^p = \quad \dot{\gamma}\, \partial_{\mathbf{T}} \Phi \quad = \quad \dot{\gamma} \left\{ (\partial_S \Phi)\, \mathbf{N} - \frac{1}{3}\, (\partial_p \Phi)\, \mathbf{1} \right\}. \tag{5}$$

  The parameter $\dot{\gamma}$ is determined form the dissipated power expression

  $$\mathbf{T} \cdot \mathbf{D}^p = (1 - f)\, \sigma_m\, \dot{\epsilon}_m^p, \tag{6}$$

  which gives

  $$\dot{\gamma} = \left[\frac{(1 - f)\, \sigma_m}{S\, \partial_S \Phi + p\, \partial_p \Phi} \right] \dot{\epsilon}_m^p, \tag{7}$$

  where

  $$\dot{\epsilon}_m^p = \hat{\dot{\epsilon}}_m^p(\sigma_m, \theta, s) > 0 \tag{8}$$

  is an equivalent tensile plastic strain rate in the matrix.

- Evolution equation for s:

$$\dot{s} = g(\sigma_m, \theta, s). \tag{9}$$

- Evolution equation for f:

  Neglecting void nucleation effects, from plastic incompressibility of the matrix and the balance of mass, the evolution equation for f is

$$\dot{f} = (1 - f)\ \mathrm{tr}\,\mathbf{D}^p. \tag{10}$$

- Evolution equation[†] for θ:

$$\dot{\theta} \doteq (\rho c)^{-1}\ \{\mathrm{div}\,(\lambda\,\mathrm{grad}\theta) + \omega\,\mathbf{T}\cdot\mathbf{D}^p\}, \tag{11}$$

  where $c = \hat{c}(\theta, f)$ is the specific heat, and $\lambda = \hat{\lambda}(\theta, f)$ is the thermal conductivity. Also ω is a scalar in the range $0.85 \leq \omega \leq 1$ which represents the fraction of plastic work converted to heat.

Specific Constitutive Functions:

From the constitutive framework for the rate and temperature dependent deformation behavior for isotropic porous metals outlined above, it is clear that to complete the thermoelastic part of the constitutive model we need to provide specific forms of the functions $\mu = \hat{\mu}(\theta, f)$, $\kappa = \hat{\kappa}(\theta, f)$, and $\alpha = \hat{\alpha}(\theta, f)$ for the shear modulus, the bulk modulus, and the coefficient of thermal expansion, respectively. Also, for the thermal part of the problem we need to specify the functions $c = \hat{c}(\theta, f)$, and $\lambda = \hat{\lambda}(\theta, f)$ for the specific heat and the thermal conductivity. The results of theoretical estimates for the dependence of μ, κ, α, c, and λ on f and the corresponding properties of the matrix material (denoted by a subscript m), based on "self-consistent" calculations for a macroscopically isotropic composite of a random dispersion of roughly spherical holes in a matrix material have been summarized by Budiansky[35] , and these are repeated below for convenience:

- Elastic moduli:

$$\begin{aligned} f\,[1 - a]^{-1} + (1 - f)\,[1 - a + a(\kappa_m/\kappa)]^{-1} &= 1, & (12)\\ f\,[1 - b]^{-1} + (1 - f)\,[1 - b + b(\mu_m/\mu)]^{-1} &= 1, & (13)\end{aligned}$$

  where

$$\begin{aligned} a &= \frac{1}{3}\left(\frac{1+\nu}{1-\nu}\right), & (14)\\ b &= \frac{2}{15}\left(\frac{4-5\nu}{1-\nu}\right), & (15)\\ \nu &= \left(\frac{3\kappa - 2\mu}{6\kappa + 2\mu}\right), & (16)\end{aligned}$$

[†] From the equation of energy balance and Fourier's law of heat conduction.

with $\mu_m = \hat{\mu}_m(\theta)$ and $\kappa_m = \hat{\kappa}_m(\theta)$ the temperature dependent moduli of the matrix material. Equations (12) and (13) are a pair of simultaneous equations for the overall effective moduli which need to be solved numerically.

For the temperature dependence of the elastic moduli of the matrix, it is found that the temperature variation is linear with respect to the homologous temperature (θ/θ_m) for a reasonably large range about a reference temperature (θ_0/θ_m) (e.g. Simmons and Wang[36], Frost and Ashby[37]):

$$\mu_m = \mu_{m,0}\left[1 - \chi_1\left\{(\theta/\theta_m) - (\theta_0/\theta_m)\right\}\right], \tag{17}$$

$$\kappa_m = \kappa_{m,0}\left[1 - \chi_2\left\{(\theta/\theta_m) - (\theta_0/\theta_m)\right\}\right], \tag{18}$$

where $\mu_{m,0}, \kappa_{m,0}$ are values of the elastic moduli of the matrix at the reference temperature θ_0, χ_1, χ_2 are constants, and θ_m is the melting temperature of the material.

- Coefficient of thermal expansion:

$$\alpha = \alpha_m, \qquad \alpha_m = \hat{\alpha}_m(\theta). \tag{19}$$

For a voided material, the overall bulk thermal expansion coefficient is equal to temperature dependent coefficient of thermal expansion of the matrix material.

- Specific Heat:

$$c \doteq (1 - f)\, c_m, \qquad c_m = \hat{c}_m(\theta). \tag{20}$$

- Thermal conductivity:

$$\lambda = (1 - (3/2)\, f)\ \lambda_m, \qquad \lambda_m = \hat{\lambda}_m(\theta). \tag{21}$$

To complete the viscoplastic part of the constitutive model the major task involves specifying particular forms for the flow potential Φ, the matrix strain rate function $\hat{\dot{\epsilon}}_m^p$ and the evolution equation for the matrix deformation resistance s. For the flow potential, the most widely used form is the Gurson-Tvergaard-Needleman form

$$\Phi = \left\{\frac{(3/2)\, S^2}{\sigma_m^2} - 1 + 2\, q_1\, f^*\, \cosh\left((3/2)\, q_2\, \frac{-p}{\sigma_m}\right) - (q_1\, f^*)^2\right\} = 0. \tag{22}$$

Tvergaard[14] suggests values of $q_1 = 1.5$ and $q_2 = 1$. Further,

$$f^* = \hat{f}^*(f) = \left\{ \begin{array}{ll} f & \text{if } f \leq f_c \\ f_c + ((f_u^* - f_c)/(f_f - f_c))\, (f - f_c) & \text{otherwise} \end{array} \right\}. \tag{23}$$

In equation (23) $f_u^* \equiv 1/q_1$, and f_c and f_f are material parameters called the critical void volume fraction and the final void volume fraction, respectively. Tvergaard and Needleman[18] suggest the values $f_c \approx 0.15$, and $f_f \approx 0.25$. In this model, as $f \rightarrow f_f$, $f^* \rightarrow f_u^*$, and the material looses all stress carrying capacity.

For the matrix strain rate function there is a paucity of good data at high strain rates. In our calculations we will use the following function suggested by Lindholm and Johnson[38]:

$$\dot{\epsilon}_m^p = \dot{\epsilon}_0 \exp \left[\frac{1}{C} \left\{ \frac{\sigma_m}{s \left(\frac{\theta_m - \theta}{\theta_m - \theta_0} \right)^a} - 1 \right\} \right], \tag{24}$$

with

$$s(t) \equiv A + B \left(\epsilon_m^p(t) \right)^n, \tag{25}$$

where $\epsilon_m^p(t) = \int_0^t \dot{\epsilon}_m^p \, dt$ is the equivalent tensile plastic strain in the matrix. With s so defined, there is no need for a separate evolution equation for s. However, it is important to note that such a constitutive assumption does not capture strain rate history effects, which are observed in a wide variety of materials.

IV. TIME-INTEGRATION PROCEDURE

Typical "implicit" finite element procedures for coupled thermo-mechanical problems which use nonlinear constitutive models, generate estimates of increments in nodal displacements and temperatures which are used to calculate the integration point values of the stress $\mathbf{T}$, temperature θ, and other field variables at the end of a time increment. If these stresses and temperatures do not satisfy the weak forms of the equations for equilibrium and balance of energy, then the estimates of the incremental displacement and temperatures are revised, and new end of increment stresses and temperatures are calculated. Iteration continues until the weak forms of the equilibrium equation and the equation for energy balance are satisfied to within acceptable tolerances.

Accordingly, we assume (i) that we are given $(\mathbf{x}, \theta) \in \mathcal{B}_t$ and the list of variables

$$\{\mathbf{T}(\mathbf{x}, t), s(\mathbf{x}, t), f(\mathbf{x}, t)\}, \tag{26}$$

at time t, with the Cauchy stress $\mathbf{T}(\mathbf{x}, t)$ satisfying equilibrium; and (ii) that we are also given $(\mathbf{z}, \theta) \in \mathcal{B}_\tau$. With these given, we take the computational problems to be:

1. A stable, accurate and efficient computation of of the list $\{\mathbf{T}(\mathbf{z}, \tau), s(\mathbf{z}, \tau), f(\mathbf{z}, \tau)\}$.

2. The computation of derivatives, consistent with the time integration procedure, to be used in a Newton type iterative method for revising the estimated nodal displacements and temperatures.

These are the main problems at hand, with item 1 above being the *central problem*, because derivative matrices are used only in the search for displacement and temperature fields but in the end have no effect on the accuracy of the solution. Indeed, in "explicit" finite element procedures, which are widely used in large scale inelastic analysis, derivative matrices are not required, and item 1 above is the only function required of a "constitutive equation subroutine".

Accordingly, we detail our time-integration procedure in what follows, and relegate a summary of the derivatives to the APPENDIX. The time-integration procedure discussed below is for for the general form of the constitutive equations (1 – 11). The specific forms (12 – 25) are used for the illustrative calculations discussed in Section V.

Thus, the problem at hand is that given an assumed relative deformation gradient $\mathbf{F}_t(\tau)$ and a temperature increment field $\Delta\theta = \theta(\tau) - \theta(t)$ between two neighboring configurations $\mathcal{B}_t$ and $\mathcal{B}_\tau$ of a body, we need to integrate the constitutive equations across a time-step[‡], $\Delta t = \tau - t$, to obtain $\{\mathbf{T}(\mathbf{z},\tau), s(\mathbf{z},\tau), f(\mathbf{z},\tau)\}$. To this end, in the next subsection we first transform the constitutive equations to a convenient form for performing such an integration.

A Transformed Set of Constitutive Equations

In the constitutive equations considered here, the elasticity is modeled in hypoelastic form, with the stress rate being taken as the Jaumann derivative, so as to make the constitutive model "frame-indifferent" or "objective". The formulation of numerical time-integration procedures which ensure objectivity during computations has been endeavored by many authors, here, we describe an incrementally objective procedure based on the recent work of Weber, Lush, Zavaliangos, and Anand[34].

Let $\mathbf{P}(\zeta)$ be a rotation tensor which is defined to be the solution of the initial-value problem

$$\dot{\mathbf{P}}(\zeta) = \mathbf{W}(\zeta)\mathbf{P}(\zeta), \qquad t \leq \zeta \leq \tau, \tag{27}$$

$$\mathbf{P}(t) = \mathbf{1}, \tag{28}$$

where $\mathbf{W}(\zeta)$ is the spin tensor.

Using rotations $\mathbf{P}(\zeta)$ so-defined, we define the *bar-transformation* of a symmetric second-order spatial tensor $\mathbf{A}(\zeta)$ by

$$\bar{\mathbf{A}}(\zeta) \equiv \mathbf{P}^T(\zeta)\,\mathbf{A}(\zeta)\,\mathbf{P}(\zeta). \tag{29}$$

In particular,

$$\bar{\mathbf{T}}(\zeta) = \mathbf{P}^T(\zeta)\mathbf{T}(\zeta)\mathbf{P}(\zeta), \quad \text{with} \quad \bar{\mathbf{T}}(t) = \mathbf{T}(t). \tag{30}$$

Further, upon using (27) and (30) we have the important result

$$\dot{\bar{\mathbf{T}}}(\zeta) = \mathbf{P}^T(\zeta)\mathbf{T}^{\nabla}(\zeta)\mathbf{P}(\zeta). \tag{31}$$

We shall use these definitions and results to obtain a "bar-transformation" of the constitutive model of Section III. After transformation, the evolution equations for stress in both models involve only the material time derivative of $\bar{\mathbf{T}}$ instead of the more complicated Jaumann derivative of $\mathbf{T}$, and this greatly aids the integration procedure.

[‡] Since plasticity is path-dependent, we must restrict the time increment Δt, the relative deformation gradient $\mathbf{F}_t(\tau) \equiv \mathbf{F}(\tau)\mathbf{F}(t)^{-1}$ and the temperature increment $\Delta\theta$ to be (in some sense) "small".

Using (2 - 11), the isotropy of $\mathcal{L}$, and the isotropy of the other constitutive functions, we obtain the following bar form of the constitutive equations:

1. Evolution equation for the stress $\bar{\mathbf{T}}$:

$$\dot{\bar{\mathbf{T}}} = \mathcal{L}\left[\bar{\mathbf{D}} - \bar{\mathbf{D}}^p - \alpha\dot{\theta}\mathbf{1}\right], \tag{32}$$

with

$$\bar{\mathbf{D}}^p = \quad \dot{\gamma}\left\{(\partial_S\Phi)\,\bar{\mathbf{N}} - (1/3)\,(\partial_p\Phi)\,\mathbf{1}\right\}, \tag{33}$$

where

$$\begin{aligned}
p &= -(1/3)\,(\mathrm{tr}\,\bar{\mathbf{T}})\,, && (34)\\
\bar{\mathbf{S}} &= \bar{\mathbf{T}} + p\mathbf{1}, && (35)\\
S &= \sqrt{\bar{\mathbf{S}}\cdot\bar{\mathbf{S}}}, && (36)\\
\bar{\mathbf{N}} &= \bar{\mathbf{S}}/S, && (37)\\
0 &= \hat{\Phi}\,(S,p,f,\sigma_m)\,, && (38)\\
\dot{\gamma} &= \left[\frac{(1-f)\,\sigma_m}{S\,\partial_S\Phi\,+\,p\,\partial_p\Phi}\right]\dot{\epsilon}^p_m\,, && (39)\\
\dot{\epsilon}^p_m &= \hat{\dot{\epsilon}}^p_m(\sigma_m,\theta,s). && (40)
\end{aligned}$$

2. Evolution equation for the deformation resistance s :

$$\dot{s} = g(\sigma_m,\theta,s). \tag{41}$$

3. Evolution equation for the void volume fraction f :

$$\dot{f} = (1-f)\,\mathrm{tr}\,\bar{\mathbf{D}}^p. \tag{42}$$

4. Evolution equation for the temperature θ:

$$\dot{\theta} \doteq (\rho c)^{-1}\left\{\mathrm{div}\,(\lambda\,\mathrm{grad}\theta) + \omega\,\bar{\mathbf{T}}\cdot\bar{\mathbf{D}}^p\right\}. \tag{43}$$

Once the constitutive equations are expressed in the bar form, the response of the material to imposed increments of deformation and temperature are obtained by first integrating the constitutive problem expressed in terms of $\dot{\bar{\mathbf{T}}}$, $\dot{s}$, and $\dot{f}$. *Note that $\bar{\mathbf{D}}$ and $\dot{\theta}$ are the driving quantities in this integration problem.* After integration of the constitutive problem, the stress tensor $\bar{\mathbf{T}}(\tau)$ is transformed to obtain

$$\mathbf{T}(\tau) = \mathbf{P}(\tau)\bar{\mathbf{T}}(\tau)\mathbf{P}^T(\tau)\,. \tag{44}$$

To this end, one needs to interpolate for $\bar{\mathbf{D}}(\zeta) \equiv \mathbf{P}^T(\zeta)\mathbf{D}(\zeta)\mathbf{P}(\zeta)$ for all times $\zeta \in [t,\tau]$, and $\mathbf{P}(\tau)$. We consider this interpolation problem below.

Incremental Objectivity

Consider a relative motion

$$\mathbf{y} = \bar{\mathbf{x}}_t(\mathbf{x}, \zeta), \qquad t \leq \zeta \leq \tau, \tag{45}$$

and let $\bar{\mathbf{x}}_t^*$ be another motion of the body which is related to $\bar{\mathbf{x}}_t$ by a change in frame:

$$\bar{\mathbf{x}}_t^*(\mathbf{x}, \zeta) = \mathbf{q}(\zeta) + \mathbf{Q}(\zeta)\left[\bar{\mathbf{x}}_t(\mathbf{x}, \zeta) - \mathbf{o}\right], \tag{46}$$

where $\mathbf{q}(\zeta)$ is a point in space, $\mathbf{o}$ is a fixed origin, and $\mathbf{Q}(\zeta)$ is a rotation with $\mathbf{Q}(t) = \mathbf{1}$. A two-point time-integration algorithm for the evolution equations for $\{\mathbf{T}, s, f\}$ is said to be incrementally objective if for all relative motions $\mathbf{z} = \bar{\mathbf{x}}_t(\mathbf{x}, \tau)$ the numerical approximations to $\mathbf{T}(\tau)$, $s(\tau)$ and $f(\tau)$ transform under a change in frame according to the same rules as the physical quantities themselves; that is, if

$$\begin{aligned} \mathbf{T}^*(\tau) &= \mathbf{Q}(\tau)\mathbf{T}(\tau)\mathbf{Q}^T(\tau), && (47)\\ s^*(\tau) &= s(\tau), && (48)\\ f^*(\tau) &= f(\tau). && (49) \end{aligned}$$

In a two-point problem, $\{\mathbf{x} | \mathbf{x} \in \mathcal{B}_t\}$ and $\{\mathbf{z} | \mathbf{z} \in \mathcal{B}_\tau\}$ *are the only kinematic data.* Let

$$\mathbf{F}_t(\tau) \equiv \mathbf{F}(\tau)\mathbf{F}(t)^{-1}, \tag{50}$$

be the known relative deformation gradient, and

$$\mathbf{F}_t(\tau) = \mathbf{R}_t(\tau)\,\mathbf{U}_t(\tau) \tag{51}$$

its right polar decomposition. Weber *et al.*[34] show that in such a problem, a numerical time-integration algorithm will be absolutely incrementally objective for the following forms of the interpolation functions for $\bar{\mathbf{D}}(\zeta)$ and $\mathbf{P}(\tau)$:

$$\begin{aligned} \bar{\mathbf{D}}(\zeta) &= \hat{\bar{\mathbf{D}}}(\mathbf{U}_t(\tau), \zeta), \quad \text{with} \quad \hat{\bar{\mathbf{D}}}(\mathbf{1}, \zeta) = \mathbf{0}, && (52)\\ \mathbf{P}(\tau) &= \mathbf{R}_t(\tau). && (53) \end{aligned}$$

Thus, to obtain an absolutely incrementally objective time integration algorithm, one needs to take $\mathbf{P}(\tau) = \mathbf{R}_t(\tau)$, and that the interpolation for $\bar{\mathbf{D}}(\zeta)$ be a function of only the right relative stretch tensor $\mathbf{U}_t(\tau)$ and $\zeta \in [t, \tau]$. Various interpolation functions for $\bar{\mathbf{D}}(\zeta)$ satisfying the above requirement may be envisaged, here, following Nagtegaal & Rebelo[33], and Weber *et al*[34]. We propose the use of the *constant* interpolant

$$\begin{aligned} \bar{\mathbf{D}}(\zeta) &\equiv \bar{\mathbf{D}}_l \quad \cdots\cdots \quad \text{constant, with} && (54)\\ \bar{\mathbf{D}}_l &= \frac{1}{\Delta t} \ln \mathbf{U}_t(\tau), \quad \Delta t = \tau - t. && (55) \end{aligned}$$

We adopt (53-55) in all what follows.

Time-Integration Algorithm

Assume that the state $(\mathbf{T}(t), s(t), f(t), \theta(t))$ at time t is known (note that $\bar{\mathbf{T}}(t) = \mathbf{T}(t)$), and that the relative deformation gradient $\mathbf{F}_t(\tau)$ and the temperature increment $\Delta\theta$ are given. Then the problem is to integrate the evolution equations for $\bar{\mathbf{T}}$, s and f across a time increment $\Delta t = \tau - t$ and thereby calculate $(\bar{\mathbf{T}}(\tau), s(\tau), f(\tau))$, transform $\bar{\mathbf{T}}(\tau)$ to $\mathbf{T}(\tau)$, and march forward in time.

An algorithm to integrate the rate evolution equations should in general be (a) consistent with the constitutive equations, (b) it should be numerically stable, and (c) incrementally objective. We have considered the problem of incremental objectivity. Regarding the other two characteristics, we will use a forward-gradient approximation of the *Euler-backward* method of integration. This method, while consistent, is stable only for small time increments. In our numerical algorithm described below, we will utilize a variable time-marching scheme which will reduce the time step, when necessary, to ensure a stable and accurate procedure. From equations (32-42) and (55), together with the use of the definition of $\mathcal{L}$(see equation (4)), for the Euler-backward method we obtain

$$\begin{aligned}
\bar{\mathbf{S}}(\tau) &= \bar{\mathbf{S}}^*(\tau) - \Delta t\, 2\mu(\tau)\, (\dot{\gamma}\, \partial_S \Phi)(\tau)\, \bar{\mathbf{N}}(\tau), && (56)\\
p(\tau) &= p^*(\tau) - \Delta t\, \kappa(\tau)\, (\dot{\gamma}\partial_p \Phi)(\tau) + 3\,\kappa(\tau)\,\alpha(\tau)\,\Delta\theta, && (57)\\
s(\tau) &= s(t) + \Delta t\, g\left(\sigma_m(\tau), s(\tau), \theta(\tau)\right), && (58)\\
f(\tau) &= f(t) - (1 - f(\tau))\, \Delta t\, (\dot{\gamma}\partial_p \Phi)(\tau), && (59)
\end{aligned}$$

where

$$\begin{aligned}
\bar{\mathbf{S}}^*(\tau) &= \bar{\mathbf{S}}(t) + 2\mu(\tau)\,\Delta\bar{\mathbf{E}}', && (60)\\
p^*(\tau) &= p(t) - \kappa(\tau)\,\mathrm{tr}\,\Delta\bar{\mathbf{E}}, && (61)\\
& && (62)
\end{aligned}$$

are *trial* values for the stress deviator and the pressure at the end of the increment, with

$$\Delta\bar{\mathbf{E}} \equiv \ln \mathbf{U}_t(\tau) \tag{63}$$

the incremental logarithmic strain, and $\Delta\bar{\mathbf{E}}'$ its deviator. For simplicity, since the dependence on f of the thermo-elastic constants is not expected to be strong, in the equations above the values of μ and κ, are taken to be functions of the porosity f at the beginning of the time-step.

In a displacement based finite element program, $\Delta\bar{\mathbf{E}}$ can be computed from known kinematic information. Thus, $\bar{\mathbf{S}}^*(\tau)$ and $p^*(\tau)$ are known at the beginning of the increment. Further, from (56) we observe that

$$\bar{\mathbf{N}}(\tau) = \bar{\mathbf{S}}^*(\tau)/S^*(\tau), \qquad S^*(\tau) \equiv \sqrt{\bar{\mathbf{S}}^*(\tau)\cdot\bar{\mathbf{S}}^*(\tau)}, \tag{64}$$

and hence $\bar{\mathbf{N}}(\tau)$ is also known at the beginning of the solution process. Thus, using (64), the set of equations (56-59) can be reduced to the following set of *scalar* equations:

$$
\begin{aligned}
S(\tau) &= S^*(\tau) - \Delta t\, 2\mu(\tau)\, (\dot\gamma\, \partial_S \Phi)(\tau), && (65)\\
p(\tau) &= p^*(\tau) - \Delta t\, \kappa(\tau)\, (\dot\gamma \partial_p \Phi)(\tau) + 3\kappa(\tau)\, \alpha(\tau)\, \Delta\theta, && (66)\\
s(\tau) &= s(t) + \Delta t\, g\,(\sigma_m(\tau), s(\tau), \theta(\tau))\,, && (67)\\
f(\tau) &= f(t) - (1 - f(\tau))\, \Delta t\, (\dot\gamma \partial_p \Phi)(\tau). && (68)
\end{aligned}
$$

Let

$$
\mathbf{X}(\tau) = \left\{ \begin{array}{c} S(\tau) \\ p(\tau) \\ s(\tau) \\ f(\tau) \end{array} \right\}, \tag{69}
$$

and

$$
\mathbf{G}\,(\mathbf{X}(\tau)) = \left\{ \begin{array}{c} G_1(\cdots) \\ G_2(\cdots) \\ G_3(\cdots) \\ G_4(\cdots) \end{array} \right\} = \left\{ \begin{array}{l} S^*(\tau) - \Delta t\, 2\mu(\tau)\, (\dot\gamma\, \partial_S\Phi)(\tau) \\ p^*(\tau) - \Delta t\, \kappa(\tau)\, (\dot\gamma\partial_p\Phi)(\tau) + 3\kappa(\tau)\,\alpha(\tau)\,\Delta\theta \\ s(t) + \Delta t\, g\,(\sigma_m(\tau), s(\tau), \theta(\tau)) \\ f(t) - (1 - f(\tau))\, \Delta t\, (\dot\gamma\partial_p\Phi)(\tau) \end{array} \right\}, \tag{70}
$$

then the implicit system of scalar equations to be solved for $\mathbf{X}(\tau)$ can be written as

$$
\mathbf{X}(\tau) = \mathbf{G}\,(\mathbf{X}(\tau); \theta(\tau))\,. \tag{71}
$$

For later use we note that the terms $(\dot\gamma\, \partial_S\Phi)(\tau)$ and $(\dot\gamma\partial_p\Phi)(\tau)$ in (70) may be written as

$$
\begin{aligned}
(\dot\gamma\, \partial_S\Phi)(\tau) &= a(\tau)\dot\epsilon^p_m(\tau), \qquad \text{where} \quad a(\tau) \equiv \left[\frac{(1-f)\,\sigma_m\, \partial_S\Phi}{S\,\partial_S\Phi + p\,\partial_p\Phi}\right](\tau), && (72)\\
(\dot\gamma\partial_p\Phi)(\tau) &= b(\tau)\dot\epsilon^p_m(\tau), \qquad \text{where} \quad b(\tau) \equiv \left[\frac{(1-f)\,\sigma_m\, \partial_p\Phi}{S\,\partial_S\,\Phi + p\,\partial_p\,\Phi}\right](\tau). && (73)
\end{aligned}
$$

For small changes in the solution vector, we can write

$$
\mathbf{X}(\tau) \doteq \mathbf{G}\,(\mathbf{X}(t); \theta(\tau)) + \left\{ \frac{\partial}{\partial \mathbf{X}} \mathbf{G}\,(\mathbf{X}; \theta(\tau))\Big|_{\mathbf{X}=\mathbf{X}(t)} \right\}\, (\mathbf{X}(\tau) - \mathbf{X}(t))\,, \tag{74}
$$

from which we have the following *forward-gradient* approximation to the solution vector:

$$
\mathbf{X}(\tau) \doteq \mathbf{X}(t) + \mathbf{A}^*\,(\mathbf{X}(t); \theta(\tau))\, (\mathbf{G}\,(\mathbf{X}(t); \theta(\tau)) - \mathbf{X}(t))\,, \tag{75}
$$

where

$$
\mathbf{A}^*\,(\mathbf{X}(t); \theta(\tau)) \equiv \{\mathcal{I} - \mathbf{A}\,(\mathbf{X}(t); \theta(\tau))\}^{-1}\,, \tag{76}
$$

with

$$
\mathbf{A}\,(\mathbf{X}(t); \theta(\tau)) \equiv \left\{ \frac{\partial}{\partial \mathbf{X}} \mathbf{G}\,(\mathbf{X}; \theta(\tau))\Big|_{\mathbf{X}=\mathbf{X}(t)} \right\}. \tag{77}
$$

If we make the additional approximation:

$$a(\tau) \approx b(t), \qquad b(\tau) \approx b(t), \tag{78}$$

then the equations for $\{S(\tau), p(\tau), s(\tau)\}$ become independent of $f(\tau)$, and these quantities are obtained from

$$\left\{ \begin{array}{c} S(\tau) \\ p(\tau) \\ s(\tau) \end{array} \right\} = \left\{ \begin{array}{c} S(t) \\ p(t) \\ s(t) \end{array} \right\} + \begin{bmatrix} A^*_{11} & A^*_{12} & A^*_{13} \\ A^*_{21} & A^*_{22} & A^*_{23} \\ A^*_{31} & A^*_{32} & A^*_{32} \end{bmatrix} \tag{79}$$
$$\times \begin{bmatrix} S^*(\tau) - \Delta t \, 2\,\mu(\tau)\, a(t)\, \dot{\epsilon}^p_m\,(\sigma_m(t), s(t), \theta(\tau)) - S(t) \\ p^*(\tau) - \Delta t\, \kappa(\tau)\, b(t)\, \dot{\epsilon}^p_m\,(\sigma_m(t), s(t), \theta(\tau)) + 3\,\kappa(\tau)\,\alpha(\tau)\,\Delta\theta - p(t) \\ \Delta t\, g\,(\sigma_m(t), s(t), \theta(\tau)) \end{bmatrix}.$$

For this case the components of matrix **A** of equation (77) are given in the APPENDIX.

Next, we note from (57,59) that

$$f(\tau) = \frac{f(t) - \delta}{1 - \delta}, \qquad \text{with} \quad \delta \equiv \Delta t \left(\dot{\gamma} \frac{\partial}{\partial p} \Phi \right)(t) = (p^*(\tau) - p(\tau))\,/\,\kappa(\tau) \,+\, 3\,\alpha(\tau)\,\Delta\theta. \tag{80}$$

Thus, once $p(\tau)$ has been determined, $f(\tau)$ may be determined using (80).

Assume that $\{S(\tau), p(\tau), s(\tau), f(\tau)\}$ have been obtained. Then the final step is to use (64) to calculate

$$\bar{\mathbf{T}}(\tau) = \eta(\tau)\,\bar{\mathbf{S}}^*(\tau) - p(\tau)\,\mathbf{1}, \qquad \eta(\tau) \equiv S(\tau)/S^*(\tau), \tag{81}$$

and rotate it according to (see equations (44) and (53))

$$\mathbf{T}(\tau) = \{\mathbf{R}_t(\tau)\}\;\bar{\mathbf{T}}(\tau)\;\{\mathbf{R}_t(\tau)\}^T, \tag{82}$$

to obtain the Cauchy stress at the end of the increment.

Variable Time-Stepping Algorithm

For the type of stiff constitutive equations considered here, it is extremely important to be able to perform the time integration with a variable time step. Based on previous work by Anand *et al.*[39] , we outline a simple algorithm for variable time-stepping below.

To control the stability and accuracy of the constitutive time-integrations we define two error ratios R1 and R2, and use the larger of these two error ratios to control the variable time-stepping procedure. To ensure stability, the variable time stepping procedure ensures that small time steps are taken during periods of rapidly varying equivalent tensile plastic strain rate in the matrix, such as at the knee of a stress-strain curve; the ratio R1 controls. However, when the plastic strain rates are not changing rapidly, then R2 controls, excessively large time steps are prevented, and accuracy is enhanced.

To control the stability of the time-integration procedure, we define

$$\mathrm{R1} \equiv \{|\dot{\epsilon}^p_m(\tau) - \dot{\epsilon}^p_m(t)| \times \Delta t\}\;/\,\mathrm{EPSTOL}, \tag{83}$$

where the numerator is the difference between the equivalent tensile plastic strain rate in the matrix $\dot{\epsilon}^p_m$ across an increment multiplied by the size of the time increment, and EPSTOL is a user specified tolerance based on the "yield strain" s_o/E of the matrix, as follows:

$$\text{EPSTOL} \equiv \delta(s_o/E), \qquad 0 < \delta \leq 1, \tag{84}$$

where, E is the Young's modulus for the matrix material, and s_o is the initial value of the deformation resistance. A good value for δ is 0.1.

Next, given the incremental nature of the constitutive equations, it is necessary to limit the maximum equivalent tensile plastic strain increment in the matrix in a time step. This is done by defining an error ratio

$$\text{R2} \equiv \{\dot{\epsilon}^p_m(t) \times \Delta t\} \,/\, \text{EPSLMT} \tag{85}$$

where EPSLMT is a user specified limit on the the maximum equivalent tensile plastic strain increment in the matrix allowed in a time step. A good value for EPSLMT is 0.005.

The maximum of R1 and R2 is defined as the error ratio R:

$$\text{R} = \text{MAX}(\text{R1}, \text{R2}), \tag{86}$$

and the algorithm described below operates to keep the ratio R close to 1.0 by adjusting the size of the time increments. After a solution for a time increment $\Delta t_t = \tau - t$ is found, the value of R is checked to determine whether this solution should be accepted. If R is greater than 1.25, then the solution is rejected and a new time increment is done which is smaller by the factor $(0.85/R)$. If $R \leq 1.25$, then the solution is accepted and the value of R is used to determine the first trial size for the next time increment. The following algorithm is used:

$$\begin{array}{llll} \text{If} & 0.8 < R \leq 1.25 & \text{then} & \Delta t_T = \Delta t_t/R\,; \\ \text{if} & 0.5 < R \leq 0.8 & \text{then} & \Delta t_T = 1.25\Delta t_t\,; \\ \text{if} & R \leq 0.5 & \text{then} & \Delta t_T = 1.50\Delta t_t\,. \end{array}$$

Note that the measure R is allowed to exceed 1. This is done to avoid having to recalculate increments that came out just slightly above the specified nominal value but are otherwise essentially acceptable.

V. NUMERICAL EXAMPLES

The constitutive equations and time-integration procedures described in this paper have been implemented in the implicit finite element code ABAQUS (Version 4.8)[25] , by writing a "user material" subroutine, UMAT. The subroutine UMAT is called once for each integration point in the model for every global iteration. Part of the input provided to UMAT consists of the stress $\tilde{\mathbf{T}}(t) \equiv \mathbf{Q}_{HW}\,\mathbf{T}(t)\,\mathbf{Q}_{HW}^T$, $\theta(t)$, and the internal state variables $(s(t), f(t))$ at the beginning of the increment, plus a strain increment and a temperature increment $\Delta\theta$. The relative rotation $\mathbf{Q}_{HW}$, between the local configuration of a material neighborhood at time t and that at time τ, calculated by using the Hughes & Winget[27] algorithm, is also supplied as input. In order to use our time-integration algorithm, we have to first calculate $\mathbf{T}(t)$ from $\tilde{\mathbf{T}}(t)$ and $\mathbf{Q}_{HW}$. Next, from ABAQUS it is possible to obtain the deformation gradients $\mathbf{F}(t)$ and $\mathbf{F}(\tau)$ at the beginning and the end of an increment[§]. With these inputs, the output expected from UMAT consists of the values of the stress and the internal state variables at the end of the increment, $(\mathbf{T}(\tau), s(\tau), f(\tau))$, the plastic power dissipation $r^{pl}(\tau) \equiv \omega\,\mathbf{T}(\tau)\cdot\mathbf{D}^p(\tau)$, plus the consistent derivative matrices $\mathcal{C}$, $\mathbf{C}$, $\mathbf{H}$, and H (see the APPENDIX), to be used in the Newton scheme for global balance of equilibrium and energy.

All ABAQUS calculations presented here were performed by using its coupled temperature-displacement analysis procedure. Variable time-stepping to control the stability and accuracy of the constitutive time-integrations, as discussed in Section IV, was implemented by suitably modifying this analysis procedure.

Before describing our localization simulations, we list below the values of material parameters in the specific constitutive functions of Section III, which we have used in our calculations. We have used material parameters for a 2024-T351 Aluminum alloy for which Lindholm and Johnson[38] provide the following values for the constants in the viscoplastic constitutive functions (24) and (25) :

$$\begin{array}{llll} A = 263.28\,\text{MPa}, & B = 421.72\,\text{MPa}, & C = 0.015, & n = 0.34, \\ \dot{\epsilon}_o = 0.577\text{s}^{-1}, & \theta_0 = 300^\circ\text{K}, & \theta_m = 775^\circ\text{K}, & a = 2. \end{array}$$

For the thermo-elastic properties we use:

$$\begin{array}{llll} \mu_{m,0} = 26\,\text{GPa}, & \kappa_{m,0} = 68\,\text{GPa}, & \chi_1 = 0.5, & \chi_2 = 0.333, \\ \alpha_m = 22.6 \times 10^{-6}/^\circ\text{K}, & \rho_m = 2,770\text{kg/m}^3, & c_m = 875\text{J/(kg}^\circ\text{K)}, & \lambda_m = 160\,(\text{W/m}^\circ\text{K}), \\ \omega = 0.9. & & & \end{array}$$

For simplicity we take α_m, c_m and λ_m independent of temperature. Also, at present, ABAQUS does not have any provisions to provide for variations of the specific heat c and the thermal

---

[§] This information is not currently routinely supplied as input to UMAT. Instead, ABAQUS supplies a strain increment calculated by using the Hughes & Winget[27] algorithm. Appropriate subroutines that need to be called to obtain $\mathbf{F}(t)$ and $\mathbf{F}(\tau)$ were kindly supplied to us by Dr. H. D. Hibbitt of HKS, Inc. We use this information about the deformation gradients to construct the incremental kinematic quantities for our time-integration procedure.

conductivity λ with internal state variables of the constitutive model. Therefore, the dependence of these quantities on the void volume fraction f (see equations (20) and (21)) is also neglected.

The numerical example considered here is the simulation of a plane strain tension test. The geometry and the initial mesh chosen to model one quarter of the specimen are shown in Fig. 1. The top boundary of the specimen is pulled at a constant speed v=2.5m/sec, which for the geometry of the specimen considered here gives a nominal strain rate of ≈500/sec in the central gage section. The boundaries of the specimen are taken to be insulated and therefore there is no heat conduction away from the surface of the specimen to the environment. Due the geometry of the specimen, the deformation is slightly inhomogeneous right from the beginning and thus there is no need or any perturbation of the initial data, to trigger the diffuse necking and the shear band localization phenomena. In what follows, we report on our numerical simulations for specimens made from both the fully dense material (also see Kim and Anand[40]) and a porous material with an initial void volume fraction of 5%.

A remeshing program (Lush[41]) was utilized in order to follow the development of the shear band by refining locally in regions of high strain rate gradients. For example, the sequence of the meshes employed for the analysis of a fully dense material is shown in Fig. 2. After the second remeshing the complete mesh consists of 376 8-noded ABAQUS type CPE8RT elements with 1277 nodes. The CPE8RT is a quadratic plane strain element with reduced integration and linear interpolation of the temperature. The correct transition from one mesh density to the next one is obtained by multi-point constraints on the edges of elements where the change of mesh density occurs. In the numerical analysis the effects of inertia are neglected and using the coupled temperature-displacement procedure of the finite element code ABAQUS, the fully-coupled thermomechanical problem was solved.

In Fig. 3 load versus time curves are plotted for both the fully dense and initially porous material. As is expected (a) the flow curve for the porous material is lower than that for the fully dense material, (b) diffuse necking initiates in the vicinity of the peak of their load-displacement curves for both materials, and (c) the plane strain ductility for the porous material is lower than that for the dense material. In order to demonstrate the effect of the heat conduction, the value of the thermal conductivity was artificially amplified by 4 orders of magnitude [¶]. The resulting load-time plots are also shown in Fig. 3.

In Figs. 4–6 the evolution of the equivalent tensile plastic strain rate, the equivalent tensile plastic strain, the temperature and the porosity is shown through the course of the deformation at two points, one at the center of the specimen (point A) and one outside the central region on the axis of symmetry (point B). These figures clearly bring out the rapid increase in the strain rate, temperature and porosity at point A where the shear band starts to develop. Also clear from these figures is the suppression in the rate of shear band development when the thermal conductivity is increased.

The level contours of $\dot{\epsilon}^p_m$, ϵ^p_m, θ at representative time increments (keyed to the load-time

---

[¶] Similar calculations in plane strain compression have been previously performed by Anand, Lush and Kim[42]; also see Lush[41].

plot) are shown in Figs. 7-20.

For the fully dense material, the shear band "initiates" at an inclination of approximately 45° with respect with the horizontal (see Fig. 7a), and it quickly (see Fig. 7d) collapses to the minimum width resolvable by the finite element mesh[‖]. See the evolution of the level contours in Fig. 7-9 for the process of shear localization in the tension test. The collapse of the shear bands implies that the characteristic length associated with heat conduction was much too small to be resolved by the mesh employed.

Figs. 10-12 show the resulting load-time plots and some representative level contours for the field variables for the fully dense material with the thermal conductivity artificially enhanced to $\lambda = 1.6 \times 10^6 W/(m^o K)$. When the thermal conductivity is increased so dramatically, the formation of the shear bands in the fully dense material was suppressed. The thermal softening, which was previously the cause of the localization is now inhibited by the amplified heat conduction away from the localizing bands. The resulting temperature distribution shown in Fig. 12 is substantially smoother than the one observed in the calculation with $\lambda = 160 W/(m^o K)$ in Fig. 9. The load drops gradually due to the decrease of the cross section of the specimen at the neck. However at the very end of the deformation a broad band-like structure does appear inside the neck, see Fig. 10d.

In the case of the initially porous specimen thermal softening and growth of voids are two competing and interacting softening mechanisms. In the simulation with $\lambda = 160 W/(m^o K)$, thermal softening is the major reason for the shear band development and it is assisted by the growth of voids. For this reason the time at localization is shorter compared to the fully dense case (Fig. 3). Due to the pressure dependence of the constitutive model, the initial inclination of the shear band is different from 45° and it was roughly estimated to 40° with respect to the horizontal (Fig. 13b). As the shear band localizes the void growth takes over at the center of the specimen. As can be seen in Fig. 16 the porosity outside the shear band was increased only to 7%, while inside the band it reached values ranging from 11% to the failure value 25% at the center of the specimen. Due to the special form of the plastic potential with the "accelerated porosity" term f^*, once the porosity reaches the critical value f_c at one integration point, it subsequently increases much faster there than in the surrounding area, and once the failure value f_f is reached the element looses all stress carrying capacity. To avoid numerical problems, we terminated our calculations slightly prior to this failure point.

For the porous specimen, with the thermal conductivity increased to $\lambda = 1.6 \times 10^6 W/(m^o K)$ the role of the two softening mechanisms is reversed. The thermal softening tends to form a band-like structure but its effect is weak. Void growth at the center of the specimen (where the triaxiality is slightly higher) is the dominant mode of softening, and it leads quickly to initiation of failure at that location, see Fig. 20.

VI. DISCUSSION AND CONCLUSIONS

[‖] It is important to note that the values of the various field variables at the very end of the simulation should be considered only qualitatively correct because of the unavoidable mesh effects and the associated interpolation errors.

We have formulated a new semi-implicit time integration algorithm for a set of state variable constitutive equations describing thermo-elasto-viscoplastic microporous materials. This algorithm offers substantial improvement over the widely used scheme of Pierce, Shih and Needleman[19]. It is incrementally objective, it takes better account of possible changes in the direction of plastic flow, it has variable time stepping to control the stability and accuracy of the procedure, and it takes full account of thermo-mechanical coupling.

Using this procedure we have performed finite elements simulations of a plane strain tension test for fully dense and microporous solids. To the best of our knowledge, ours is the first full two-dimensional localization analysis in a plane strain tension test of a rate sensitive and temperature dependent microporous solid under fully-coupled conditions. Elasticity, thermal expansion and large geometry changes are accounted for, but inertial effects have been neglected. We have used the numerical simulation of the plane strain tension test to follow the initiation and growth of band-like regions of localization though slow early growth to severe localization and ductile fracture initiation. The competing effects of thermal softening and porosity softening have been examined using a parametric study.

If realistic investigations of thermo-viscoplastic localization at high strain rates are to be pursued, then more accurate constitutive equations than those used in this paper must be utilized. Apart from the concerns of appropriate constitutive models, much remains to be done concerning the spatial discretization methods and adaptive meshing techniques employed in finite element procedures. As is clear from the calculations presented above, for realistic values of the thermal conductivity of metals, in conventional finite elements the mesh size sets the lower limit to the spatial resolution of the shear band. Development of specialized elements for shear band calculations is an active area of current research (e.g. Ortiz *et al.*[43], Belytschko *et al.*[44]). For a recent detailed discussion of these and other research issues concerning shear bands and transition to ductile failure see the recent report [45] of an NSF workshop on localized plastic instabilities and failure criteria.

ACKNOWLEDGEMENTS.

Helpful discussions with G. Weber and A. M. Lush are gratefully acknowledged. Support for this work was provided by the U. S. National Science Foundation (Grant No. MSS-8808556).

VII. REFERENCES

1. Tipper, C. F., “The Fracture of Metals,” *Metallurgia*, **39**, pp. 133 - 138, 1949.
2. Puttick, K. E., “Ductile Fracture in Metals,” *Philosophical Magazine*, **4**, pp. 964 - 969, 1959.
3. Puttick, K. E., “The Shear Component of Ductile Fracture,” *Philosophical Magazine*, **5**, pp. 759 - 762, 1960.
4. Rogers, H. C., “Tensile Fracture of Ductile Metals,” *Transactions of TMS-AIME*, **28**, pp. 498 - 506, 1960.
5. Bluhm, J. I., and Morrisey, J. R., “Fracture In A Tensile Specimen’,” Proceedings of 3rd International Conference on Fracture, Yokobori, T., Kawasaki, T., and Swedlow, J. L., eds., Vol iii, Japanese Society for Strength and Fracture of Materials, Sendai, pp. 1739 - 1780, 1966.
6. McClintock, F. A.,“A Criterion For Ductile Fracture by the Growth of Holes,” *Journal of Applied Mechanics*, **35**, 363 - 371, 1968.
7. McClintock, F. A., “On the Mechanics of Fracture from Inclusions,” in Paxton, H. W. ed., *Ductility*, ASM, Metals Park, Ohio, pp. 255 - 277 , 1968.
8. Rice, J. R., and Tracey, D. M., “On the Ductile Enlargement of Voids in Triaxial Stress States,” *J. Mech. Phys. Solids*, **17**, pp. 201 - 217, 1969.
9. Budiansky, B., Hutchinson, J. W. and Slutsky, S., “Void Growth and Collapse in Viscous Solids,” *Mechanics of Solids*, The Rodney Hill 60th Anniversary Volume, Hopkins, H.G., and Sewell, M. J., eds., Pergamon Press, Oxford, pp. 13 - 45, 1982.
10. Kuhn, H. A., and Downey, C. L., “Deformation Characteristics and Plasticity Theory of Sintered Powder Materials,” *Int. J. Powder Metall.*, **7**, pp. 15 - 25, 1971.
11. Green, R. J., “ A Plasticity Theory For Porous Solids,” *Int. J. Mech. Sci.*, **14**, pp. 215 - 224, 1972.
12. Gurson, A. L., “Continuum Theory of Ductile Rupture by Void Nucleation and Growth: Part 1 - Yield Criteria and Flow Rules for Porous Ductile Media,” *ASME J. Engng. Materials Technol.*, **99**, pp. 2 - 15, 1977.
13. Shima, S. and Oyane, M., “Plasticity Theory for Ductile Metals,” *Int. J. Mech. Sci.*, **18**, pp. 285 - 291, 1976.
14. Tvergaard, V., “Influence Of Voids On Shear Band Instabilities Under Plane Strain Conditions,” *Int. J. Frac.*, **17**, pp. 389-407, 1981.
15. Tvergaard, V., “On Localization in Ductile Materials Containing Spherical Voids,” *Int. J. Frac.*, **18**, pp. 237-252, 1982.
16. Hom. C. L., and McMeeking, R. M., “Void Growth in Elastic-Plastic Materials,” *ASME Journal of Applied Mechanics*, **56**, pp. 309 - 317, 1989.
17. Pan, J., Saje, M., and Needleman, A., “Localization of Deformation in Rate Sensitive Porous Plastic Solids,” *Int. J. Fracture*, **21**, pp. 261 - 278, 1983.
18. Tvergaard, V., and Needleman, A., “Analysis of the Cup-Cone Fracture in a Round Tensile Bar,” *Acta Metallurgica*, **32**, pp. 157 - 196, 1984.

19. Peirce, D., Shih, C. F., and Needleman, A., "A Tangent Modulus Method for Rate Dependent Solids," *Computers and Structures*, **18**, pp. 875-887, 1984.
20. Becker, R., and Needleman, A., "Effect of Yield Surface Curvature on Necking and Failure in Porous Plastic Solids," *J. Appl. Mech.*, **53**, pp. 491-499, 1986.
21. Aravas, N., "On The Numerical Integration of a Class of Pressure Dependent Plasticity Models," *Int. J. Num. Methods in Engin.*, **24**, pp. 1395 – 1416, 1987.
22. Tvergaard, V., and Needleman, A., "Effect of Material Rate Sensitivity on Failure Modes in Charpy V-Notch Test," *J. Mech. Phys. Solids*, **34**, pp. 213 – 241, 1986.
23. Becker, R., Needleman, A., Richmond, O., and Tvergaard, V., "Void Growth and Failure in Notched Bars," *J. Mech. Phys. Solids.*, **36**, pp. 317 – 354, 1988.
24. Tvergaard, V., "Mechanical Modelling of Failure," in *Constitutive Relations and Their Physical Basis*, Andersen *et al.* (eds.), Proceedings of the 8th International Symposium on Metallurgy and Materials Science, pp. 173 – 189, 1987.
25. ABAQUS, Reference Manuals, Hibbitt, Karlsson & Sorensen Inc., 100 Medway Street, Providence, RI, 02906-4402, 1989.
26. Anand, L., "Constitutive Equations For Hot-Working Of Metals," International Journal of Plasticity, **1**, pp. 213-231, 1985.
27. Hughes, T. J. R. and Winget, J., "Finite Rotation Effects In Numerical Integration Of Rate Constitutive Equations Arising In Large-Deformation Analysis," International Journal for Numerical Methods in Engineering, **15**, pp. 1862-1867, 1980.
28. Rubenstein, R. and Atluri, S. N., "Objectivity Of Incremental Constitutive Relations Over Finite Time Steps In Computational Finite Deformation Analyses," Computer Methods in Applied Mechanics And Engineering, **36**, pp. 277-290, 1983.
29. Reed, K. W. and Atluri, S. N., "Analyses Of Large Quasistatic Deformations Of Inelastic Bodies By A New Hybrid-Stress Finite Element Algorithm," Computer Methods In Applied Mechanics And Engineering, **39**, pp. 245-295, 1983.
30. Reed, K. W. and Atluri, S. N., "Constitutive Modelling And Computational Implementation For Finite Strain Plasticity," International Journal of Plasticity, **1**, pp. 63-87, 1985.
31. Nagtegaal, J. C. and Veldpaus, F. E., "On The Implementation Of Finite Strain Plasticity Equations In A Numerical Model," in Pittman, J. F. T., *et al.* (eds.), Numerical Analysis Of Forming Processes, John Wiley & Sons Ltd., New York, pp. 351-371, 1984.
32. Hughes, T. J. R., "Numerical Implementation Of Constitutive Models: Rate-Independent Deviatoric Plasticity," in Nemat-Nasser S., Asaro, R. J. and Hegemier, G. A. (eds.) Theoretical Foundation For Large-Scale Computations Of Nonlinear Material Behavior, Martinus Nijhoff Publishers, Boston, pp. 29-57, 1984.
33. Nagtegaal, J. C. and Rebelo, N., "On The Development Of A General Purpose Finite Element Program For Analysis Of Forming Processes," in Mattiasson, K. *et al.* (eds.), Proceedings of the 2nd International Conference on Numerical Methods in Industrial Forming Processes, pp. 41-49, 1986.

34. Weber G., Lush A., Zavaliangos A., Anand L., "An Objective Time-Integration Procedure For Isotropic Rate-Independent And Rate-Dependent Elastic-Plastic Constitutive Equations", accepted for publication in *International Journal of Plasticity.*

35. Budiansky, B., "Thermal and Thermoelastic Properties of Isotropic Composites," Journal of Composite Materials, 4, pp. 286 - 295, 1970.

36. Simmons G., Wang H., "Single Crystal Elastic Constants and Calculated Aggregate Properties", The MIT Press, Cambridge MA, 1971.

37. Frost H. J., Ashby M. F., "Deformation-Mechanism Maps: The Plasticity and Creep of Metals and Ceramics", Pergamon Press, 1982.

38. Lindholm U. S. and Johnson G.R., "Strain-Rate Effects in Metals in Large Shear Strains," in : Mescall, J. and Weiss V., (eds.) *Material Behavior Under Very High Stress and Ultrahigh Loading Rates* , Sagamore Army Materials Research Conference Proceedings, 29, Plenum Press, pp. 61 – 79, 1983.

39. Anand, L., Lush, A., Briceno, M. F., and Parks, D. M., " A Time-integration Procedure For A Set Of Internal Variable Type Constitutive Equations," Report of Research in Mechanics of Materials, Department of Mechanical Engineering, M.I.T., 1985.

40. Kim K. H., Anand L., "A Note on Adiabatic Flow Localization in Viscoplastic Solids", in: Predeleanu M., (ed.) *Computational Methods for Predicting Material Processing Defects,* Elsevier Science Publishers B.V., Amsterdam, pp. 181 – 192, 1987.

41. Lush A.M., "Computational Procedures for Finite Element Analysis Of Hot-Working", PhD Thesis, M.I.T., 1990.

42. Anand L., Lush A. M. and Kim K. H., "Thermal Aspects Of Shear Localization In Viscoplastic Solids", in Attia M.H. and Kops L. (eds.) *Thermal Aspects Of Manufacturing,* ASME PED-30, pp. 89 – 103, 1988.

43. Ortiz M., Leroy Y., and Needleman A., "A Finite Element Method For Localized Failure Analysis", *Computer Methods in Applied Mechanics and Engineering,* **61**, pp. 189 – 214, 1987.

44. Belytchko T., Moran B., Kulkarni M., "Stability and imperfections in quasi-static viscoplastic solutions" Chen C. F. (ed.) "Mechanics 1990: Proceedings of 11th National Congress of Applied Mechanics, Tuscon Arizona", pp. 251 – 255, 1990.

45. Anand L., Dillon O., Place T. A. and von Turkovich B. F., "Report Of The NSF Workshop On Localized Plastic Instabilities and Failure Criteria", *International Journal of Plasticity,* **36**, 2, 1990.

APPENDIX

In this Appendix we list the components of the matrix **A** in equation (77), and we summarize the derivatives, consistent with the time integration procedure of Section IV, to be used in a Newton type iterative method for revising the estimates of nodal displacements and temperatures in implicit finite-element procedures for coupled thermo-mechanical problems.

The matrix A:

$$\begin{aligned}
A_{11} &= -\Delta t\, 2\mu(\tau)\, a(t) \left\{ \frac{\partial}{\partial \sigma_m(t)} \dot{\epsilon}^p_m \left(\sigma_m(t), s(t), \theta(\tau)\right) \right\} \left\{ \frac{\partial}{\partial S(t)} \sigma_m(t) \right\}, \qquad (87)\\
A_{12} &= -\Delta t\, 2\mu(\tau)\, a(t) \left\{ \frac{\partial}{\partial \sigma_m(t)} \dot{\epsilon}^p_m \left(\sigma_m(t), s(t), \theta(\tau)\right) \right\} \left\{ \frac{\partial}{\partial p(t)} \sigma_m(t) \right\},\\
A_{13} &= -\Delta t\, 2\mu(\tau)\, a(t) \left\{ \frac{\partial}{\partial s(t)} \dot{\epsilon}^p_m \left(\sigma_m(t), s(t), \theta(\tau)\right) \right\},\\
A_{21} &= -\Delta t\, \kappa(\tau)\, b(t) \left\{ \frac{\partial}{\partial \sigma_m(t)} \dot{\epsilon}^p_m \left(\sigma_m(t), s(t), \theta(\tau)\right) \right\} \left\{ \frac{\partial}{\partial S(t)} \sigma_m(t) \right\},\\
A_{22} &= -\Delta t\, \kappa(\tau)\, b(t) \left\{ \frac{\partial}{\partial \sigma_m(t)} \dot{\epsilon}^p_m \left(\sigma_m(t), s(t), \theta(\tau)\right) \right\} \left\{ \frac{\partial}{\partial p(t)} \sigma_m(t) \right\},\\
A_{23} &= -\Delta t\, \kappa(\tau)\, b(t) \left\{ \frac{\partial}{\partial s(t)} \dot{\epsilon}^p_m \left(\sigma_m(t), s(t), \theta(\tau)\right) \right\},\\
A_{31} &= \Delta t \left\{ \frac{\partial}{\partial \sigma_m(t)} g \left(\sigma_m(t), s(t), \theta(\tau)\right) \right\} \left\{ \frac{\partial}{\partial S(t)} \sigma_m(t) \right\},\\
A_{32} &= \Delta t \left\{ \frac{\partial}{\partial \sigma_m(t)} g \left(\sigma_m(t), s(t), \theta(\tau)\right) \right\} \left\{ \frac{\partial}{\partial p(t)} \sigma_m(t) \right\},\\
A_{33} &= \Delta t \left\{ \frac{\partial}{\partial s(t)} g \left(\sigma_m(t), s(t), \theta(\tau)\right) \right\},
\end{aligned}$$

with

$$\begin{aligned}
\frac{\partial}{\partial S(t)} \sigma_m(t) &= -\frac{\partial}{\partial S(t)} \Phi(t) \Big/ \frac{\partial}{\partial \sigma_m(t)} \Phi(t), \qquad (88)\\
\frac{\partial}{\partial p(t)} \sigma_m(t) &= -\frac{\partial}{\partial p(t)} \Phi(t) \Big/ \frac{\partial}{\partial \sigma_m(t)} \Phi(t).
\end{aligned}$$

The derivatives matrices:

From (56-62,81,82) we may write the Cauchy stress at the end of the increment as

$$\mathbf{T}(\tau) = \mathbf{T}(t) + 2\mu(\tau)\,\Delta\mathbf{E}' + \kappa(\tau)\,(\mathrm{tr}\,\Delta\mathbf{E})\,\mathbf{1} + \{S(\tau) - S^*(\tau)\}\,\mathbf{N}(\tau) + \{p^*(\tau) - p(\tau)\}\,\mathbf{1}, \qquad (89)$$

where

$$\Delta\mathbf{E} = \{\mathbf{R}_t(\tau)\}\,\Delta\bar{\mathbf{E}}\,\{\mathbf{R}_t(\tau)\}^T. \qquad (90)$$

Also, from (6,11) the power dissipation in the matrix at the end of the time-step is

$$r^{pl}(\tau) = \omega\,\mathbf{T}(\tau)\cdot\mathbf{D}^p(\tau) = \omega\,\{1 - f(\tau)\}\,\sigma_m(\tau)\,\dot{\bar{\epsilon}}^p_m(\tau). \tag{91}$$

The necessary derivatives to be computed pertain to the variations of these quantities with respect to variations in $\Delta\mathbf{E}$ and $\Delta\theta$, and are:

$$\begin{aligned} \mathcal{C} &= \frac{\partial}{\partial\Delta\mathbf{E}}\,\mathbf{T}(\tau), && (92)\\ \mathbf{C} &= \frac{\partial}{\partial\Delta\theta}\,\mathbf{T}(\tau), && (93)\\ \mathbf{H} &= \frac{\partial}{\partial\Delta\mathbf{E}}\,r^{pl}(\tau) && (94)\\ H &= \frac{\partial}{\partial\Delta\theta}\,r^{pl}(\tau). && (95) \end{aligned}$$

In what follows, we assume for simplicity that the dependence of the thermoelastic moduli on (f,θ) are weak, so that variation of these moduli may be neglected in the calculation of the derivatives.

The Derivative $\mathcal{C}$:

From (89)

$$\begin{aligned} \mathcal{C} \;=\;& 2\mu(\tau)\left\{\mathcal{I} - \frac{1}{3}(\mathbf{1}\otimes\mathbf{1})\right\} + \kappa(\tau)\,\mathbf{1}\otimes\mathbf{1} + \{S(\tau) - S^*(\tau)\}\,\frac{\partial}{\partial\Delta\mathbf{E}}\,\mathbf{N}(\tau) && (96)\\ &+\mathbf{N}(\tau)\otimes\frac{\partial}{\partial\Delta\mathbf{E}}\,\{S(\tau) - S^*(\tau)\} + \mathbf{1}\otimes\frac{\partial}{\partial\Delta\mathbf{E}}\,\{p^*(\tau) - p(\tau)\} \end{aligned}$$

Using

$$\begin{aligned} \mathbf{S}^*(\tau) &= \mathbf{S}(t) + \hat{\mathcal{L}}(\tau)[\Delta\mathbf{E}], \qquad \hat{\mathcal{L}}(\tau) \equiv 2\mu(\tau)\left\{\mathcal{I} - \left(\frac{1}{3}\right)\,\mathbf{1}\otimes\mathbf{1}\right\}, && (97)\\ S^*(\tau) &= \sqrt{\mathbf{S}^*(\tau)\cdot\mathbf{S}^*(\tau)}, && (98)\\ \mathbf{N}(\tau) &= \mathbf{S}^*(\tau)/S^*(\tau), && (99) \end{aligned}$$

Straightforward calculations give

$$\frac{\partial}{\partial\Delta\mathbf{E}}\,\mathbf{N}(\tau) = \frac{1}{S^*(\tau)}\left[2\mu(\tau)\left\{\mathcal{I} - \left(\frac{1}{3}\right)\,\mathbf{1}\otimes\mathbf{1}\right\} - 2\mu(\tau)\,\mathbf{N}(\tau)\otimes\mathbf{N}(\tau)\right] \tag{100}$$

Next, noting that $\Delta\mathbf{E}$ enters the equations through $S^*(\tau)$ and $p^*(\tau)$, we have

$$\frac{\partial}{\partial\Delta\mathbf{E}} \equiv \frac{\partial}{\partial S^*(\tau)}\left\{\frac{\partial}{\partial\Delta\mathbf{E}}\,S^*(\tau)\right\} + \frac{\partial}{\partial p^*(\tau)}\left\{\frac{\partial}{\partial\Delta\mathbf{E}}\,p^*(\tau)\right\}. \tag{101}$$

Also,

$$\begin{aligned} \frac{\partial}{\partial\Delta\mathbf{E}}\,S^*(\tau) &= 2\mu(\tau)\,\mathbf{N}(\tau), && (102)\\ \frac{\partial}{\partial\Delta\mathbf{E}}\,p^*(\tau) &= -\kappa(\tau)\,\mathbf{1}. && (103) \end{aligned}$$

Thus,

$$\frac{\partial}{\partial \Delta \mathbf{E}} \{S(\tau) - S^*(\tau)\} = 2\mu(\tau)\mathbf{N}(\tau)\left\{\frac{\partial}{\partial S^*(\tau)} S(\tau) - 1\right\} - \kappa(\tau)\mathbf{1}\frac{\partial}{\partial p^*(\tau)} S(\tau), \quad (104)$$

$$\frac{\partial}{\partial \Delta \mathbf{E}} \{p^*(\tau) - p(\tau)\} = -2\mu(\tau)\mathbf{N}(\tau)\frac{\partial}{\partial S^*(\tau)} p(\tau) - \kappa(\tau)\mathbf{1}\left\{1 - \frac{\partial}{\partial p^*(\tau)} p(\tau)\right\}. \quad (105)$$

Substituting (100,104,105) in (96) and rearranging we have

$$\boldsymbol{\mathcal{C}} = c_1 \boldsymbol{\mathcal{I}} + c_2 \mathbf{1} \otimes \mathbf{1} + c_3 \mathbf{S}(\tau) \otimes \mathbf{S} + c_4 \mathbf{1} \otimes \mathbf{S}(\tau) + c_5 \mathbf{S}(\tau) \otimes \mathbf{1}, \quad (106)$$

with

$$\begin{aligned} c_1 &= 2\tilde{\mu}(\tau), \quad (107)\\ c_2 &= \tilde{\kappa}(\tau) - (2/3)\,\tilde{\mu}(\tau),\\ c_3 &= -2\mu(\tau)\,(\eta(\tau) - d_1(\tau))\,/S^2(\tau),\\ c_4 &= -2\mu(\tau)\,d_3(\tau)/S(\tau),\\ c_5 &= -\kappa(\tau)\,d_2(\tau)/S(\tau), \end{aligned}$$

where

$$\begin{aligned} \eta(\tau) &= S(\tau)/S^*(\tau), \quad (108)\\ \tilde{\mu}(\tau) &= \eta(\tau)\,\mu(\tau),\\ d_1(\tau) &= \frac{\partial}{\partial S^*(\tau)} S(\tau),\\ d_2(\tau) &= \frac{\partial}{\partial p^*(\tau)} S(\tau),\\ d_3(\tau) &= \frac{\partial}{\partial S^*(\tau)} p(\tau),\\ d_4(\tau) &= \frac{\partial}{\partial p^*(\tau)} p(\tau),\\ \tilde{\kappa}(\tau) &= d_4(\tau)\,\kappa(\tau). \end{aligned}$$

Consistent with the forward gradient approximation, we use

$$d_i(\tau) \approx d_i(t), \qquad (i = 1,4) \quad (109)$$

and these quantities are calculated as follows. With

$$\mathbf{X}(\tau) \equiv \left\{ \begin{array}{c} S(\tau) \\ p(\tau) \\ s(\tau) \end{array} \right\}, \quad (110)$$

we may rewrite the system of equations to be solved as

$$\mathbf{X}(\tau) = \mathbf{G}\left(\mathbf{X}(\tau); \mathbf{Y}(\tau)\right), \qquad \text{where} \quad \mathbf{Y}(\tau) = \left\{ \begin{array}{c} S^*(\tau) \\ p^*(\tau) \end{array} \right\};$$

then

$$\mathrm{d}\,\mathbf{X}(t) = \left\{ \frac{\partial}{\partial \mathbf{X}} \mathbf{G}(\mathbf{X};\mathbf{Y}) \Big|_{\mathbf{X}=\mathbf{X}(t),\mathbf{Y}=\mathbf{Y}(t)} \right\} \mathrm{d}\,\mathbf{X}(t) + \left\{ \frac{\partial}{\partial \mathbf{Y}} \mathbf{G}(\mathbf{X};\mathbf{Y}) \Big|_{\mathbf{X}=\mathbf{X}(t),\mathbf{Y}=\mathbf{Y}(t)} \right\} \mathrm{d}\,\mathbf{Y}(t),$$

from which

$$\mathrm{d}\mathbf{X}(t) = \mathbf{A}^{*} \left\{ \frac{\partial}{\partial \mathbf{Y}} \mathbf{G}(\mathbf{X};\mathbf{Y}) \Big|_{\mathbf{X}=\mathbf{X}(t),\mathbf{Y}=\mathbf{Y}(t)} \right\} \mathrm{d}\mathbf{Y}(t) \tag{111}$$

with $\mathbf{A}^{*}$ given in (76). Equation (109) gives

$$d_1(t) = A^{*}_{11}, \quad d_2(t) = A^{*}_{12}, \quad d_3(t) = A^{*}_{21}, \quad d_4(t) = A^{*}_{22}. \tag{112}$$

For future use we identify the rest of the coefficients of the matrix $\mathbf{A}^{*}$ as

$$\begin{bmatrix} A^{*}_{11} & A^{*}_{12} & A^{*}_{13} \\ A^{*}_{21} & A^{*}_{22} & A^{*}_{23} \\ A^{*}_{31} & A^{*}_{32} & A^{*}_{32} \end{bmatrix} \equiv \begin{bmatrix} d_1 & d_2 & d_7 \\ d_3 & d_4 & d_8 \\ d_5 & d_6 & d_9 \end{bmatrix}. \tag{113}$$

Note that although it is not obvious from (106), $c_4 = c_5$, and $\boldsymbol{C}$ is symmetric.

The Derivative C:

From (89)

$$\mathbf{C} \equiv \frac{\partial}{\partial \Delta\theta} \mathbf{T}(\tau) = \left\{ \frac{\partial}{\partial \Delta\theta} S(\tau) \right\} \mathbf{N}(\tau) - \left\{ \frac{\partial}{\partial \Delta\theta} p(\tau) \right\} \mathbf{1}. \tag{114}$$

Next from

$$\mathbf{X}(\tau) \doteq \mathbf{X}(t) + \mathbf{A}^{*}(\mathbf{X}(t);\theta(\tau))\,(\mathbf{G}(\mathbf{X}(t);\theta(\tau)) - \mathbf{X}(t)), \tag{115}$$

we have

$$\begin{aligned} \frac{\partial}{\partial \Delta\theta} \mathbf{X}(\tau) = \frac{\partial}{\partial \theta(\tau)} \mathbf{X}(\tau) \quad &= \quad \mathbf{A}^{*}(\mathbf{X}(t);\theta(\tau))\, \frac{\partial}{\partial \theta(\tau)} (\mathbf{G}(\mathbf{X}(t);\theta(\tau)) - \mathbf{X}(t)) \\ &\quad + \mathbf{B}^{*}(\mathbf{X}(t);\theta(\tau))\,(\mathbf{G}(\mathbf{X}(t);\theta(\tau)) - \mathbf{X}(t)), \end{aligned} \tag{116}$$

where

$$\mathbf{B}^{*}(\mathbf{X}(t);\theta(\tau)) = \frac{\partial}{\partial \theta(\tau)} \mathbf{A}^{*}(\mathbf{X}(t);\theta(\tau)). \tag{117}$$

Thus, from (79)

$$\frac{\partial}{\partial \Delta\theta} S(\tau) \quad = \quad d_1 w_1 + d_2 w_2 + d_7 w_3 + dd_1\,\mathrm{ESIGB} + dd_2\,\mathrm{EP} + dd_7\,\mathrm{ES}, \tag{118}$$

$$\frac{\partial}{\partial \Delta\theta} p(\tau) \quad = \quad d_3 w_1 + d_4 w_2 + d_4 w_3 + dd_3\,\mathrm{ESIGB} + dd_4\,\mathrm{EP} + dd_8\,\mathrm{ES}, \tag{119}$$

$$\frac{\partial}{\partial \Delta\theta} s(\tau) \quad = \quad d_5 w_1 + d_6 w_2 + d_9 w_3 + dd_5\,\mathrm{ESIGB} + dd_6\,\mathrm{EP} + dd_9\,\mathrm{ES}, \tag{120}$$

where d_i are given as before in (113),

$$
\begin{aligned}
\text{ESIGB} &= S^*(\tau) - \Delta t\, 2\,\mu(\tau)\, a(t)\, \dot\epsilon^p_m\left(\sigma_m(t), s(t), \theta(\tau)\right) - S(t)\,, && (121)\\
\text{EP} &= p^*(\tau) - \Delta t\, \kappa(\tau)\, b(t)\, \dot\epsilon^p_m\left(\sigma_m(t), s(t), \theta(\tau)\right) + 3\,\kappa(\tau)\,\alpha(\tau)\,\Delta\theta - p(t)\,, && (122)\\
\text{ES} &= \Delta t\, g\left(\sigma_m(t), s(t), \theta(\tau)\right), && (123)
\end{aligned}
$$

$$
\begin{aligned}
w_1 &= -\Delta t\, 2\,\mu(\tau)\, a(t)\, \frac{\partial}{\partial\theta(\tau)} \dot\epsilon^p_m\left(\sigma_m(t), s(t), \vartheta(\tau)\right)\,, && (124)\\
w_2 &= -\Delta t\, \kappa(\tau)\, b(t)\, \frac{\partial}{\partial\theta(\tau)} \dot\epsilon^p_m\left(\sigma_m(t), s(t), \theta(\tau)\right) + 3\,\kappa(\tau)\,\alpha(\tau)\,, && (125)\\
w_3 &= \Delta t\, g\left(\sigma_m(t), s(t), \theta(\tau)\right), && (126)
\end{aligned}
$$

and

$$
\begin{bmatrix} dd_1 & dd_2 & dd_7 \\ dd_3 & dd_4 & dd_8 \\ dd_5 & dd_6 & dd_9 \end{bmatrix} \equiv \begin{bmatrix} B^*_{11} & B^*_{12} & B^*_{13} \\ B^*_{21} & B^*_{22} & B^*_{23} \\ B^*_{31} & B^*_{32} & B^*_{33} \end{bmatrix}. \qquad (127)
$$

For later use we note from (80) that

$$
\frac{\partial}{\partial\Delta\theta} f(\tau) = \zeta \left\{ \frac{1}{\kappa(\tau)} \frac{\partial}{\partial\Delta\theta} p(\tau) - 3\,\alpha(\tau) \right\}, \quad \text{where} \quad \zeta \equiv \left\{ \frac{1 - f(t)}{(1-\delta)^2} \right\}. \qquad (128)
$$

The Derivative H:

From (91)

$$
\begin{aligned}
\mathbf{H} \equiv \frac{\partial}{\partial\Delta\mathbf{E}}\, r^{pl} &= -\omega \left\{ \frac{\partial}{\partial\Delta\mathbf{E}} f(\tau) \right\} \sigma_m(\tau)\, \dot\epsilon^p_m(\tau) && (129)\\
&\quad + \omega\, (1 - f(\tau)) \left[\dot\epsilon^p_m(\tau) \frac{\partial}{\partial\Delta\mathbf{E}} \sigma_m(\tau) + \sigma_m(\tau) \frac{\partial}{\partial\Delta\mathbf{E}} \dot\epsilon^p_m(\tau) \right].
\end{aligned}
$$

Using

$$
\begin{aligned}
\frac{\partial}{\partial\Delta\mathbf{E}} \dot\epsilon^p_m(\tau) &= \left\{ \frac{\partial}{\partial\sigma_m(\tau)} \dot\epsilon^p_m(\tau) \right\} \frac{\partial}{\partial\Delta\mathbf{E}} \sigma_m(\tau) + \left\{ \frac{\partial}{\partial s(\tau)} \dot\epsilon^p_m(\tau) \right\} \frac{\partial}{\partial\Delta\mathbf{E}} s(\tau), && (130)\\
\frac{\partial}{\partial\Delta\mathbf{E}} f(\tau) &= \left\{ \zeta \frac{2\,\mu(\tau)}{S(\tau)} \frac{d_3}{\kappa(\tau)} \right\} \mathbf{S}(\tau) + \zeta\, (1 - d_4)\, \mathbf{1}, \\
\frac{\partial}{\partial\Delta\mathbf{E}} \sigma_m(\tau) &= \begin{bmatrix} d_1 \frac{2\mu(\tau)}{S(\tau)} \frac{\partial}{\partial S(\tau)} \sigma_m(\tau) + \\ d_3 \frac{2\mu(\tau)}{S(\tau)} \frac{\partial}{\partial p(\tau)} \sigma_m(\tau) + \\ d_3 \frac{2\mu(\tau)}{S(\tau)} \frac{\zeta}{\kappa(\tau)} \frac{\partial}{\partial f(\tau)} \sigma_m(\tau) \end{bmatrix} \mathbf{S}(\tau)
\end{aligned}
$$

$$
\begin{aligned}
& + \begin{bmatrix} - d_2 \, \kappa(\tau) \, \dfrac{\partial}{\partial S(\tau)} \, \sigma_m(\tau) \\ - d_4 \, \kappa(\tau) \, \dfrac{\partial}{\partial p(\tau)} \, \sigma_m(\tau) \\ + (1 - d_4) \, \zeta \, \dfrac{\partial}{\partial f(\tau)} \, \sigma_m(\tau) \end{bmatrix} \mathbf{1}, \\
\frac{\partial}{\partial \Delta \mathbf{E}} \, s(\tau) \quad &= \quad \left\{ d_5 \, \frac{2\,\mu(\tau)}{S(\tau)} \right\} \mathbf{S}(\tau) + \{ - d_6 \, \kappa(\tau) \} \; \mathbf{1},
\end{aligned}
$$

in (129) and rearranging we obtain

$$
\mathbf{H} = \xi \, \mathbf{S}(\tau) + \beta \, \mathbf{1}, \tag{131}
$$

with

$$
\begin{aligned}
\xi &= \xi_1 + \xi_2 + \xi_3, && (132) \\
\beta &= \beta_1 + \beta_2 + \beta_3, && (133)
\end{aligned}
$$

where

$$
\begin{aligned}
\xi_1 &= \{ - \omega \, \sigma_m(\tau) \, \dot{\epsilon}^p_m(\tau) \, \zeta \} \; \frac{2\,\mu(\tau)}{S(\tau)} \, \frac{d_3}{\kappa}, && (134) \\
\xi_2 &= \omega \, (1 - f(\tau)) \left\{ \dot{\epsilon}^p_m(\tau) + \sigma_m(\tau) \, \frac{\partial}{\partial \sigma_m(\tau)} \, \dot{\epsilon}^p_m(\tau) \right\} \\
& \quad \times \frac{2\,\mu(\tau)}{S(\tau)} \left[d_1 \, \frac{\partial}{\partial S(\tau)} \, \sigma_m(\tau) + d_3 \, \frac{\partial}{\partial p(\tau)} \, \sigma_m(\tau) + d_3 \, \frac{\zeta}{\kappa(\tau)} \, \frac{\partial}{\partial f(\tau)} \, \sigma_m(\tau) \right], \\
\xi_3 &= \left\{ \omega \, (1 - f(\tau)) \, \sigma_m(\tau) \, \frac{\partial}{\partial s(\tau)} \, \dot{\epsilon}^p_m(\tau) \right\} \; d_5 \, \frac{2\,\mu(\tau)}{S(\tau)}
\end{aligned}
$$

and

$$
\begin{aligned}
\beta_1 &= \{ - \omega \, \sigma_m(\tau) \, \dot{\epsilon}^p_m(\tau) \, \zeta \} \; (1 - d_4), && (135) \\
\beta_2 &= \omega \, (1 - f(\tau)) \left\{ \dot{\epsilon}^p_m(\tau) + \sigma_m(\tau) \, \frac{\partial}{\partial \sigma_m(\tau)} \, \dot{\epsilon}^p_m(\tau) \right\} \\
& \quad \times \kappa(\tau) \left[- d_2 \, \frac{\partial}{\partial S(\tau)} \, \sigma_m(\tau) - d_4 \, \frac{\partial}{\partial p(\tau)} \, \sigma_m(\tau) + (1 - d_4) \, \frac{\zeta}{\kappa(\tau)} \, \frac{\partial}{\partial f(\tau)} \, \sigma_m(\tau) \right], \\
\beta_3 &= \left\{ \omega \, (1 - f(\tau)) \, \sigma_m(\tau) \, \frac{\partial}{\partial s(\tau)} \, \dot{\epsilon}^p_m(\tau) \right\} \; d_6 \, (- \kappa(\tau))
\end{aligned}
$$

The Derivative H:

From

$$r^{pl}(\tau) = \omega\, \mathbf{T}(\tau) \cdot \mathbf{D}^{p}(\tau) = \omega\, \{1 - f(\tau)\}\, \sigma_m(\tau)\, \dot{\epsilon}^{p}_{m}\, (\sigma_m(\tau), \theta(\tau), s(\tau))\,,$$

we have

$$\begin{aligned} H \equiv \frac{\partial}{\partial \Delta\theta}\, r^{pl} &= -\omega \left\{ \frac{\partial}{\partial \Delta\theta}\, f(\tau) \right\} \sigma_m(\tau)\, \dot{\epsilon}^{p}_{m}(\tau) && (136) \\ &\quad + \omega\, (1 - f(\tau)) \left\{ \dot{\epsilon}^{p}_{m}(\tau)\, \frac{\partial}{\partial \Delta\theta} \sigma_m(\tau) + \sigma_m(\tau)\, \frac{\partial}{\partial \Delta\theta}\, \dot{\epsilon}^{p}_{m}(\tau) \right\}. \end{aligned}$$

From

$$\Phi\, (S(\tau), p(\tau), f(\tau), \sigma_m(\tau)) = 0$$

we have

$$\begin{aligned} \frac{\partial}{\partial \Delta\theta}\, \sigma_m(\tau) &= \left\{ \frac{\partial}{\partial S(\tau)}\, \sigma_m(\tau) \right\} \frac{\partial}{\partial \Delta\theta}\, S(\tau) + \left\{ \frac{\partial}{\partial p(\tau)}\, \sigma_m(\tau) \right\} \frac{\partial}{\partial \Delta\theta}\, p(\tau) && (137) \\ &\quad + \left\{ \frac{\partial}{\partial f(\tau)}\, \sigma_m(\tau) \right\} \frac{\partial}{\partial \Delta\theta}\, f(\tau), && (138) \end{aligned}$$

where

$$\begin{aligned} \frac{\partial}{\partial S(\tau)}\, \sigma_m(\tau) &= -\frac{\partial}{\partial S(\tau)}\, \Phi(\tau) \Big/ \frac{\partial}{\partial \sigma_m(\tau)}\, \Phi(\tau) && (139) \\ \frac{\partial}{\partial p(\tau)}\, \sigma_m(\tau) &= -\frac{\partial}{\partial p(\tau)}\, \Phi(\tau) \Big/ \frac{\partial}{\partial \sigma_m(\tau)}\, \Phi(\tau) \\ \frac{\partial}{\partial f(\tau)}\, \sigma_m(\tau) &= -\frac{\partial}{\partial f(\tau)}\, \Phi(\tau) \Big/ \frac{\partial}{\partial \sigma_m(\tau)}\, \Phi(\tau). \end{aligned}$$

Also

$$\frac{\partial}{\partial \Delta\theta}\, \dot{\epsilon}^{p}_{m}(\tau) = \left\{ \frac{\partial}{\partial \sigma_m(\tau)} \dot{\epsilon}^{p}_{m}(\tau) \right\} \frac{\partial}{\partial \Delta\theta}\, \sigma_m(\tau) + \left\{ \frac{\partial}{\partial s(\tau)} \dot{\epsilon}^{p}_{m}(\tau) \right\} \frac{\partial}{\partial \Delta\theta}\, s(\tau) + \left\{ \frac{\partial}{\partial \theta(\tau)}\, \dot{\epsilon}^{p}_{m}(\tau) \right\}. \qquad (140)$$

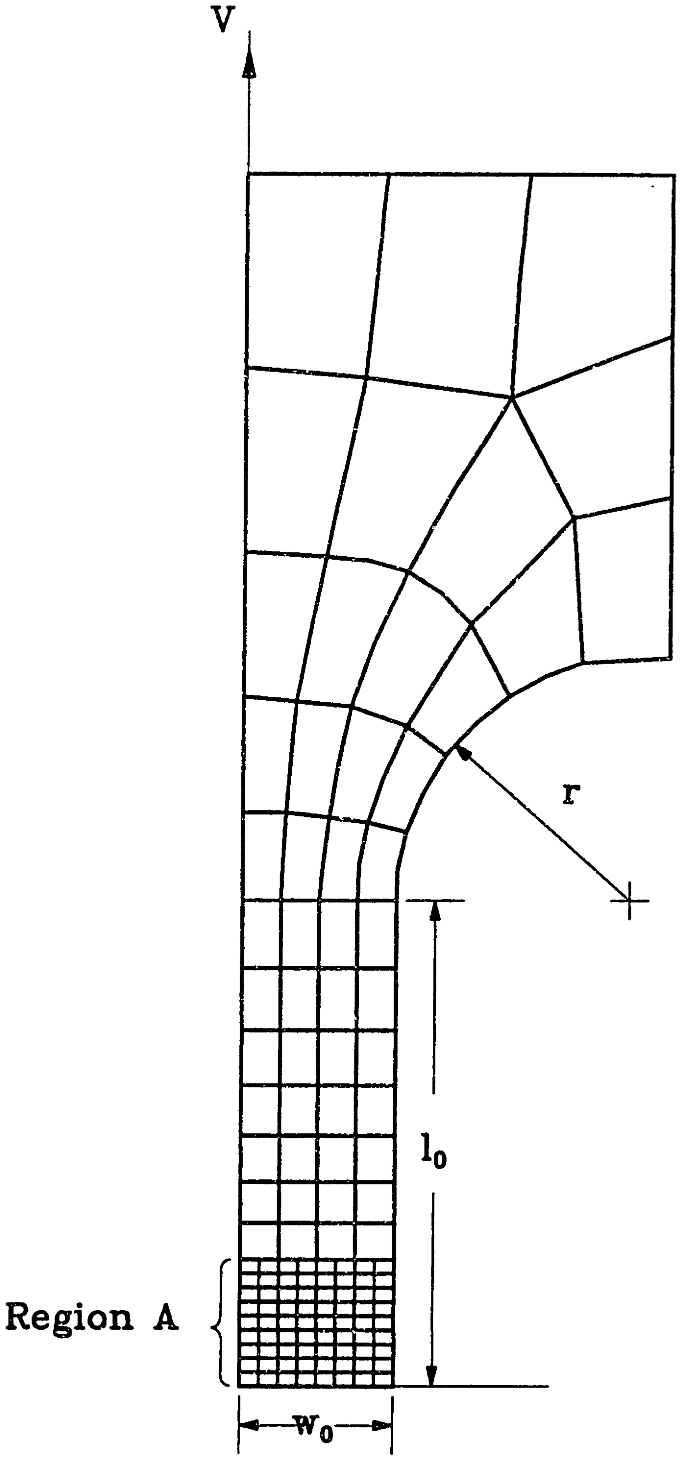

$v = 2.5$ m/s
$w_0 = (8/25)\ l_0$
$r = l_0/2$
$l_0 = 50$ mm

Fig. 1 Geometry of the plane strain tension test. The mesh represents only one quarter of the specimen. All views of the specimen in subsequent figures show only region A of the complete mesh.

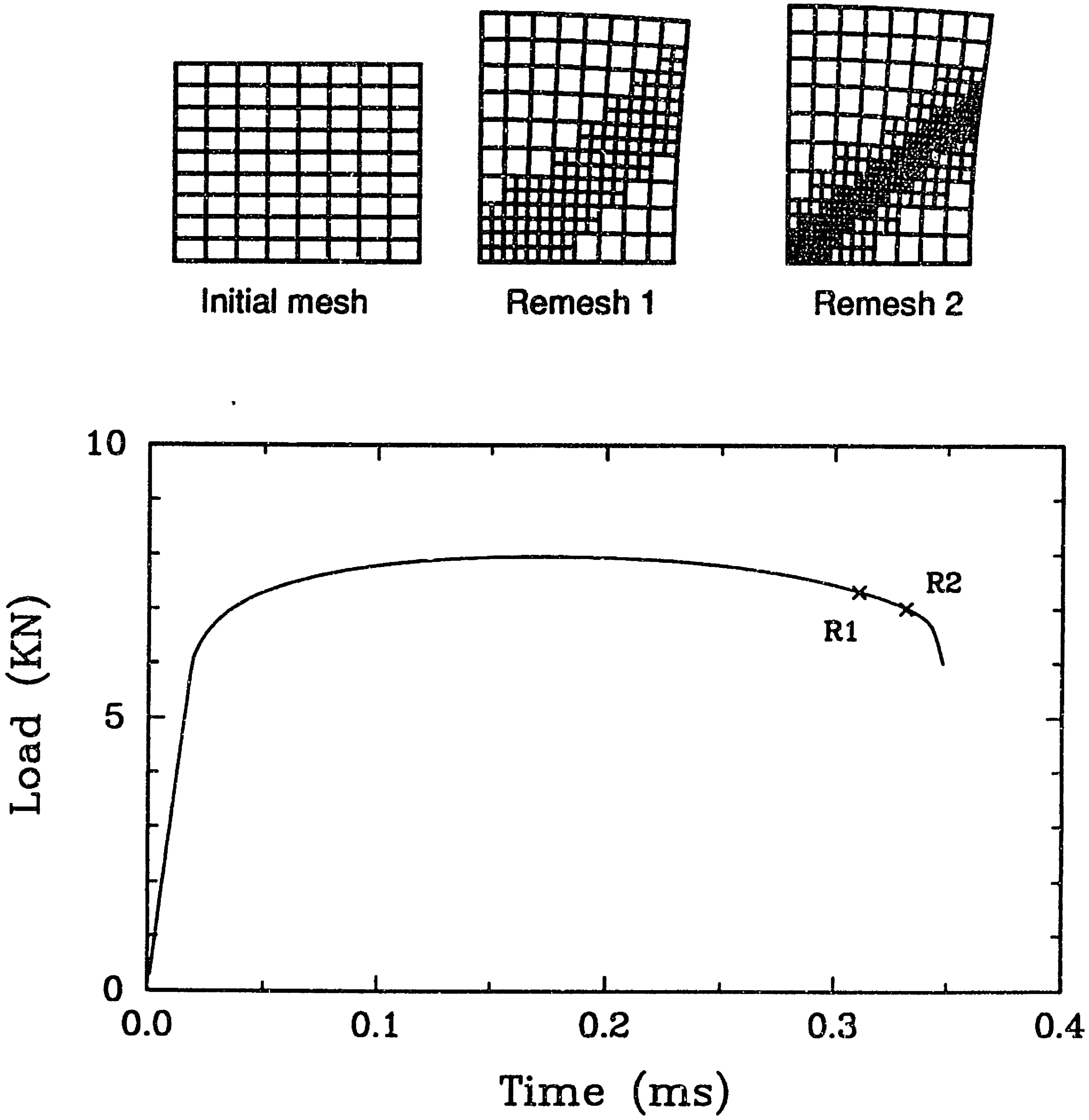

Fig. 2 Remeshing sequence for the case of fully dense material with λ=160. W/(m°K). (R1=Remesh1, R2=Remesh2)

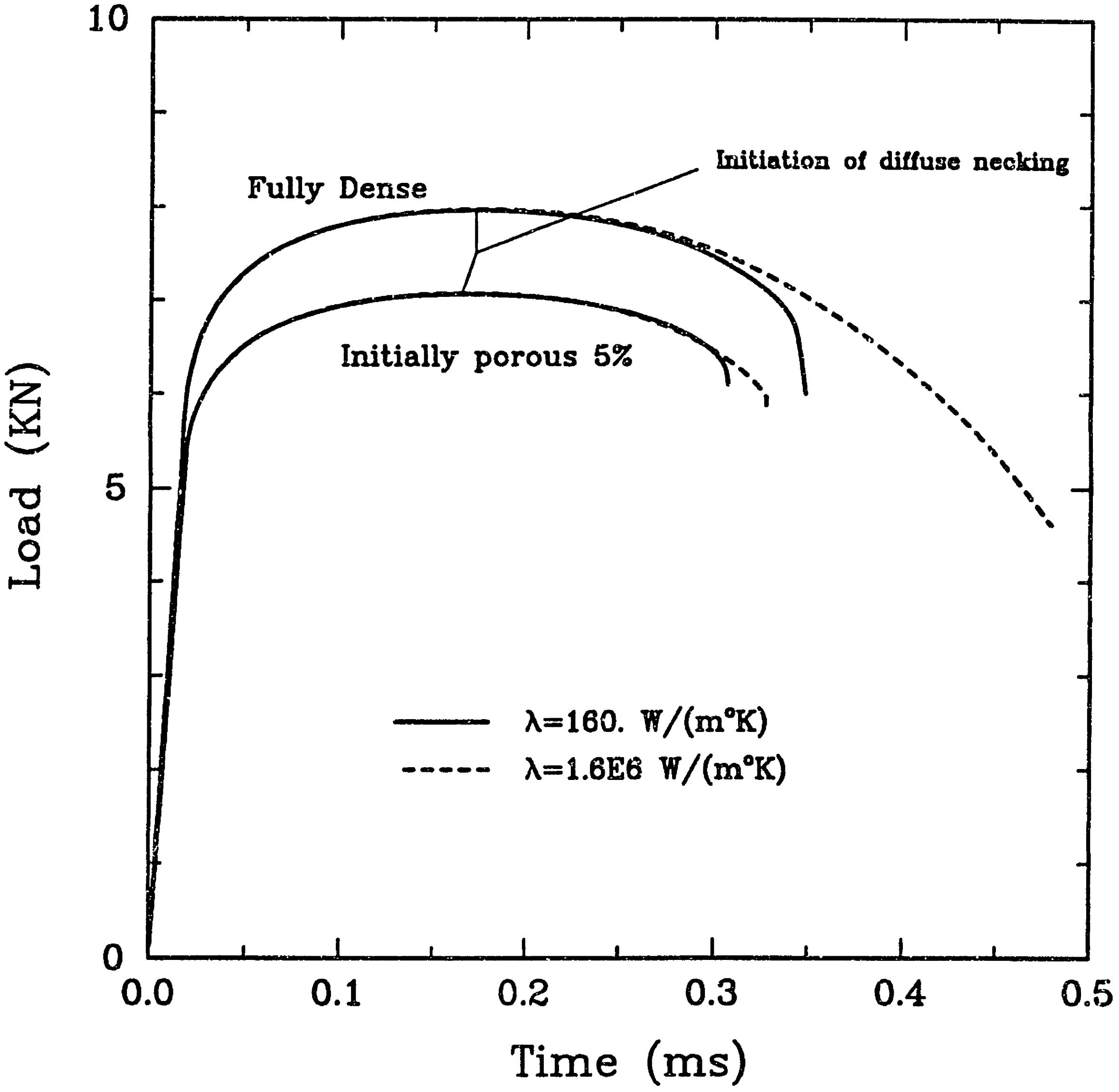

Fig. 3 Load versus time curves for fully dense and porous materials with a realistic value of thermal conductivity, λ=160 W/(m°K), and an artificialy enhanced value of thermal conductivity, λ=1.6E6 W/(m°K).

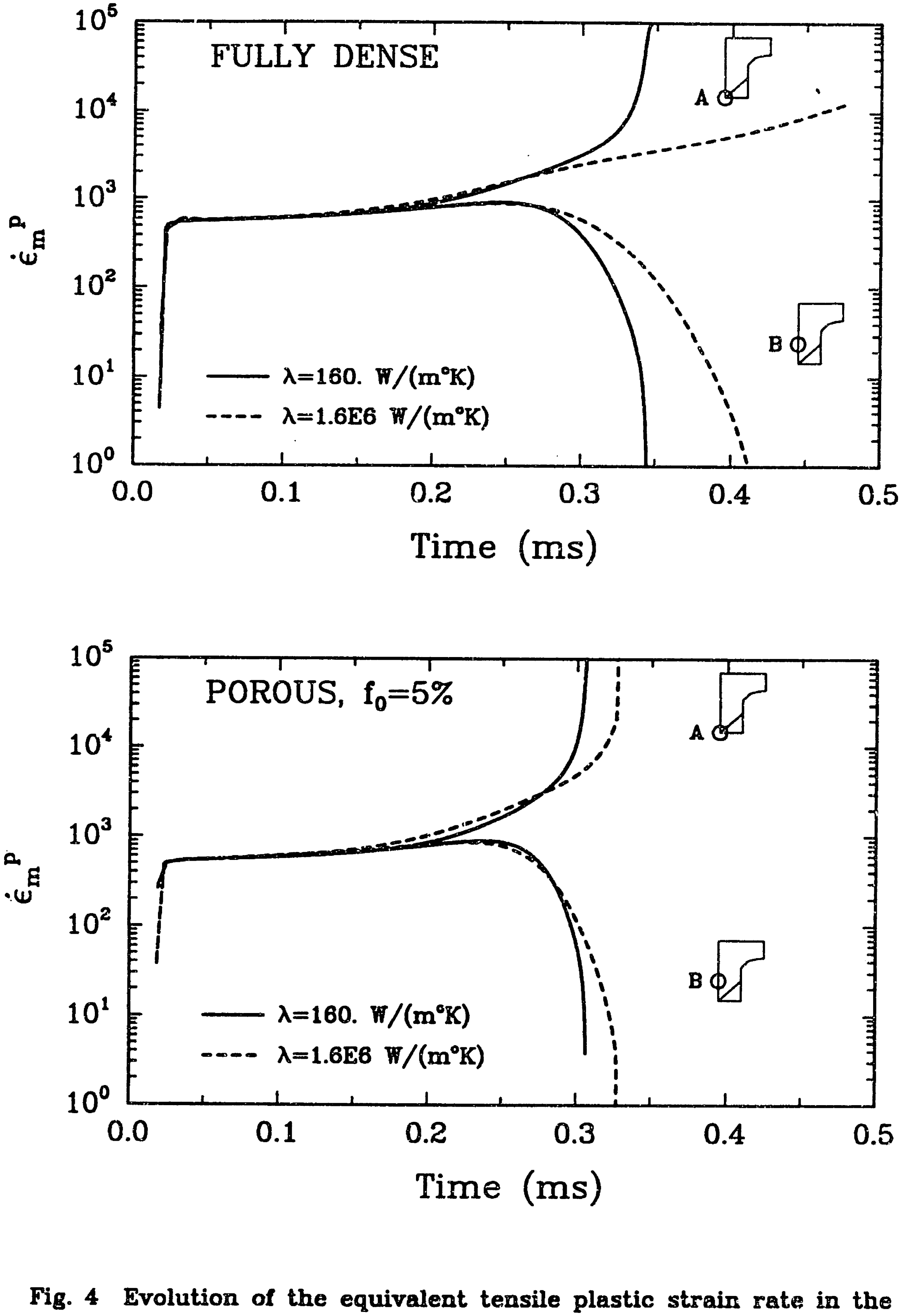

Fig. 4 Evolution of the equivalent tensile plastic strain rate in the fully dense and initially porous specimens during the course of the deformation at two points, one at the center of the specimen (A) and one outside the central region on the axis of symmetry (B).

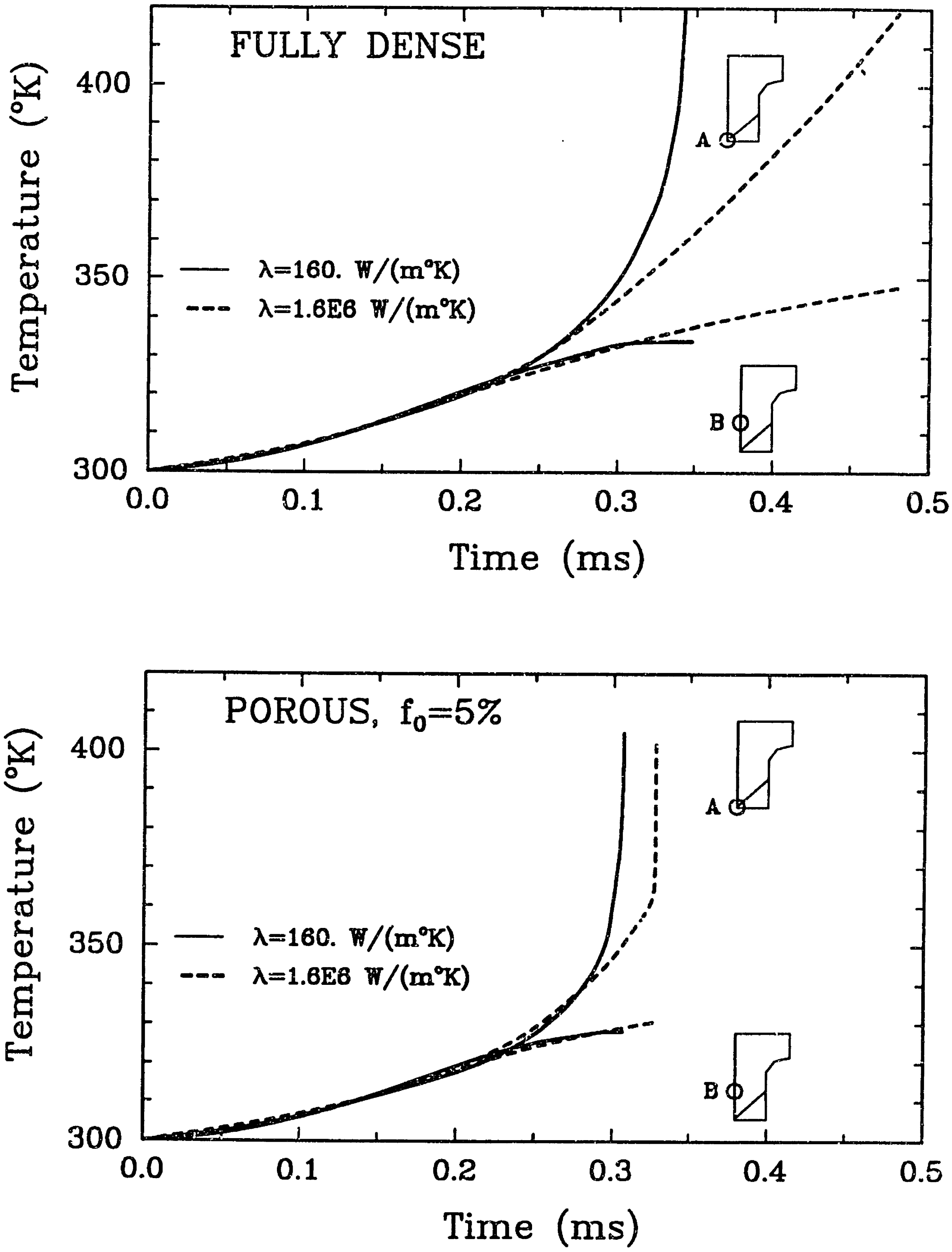

Fig. 5 Evolution of the temperature in the fully dense and initially porous specimens during the course of the deformation at two points, one at the center of the specimen (A) and one outside the central region on the axis of symmetry (B).

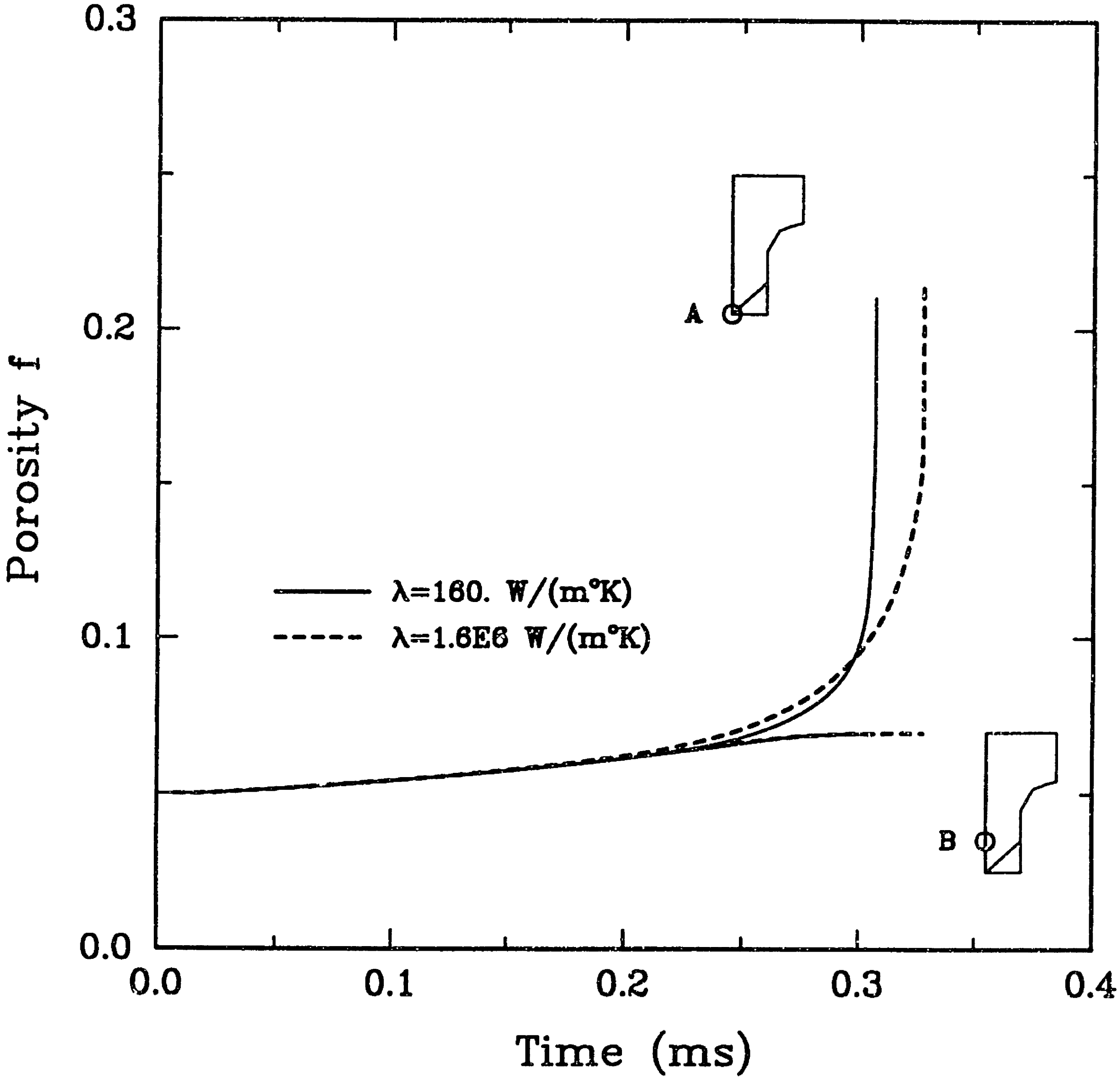

Fig. 6 Evolution of the porosity in the initially porous specimens during the course of the deformation at two points, one at the center of the specimen (A) and one outside the central region on the axis of symmetry (B).

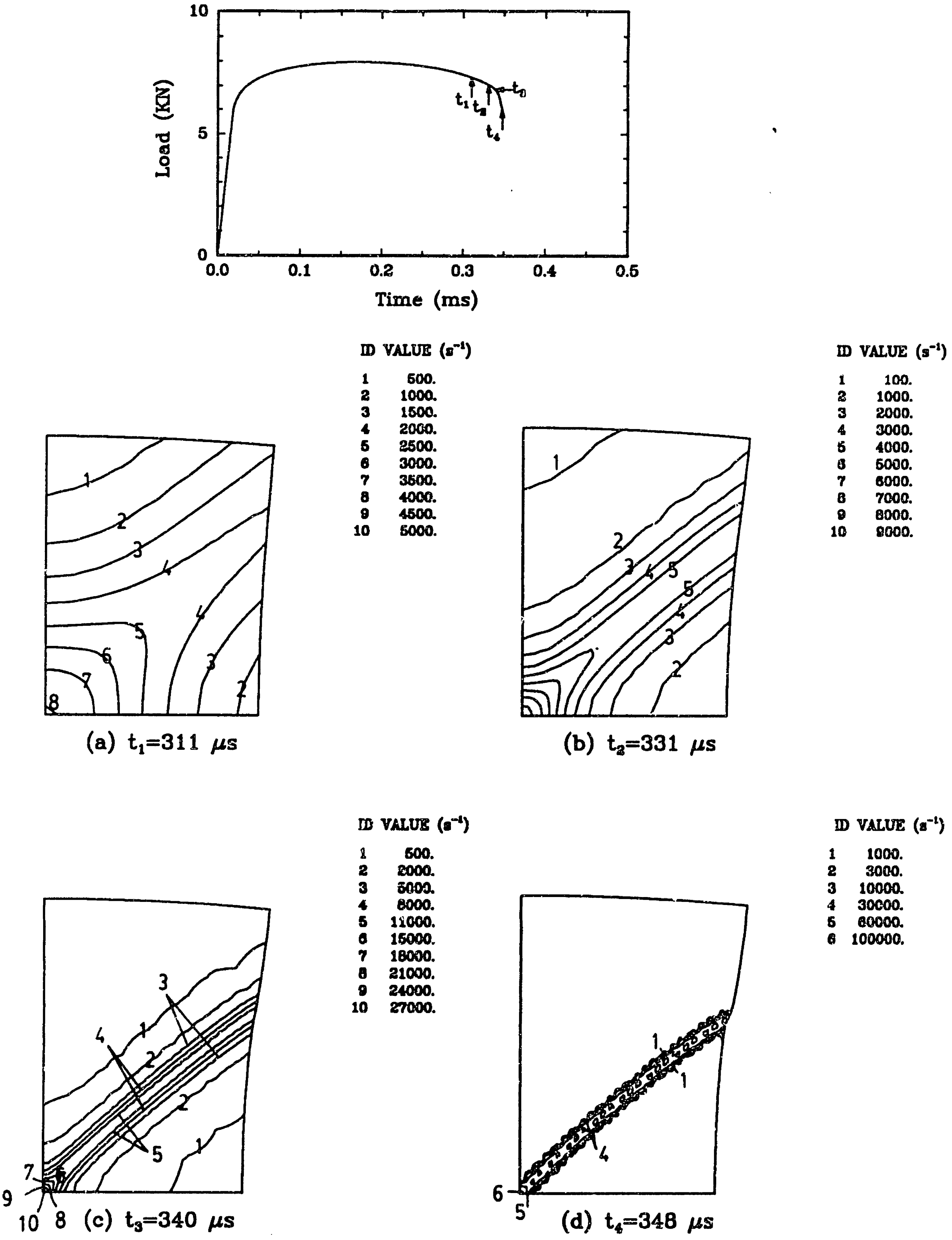

(a) t_1=311 μs

(b) t_2=331 μs

(c) t_3=340 μs

(d) t_4=348 μs

Fig. 7 Contours of equivalent plastic strain rate in a fully dense material with λ=160. W/(m°K)

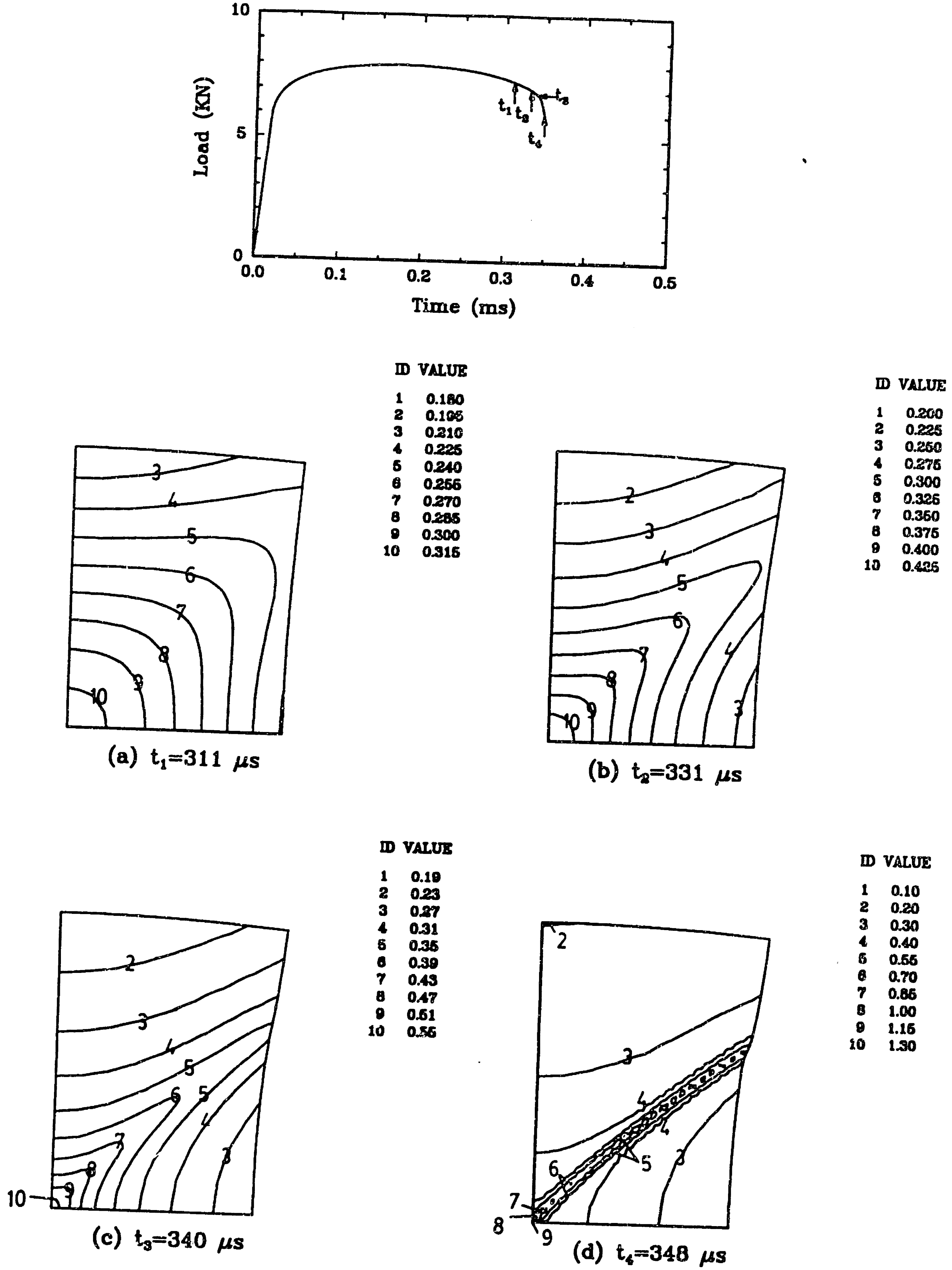

(a) t_1=311 μs

(b) t_2=331 μs

(c) t_3=340 μs

(d) t_4=348 μs

Fig. 8 Contours of equivalent tensile plastic strain in a fully dense material with λ=160. W/(m°K)

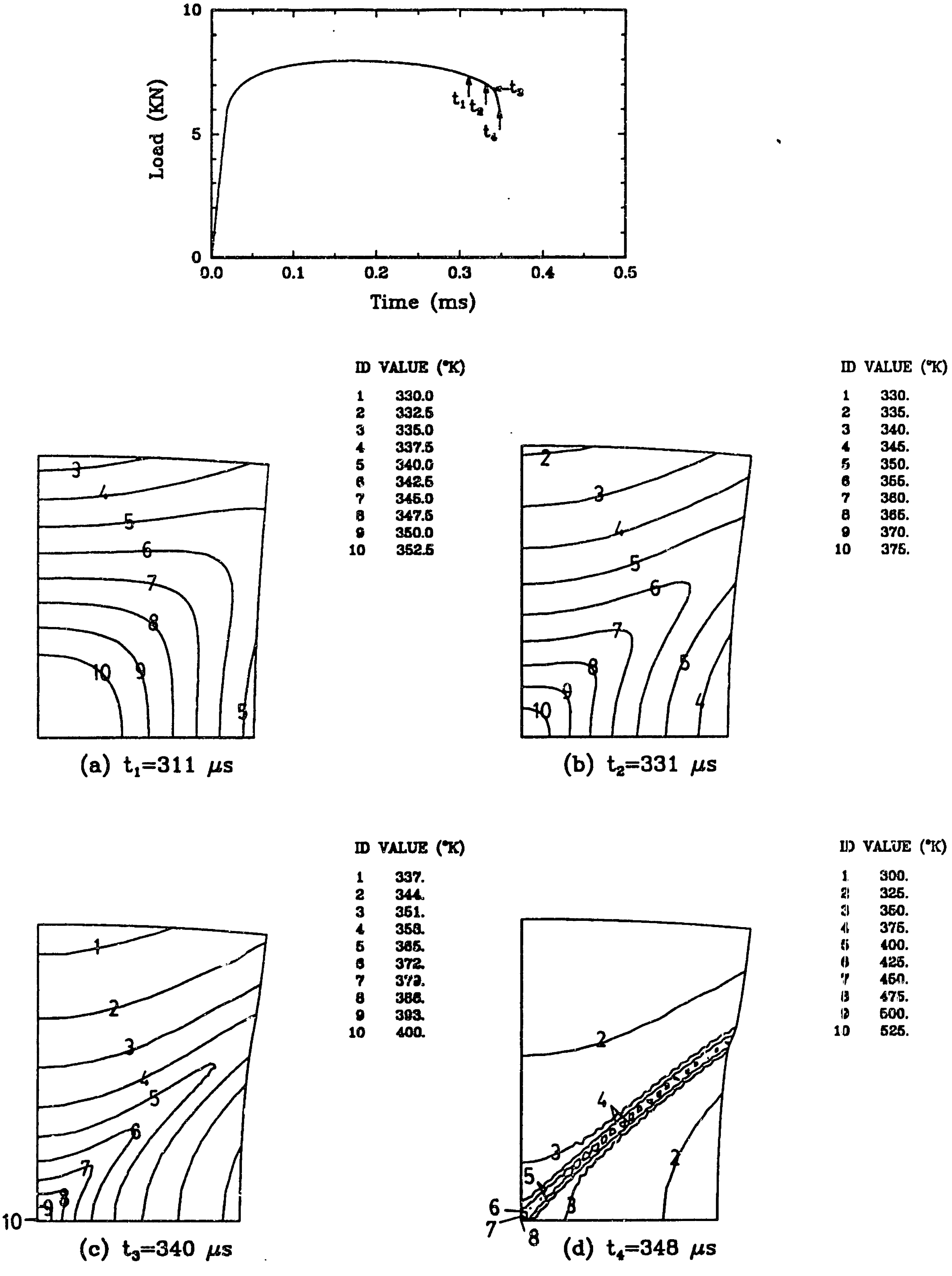

(a) t_1=311 μs

(b) t_2=331 μs

(c) t_3=340 μs

(d) t_4=348 μs

Fig. 9 Contours of temperature in a fully dense material with λ=160. W/m°K

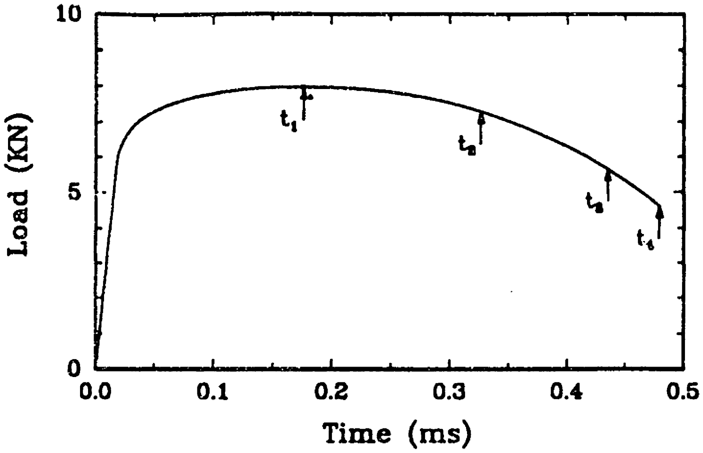

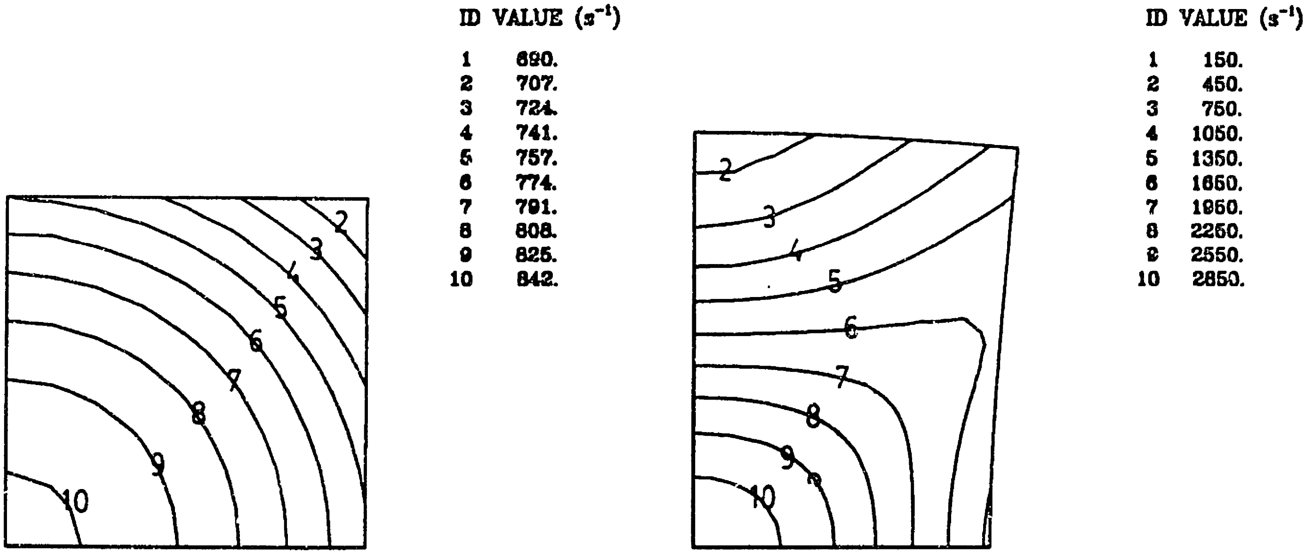

ID	VALUE (s^{-1})
1	690.
2	707.
3	724.
4	741.
5	757.
6	774.
7	791.
8	808.
9	825.
10	842.

ID	VALUE (s^{-1})
1	150.
2	450.
3	750.
4	1050.
5	1350.
6	1650.
7	1950.
8	2250.
9	2550.
10	2850.

(a) t_1=176 μs (b) t_2=327 μs

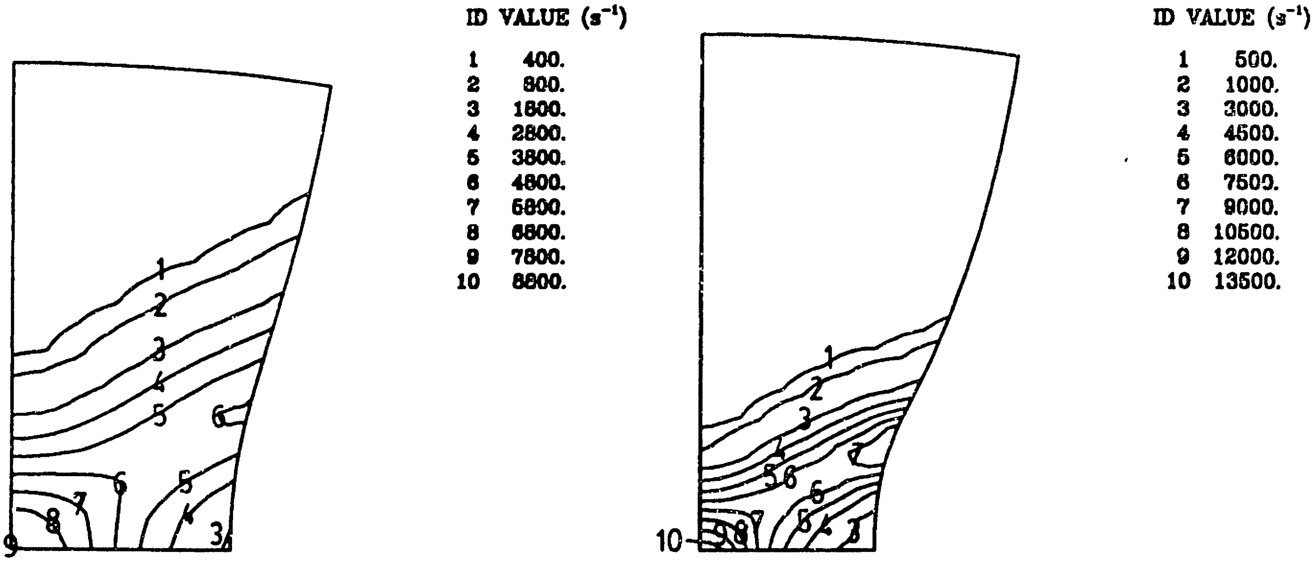

ID	VALUE (s^{-1})
1	400.
2	800.
3	1800.
4	2800.
5	3800.
6	4800.
7	5800.
8	6800.
9	7800.
10	8800.

ID	VALUE (s^{-1})
1	500.
2	1000.
3	3000.
4	4500.
5	6000.
6	7500.
7	9000.
8	10500.
9	12000.
10	13500.

(c) t_3=435 μs (d) t_4=479 μs

Fig. 10 Contours of equivalent tensile plastic strain rate in a fully dense material with λ=1.6E6 W/(m°K)

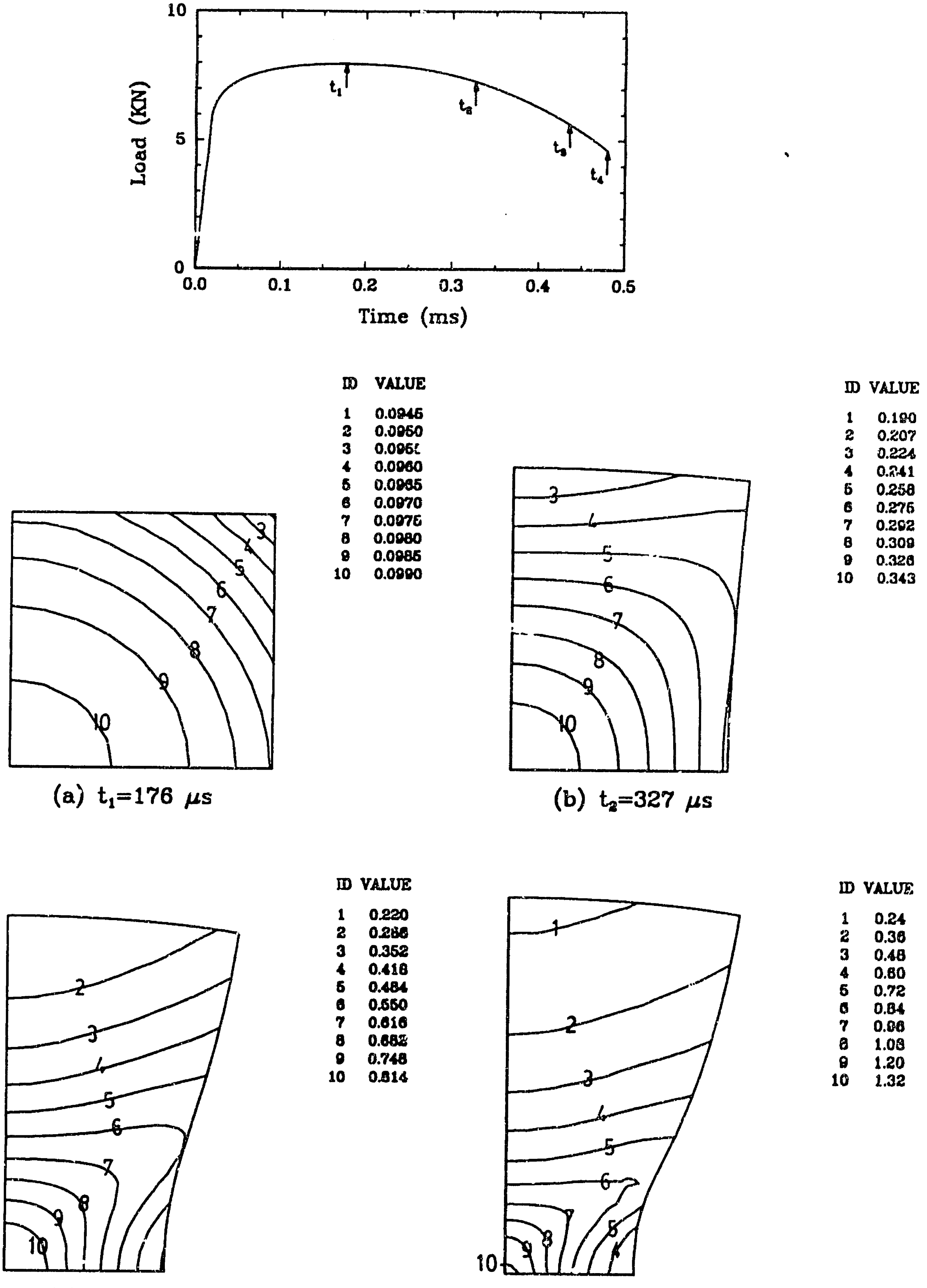

(a) t_1=176 μs

(b) t_2=327 μs

(c) t_3=435 μs

(d) t_4=479 μs

Fig. 11 Contours of equivalent tensile plastic strain in a fully dense material with λ=1.6E6 W/(m°K)

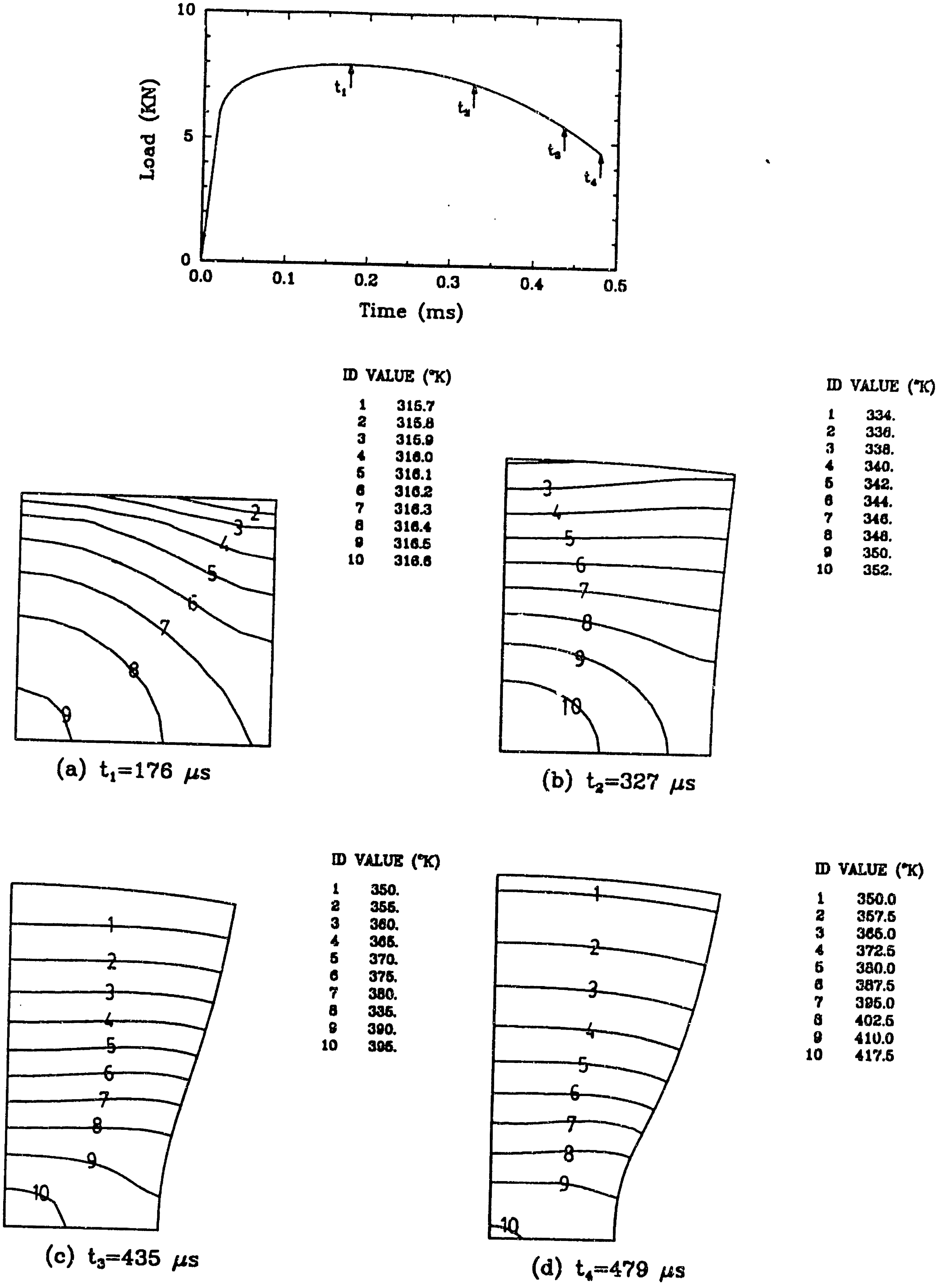

(a) t_1=176 μs

(b) t_2=327 μs

(c) t_3=435 μs

(d) t_4=479 μs

Fig. 12 Contours of temperature in a fully dense material with λ=1.6E6 W/(m°K)

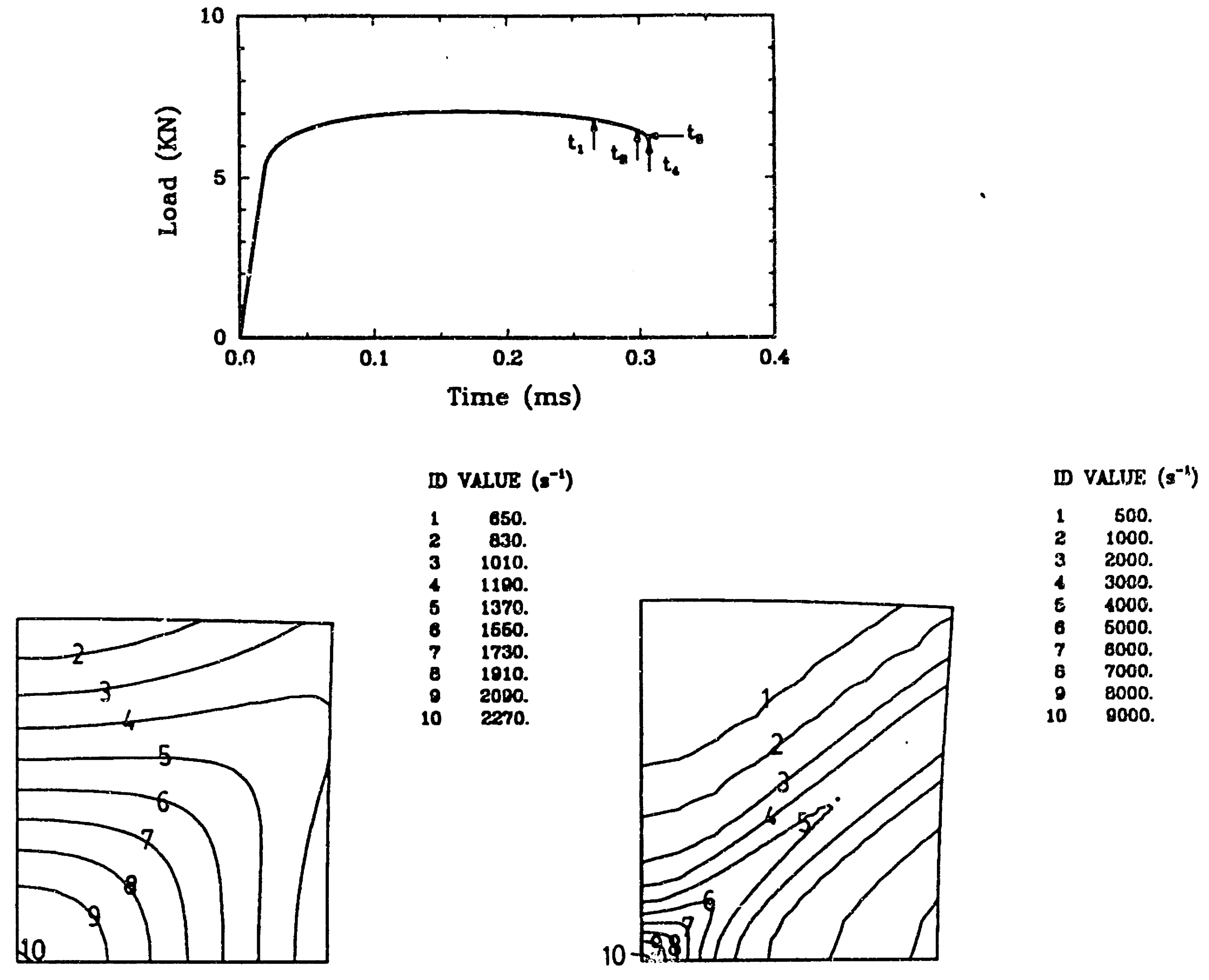

ID	VALUE (s^{-1})
1	650.
2	830.
3	1010.
4	1190.
5	1370.
6	1550.
7	1730.
8	1910.
9	2090.
10	2270.

ID	VALUE (s^{-1})
1	500.
2	1000.
3	2000.
4	3000.
5	4000.
6	5000.
7	6000.
8	7000.
9	8000.
10	9000.

(a) t_1=265 μs (b) t_2=298 μs

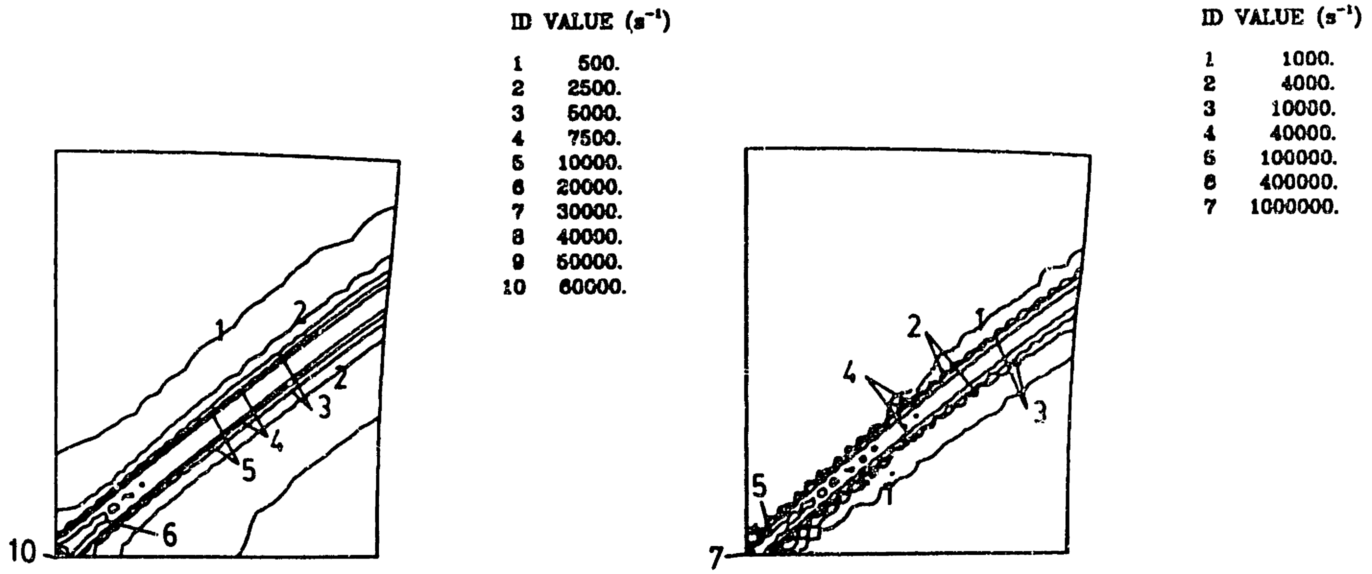

ID	VALUE (s^{-1})
1	500.
2	2500.
3	5000.
4	7500.
5	10000.
6	20000.
7	30000.
8	40000.
9	50000.
10	60000.

ID	VALUE (s^{-1})
1	1000.
2	4000.
3	10000.
4	40000.
5	100000.
6	400000.
7	1000000.

(c) t_3=305 μs (d) t_4=307 μs

Fig. 13 Contours of equivalent tensile plastic strain rate in the matrix in a porous material with λ=160. W/(m°K)

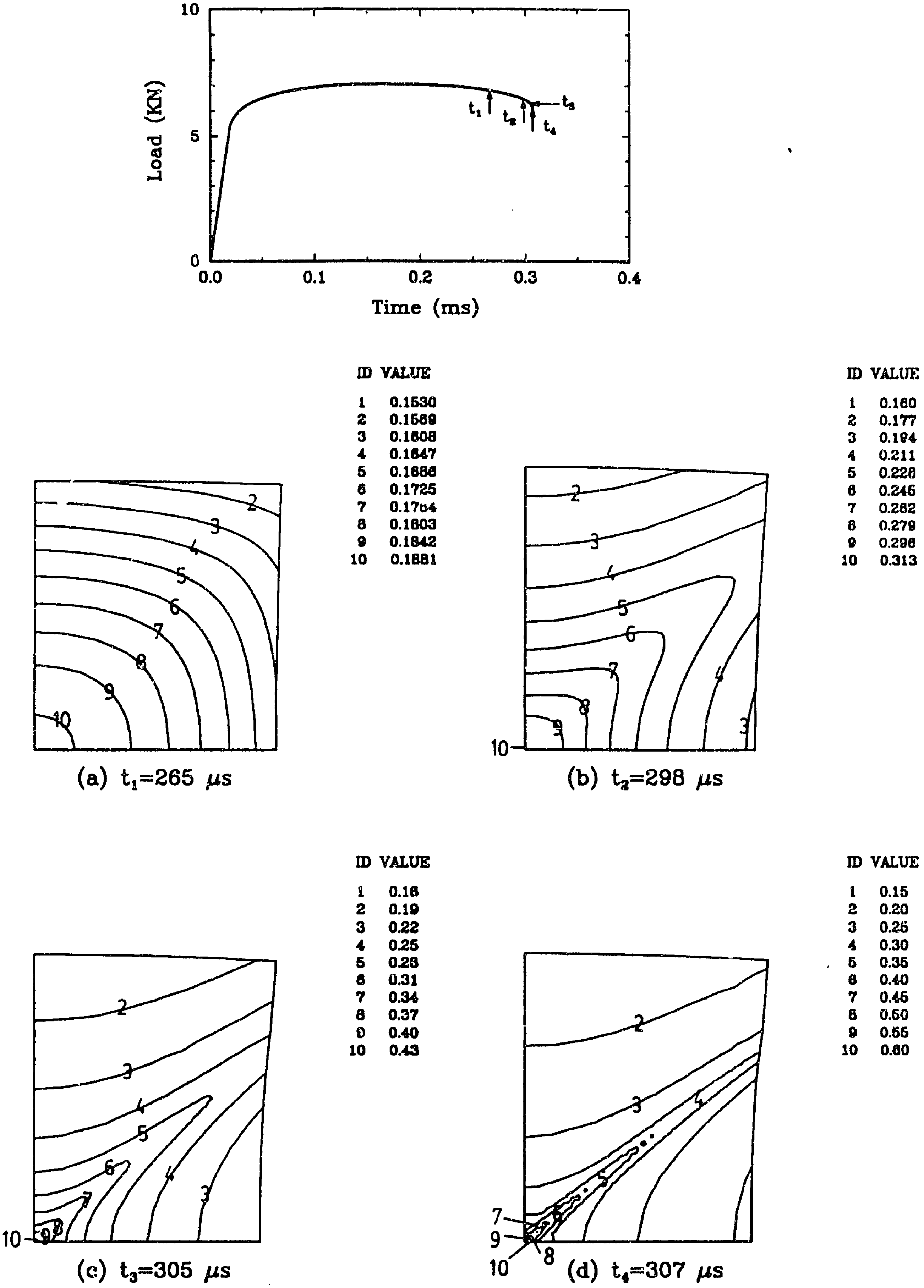

(a) t_1=265 μs

(b) t_2=298 μs

(c) t_3=305 μs

(d) t_4=307 μs

Fig. 14 Contours of equivalent tensile plastic strain in the matrix in a porous material with λ=160. W/(m°K)

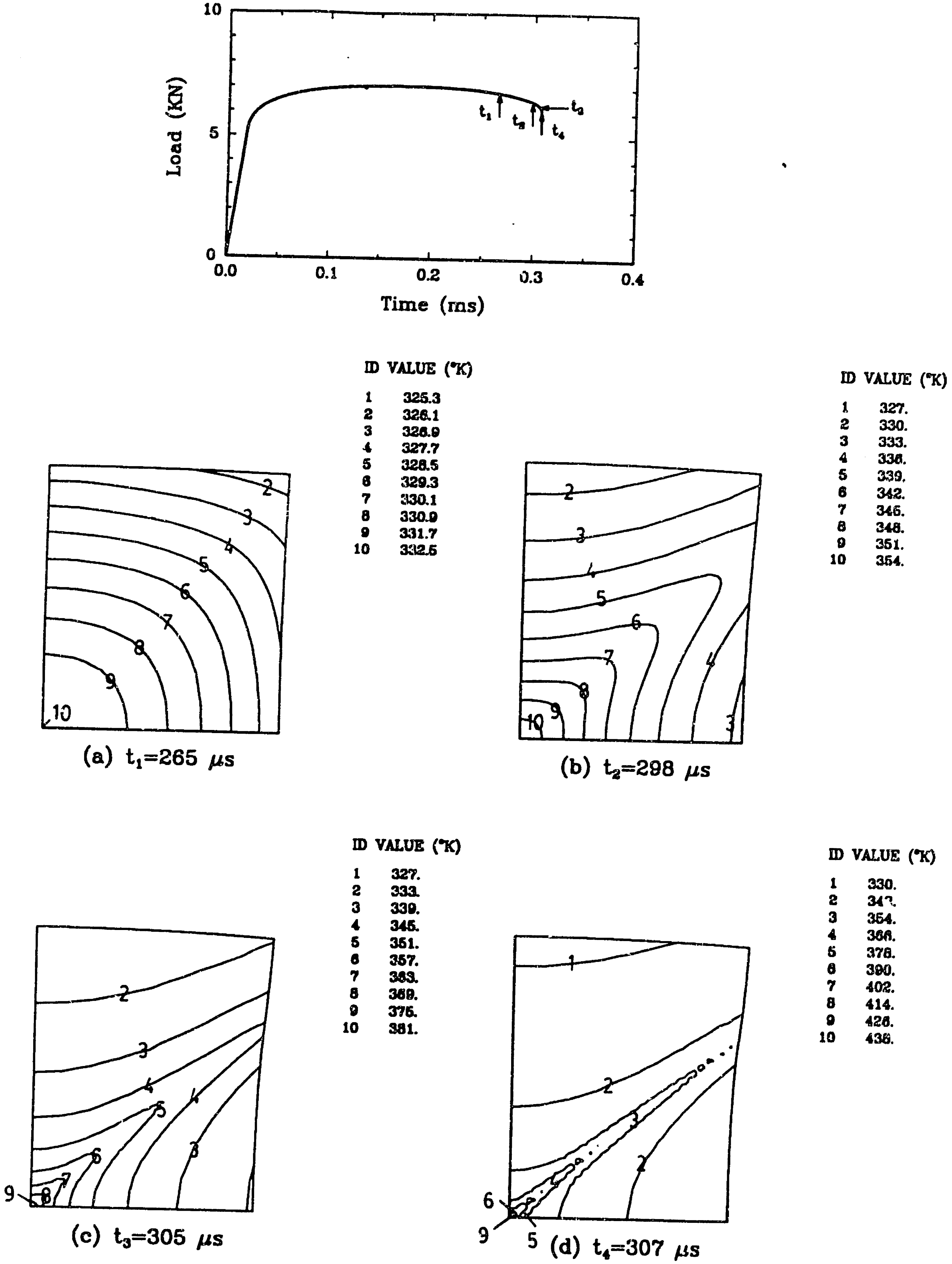

(a) t_1=265 μs

(b) t_2=298 μs

(c) t_3=305 μs

(d) t_4=307 μs

Fig. 15 Contours of temperature in a porous material with λ=160. W/(m°K)

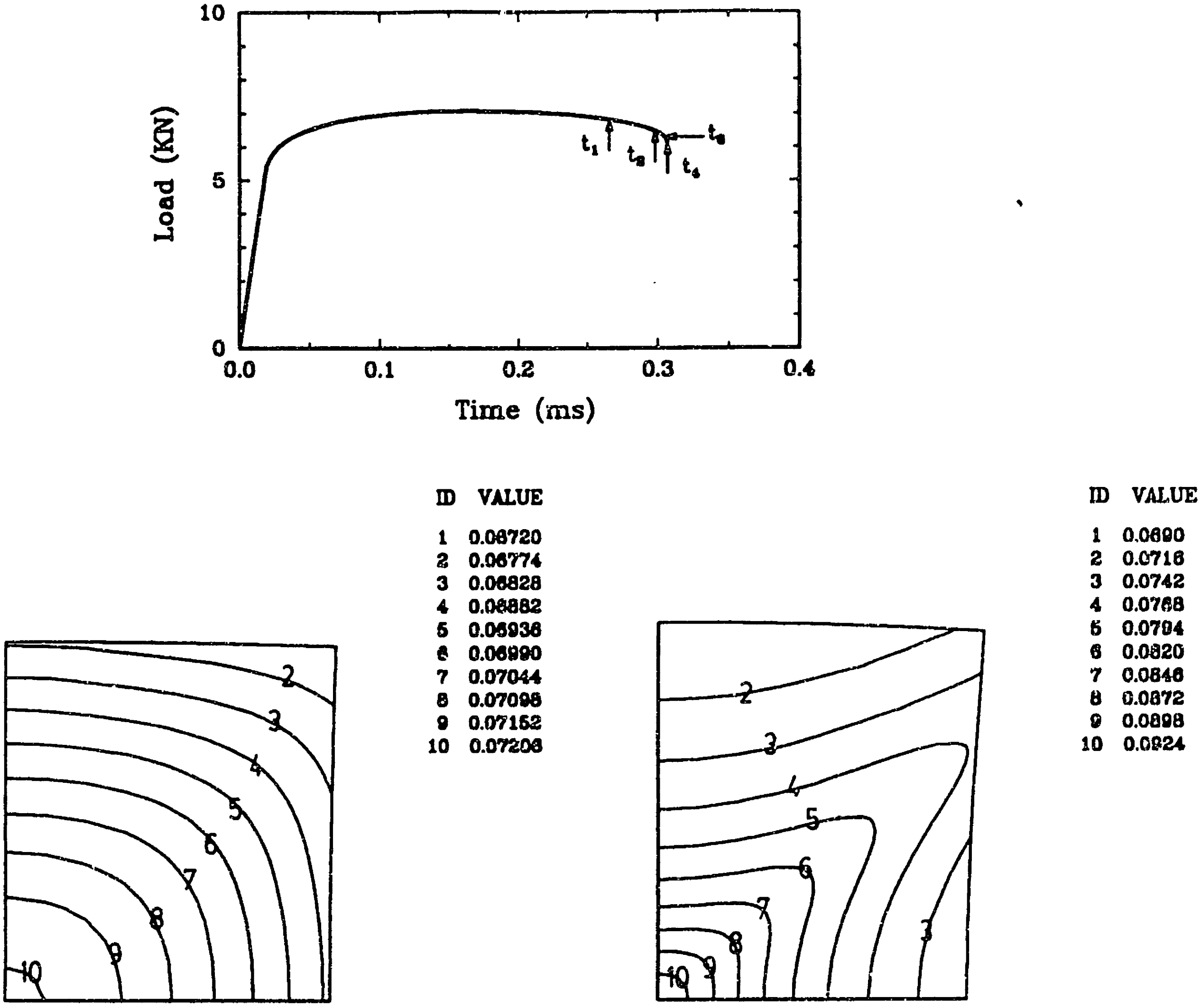

ID	VALUE
1	0.06720
2	0.06774
3	0.06828
4	0.06882
5	0.06936
6	0.06990
7	0.07044
8	0.07098
9	0.07152
10	0.07206

ID	VALUE
1	0.0690
2	0.0716
3	0.0742
4	0.0768
5	0.0794
6	0.0820
7	0.0846
8	0.0872
9	0.0898
10	0.0924

(a) t_1=265 μs

(b) t_2=298 μs

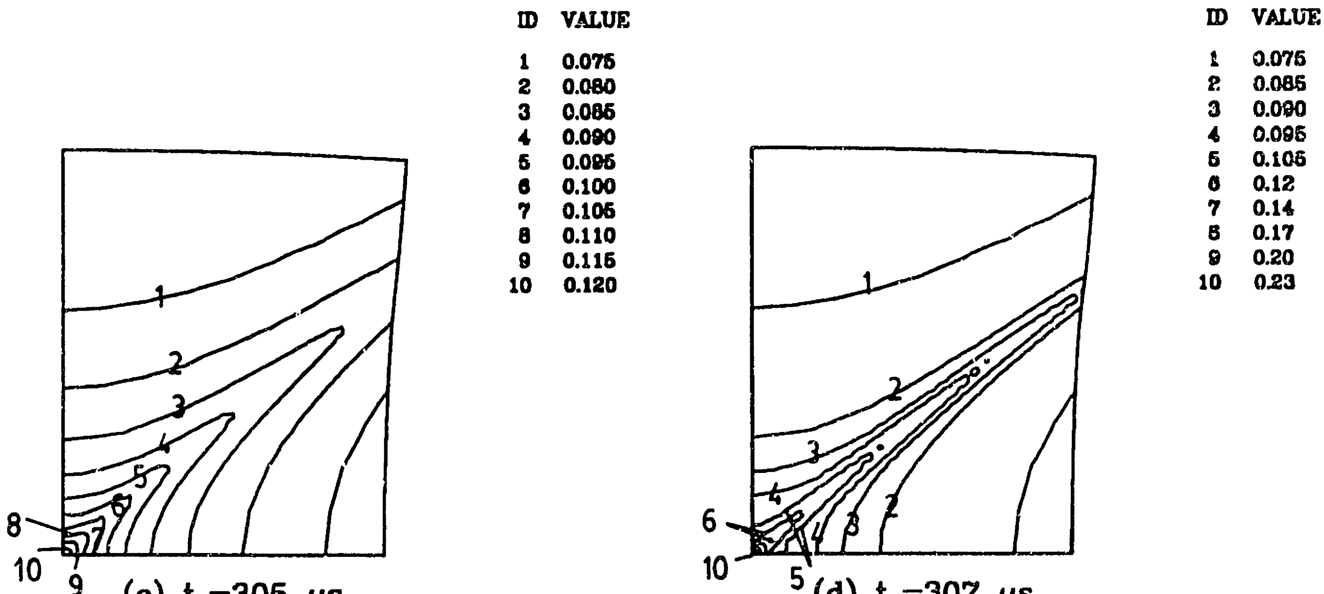

ID	VALUE
1	0.075
2	0.080
3	0.085
4	0.090
5	0.095
6	0.100
7	0.105
8	0.110
9	0.115
10	0.120

ID	VALUE
1	0.075
2	0.085
3	0.090
4	0.095
5	0.105
6	0.12
7	0.14
8	0.17
9	0.20
10	0.23

(c) t_3=305 μs

(d) t_4=307 μs

Fig. 16 Contours of porosity in a porous with λ=160. W/(m°K)

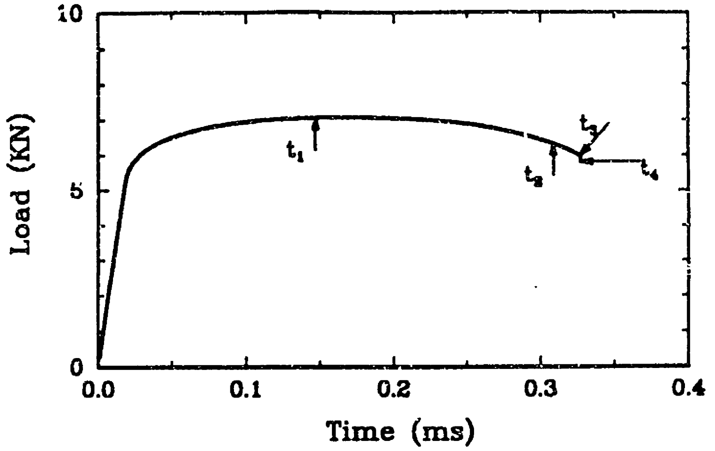

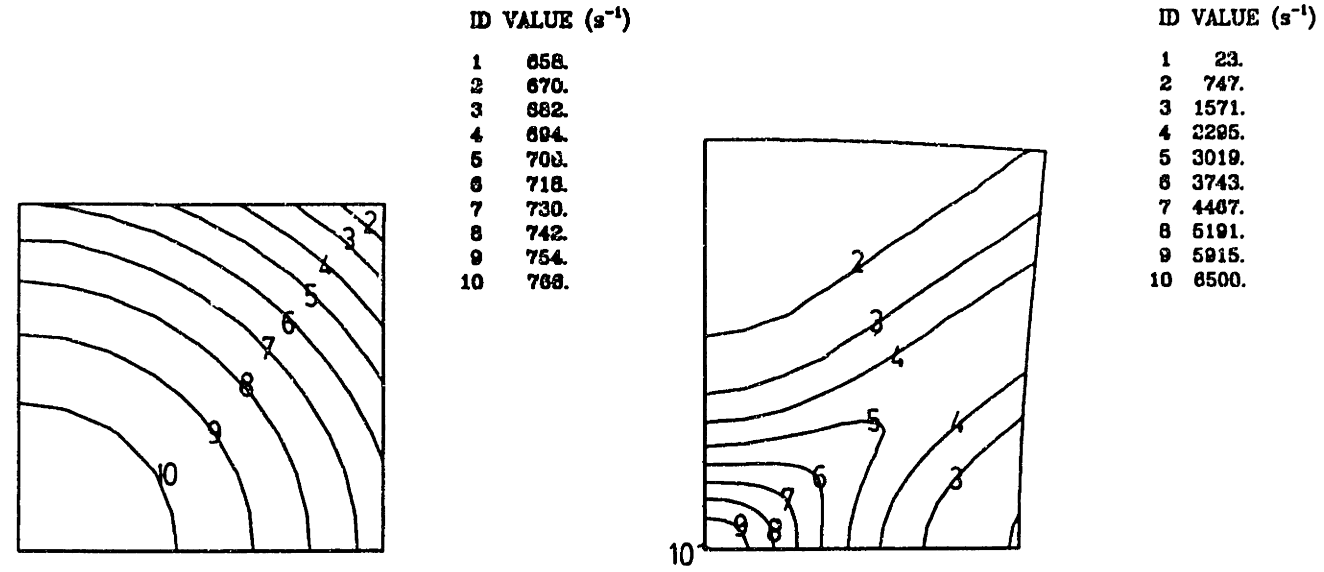

(a) t_1=147 μs

(b) t_2=308 μs

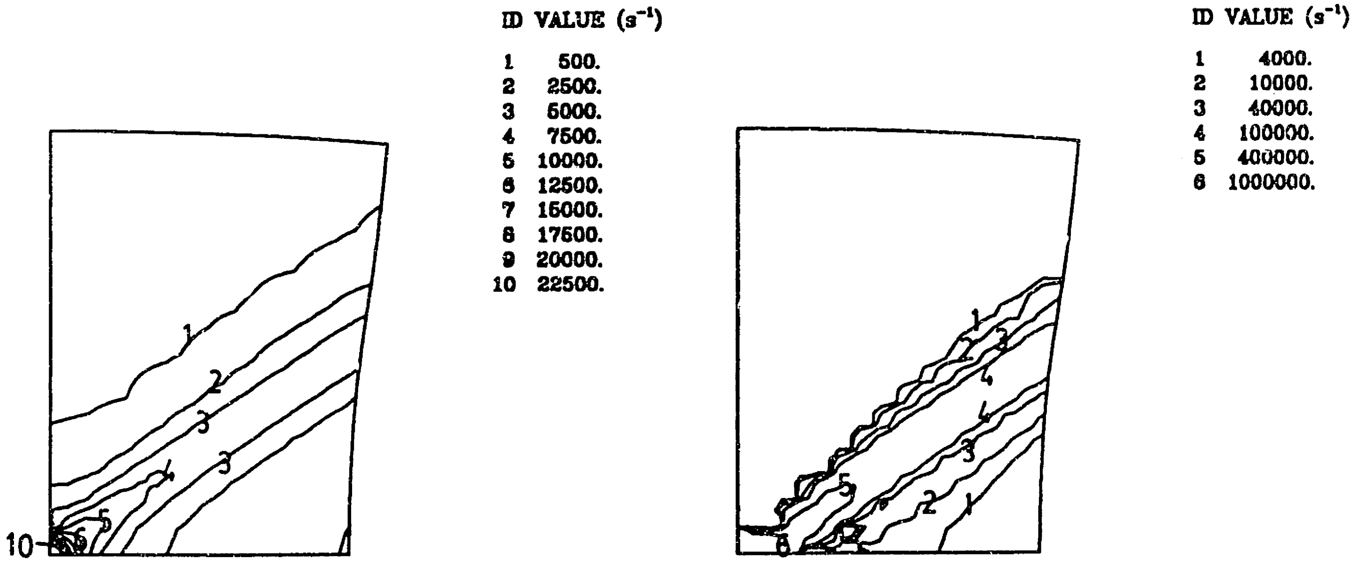

(c) t_3=346 μs

(d) t_4=367 μs

Fig. 17 Contours of equivalent tensile plastic strain rate in the matrix in a porous material with λ=1.6E6 W/(m°K)

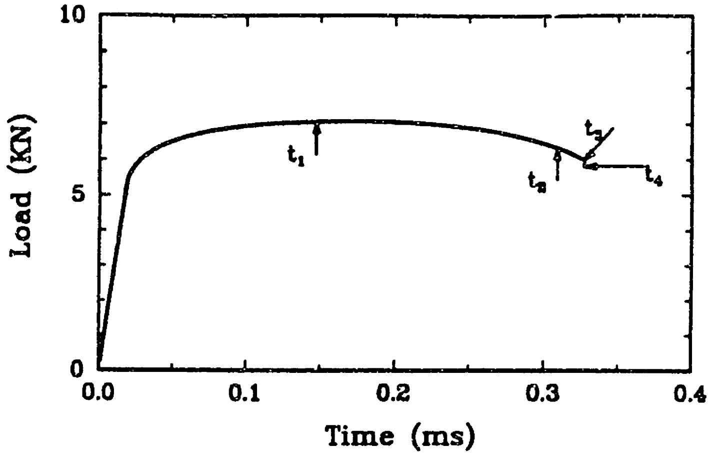

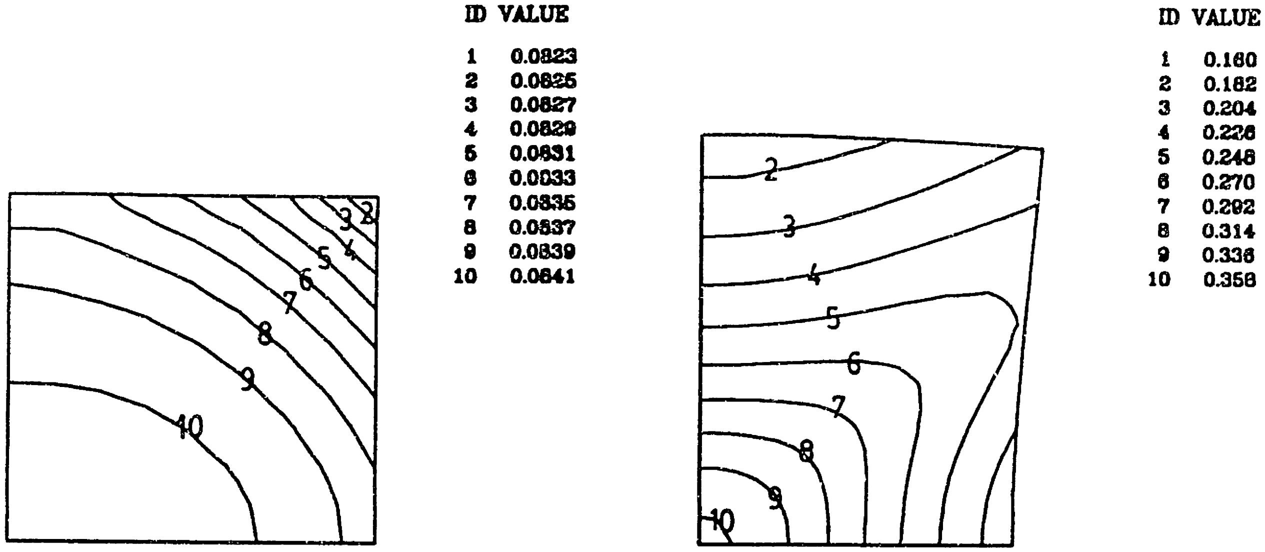

(a) t_1=147 μs (b) t_2=308 μs

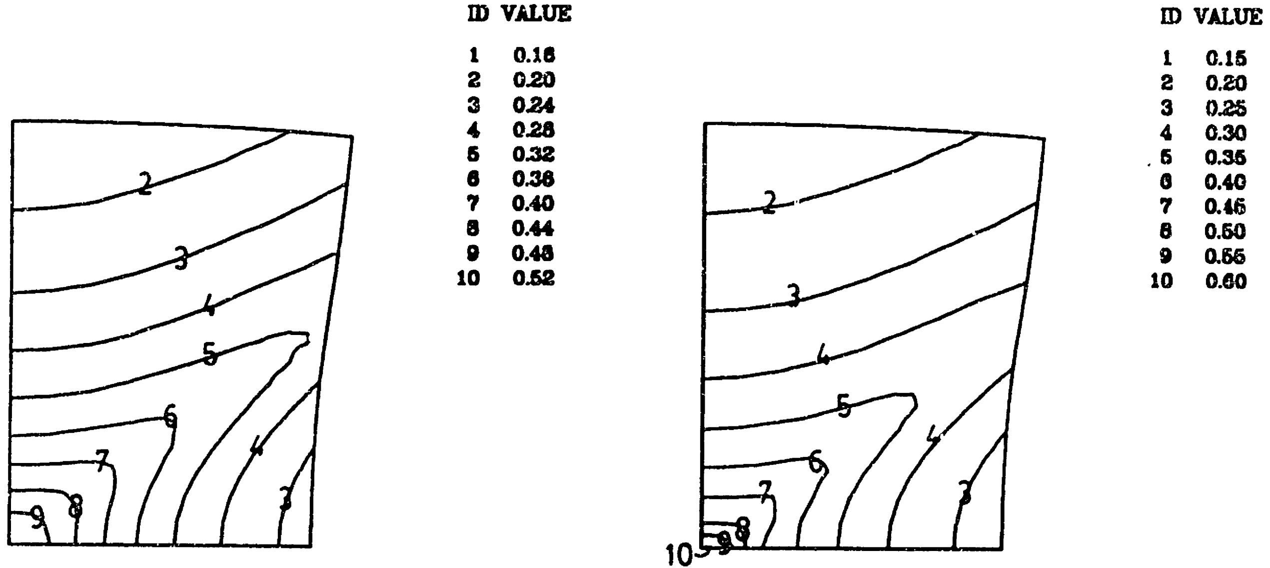

(c) t_3=346 μs (d) t_4=367 μs

Fig. 18 Contours of equivalent tensile plastic strain in the matrix in a porous material with λ=1.6E6 W/(m°K)

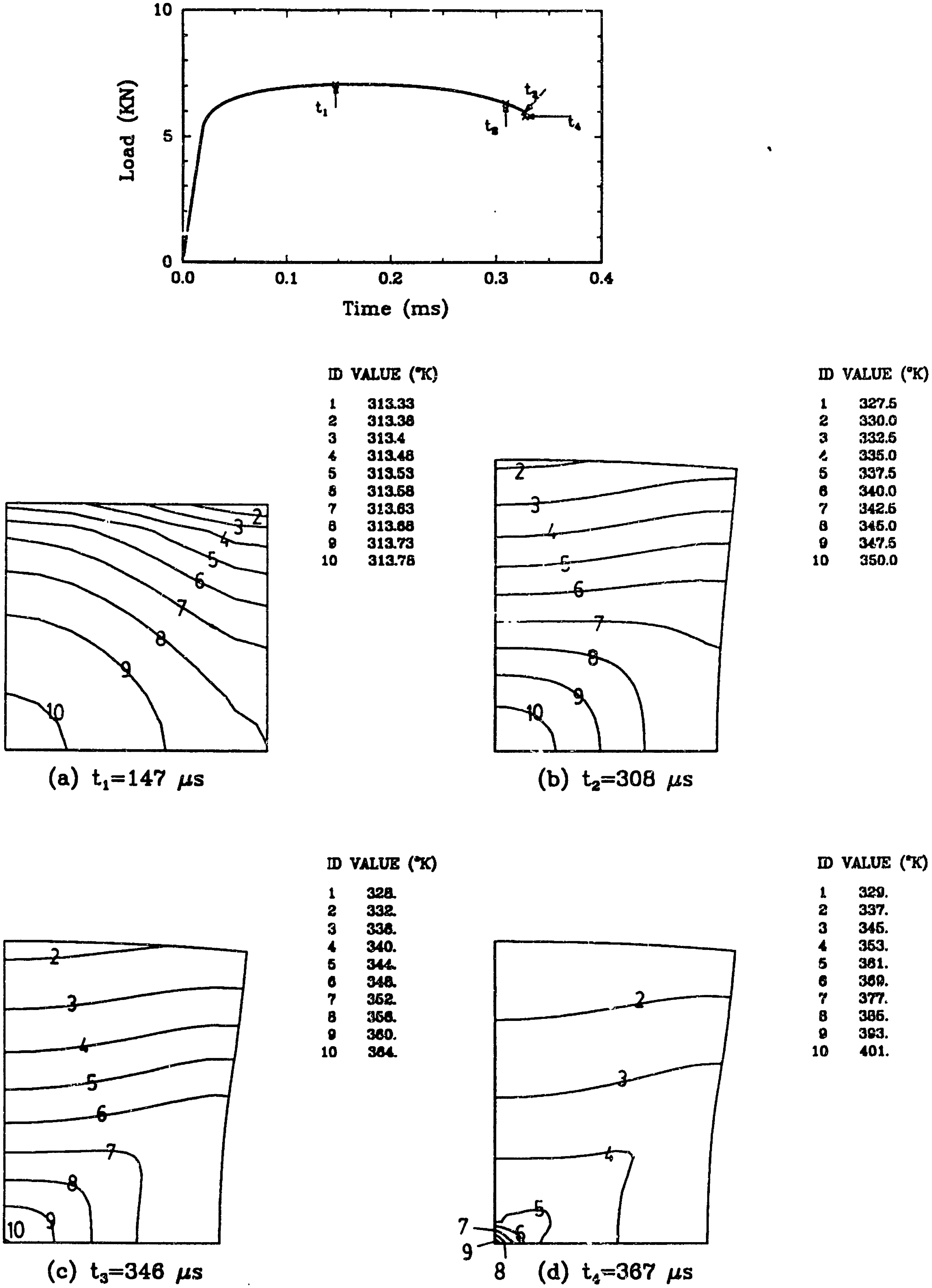

(a) $t_1=147\ \mu s$

(b) $t_2=308\ \mu s$

(c) $t_3=346\ \mu s$

(d) $t_4=367\ \mu s$

Fig. 19 Contours of temperature in a porous material with $\lambda=1.6E6$ W/(m°K)

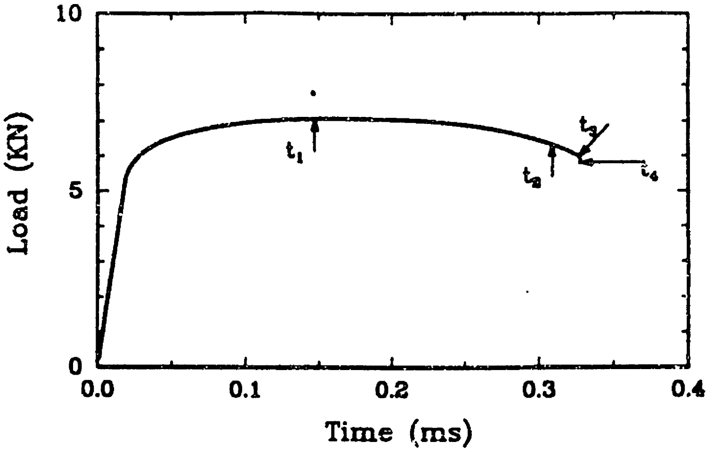

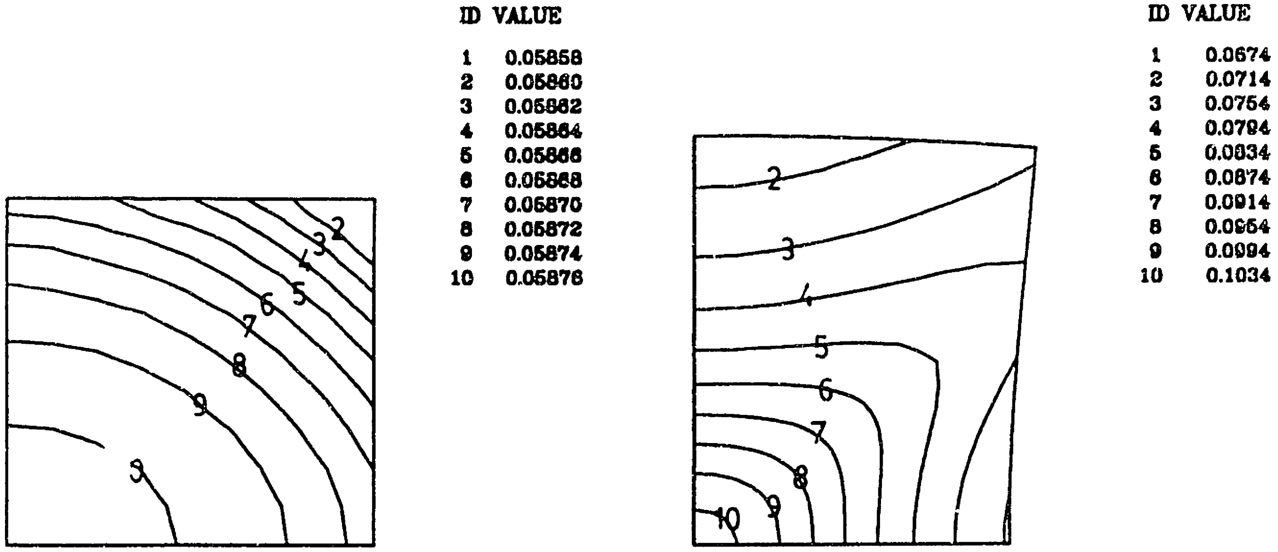

(a) t_1=147 μs

(b) t_2=308 μs

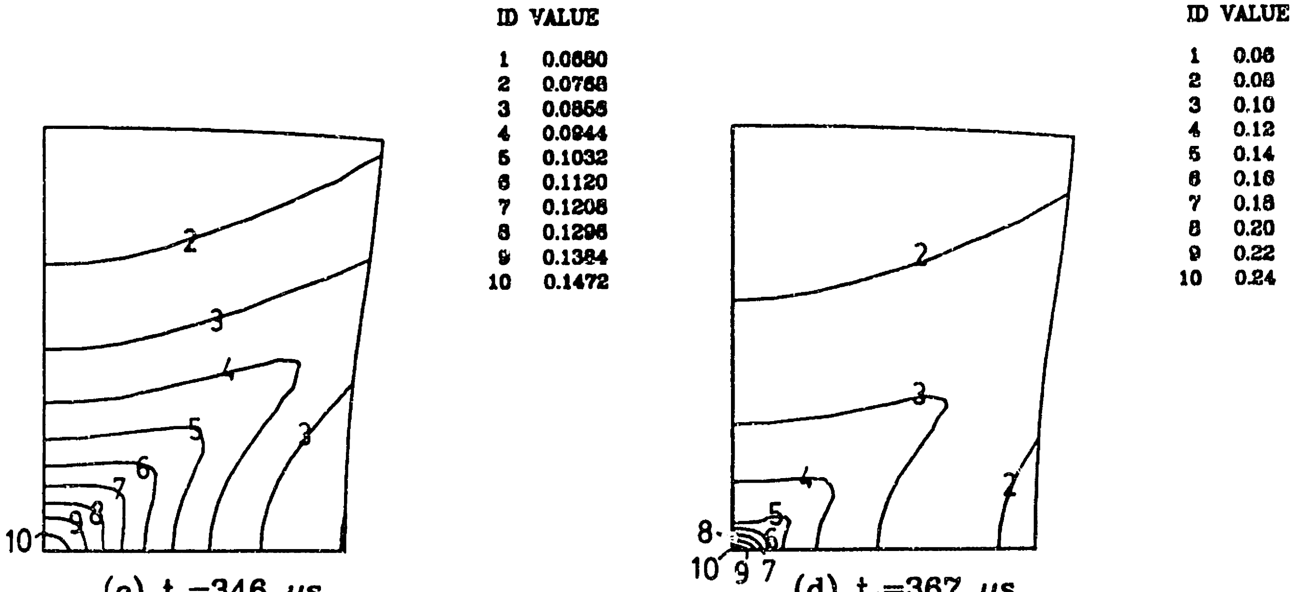

(c) t_3=346 μs

(d) t_4=367 μs

Fig. 20 Contours of porosity in a porous material with λ=1.6E6 W/(m°K)

Appendix F

Paper 2

Towards A Capability For Predicting The Formation Of Defects During Bulk Deformation Processing

by

A. ZAVALIANGOS & L. ANAND

To appear in *Annals of CIRP*, August 1991.
January 1991.

Towards A Capability For Predicting The Formation Of Defects During Bulk Deformation Processing

A. Zavaliangos, and L. Anand

Department of Mechanical Engineering, Massachusetts Institute of Technology
Cambridge, MA, USA 02139

SUMMARY

A set of constitutive equations for large deformations of isotropic, thermo-elasto-viscoplastic, microporous materials, and a new fully-implicit, incrementally objective, fully-thermo-mechanically coupled, time integration procedure for these constitutive equations have been developed. The constitutive equations and the time integration procedure have been incorporated into a finite element computer program, and this program is used to study the formation of material related defects (e.g. surface and internal porosity/damage, shear bands) which may occur in various stages of representative bulk deformation processing operations.

KEY WORDS: Forming, defect prediction

INTRODUCTION

In some recent work, summarized in [1], Anand and co-workers have formulated a constitutive model using a single scalar state variable to model the isotropic deformation resistance offered by the material to viscoplastic flow. This previous work focussed on constitutive modeling for deformation of *intact* material. In this paper we turn our attention to a constitutive model which may prove useful for modeling "workability". The major factors which influence the workability of a metal are its microstructural *internal state variables* (e.g., porosity/damage, dislocation and subgrain structure, crystallographic texture, grain shape and size, etc.) and their evolution, and the *external process variables* of stress, temperature, strain, strain rate, frictional and heat transfer boundary conditions, and their evolution. Workability is often defined as the degree of deformation that can be achieved in a particular metalworking process without "failure". Failure may be the basic metallurgical phenomena of cracking or fracture, but it could also be any other undesirable condition, for example lack of die fill, poor surface finish, etc.. Here we shall limit our attention to the basic material related defects. During deformation processing the dominant material related defects are expected to be associated with the nucleation, growth and coalescence of pores, and due to the formation of shear bands.

Much attention has been paid to the study of void nucleation, growth and coalescence as a micromechanism of ductile fracture, and to the formulation of constitutive models for microporous ductile solids. Gurson's constitutive model [2] is probably the most complete and widely used model of its type available for the *rate-independent, isothermal*, idealization of plastic flow at low temperatures. Over the years this model has been variously modified to account for *rate-dependent* plastic flow of the matrix, and rapid void coalescence at failure; for the most recent version of this model see the review paper by Tvergaard [3]. This constitutive model has been implemented in finite element programs, which employ a semi-implicit [1] "forward gradient" type time-integration procedure developed by Peirce, Shih, and Needleman [4]. Using their constitutive models and computational procedures Needleman, Tvergaard and co-workers have developed a computational capability for dealing with the mechanics of void growth as a basic failure mechanism. They have performed numerical analyses of various "standard test specimens" to illustrate the ability of the constitutive models of porous ductile solids to simulate tensile ductile fracture in structural materials. The studies of Needleman, Tvergaard and co-workers have clearly shown that localization of deformation into shear bands plays an important role in the ductile fracture process governed by flow softening due to hole growth. At high rates of deformation softening may also result due to thermal effects. The results of the work of Needleman and Tvergaard are encouraging to the point that it is important to extend their work to include the effects of deformation heating, and to explore the applicability of the constitutive model and appropriate computational procedures to predict material processing defects.

The purpose of this paper is to report on the framework of a simple state variable constitutive model for large deformations of isotropic, thermo-elastic-viscoplastic, porous materials, and a new fully-implicit, incrementally objective, fully thermo-mechanically coupled time-integration procedure for these constitutive equations. The constitutive equations and time-integration procedure have been implemented in the finite element program ABAQUS [6], and used to study the formation of material related defects (e.g. surface and internal porosity/damage, shear bands) which may occur in various stages of representative bulk deformation processing operations. The numerical examples explored are: (1) *Isothermal*: (a) Formation of internal and surface damage in a wire drawing

---

[1] A fully implicit Euler backward algorithm for the isothermal, rate-independent Gurson model has been formulated by Aravas [5].

operation at low homologous temperatures. (b) Hot compression of a tapered disk made from an initially porous material, to illustrate the effect of secondary tensile stresses on hot workability of such metals. (2) *Fully thermo-mechanically coupled*: Shear band formation and ductile failure initiation in a plane strain tension test, to illustrate the physical effects of flow softening due the combined effects of void growth and deformation heating.

It is important to note that this new computational capability allows one to explore the formation of defects during both cold-working when the material rate sensitivity is low, as well as hot-working when the material is highly rate sensitive.

CONSTITUTIVE EQUATIONS

We use the following notation: $\mathbf{F}$, deformation gradient; $\mathbf{L}$, velocity gradient; $\mathbf{D}$, stretching; $\mathbf{W}$, spin; θ, absolute temperature; $\mathbf{T}$, Cauchy stress; $p = -(1/3)\,\mathrm{tr}\,\mathbf{T}$, mean normal pressure; $\mathbf{S} = \mathbf{T} + p\mathbf{1}$, Cauchy stress deviator; $S = \sqrt{\mathbf{S}\cdot\mathbf{S}}$, magnitude of stress deviator; $\mathbf{N} = \mathbf{S}/S$, direction of the stress deviator; $\mathbf{T}^{\nabla} \equiv \dot{\mathbf{T}} - \mathbf{W}\mathbf{T} + \mathbf{T}\mathbf{W}$, Jaumann derivative of stress.

We confine our attention to moderately voided materials which may be reasonably considered to be isotropic in their overall macroscopic response. The external state variables for the constitutive model are taken to be the pair $(\mathbf{T}, \theta)$, where $\mathbf{T}$ is the applied Cauchy stress and θ is the absolute temperature. The internal state variables are taken to be the scalars (f, s). The variable f is the volume fraction of voids. The variable s has the physical dimensions of stress, it represents an isotropic resistance to plastic flow offered by the matrix material. Changes in the value of s account for isotropic strain hardening of the matrix. Further, an equivalent tensile stress in the matrix, σ_m, is implicitly defined by the solution to an equation of the form:

$$\Phi = \hat{\Phi}(S, p, f, \sigma_m) = 0. \tag{1}$$

The rate-dependent constitutive model that we shall consider consists of coupled differential evolution equations for the state variables $(\mathbf{T}, s, f)$. The evolution equation for θ is provided by the equation for balance of energy. The evolution equations of the governing variables $(\mathbf{T}, s. f, \theta)$ are:

Evolution equation for the stress $\mathbf{T}$:

$$\mathbf{T}^{\nabla} = \mathcal{L}[\mathbf{D} - \mathbf{D}^p - \alpha\,\dot{\theta}\mathbf{1}], \tag{2}$$

where $\mathcal{L} \equiv 2\mu\mathcal{I} + \{\kappa - (2/3)\mu\}\mathbf{1} \otimes \mathbf{1}$, with $\mu = \hat{\mu}(\theta, f)$, $\kappa = \hat{\kappa}(\theta, f)$, $\mathbf{1}$, and $\mathcal{I}$, the shear modulus, the bulk modulus, the second order identity, and the fourth order identity, respectively, is the elasticity tensor; $\mathbf{D}^p$ is the plastic stretching tensor; and $\alpha = \hat{\alpha}(\theta, f)$ the coefficient of thermal expansion.

The plastic stretching tensor $\mathbf{D}^p$ is given by a normality flow rule:

$$\mathbf{D}^p = \quad \dot{\gamma}\,\partial_{\mathbf{T}}\,\Phi \quad = \quad \dot{\gamma}\left\{(\partial_S\,\Phi)\,\mathbf{N} - \frac{1}{3}\,(\partial_p\,\Phi)\,\mathbf{1}\right\}. \tag{3}$$

The parameter $\dot{\gamma}$ is determined form the dissipated power expression $\mathbf{T}\cdot\mathbf{D}^p = (1 - f)\,\sigma_m\,\dot{\epsilon}^p_m$, which gives

$$\dot{\gamma} = \left[\frac{(1 - f)\,\sigma_m}{\bar{S}\,\partial_S\,\Phi\, +\, p\,\partial_p\,\Phi}\right]\,\dot{\epsilon}^p_m\,. \tag{4}$$

where

$$\dot{\epsilon}^p_m = \hat{\dot{\epsilon}}^p_m(\sigma_m, \theta, s) > 0 \tag{5}$$

is an equivalent tensile plastic strain rate in the matrix.

Evolution equation for s:

$$\dot{s} = g(\sigma_m, \theta, s). \tag{6}$$

Evolution equation for f:

$$\dot{f} = (1 - f)\ \mathrm{tr}\,\mathbf{D}^p. \tag{7}$$

Additional terms describing the increase in porosity due to the nucleation of new voids may be included, but this is not pursued in this paper.

Evolution equation[2] for θ:

$$\dot{\theta} \doteq (\rho c)^{-1}\ \{\mathrm{div}\,(\lambda\,\mathrm{grad}\theta) + \omega\,\mathbf{T}\cdot\mathbf{D}^p\}, \tag{8}$$

where $c = \hat{c}(\theta, f)$ is the specific heat, and $\lambda = \hat{\lambda}(\theta, f)$ is the thermal conductivity. Also ω is a scalar in the range $0.85 \leq \omega \leq 1$ which represents the fraction of plastic work converted to heat.

To complete the thermoelastic part of the constitutive model we need to provide specific forms of the functions $\mu = \hat{\mu}(\theta, f)$, $\kappa = \hat{\kappa}(\theta, f)$, and $\alpha = \hat{\alpha}(\theta, f)$ for the shear modulus, the bulk modulus, and the coefficient of thermal expansion, respectively. Also, for the thermal part of the problem we need to specify the functions $c = \hat{c}(\theta, f)$, and $\lambda = \hat{\lambda}(\theta, f)$ for the specific heat and the thermal conductivity. The results of theoretical estimates for the dependence of $\mu, \kappa, \alpha, c,$ and λ on f and the corresponding properties of the matrix material, based on "self-consistent" calculations for a macroscopically isotropic composite of a random dispersion of roughly spherical holes in a matrix material have been summarized by Budiansky [7].

To complete the viscoplastic part of the constitutive model the major task involves specifying particular forms for the flow potential Φ, the matrix strain rate function $\dot{\bar{\epsilon}}_m^p$ and the evolution equation for the matrix deformation resistance s. For the specific applications discussed later, we will use the Gurson-Tvergaard-Needleman form for Φ, and depending on the temperature and strain rate of interest, we will consider different functional forms for the matrix strain rate function $\dot{\bar{\epsilon}}_m^p$ and the evolution equation for s.

---

[2] From the equation of energy balance and Fourier's law of heat conduction.

TIME-INTEGRATION PROCEDURE

Assume that we are given the deformation and temperature field at time t, and the list of variables $\{\mathbf{T}(t), s(t). f(t)\}$, with the Cauchy stress $\mathbf{T}(t)$ satisfying equilibrium, and that we are also given the deformation and temperature field at time $\tau = t + \Delta t$. With these given, we take the computational problems to be: (1) A stable, accurate and efficient computation of of the list $\{\mathbf{T}(\tau), s(\tau), f(\tau)\}$; and (2) the computation of derivatives, consistent with the time integration procedure, to be used in a Newton type iterative method for revising the estimated nodal displacements and temperatures in "implicit" finite element procedures for coupled thermo-mechanical problems. These are the main problems at hand, with item 1 being the *central problem*. because derivative matrices are used only in the search for displacement and temperature fields but in the end have no effect on the accuracy of the solution. Accordingly, we briefly outline our *fully-implicit* time-integration procedure in what follows. A summary of the procedures for calculating the required derivatives may be found in our recent paper, Zavaliangos and Anand [8], where we have detailed a complete time integration procedure and the corresponding derivatives for a *semi-implicit* scheme. The time-integration procedure discussed below is for for the general form of the constitutive equations $(1 - 7)$.

In the constitutive equations considered here, the elasticity is modeled in hypoelastic form, with the stress rate being taken as the Jaumann derivative, so as to make the constitutive model "frame-indifferent" or "objective". The formulation of numerical time-integration procedures which ensure objectivity during computations has been endeavored by many authors; here, we briefly describe an incrementally objective procedure based on the recent work of Weber, Lush, Zavaliangos, and Anand [9]. Let $\mathbf{P}(\zeta)$ be a rotation tensor which is defined to be the solution of the initial-value problem $\dot{\mathbf{P}}(\zeta) = \mathbf{W}(\zeta)\mathbf{P}(\zeta),\ t \leq \zeta \leq \tau$, with $\mathbf{P}(t) = \mathbf{1}$, where $\mathbf{W}(\zeta)$ is the spin tensor. Using rotations

$\mathbf{P}(\zeta)$ so-defined, we define the *bar-transformation* of a symmetric second-order spatial tensor $\mathbf{A}(\zeta)$ by $\bar{\mathbf{A}}(\zeta) \equiv \mathbf{P}^T(\zeta)\,\mathbf{A}(\zeta)\,\mathbf{P}(\zeta)$. In particular, $\bar{\mathbf{T}}(\zeta) = \mathbf{P}^T(\zeta)\mathbf{T}(\zeta)\mathbf{P}(\zeta)$, with $\bar{\mathbf{T}}(t) = \mathbf{T}(t)$. Further, we have the important result $\dot{\bar{\mathbf{T}}}(\zeta) = \mathbf{P}^T(\zeta)\mathbf{T}^{\nabla}(\zeta)\mathbf{P}(\zeta)$. These definitions and results may be used to obtain a "bar-transformation" of the constitutive model. After transformation, the evolution equations for stress involves only the material time derivative of $\bar{\mathbf{T}}$ instead of the more complicated Jaumann derivative of $\mathbf{T}$, and this greatly aids the integration procedure.

Once the constitutive equations are expressed in the bar form, the response of the material to imposed increments of deformation and temperature are obtained by first integrating the constitutive problem expressed in terms of $\dot{\bar{\mathbf{T}}}$, $\dot{s}$, and $\dot{f}$. After integration of the constitutive problem, the stress tensor $\bar{\mathbf{T}}(\tau)$ is transformed to obtain $\mathbf{T}(\tau) = \mathbf{P}(\tau)\bar{\mathbf{T}}(\tau)\mathbf{P}^T(\tau)$. To this end, one needs to interpolate for $\bar{\mathbf{D}}(\zeta) \equiv \mathbf{P}^T(\zeta)\mathbf{D}(\zeta)\mathbf{P}(\zeta)$ for all times $\zeta \in [t, \tau]$, and $\mathbf{P}(\tau)$. In a two-point problem, the positions of the material points of the bodies at times t and τ are the only kinematic data. Let $\mathbf{F}_t(\tau) \equiv \mathbf{F}(\tau)\mathbf{F}(t)^{-1}$, be the known relative deformation gradient, and $\mathbf{F}_t(\tau) = \mathbf{R}_t(\tau)\,\mathbf{U}_t(\tau)$ its right polar decomposition. Weber *et al.* [9] show that in such a two-point problem, a numerical time-integration algorithm will be absolutely incrementally objective for the following forms of the interpolation functions for $\bar{\mathbf{D}}(\zeta)$ and $\mathbf{P}(\tau)$: $\bar{\mathbf{D}}(\zeta) = \frac{1}{\Delta t}\ln \mathbf{U}_t(\tau) \equiv \text{constant}$, and $\mathbf{P}(\tau) = \mathbf{R}_t(\tau)$. We adopt these interpolation formulae for $\bar{\mathbf{D}}(\zeta)$ and $\mathbf{P}(\tau)$.

Assume that the state $(\mathbf{T}(t), s(t), f(t), \theta(t))$ at time t is known (note that $\bar{\mathbf{T}}(t) = \mathbf{T}(t)$), and that the relative deformation gradient $\mathbf{F}_t(\tau)$ and the temperature increment $\Delta\theta$ are given. Then the problem is to integrate the evolution equations for $\bar{\mathbf{T}}$, s and f across a time increment $\Delta t = \tau - t$ and thereby calculate $(\bar{\mathbf{T}}(\tau), s(\tau), f(\tau))$, transform $\bar{\mathbf{T}}(\tau)$ to $\mathbf{T}(\tau)$, and march forward in time.

An algorithm to integrate the rate evolution equations should in general be (a) consistent with the constitutive equations, (b) it should be numerically stable, and (c) incrementally objective. We have considered the problem of incremental objectivity. Regarding the other two characteristics, we will use the consistent and stable *Euler-backward* method of integration. From the bar form of the constitutive equations (1 - 7), together with the use of the definition of $\boldsymbol{\mathcal{L}}$ (see equation (2)), for the Euler-backward method we obtain

$$\begin{aligned} \bar{\mathbf{S}}(\tau) &= \bar{\mathbf{S}}^{*}(\tau) - \Delta t\, 2\mu(\tau)\, (\dot{\gamma}\, \partial_S \Phi)(\tau)\, \bar{\mathbf{N}}(\tau), & (9) \\ p(\tau) &= p^{*}(\tau) - \Delta t\, \kappa(\tau)\, (\dot{\gamma} \partial_p \Phi)(\tau) + 3\, \kappa(\tau)\, \alpha(\tau)\, \Delta\theta, & (10) \\ s(\tau) &= s(t) + \Delta t\, g\, (\sigma_m(\tau), s(\tau), \theta(\tau)), & (11) \\ f(\tau) &= f(t) - (1 - f(\tau))\, \Delta t\, (\dot{\gamma} \partial_p \Phi)(\tau), & (12) \end{aligned}$$

where

$$\begin{aligned} \bar{\mathbf{S}}^{*}(\tau) &= \bar{\mathbf{S}}(t) + 2\mu(\tau)\, \Delta \bar{\mathbf{E}}', & (13) \\ p^{*}(\tau) &= p(t) - \kappa(\tau)\, \mathrm{tr}\, \Delta \bar{\mathbf{E}}, & (14) \end{aligned}$$

are *trial* values for the stress deviator and the pressure at the end of the increment, with $\Delta \bar{\mathbf{E}} \equiv \ln \mathbf{U}_t(\tau)$ the incremental logarithmic strain, and $\Delta \bar{\mathbf{E}}'$ its deviator. For simplicity, since the dependence on f of the thermo-elastic constants is not expected to be strong, in the equations above the values of μ and κ, are taken to be functions of the porosity f at the beginning of the time-step.

In a displacement based finite element program, $\Delta \bar{\mathbf{E}}$ can be computed from known kinematic information. Thus, $\bar{\mathbf{S}}^{*}(\tau)$ and $p^{*}(\tau)$ are known at the beginning of the increment. Further, from equation (9) we observe that

$$\bar{\mathbf{N}}(\tau) = \bar{\mathbf{S}}^{*}(\tau)/S^{*}(\tau), \qquad S^{*}(\tau) \equiv \sqrt{\bar{\mathbf{S}}^{*}(\tau) \cdot \bar{\mathbf{S}}^{*}(\tau)}, \tag{15}$$

and hence $\bar{\mathbf{N}}(\tau)$ is also known at the beginning of the solution process. Thus, using (15), the set of equations (9 – 12) can be reduced to:

$$S(\tau) = S^{*}(\tau) - \Delta t\, 2\, \mu(\tau)\, (\dot{\gamma}\, \partial_S \Phi)(\tau), \tag{16}$$

$$
\begin{aligned}
p(\tau) &= p^*(\tau) - \Delta t\, \kappa(\tau)\, (\dot\gamma \partial_p \Phi)(\tau) + 3\kappa(\tau)\, \alpha(\tau)\, \Delta\theta, && (17)\\
s(\tau) &= s(t) + \Delta t\, g\left(\sigma_m(\tau), s(\tau), \theta(\tau)\right), && (18)\\
f(\tau) &= f(t) - (1 - f(\tau))\, \Delta t\, (\dot\gamma \partial_p \Phi)(\tau). && (19)
\end{aligned}
$$

The time integration problem is therefore reduced to the solution of the *scalar* set of equations above. This system is solved iteratively by a constrained Newton-Raphson method.

NUMERICAL EXAMPLES

The constitutive equations and time-integration procedure described in this paper have been implemented in the implicit finite element program ABAQUS [6] , by writing a "user material" subroutine, UMAT. Details of implementation, for the class of constitutive models considered here, may be found in Zavaliangos and Anand [8]. The ABAQUS calculations presented here were performed by using either its static or coupled temperature-displacement procedures. A variable time-stepping algorithm to control the accuracy of the constitutive time-integrations, as described in Lush, Weber and Anand [10], was implemented by suitably modifying these procedures.

In all our calculations presented below, for the flow potential we adopt the widely used Gurson-Tvergaard-Needleman form:

$$\Phi = \left\{ \frac{(3/2)\, S^2}{\sigma_m^2} - 1 + 2\, q_1\, f^*\, \cosh\left((3/2)\, q_2\, \frac{p}{\sigma_m} \right) - (q_1\, f^*)^2 \right\} = 0, \qquad (20)$$

with $q_1 = 1.5$ and $q_2 = 1$. Further,

$$f^* = \hat f^*(f) = \left\{ \begin{array}{ll} f & \text{if } f \le f_c \\ f_c + ((f_u^* - f_c)/(f_f - f_c))\,(f - f_c) & \text{otherwise} \end{array} \right\}. \qquad (21)$$

In equation (21) $f_u^* \equiv 1/q_1$, and f_c and f_f are material parameters called the critical void volume fraction and the final void volume fraction, respectively. Tvergaard and Needleman suggest the values $f_c \approx 0.15$, and $f_f \approx 0.25$. They introduced the function $\hat f^*(f)$ to represent the rapid loss of stress carrying capacity associated with void coalescence. This modification of f becomes active when f exceeds the critical value f_c, and as $f \rightarrow f_f$, $f^* \rightarrow f_u^*$, and the material looses all stress carrying capacity.

The numerical examples explored below are: (a) formation of internal and surface damage in the drawing of a rod at low homologous temperatures; (b) hot compression of a tapered disk made from an initially porous material, to illustrate the effect of secondary tensile stresses on hot workability of such metals; and (c) shear band formation and ductile failure initiation in a plane strain tension test, to illustrate the physical effects of flow softening due the combined effects of void growth and deformation heating.

Rod Drawing:

The development of internal fracture in the form of central bursts is occasionally encountered in cold drawing or extrusion. Central bursts usually occur for large die angles and small area reductions, after severe cold working of the billet, usually during the final light step of a multi-step extrusion/drawing process [e.g., 5]. Here we simulate an *isothermal*, *frictionless* rod drawing operation with a die of average semicone angle 15°, and a diameter reduction of 8.5%. For the material properties we use values representative of a cold-worked aluminum alloy. The elastic constants of the matrix are taken to be $E = 69.2\text{GPa}$, $\nu = 0.33$, and the viscoplasticity is modeled as power-law with low material strain rate sensitivity m, and the matrix is assumed not to harden:

$$\dot{\epsilon}^p_m = \dot{\epsilon}_0 \left(\frac{\sigma_m}{s}\right)^{\frac{1}{m}}, \quad \dot{\epsilon}_0 = 10^{-3}/\text{s}, \quad m = 0.05, \quad s = s_o = 150\,\text{MPa}.$$

To numerically trigger the development of defects, the material was assumed to have an initial porosity of $f_o = 0.01$. The geometry of the drawing operation, and the deformed finite element mesh is shown in Fig. 1a.

The numerical simulation qualitatively shows the major features of the problem. Fig. 1b which shows the contours of the equivalent plastic strain rate in the matrix, and this figure indicates, as expected, that the material is deforming plastically primarily in the reduction region of the dies. Fig. 1c shows contours of the mean normal pressure p. These contours show that under high semicone angles and small area reductions a substantial negative pressure can develop along the axis of the billet, and it is this negative pressure that promotes void growth. Fig. 1d shows the level contours of the void volume fraction f. After the material leaves the reduction region, the porosity along the axis has increased by as much as 80%. Note that Fig. 1c also shows that the material on the surface is first subjected to a positive pressure in the reduction zone and then to a negative pressure after exit from the die. This residual surface negative pressure should have some connection with the formation of surface cracks which occasionally appear during drawing or extrusion.

These results reinforce those obtained by Aravas [5]. They show that the computational procedures of the type described in this paper can be used to check approximately whether a particular die-design will lead to central burst formation. In addition, different die designs can be analyzed to plot "processing maps" to delineate safe and unsafe combinations of die semicone angles and area reductions for a particular material.

Tapered-Disk Compression Test:

The compression of an axisymmetric tapered disk between parallel dies has been proposed to evaluate the effect of secondary tensile stresses on the hot-workability of metals [11]. As the material is compressed along the vertical direction in the center of the specimen, an outward radial flow is induced, and since the material at the perimeter of the specimen is unconstrained and initially not subject to compressive displacements there, a tensile hoop stress and a negative pressure develops in this region and this can cause void growth, leading to fracture.

An *isothermal*, hot-compression tapered disk test on an *initially* porous $f_o = 0.05$, material has been simulated. One quarter of the geometry of the specimen and the initial finite element mesh is shown in Fig. 2a. The friction conditions at the interface between the dies and the disk was modeled as "sticking friction". The dies were moved at rate which corresponds to a nominal compressive strain rate of 0.02/s in the disk. The matrix material of the tapered disk chosen for this simulation corresponds to Fe-2%Si at 1000°C whose flow and hardening behavior is reported by Brown, Kim and Anand [12], and is described by:

$$\dot{\epsilon}^p_m = A\exp\left(-\frac{Q}{R\theta}\right)\left[\sinh\left(\xi\frac{\sigma_m}{s}\right)\right]^{\frac{1}{m}}, \ \dot{s} = h_o\left|1-\frac{s}{s^*}\right|^a \dot{\epsilon}^p_m, \ s^* = \tilde{s}\left(\frac{\dot{\epsilon}^p_m}{A\exp\left(-\frac{Q}{R\theta}\right)}\right)^n$$

where $A = 6.436 \times 10^{-11}\,\mathrm{s}^{-1}$, $Q = 312.35\mathrm{kJ/mole}$, R is the universal gas constant. $\xi = 3.25$, $m = 0.1856$, $h_0 = 3093.1\,\mathrm{MPa}$, $a = 1.5$, $\tilde{s} = 125.1\,\mathrm{MPa}$, $n = 0.06869$, and the initial value of the deformation resistance at 1000°C is $s_o = 66.1$ Mpa. The values of the elastic constants of the matrix at this temperature are taken as $E = 105\,\mathrm{GPa}$ and $\nu = 0.41$.

Fig. 2b shows the deformed geometry and the contours of pressure at a late stage of the deformation. Fig. 2c shows the corresponding contours of porosity; this figure shows that near the surface of the cylinder the void volume fraction has grown, while at the center void closure is observed. Fig. 2d shows a plot of the porosity as a function of time at point A on the surface of the specimen.

The major qualitative features of the tapered disk compression test are captured by the simulation procedures.

Shear Band Formation In Plane Strain Tension:

Here we simulate a plane strain tension test. The geometry and the initial mesh chosen to model one quarter of the specimen are shown in Fig. 3a. The top boundary of the specimen is pulled at a constant speed v=2.5m/sec, which for the geometry of the specimen considered here gives a nominal strain rate of ≈500/sec in the central gage section. The boundaries of the specimen are taken to be insulated and therefore there is no heat conduction away from the surface of the specimen to the environment. Due the geometry of the specimen, the deformation is slightly inhomogeneous right from the beginning and thus there is no need for any perturbation of the initial data. to trigger the diffuse necking and the shear band localization phenomena. In what follows, we report on our numerical simulations for specimens made from both the fully dense material and a porous material with an initial void volume fraction of $f_o = 0.05$.

For the matrix strain rate function we use the following function suggested by Lindholm and Johnson [13]:

$$\dot{\epsilon}^p_m = \dot{\epsilon}_o \exp\left[\frac{1}{C}\left\{\frac{\sigma_m}{s\,\left(\frac{\theta_m-\theta}{\theta_m-\theta_0}\right)^a} - 1\right\}\right], \quad \text{with} \quad s(t) \equiv A + B\,(\epsilon^p_m(t))^n\,,$$

where $\epsilon^p_m(t) = \int_0^t \dot{\epsilon}^p_m\,dt$ is the equivalent tensile plastic strain in the matrix. With s so defined, there is no need for a separate evolution equation for s. We have used material parameters for a 2024-T351 Aluminum alloy for which Lindholm and Johnson provide the following values for the constants in the constitutive functions: $A = 263.28\,\text{MPa}, B = 421.72\,\text{MPa}, C = 0.015, n = 0.34, \dot{\epsilon}_o = 0.577\text{s}^{-1}, \theta_0 = 300°\text{K}, \theta_m = 775°\text{K}, a = 2$. For the thermo-elastic properties of the matrix we use: $\mu = 26\,\text{GPa}, \kappa = 68\,\text{GPa}, \alpha = 22.6 \times 10^{-6}/°\text{K}, \rho = 2,770\text{kg/m}^3, c = 875\text{J/(kg°K)}, \lambda = 160\,(\text{W/m°K})$, and we take $\omega = 0.9$.

A remeshing program (Lush [14]) was utilized to follow the development of the shear band by refining the finite element mesh locally in regions of high strain rate gradients. For example, the sequence of the meshes employed for the analysis of a fully dense material is shown in Fig. 3b. In the numerical analysis the effects of inertia are neglected and using the coupled temperature-displacement procedure of the finite element code ABAQUS, the fully-coupled thermomechanical problem was solved.

In Fig. 3c load versus time curves are plotted for both the fully dense and initially porous material. As is expected, (a) the flow curve for the porous material is lower than that for the fully dense material; (b) diffuse necking initiates in the vicinity of the peak of their load-displacement curves for both materials; and (c) the plane strain ductility for the porous material is lower than that for the dense material.

The level contours of $\dot{\epsilon}^p_m$, θ, f at representative time increments (keyed to the load-time plot) are shown in Figs. 4 and 5 for the fully dense and the porous material respectively.

For the fully dense material, the shear band "initiates" at an inclination of approximately 45^o with respect with the horizontal (see Fig. 4b), and it quickly (see Fig. 4d) collapses to the minimum width resolvable by the finite element mesh[3]. Figs. 4e through 4g show the level contours of temperature during the process of shear band formation. The collapse of the shear bands implies that the characteristic length associated with heat conduction was much too small to be resolved by the mesh employed.

In the case of the initially porous specimen, thermal softening and growth of voids are two competing and interacting softening mechanisms. In this simulation thermal softening is the major reason for the shear band development and it is *assisted* by the growth of voids. For this reason the time at localization is shorter compared to the fully dense case (Fig. 3b). Due to the pressure dependence of the constitutive model, the initial inclination of the shear band is different from 45^o and it was roughly estimated to be 40^o with respect to the horizontal (Fig. 5b). As the shear band localizes the void growth takes over at the center of the specimen. As can be seen in Fig. 5j the porosity outside the shear band was increased only to 7%, while inside the band it reached values ranging from 11% to the failure value 25% at the center of the specimen. Due to the special form of the plastic potential with the "accelerated porosity" term f^*, once the porosity reaches

---

[3] It is important to note that the values of the various field variables at the very end of the simulation should be considered only qualitatively correct because of the unavoidable mesh effects and the associated interpolation errors.

the critical value f_c at one integration point, it subsequently increases much faster there than in the surrounding area, and once the failure value f_f is reached the element looses all stress carrying capacity. To avoid numerical problems, we terminated our calculations slightly prior to this failure point.

CONCLUDING REMARKS

We have formulated a new fully-implicit time integration algorithm for a set of state variable constitutive equations describing thermo-elasto-viscoplastic microporous materials. This algorithm offers substantial improvement over all previous schemes for this class of constitutive equations. It is stable, incrementally objective, it takes better account of possible changes in the direction of plastic flow, it has variable time stepping to control the accuracy of the procedure, and it takes full account of thermo-mechanical coupling. The constitutive equations and the time integration procedure have been incorporated into the general purpose finite element computer program ABAQUS via its "user material" subroutine option, and this program has been used to study the formation of material related defects (surface and internal porosity/damage, shear bands) which may occur in various stages of representative bulk deformation processing operations.

This study, along with similar other studies which have recently appeared in the literature, represents only the beginnings of a truly predictive simulation capability for the formation of defects during bulk deformation processing. For a detailed discussion of future research needs, see the recent report [15] of a NSF workshop on localized plastic instabilities and failure criteria.

Acknowledgement — Support for this work was provided by the U. S. National Science Foundation (Grant No. MSS-8808556).

REFERENCES

(1) Anand, L., and Zavaliangos, A., 1990, "Hot Working – Constitutive Equations and Computational Procedures", Annals of CIRP, 39:235–238.

(2) Gurson, A. L., 1977, "Continuum Theory of Ductile Rupture by Void Nucleation and Growth: Part 1 – Yield Criteria and Flow Rules for Porous Ductile Media," ASME J. Engng. Materials Technol., 99:2–15.

(3) Tvergaard, V., 1989, "Material Failure by Void Growth to Coalescence," Advances In Applied Mechanics, 27:83 – 151.

(4) Peirce, D., Shih, C. F., and Needleman, A., 1984, "A Tangent Modulus Method for Rate Dependent Solids," Computers and Structures, 18:875-887.

(5) Aravas, N., 1987, "On The Numerical Integration of a Class of Pressure Dependent Plasticity Models," Int. J. Num. Methods in Engin., 24:1395 – 1416.

(6) ABAQUS, Reference Manuals, Hibbitt, Karlsson & Sorensen Inc., 100 Medway Street, Providence, RI, 02906-4402, 1989.

(7) Budiansky, B., 1970, "Thermal and Thermoelastic Properties of Isotropic Composites," Journal of Composite Materials, 4:286 - 295.

(8) Zavaliangos, A., and Anand, L.,"Thermal Aspects Of Shear Localization In Microporous Viscoplastic Solids," submitted for publication to International Journal of Numerical Methods in Engineering.

(9) Weber, G. G., Lush, A. M., Zavaliangos, A., and Anand, L., 1990, "An Objective Time-Integration Procedure For Isotropic Rate-Independent And Rate-Dependent Elastic-Plastic Constitutive Equations," International Journal of Plasticity, 6:701–744.

(10) Lush, A. M., Weber, G., and Anand, L., 1989, "An Implicit Time-Integration Procedure For A Set Of Internal Variable Constitutive Equations For Isotropic Elasto-Viscoplasticity", International Journal of Plasticity, 5:521-549.

(11) Malas, J. C., Gegel, H. L., Oh, S. I., and Lahoti, G. D., 1983, "Metallurgical

Validation Of A Finite-Element Program For The Modeling Of Isothermal Forging Processes," in Experimental Verification Of Process Models, American Society of Metals, Ohio, pp. 358–372.

(12) Brown, S. B., Kim, K. H., and Anand, L., 1989, "An Internal Variable Constitutive Model for Hot Working of Metals", International Journal of Plasticity, 5:95-130.

(13) Lindholm U. S., and Johnson G.R., 1983, "Strain-Rate Effects in Metals in Large Shear Strains," in : Mescall, J. and Weiss V., (eds.) Material Behavior Under Very High Stress and Ultrahigh Loading Rates , Sagamore Army Materials Research Conference Proceedings, Plenum Press, 29:61 - 79.

(14) Lush A.M., 1990, "Computational Procedures for Finite Element Analysis Of Hot-Working", PhD Thesis, M.I.T.

(15) Anand L., Dillon O., Place T. A. and von Turkovich B. F., 1990, "Report Of The NSF Workshop On Localized Plastic Instabilities and Failure Criteria", International Journal of Plasticity, 36: 2.

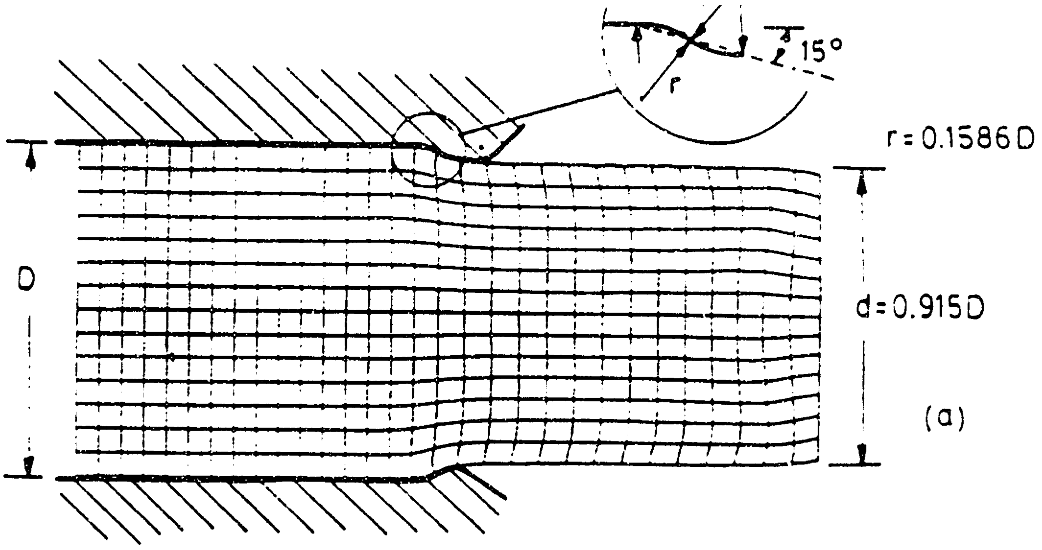

(b) $\dot{\epsilon}_m{}^p$ (s^{-1})

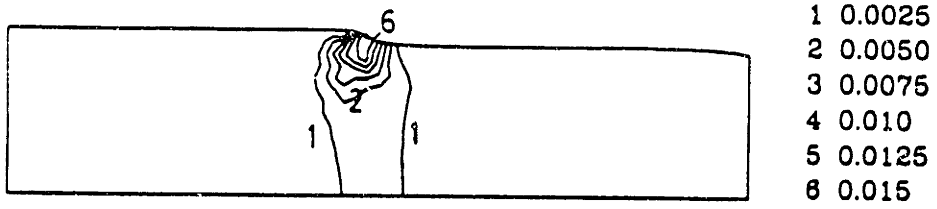

(c) Pressure, p (MPa)

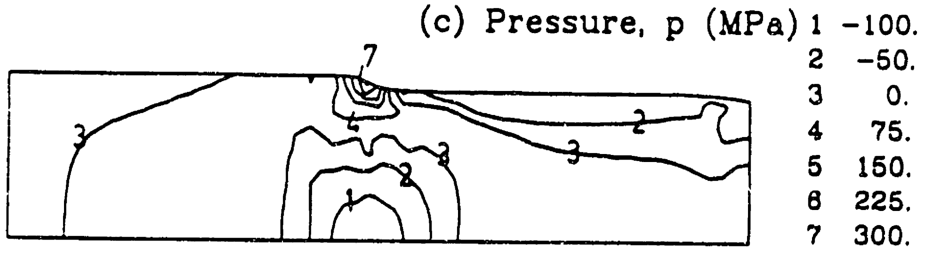

(d) Porosity, f

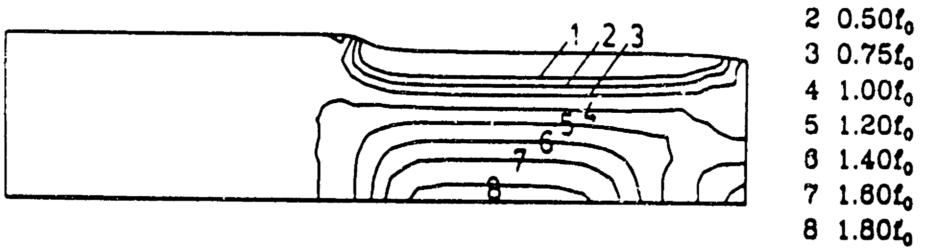

Fig. 1 Defect formation in rod drawing.

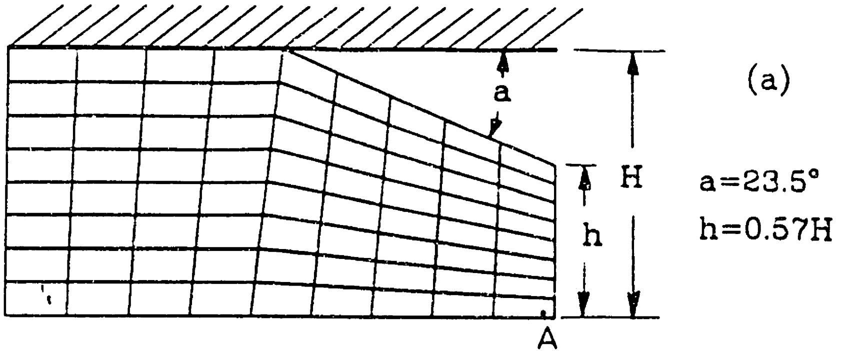

(b) Pressure, p (MPa)

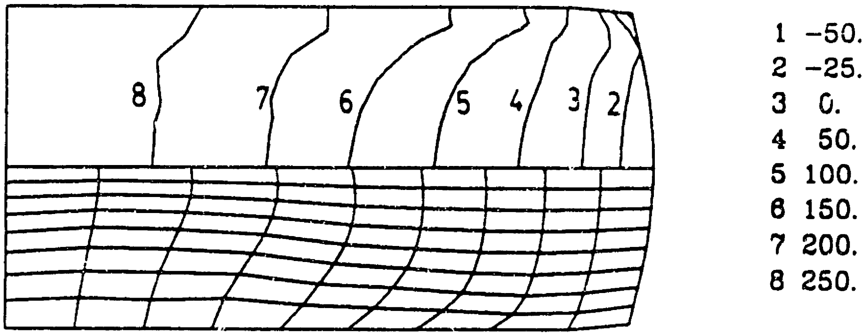

(c) Porosity, f

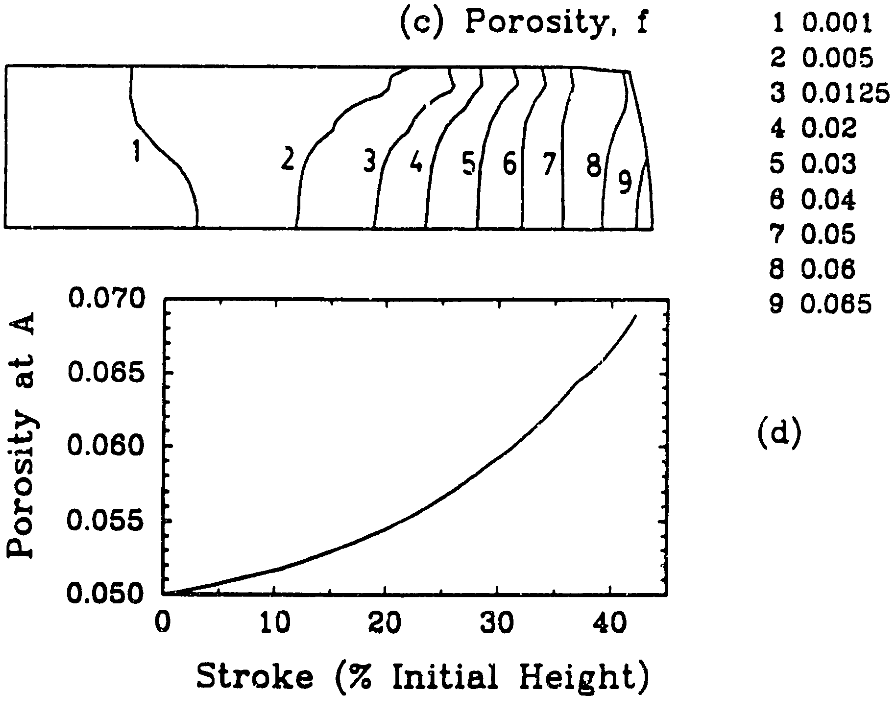

Fig.2 Tapered disk compression test for workability evaluation.

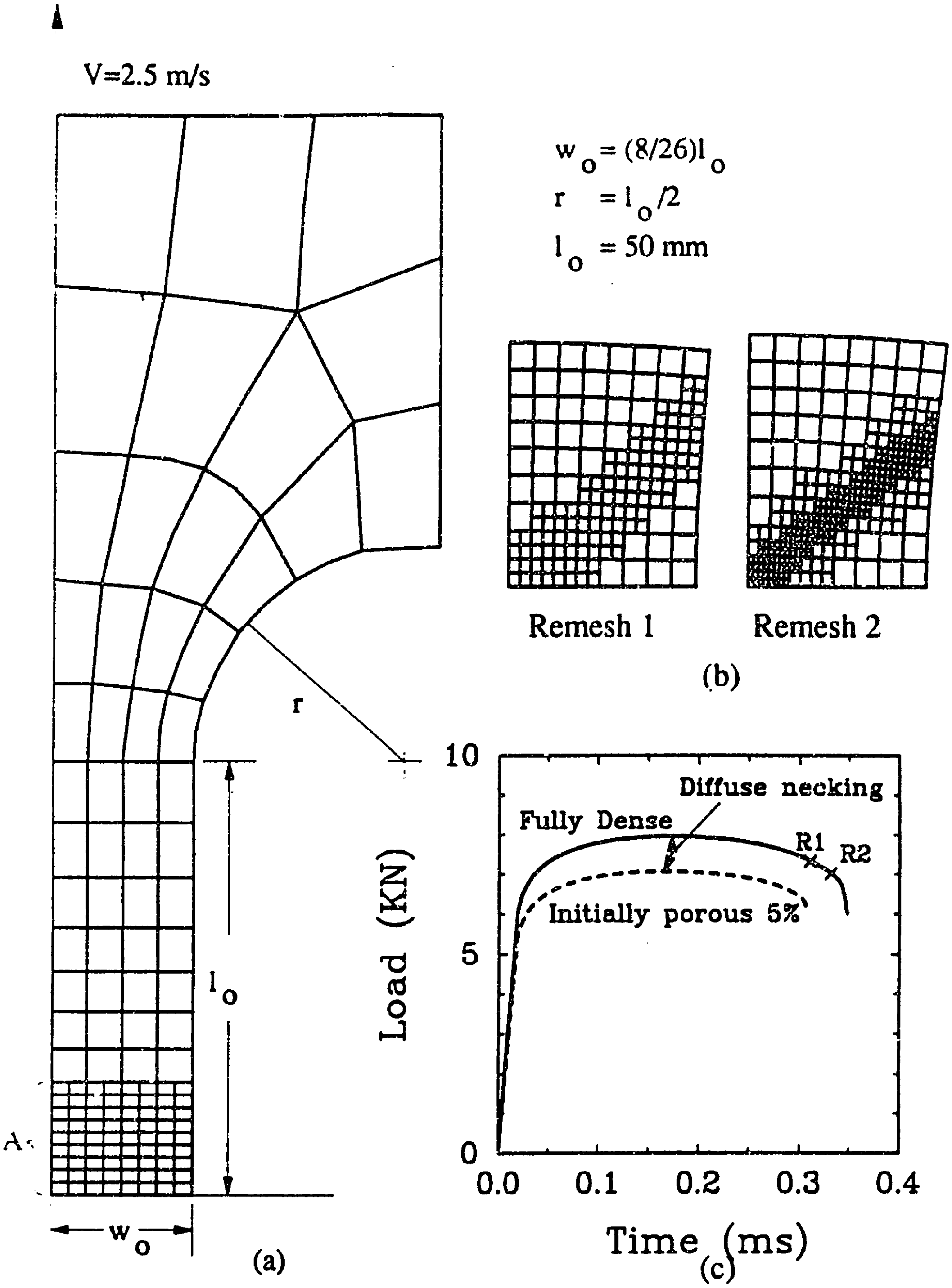

Fig. 3 (a) Geometry of a plane strain tension test.
b) Remeshing of region A (Fig.3a) at times R1 and R2 shown in Fig. 3c.
(c) Load vs time curves for fully dense and porous materials.

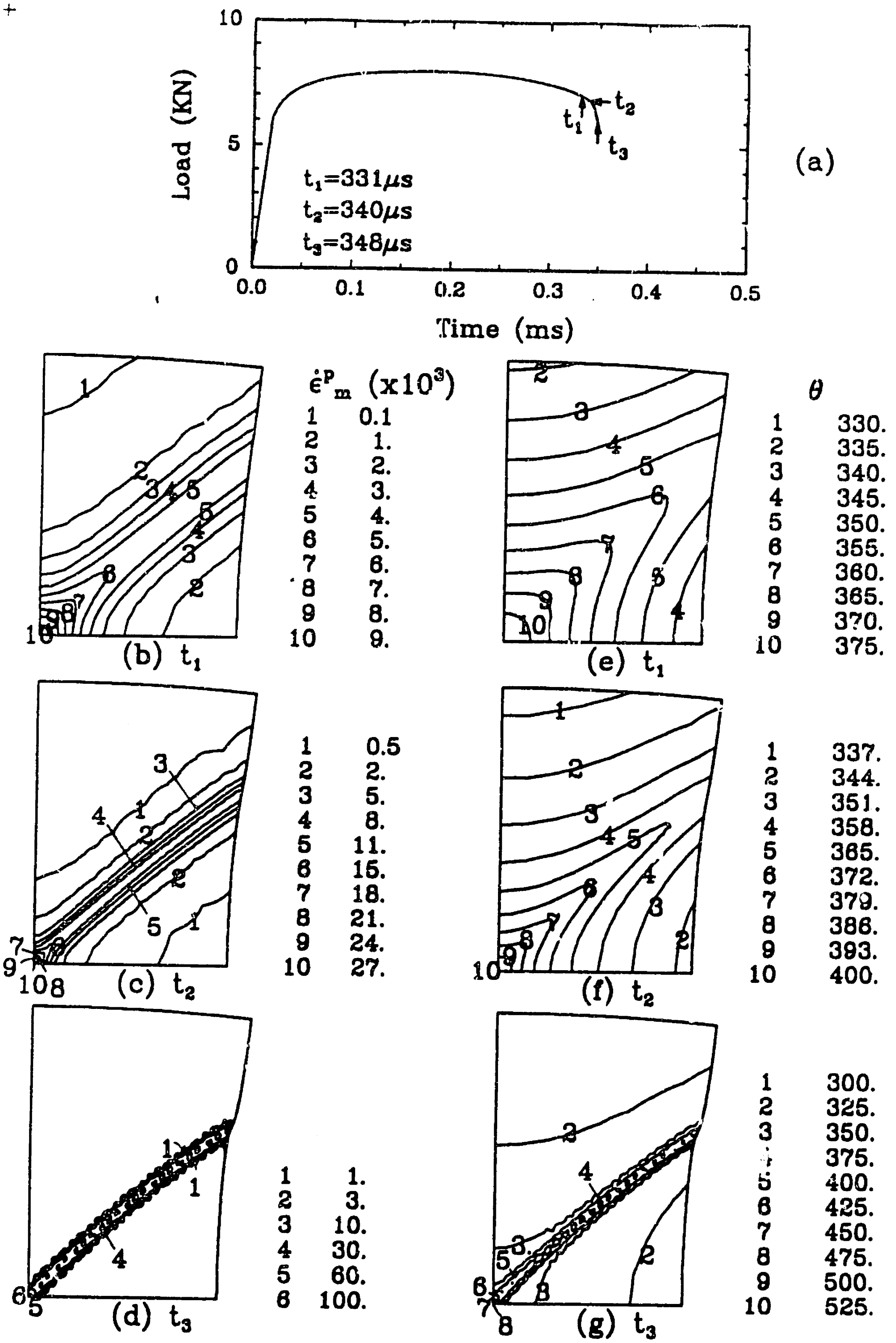

Fig. 4 Contours of equivalent plastic strain rate and temperature for the fully dense specimen.

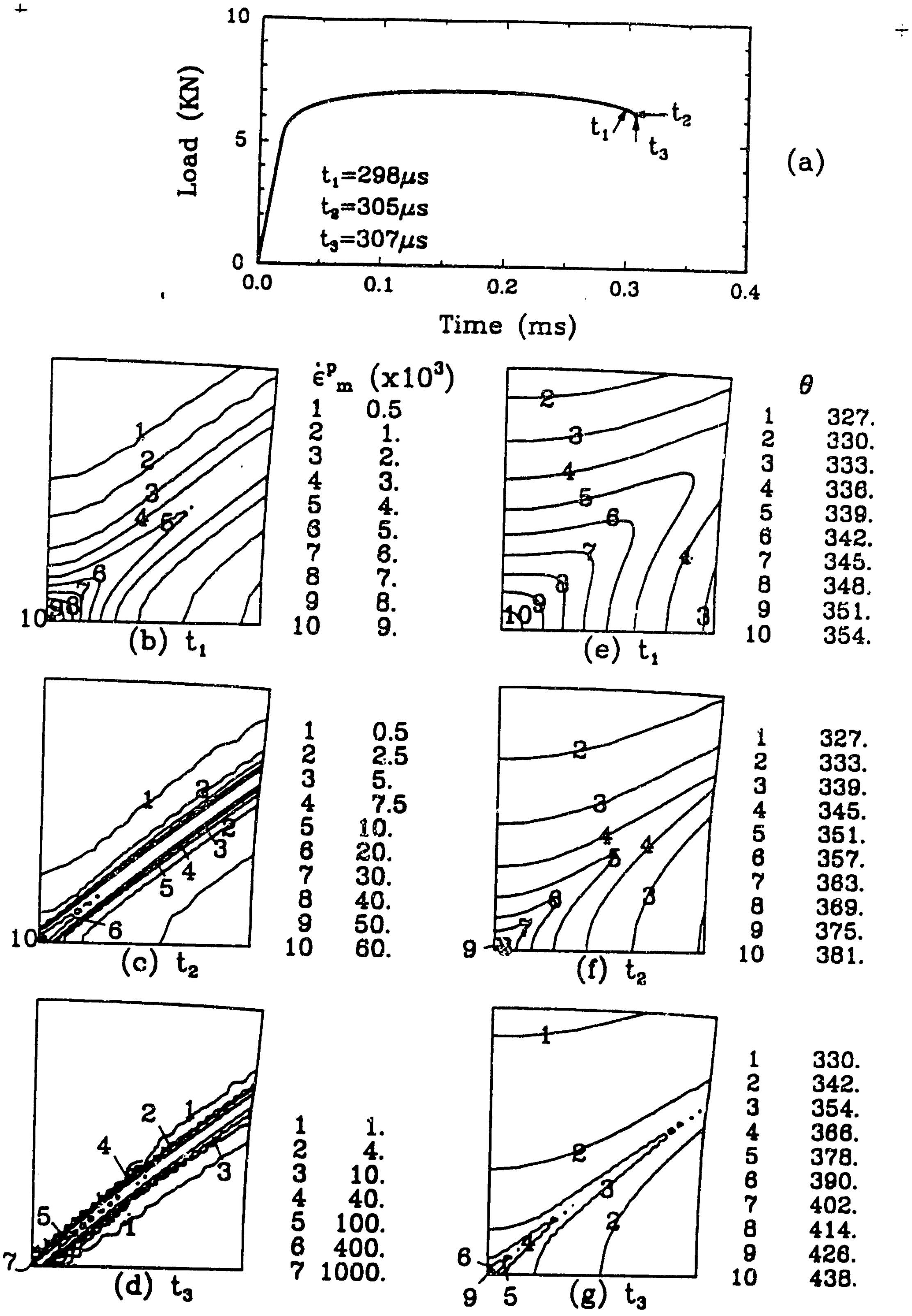

10
5
0
Load (KN)
0.0
0.1
0.2
0.3
0.4
Time (ms)
t₁
t₂
t₃
t₁=298μs
t₂=305μs
t₃=307μs
(a)
ε̇ᵖₘ (x10³)
1 0.5
2 1.
3 2.
4 3.
5 4.
6 5.
7 6.
8 7.
9 8.
10 9.
(b) t₁
1 0.5
2 2.5
3 5.
4 7.5
5 10.
6 20.
7 30.
8 40.
9 50.
10 60.
(c) t₂
1 1.
2 4.
3 10.
4 40.
5 100.
6 400.
7 1000.
(d) t₃
θ
1 327.
2 330.
3 333.
4 336.
5 339.
6 342.
7 345.
8 348.
9 351.
10 354.
(e) t₁
1 327.
2 333.
3 339.
4 345.
5 351.
6 357.
7 363.
8 369.
9 375.
10 381.
(f) t₂
1 330.
2 342.
3 354.
4 366.
5 378.
6 390.
7 402.
8 414.
9 426.
10 438.
(g) t₃

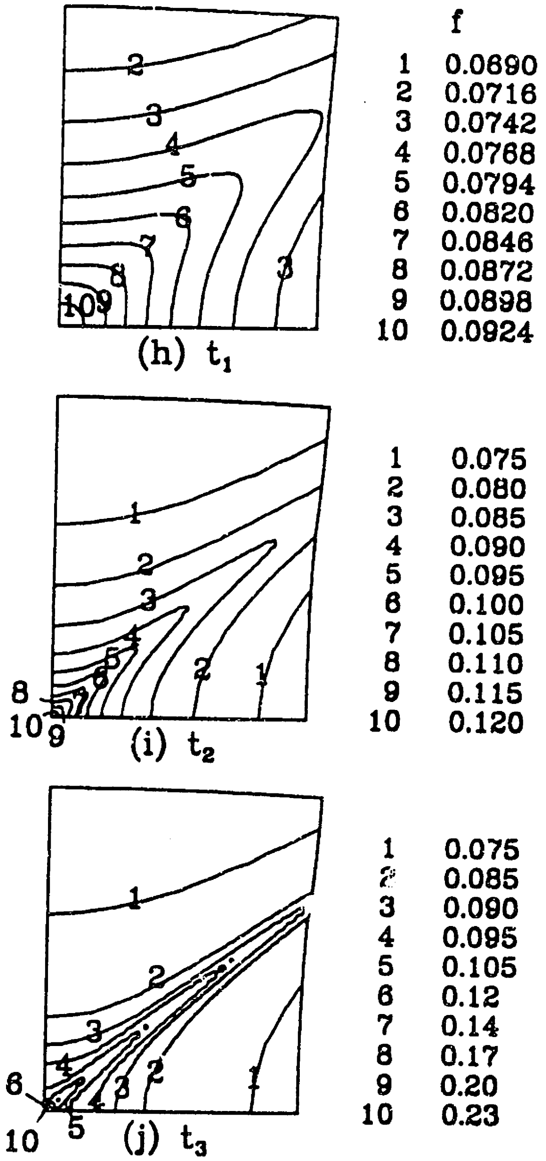

Fig. 5 Contours of equivalent plastic strain rate, temperature and porosity in the porous specimen. Only region A (Fig. 3a) is shown.

Bibliography

[1] Torre, C.: " The Theory and Behaviour of Compressed Powders", Berg Hüttenmänn. Monatsh., **93**, 62, 1948.

[2] Tipper, C., F.: "The Fracture of Metals", Metallurgia, **39**, 133 – 138, 1949.

[3] Puttick, K. E.: "Ductile Fracture in Metals", Philosophical Magazine, **4**, 964 – 969, 1959.

[4] Puttick, K. E.: "The Shear Component of Ductile Fracture", Philosophical Magazine, **5**, 759 – 762, 1960.

[5] Rogers H.C.: "Tensile Fracture in Ductile Materials", Trans AIME, **218**, 498 – 506, 1960.

[6] Hill, R.: "A Self-Consistent Mechanics of Composite Materials", J. Mech. Phys. Solids, **13**, 213 – 222, 1965.

[7] Bluhm, J. I., and Morrisey, J. R.: "Fracture in a Tensile Specimen", Proceedings of 3rd International Conference on Fracture, Yokobori, T., Kawasaki, T., and Swedlow, J. L., eds., Vol iii, Japanese Society for Strength and Fracture of Materials, Sendai, 1739 – 1780, 1966.

[8] Budiansky, B.: "On the Elastic Moduli of Some Heterogeneous Metals", J. Mech. Phys. Solids, **13**, 223 – 227, 1967.

[9] Coffin, L.F., Rogers, H.C.: "Influence of Pressure on the Structural Damage", Trans. ASM, **60**, 672 – 686, 1967.

[10] Hill, R: "The Essential Structure of Constitutive Laws for Metal Composites and Polycrystals", J. Mech. Phys. Solids, **15**, 79 – 103 , 1967.

[11] Avitzur: "Analysis of Central Bursting Defects in Extrusion and Drawing", Trans. ASME J. Engng. Ind., **90**, 79 – 85 1968.

[12] McClintock F. A. : "A Criterion for Ductile Fracture by the Growth of Holes", Trans ASME, J. Appl. Mech. 35, 362 – 371, 1968.

[13] Rice J. R., Tracey D. M. : " On the Ductile Enlargement of Voids in Triaxial Stress Fields", J. Mech. Phys. Solids, **17**, 201 – 207,1969

[14] Budiansky, B.: "Thermal and Thermoelastic Properties of Isotropic Composites", J. Comp. Materials, **4**, 286 – 295, 1970.

[15] Zimerman Z., Avitzur B.: "Analysis of the Effect of Strain Hardening on Central Bursting Defects in Drawing and Extrusion", ASME, J. Eng. Ind., 135 – 145, 1970.

[16] Kocks U.F., Argon, A.S., and Ashby, M.F.: "Thermodynamics and Kinetics of Slip", in *Progress in Material Science*, Pergamon Press, 1975.

[17] Kuhn, H. A., and Downey, C. L., "Deformation Characteristics and Plasticity Theory of Sintered Powder Materials", Int. J. Powder Metall., **7**, 15 – 25, 1971.

[18] Rogers H.C.: "Prediction and Effects of Material Damage During Deformation Processing", in *Metal Forming: Interrelation Between Theory and Practice*, edt. by Hoffmanner, A., L., Plenum Press, 1971.

[19] Simmons, G., Wang, H.: "Single Crystal Elastic Constants and Calculated Aggregate Properties", The MIT Press, Cambridge MA, 1971.

[20] Green, R. J.: " A Plasticity Theory For Porous Solids", Int. J. Mech. Sci., **14**, 215 – 224, 1972.

[21] Needleman, A.: "Void Growth in an Elastic Plastic Medium", ASME J. Appl. Mech, 964 – 970, December 1972.

[22] Hewitt R. L. ', Wallace W., and deMalherbe M. C.: "The Effects of Strain-Hardening in Powder Compaction", Powder Metallurgy, **16**, 31, 88 -- 106, 1973.

[23] Avitzur: Wire J.,**7**, 77 1974

[24] Sanchez-Palencia E.: "Comportements Local et Macroscopique d' un Type de Millieux Physiques Hétérogènes", Int. J. Eng. Sci., **12**, 331 – 351, 1974.

[25] Wilkinson, D., S., and Ashby, M., F., "Pressure Sintering by Power Law Creep", *Acta Metall.* **23**, 1277 – 1285, 1975.

[26] Hancock, J.W., and Mackenzie, A.C.: "On the Mechanisms of Ductile Failure in High-Strength Steels Subjected to Multiaxial Stress-States", J. Mech. Phys. Solids **24**, 147 – 169, 1976.

[27] Hart, E., W.: "Constitutive Relations for Inelastic Deformation of Metals", ASME J. Eng. Materials Technology, **98**, 193 – 202, 1976.

[28] Hutchinson, J.,W.: "Bounds and Self-Consistent Estimates for Creep of Polycrystalline Solids", Proc. R. Soc. London, A**348**, 101 – 127, 1976.

[29] Johnson W., Mamalis A. G.: Proc. 17th Int. Machine Tool Design Research Conf. (ed S. A. Tobias), 607 – 621, Macmillan, London 1977.

[30] Miller, A.: "An Inelastic Constitutive Model for Monotonic Cyclic and Creep Deformation", ASME J. Eng. Materials Technology, 97 – 113, 1976.

[31] Pepe J.: "Central Burst Formation During Hydrostatic Extrusion", Metals Eng. Quart. 46 – 58, 1976.

[32] Shima, S. and Oyane, M., "Plasticity Theory for Ductile Metals", Int. J. Mech. Sci., **18**, 285 – 291, 1976.

[33] McLaughlin, R.: "A Study of the Differential Scheme for Composite MAterials", Int. J. Engng Sci., **15**, 237 – 244, 1977.

[34] Gurson, A. L.: "Continuum Theory of Ductile Rupture by Void Nucleation and Growth: Part 1 – Yield Criteria and Flow Rules for Porous Ductile Media", ASME J. Eng. Materials Technology, **99**, 2 – 15, 1977.

[35] Rice, J. R.: "The Localization of Plastic Deformation", in *Theoretical and Applied Mechanics*, Proceedings of the 14th IUTAM Congress. Delft. 1976 , edited by Koiter, W. T. , 207 – 220 North Holland, Amsterdam.

[36] Senseny, P. E., Duffy, J. and Hawley, R. H.: "Experiments on Strain Rate History and Temperature Effects During the Plastic Deformation of Close Packed Metals", Trans. ASME J. Appl. Mech. **60**, 60 – 66, 1978.

[37] Anand, L.: "On H. Hencky's Approximate Strain-Energy Function for Moderate Deformations", ASME J. Appl. Mech., **46**, 78 – 82, 1979.

[38] Brown, D. K., Hancock, J. W., Thomson, R. and Parks, D. M.: "The Effect of Dilating Plasticity on Some Elastic-Plastic Stress and Strain Concentration Problems Relevent to Fracture", *Proceedings of Second International Conference on Numerical Methods in Fracture Mechanics*, (Swansea, 7-11 July 1980) (edited by D. R. J. Owen and A. R. Luxxmoore). Pineridge Press, Swansea.

[39] Anand, L. and Spitzig W. A.: " Initiation of Localized Shear Bands in Plane Strain", J. Mech. Physics Solids, **28**, 113 – 128, 1980.

[40] Cleary, M.,P., Chen I.W., Lee S.M.:: "Self-Consistent Techniques for Heterogeneous Media", ASCE J. Eng. Mech. Div., 861 - 887, October 1980.

[41] Sanchez-Palencia E.: "Nonhomogeneous Media and Vibration Theory", *Lecture Notes in Physics n° 127*, Springer-Verlag, Berlin, 1980.

[42] Leckie, F., A., Onat, E., T.: "Tensorial Nature of Damage Measuring Internal Variables", in *Physical Non-Linearities in Structural Analysis* J. Hult and J. Lemaitre Editors, Springer-Verlag, 1981.

[43] Tvergaard, V.: "Influence of Voids on Shear Band Instabilities Under Plane Strain Conditions", Int. J. Fracture **17**, 389 - 407, 1981.

[44] Willis, J.R.: "Variational and Related Methods for the Overall Properties of Composites", in *Advances in Applied Mechanics*, **21**, 1 - 78 1981.

[45] Anand, L.: "Constitutive Equations for the Rate-Dependent Deformation of Metals at Elevated Temperatures", ASME J. Eng. Materials Technology, **104**, 12 - 17, 1982.

[46] Budiansky, B., Hutchinson, J. W. and Slutsky, S.: "Void Growth and Collapse in Viscous Solids", in *Mechanics of Solids*, The Rodney Hill 60th Anniversary Volume, Hopkins, H.G., and Sewell, M. J., eds., Pergamon Press, Oxford, 13 - 45, 1982.

[47] Cocks A.C.F., Ashby M.F. : "On Creep Fracture by Void Growth", Prog. in Materials Sci., **27**, 189 - 244, 1982.

[48] Frost, H., J., Ashby, M., F.: "Deformation-Mechanism Maps: The Plasticity and Creep of Metals and Ceramics", Pergamon Press, 1982.

[49] Tvergaard, V.: "On Localization in Ductile Materials Containing Spherical Voids", Int. J. Frac., **18**, 237 - 252, 1982.

[50] Arzt E., Ashby M.F., Easterling K.E., "Practical-Applications of Hot-Isostatic Pressing Diagrams: Four Case Studies", Met. Trans. A, **14A**, 211 – 221, 1983.

[51] Hancock, J.W., and Brown D.K.: "On the Role of Strain and Stress in Ductile Failure", J. Mech. Phys. Solids, **31**, 1 – 24, 1983.

[52] Malas, J., C., Gegel, H., L., Oh, S., I., and Lahoti, G., D.: "Metallurgical Validation Of A Finite-Element Program For The Modeling Of Isothermal Forging Processes", in *Experimental Verification Of Process Models*, American Society of Metals, Ohio, 358 – 372, 1983.

[53] Pan J., Sale M., Needleman A.: "Localization of Deformation in Rate Sensitive Porous Plastic Solids", Int. J. Fracture, **21**, 261 – 278, 1983.

[54] Roesch, L., and Sanz, G., "Effect of Material Parameters on Central Burst Formation in Wire Drawing of Steels", in *Developments in the Drawing of Metals"*, The Metals Society, London, 21 – 29, 1983.

[55] Duva, J.,M.: "A Self-Consistent Analysis of the Stiffening Effect of Rigid Inclusions on a Power Law Material", ASME J. Eng. Materials Technology, **106**, pp 317 – 321, October 1984.

[56] Duva, J. M., and Hutchinson, J. W.: "Constitutive Potentials for Dilutely Voided Nonlinear Materials", Mechanics of Materials, **3**, 41 – 54, 1984.

[57] Needleman, A. and Tvergaard, V. "An Analysis of Ductile Rupture in Notched Bars", J. Mech. Phys. Solids, **32**, 461 – 490, 1984.

[58] Peirce, D., Shih, C. F., and Needleman, A.: "A Tangent Modulus Method for Rate Dependent Solids", Computers and Structures, **18**, 875 – 887, 1984.

[59] Tvergaard V., Needleman A.: "Analysis of the Cup and Cone Fracture in a Round Tensile Bar", Acta Met., **32**, 1, 157 – 169, 1984.

[60] Anand, L.: " Constitutive Equations for Hot-Working of Metals" Int. J. Plasticity, **1**, 213 – 231, 1985.

[61] Helle A.S., Easterling K.E. and Ashby M.F., "Hot isostatic Pressing Diagramms - New Developments", Acta Metall., **33**, 2163 – 2174, 1985.

[62] Lange, K.: "The Handbook of Metal Forming", McGraw Hill, 1985.

[63] Norris, A., N.: "A Differential Scheme for the Effective Moduli of Composites", Mech. Mater., **4**, 1 – 16, 1985.

[64] Anand, L.: "Moderate Deformations in Extension-Torsion of Incompressible Isotropic Elastic Materials", J. Mech. Phys. Solids, **34**, 293 – 304, 1986.

[65] Aravas, N. : "The Analysis of Void Growth that Leads to Central Bursts During Extrusion", J. Mech. Phys. Solids, **14**, 1, 55 – 79, 1986.

[66] Becker, R., and Needleman, A.: "Effect of Yield Surface Curvature on Necking and Failure in Porous Plastic Solids", ASME J. Appl. Mech., **53**, 491 – 499, 1986.

[67] Carrol, M., M., Kim, K., T., and Nestarenko, V., F.: "The Effect of Temperature on Viscoplastic Pore Collapse", J. Appl. Phys. **59**, 6, 1962-1967, 1986.

[68] Rodin G.J. , Parks D.M. : "On Consistency Relations in Nonlinear Fracture Mechanics", Trans ASME, J. Appl. Mech. **53**, 834 – 838, 1986.

[69] Aravas, N., "On The Numerical Integration of a Class of Pressure Dependent Plasticity Models", Int. J. Num. Methods Eng., **24**, 1395 – 1416, 1987.

[70] Guennouni T., Francois D.: "Influense of the Pore Morphology and Secondary Cavities on the Plastic Behavior of Porous Metals", Fatigue Fract. Eng. Mater. Struct, **11**, 4, 267-276, 1988.

[71] Mathur K., K., and Dawson, P. R.: "On Modeling Damage Evolution During the Drawing of Metals", Mech. Materials, **6**, 179 – 196, 1987.

[72] Press W.,H., Flannery B.,P., Teukolsky S.,A., Vetterling W.,T.: "Numerical Recipes: The Art of Scientific Computing", Cambridge University Press, 1987.

[73] Tvergaard, V., "Mechanical Modelling of Failure", in *Constitutive Relations and Their Physical Basis*, Andersen *et al.* (eds.), Proceedings of the 8th International Symposium on Metallurgy and Materials Science, 173 – 189, 1987.

[74] Becker, R., Needleman, A., Richmond, O., and Tvergaard, V., "Void Growth and Failure in Notched Bars", J. Mech. Phys. Solids, **36**, 317 – 354, 1988.

[75] Fleck, N.A., Hutchinson J.W., Tvergaard, V.: "Softening by Void Nucleation and Growth in Tension and Shear", Harvard U. Report MECH-123,May 1988.

[76] Koplik, J., Needleman, A. : "Void Growth and Coalescence in Porous Plastic Solids", Int. J. Solids Structures, **24**, 8, 835 – 853, 1988.

[77] PonteCastañeda, P., Willis, J. R.: "On the Overall Properties of Nonlinearly Viscous Composites", Proc. R. Soc. London **A416**, 217 – 244, 1988.

[78] Rodin, G.,J., Parks, D.,M. : "A Self-Consistent Analysis of a Creeping Matrix with Aligned Cracks", J. Mech. Phys. Solids, **36**, 2, 237 – 249, 1988.

[79] Brown, S. B., Kim, K. H., and Anand, L.: "An Internal Variable Constitutive Model for Hot Working of Metals" Int. J. Plasticity, **5**, 95 – 130, 1989.

[80] Cocks, A. C. F.: "Inelastic Deformation of Porous Materials", J. Mech. Phys. Solids, **37**, 6, 693 – 715, 1989.

[81] Hom, C.,L., McMeeking, R.,M.: "Void Growth in Elastic-Plastic Materials", ASME, J. Appl. Mech., **56**, 309 – 317, 1989.

[82] Huang, Y.: "Accurate Dilatation Rates for Spherical Voids in triaxial Stress Fields", Harvard University Report MECH-155, 1989.

[83] Tvergaard, V.: "Numerical Study of Localization in a Void-sheet", Int. J. Solids Structures, **25**, 10, 1143 – 1156, 1989.

[84] Weber G., Lush A., Zavaliangos A., Anand L.: "An Objective Time-Integration Procedure For Isotropic Rate-Independent And Rate-Dependent Elastic-Plastic Constitutive Equations", Int. J. Plasticity, **6**, 701 – 744, 1989.

[85] Anand, L., and Zavaliangos, A.: "Hot Working – Constitutive Equations and Computational Procedures", Annals of CIRP, 39, 235 – 238, 1990.

[86] Lush, A., Weber, G., and Anand, L.: "An Implict Time Integration Procedure for a Set of Internal Variable Type Constitutive Equations", Int. J. Plasticity, **5**, 521 – 540, 1989.

[87] McMeeking, R.,M., Hom, C.,L.: "Finite Element Analysis of Void Growth in Elastic-Plastic Materials", Int. J. Fracture, **42**, 1 – 19, 1990.

[88] Tvergaard, V.: "Material Failure by Void Growth to Coalescence", in *Advances In Applied Mechanics*, **27**, 83 – 151, 1990.

[89] Weber G., and Anand L.: "Finite Deformation Contitutive Equations and a Time Integration Procedure for Isotropic Viscoplastic Solids", Comp. Meth. Appl. Mech. Engng., **79**, 173 – 202, 1990.

[90] Worswick, M.,J., Pick, R.,J.: "Void growth and Constitutive Softening in a Periodically Voided Solid", J. Mech. Physics Solids, **38**,5, 601 – 625, 1990.

[91] Abeyaratne, R. and Hou, H.: "Void Collapse in an Elastic Solid", J. Elasticity, **26**, 23 – 42, 1991.

[92] Bhanuprasad, V. V., Bhat, R. B. V., Kuruvilla, A. K., Prasad, K. S., Pandey A. B. and Mahajian Y. R.: "P/M Processing of Al-SiC Composites", Int. J. Powder Metall., **27**, 3, 227 - 235, 1991.

[93] Haghi, M. and Anand L.: 'Analysis Of Strain-Hardening Viscoplastic Thick-Walled Sphere And Cylinder Under External Pressure", Int. J. Plasticity, 7, 123 - 128, 1991.

[94] Haghi, M.: "Elasto-ViscoPlasticity of Porous Metals at Eleveted Temperatures", Ph.D. Thesis, M.I.T., December 1991.

[95] PonteCastañeda P.: "The Effective Mechanical Properties of Nonlinear Isotropic Composites", J. Mech. Physics Solids, **39**,1, 45 - 71, 1991.

[96] Weglinski, B.: "Soft Magnetic P/M Materials", in *Selective Case Studies in Powder Metallurgy*, eds. Jenkins, I., Wood, J.V., The Institute of Metals, London 1991.

[97] Zavaliangos, A., Anand, L., and von Turkovich B.F., "Towards a Capability for Predicting the Formation of Defects During Bulk Deformation Processing", *Annals of CIRP*, **40**, 267 - 271, 1991.

[98] Zehnder, A., T.: "A Model for the Plastic Heating Due to Plastic Work", Mech. Res. Comm., **18**, 1, 23 - 28, 1991.

[99] Duva, J. M., and Crow, P. D.: "The Densification of Powders by Power-Law Creep During Hot Isostatic Pressing", Acta Metall., **40**, 1, 31 - 35, 1992.

[100] Haghi M., and Anand L.: "A Constitutive Model for Isotropic, Porous Elasto-viscoplastic Metals", Mech. Materials, **13**, 37 - 53, 1992.

[101] Lee, B.,J., Mear, M.,E.: "Effect of Inclusion Shape on Stiffness of Non-Linear Two Phase Composites, Part I: Voids", to appear in J. Mech. Phys. Solids, 1992.

[102] Lee, B. J., Mear, M. E., Personal Communication, 1992.

[103] Michel, J.,C., and Suquet, P.: "The Constitutive Law of Non-Linear Viscous and Porous Materials", J. Mech. Phys. Solids., **40**, 4, 783 – 812, 1992.

[104] Needleman, A. and Tvergaard, V.: "Analyses of Plastic Flow Localization in Metals", *Applied Mechanics Reviews*, **45**, S3 – S18, 1992.

[105] Sofronis, P., McMeeking, R. M.: "Creep of a Power Law Material Containing Spherical Voids", ASME J. Appl. Mech., **59**, S88 – S95, 1992.

[106] Zavaliangos, A., and Anand, L.: "Thermal Aspects of Shear Localization in Microporous Viscoplastic Solids", Int. J. Num. Meth. Eng. , **33**, 595 – 632, 1992.

[107] Zienkiewicz, O. C.: "The Finite Element Method", McGraw-Hill, 1977.